SILICON MICROMACHINED SENSORS AND SENSOR ARRAYS FOR SHEAR-STRESS MEASUREMENTS IN AERODYNAMIC FLOWS

by

Aravind Padmanabhan

Submitted to the Department of Mechanical Engineering on February 1, 1997,

in partial fulfillment of the requirements for the degree of

Doctor of Philosophy in Mechanical Engineering

Abstract

In this thesis we report on a new micromachined floating-element shear-stress sensor for turbulent boundary layer research. Applications in low shear-stress environments such as turbulent boundary layers require extremely high sensitivity to detect the small forces (O(nN)) and correspondingly small displacements (O(Å)) of the floating-element. In addition, unsteady measurements in turbulent flows require sensors with high operating bandwidth (~20 kHz). These requirements render most of the existing shear-stress measurement techniques inadequate for this application. In response to the limitations of the existing devices, we have developed a sensor based on a new transduction scheme (optical position sensing by integrated photodiodes). The sensors developed in this thesis have a measured resolution of 0.003 Pa, with a measured range of 133 Pa and the dynamic response of the sensor has been measured to 10 kHz.

The new sensor comprises of a floating-element which is suspended by four support tethers. The element displaces in the plane of the sensor chip under the action of the wall shear stress. The displacement of the element causes a 'shuttering' of the photodiodes which are placed symmetrically underneath the element on the leading and trailing edge. Under uniform illumination from above, the differential photocurrent (normalized by the average current) from the photodiodes is directly proportional to the magnitude and sign of the shear stress. A set of analytical expressions were developed to predict the static and dynamic response characteristics of the sensor. Based on these estimates, sensors of two different floating-element sizes - 120 μm x 120 μm x 7 μm and 500 μm x 500 μm x 7 μm - were fabricated.

The devices were statically-calibrated in a laminar flow. The static calibration was performed in a custom-designed laminar-calibration flow cell. The sensors have been calibrated over a range of four orders of wall shear stress (0.003 Pa - 10 Pa) and have demonstrated a linear response over the entire regime (the measured non-linearity was 1% (or better) over the four orders of wall shear stress). In addition, the sensors have shown excellent repeatability, long-term stability and minimal drift. The lowest measured shear stress of 0.003 Pa is three orders of magnitude lower than that has been measured before using micromachined floating-element sensors.

The dynamic response of the sensors has also been experimentally verified to 10 kHz. This measurement was performed in a custom-designed plane wave tube (PWT) which was capable of generating oscillating shear stresses of known magnitudes and frequencies, via acoustic plane wave excitation. The measured shear stress showed a square-root of frequency dependence, as predicted by the theoretical relationship. This is the first time that the dynamic response of a floating-element sensor has been experimentally verified using a direct scheme.

The sensors have been tested in both laminar and turbulent boundary layers in the low-speed, low-turbulence wind tunnel at MIT. The response in the laminar boundary layer was found to be linear with the same sensitivity as measured in the laminar-calibration flow cell. The sensor was able to transduce shear stresses of 0.01 Pa and lower, in the laminar boundary layer. The same device also demonstrated a linear response during measurements in a turbulent boundary layer.

We have made design improvements in the second-generation of floating-element sensors. The first-generation sensors employed a two-photodiode differential sensing scheme. This design

was sensitive to non-uniformities in the incident illumination. In order to minimize this we have developed a new three-photodiode scheme. The new scheme was designed to null out any linear gradients in the intensity and has demonstrated 94% reduction in sensitivity to intensity variations when compared to the earlier design. The new photodiode design was implemented in the fabrication of one-dimensional arrays of sensors. The sensor arrays have been calibrated in a laminar flow environment. They exhibited a linear response with a measured sensitivity which was in good agreement with the theoretically predicted value.

Thesis Supervisor: Kenneth S. Breuer
Title: Associate Professor of Aeronautics and Astronautics

Thesis Supervisor: Martin A. Schmidt
Title: Associate Professor of Electrical Engineering and Computer Science

ACKNOWLEDGMENTS

The financial support for this research was provided by the Airforce Office of Scientific Research (contract # F49620-93-1-0194) and 3M Corporation. The SOI wafers used for the second-generation sensors were provided by Motorola Semiconductor Products Sector (Direct Wafer Bonding Group).

First of all, I would like to thank my thesis advisors, Prof. Marty Schmidt and Prof. Kenny Breuer for giving me an opportunity to work on this project and for their intellectual and moral support over the past four years. The original micromachined floating-element sensor was developed by Marty (as part of his Ph.D thesis). Several aspects of the work presented in this thesis are a direct follow-up of the original work.

Marty has been a great source of inspiration for me. His emphasis on "in-depth" understanding of a problem, constructive criticism, and words of encouragement have helped me considerably. I would also like to thank Marty for his interest and contribution in my professional and personal growth. I will always remember Kenny for his ability to come up with good ideas in an impromptu fashion. His ideas and tough questioning have helped me to "stay on track" and this thesis has benefited greatly as a result.

I would like to take this opportunity to thank Prof. Ain Sonin for agreeing to serve as the chairman of my thesis committee and for his insightful comments during various stages of this work. I would also like to thank Prof. Pat Leehey of MIT and Prof. Raimo Hakinnen of Washington University (St. Louis), for the numerous discussions on the issues associated with using floating-element sensors in turbulent boundary layers.

My association with my fellow graduate students and Post-docs has been thoroughly enjoyable and a great learning experience. I would first like to mention two people who have directly impacted this work in a big way: Dr. Howard Goldberg was an invaluable help during the design and fabrication of the first-generation sensors. He conceived of the novel interconnect scheme used for the devices. I have learned a lot about MEMS processing from Howard and I am thankful to him for that; Dr. Mark Sheplak designed the plane wave tube that we used for the dynamic calibration of the devices. I would also like to thank Mark for the endless discussions we have had on this topic and for the "interesting" lunch time conversations. Dr. Errol Arkilic was always available for "hardware" related questions. I have to specially thank him for his help during the design of the calibration flow cell and for the smooth functioning of the ECE jig. Lalitha Parameswaran and Charles Hsu showed incredible patience in answering my stupid processing related questions. I would also like to thank Charles for being my Mac-consultant. I am also thankful to Lalitha for being an excellent "tour guide" during our trip

to Stockholm! Ravi Srinivasan and Joey Wong have been great officemates. I am thankful to Ravi for being indirectly responsible for my initiation into MEMS. All the other past and present members of our research group have assisted me in some way or the other over the years. I would like to thank: Arturo Ayon, Ted Bloomstein, Rob Devoto, Samara Firebaugh, Albert Folch, John Gilbert, Stu Jacobson, CC Lin, Vince McNeil, DJ Orr, Ed Piekos, Ruben Rathnasingham, and Joel Voldman. I have been really fortunate to have some diligent UROPs work with me during different stages of this project. I would like to thank Anthony Accardi for building the measurement circuit and for his assistance in measurements, Sarah Lee for her help in setting up the plane wave tube apparatus and Mike Fedor for all the measurements in the plane wave tube.

I wish to thank all the staff of MIT Microsystems Technology Labs for keeping the equipment in the various labs in operating condition and for their assistance when I was processing. I would like to specially thank Octavio Hurtado for his invaluable assistance in TRL, Paul Tierney & Dan Adams for their help in mask making (especially overnight mask making!), Tim Tyson for implanting the wafers in quick time, Brian Foley for his help (and friendly conversations) in ICL, and Joe Walsh for his help with the e-beam and wire-bonder.

I would also like to thank Leslie Regan (in the ME Grad office), Ping Lee, Pat Varley, and Jean Sofronas for their help with all the "bureaucratic stuff".

I have made some really good friends, during my stay in Boston. I am thankful to all of them (especially Maria Ferrera) for their friendship and support.

Finally, I would like to thank my family (parents, brother, sister and brother-in-law) for their moral support and encouragement through out my educational career. My parents have made innumerable sacrifices for my education and I find it difficult to express my gratitude in just a few words. As a tribute, I dedicate this thesis to them.

CONTENTS

LIST OF FIGURES

LIST OF TABLES

Chapter 1. INTRODUCTION

The measurement of wall shear stress provides valuable information about viscous drag, transition to turbulence, flow separation and other flow phenomena. In addition, shear-stress measurement can also be used as a means of detection of turbulent structures and hence shear stress sensors are good candidates for use in the active control of turbulent flows [1]. In this thesis we report on a new micromachined floating-element shear-stress sensor for turbulent boundary layer research. The sensors developed in this thesis have a shear-stress resolution of 0.003 Pa and a measurement range of 133 Pa. Also, the dynamic response of the sensors has been experimentally verified to 10 kHz.

In this chapter we first present a brief description of the origin of wall shear stress, followed by a description of the sensor specifications that are desired to make accurate measurements in low shear-stress environments. A summary of the existing measurement techniques (with an emphasis on the floating-element sensor) and their inadequacies for low-magnitude shear-stress measurement is presented next. An overview of micromachining and a description of the commonly used micromachining technologies for sensor fabrication is also presented. The final section of this chapter presents the outline of this thesis.

1.1 Origin of Wall Shear-Stress

Whenever there is a relative motion between a surface and a fluid, the surface experiences a resultant force due to the interaction. The interaction between the surface and the fluid can be described in terms of the stresses at the fluid-surface interface. The stresses acting on the body are: (a) shear-stress, τ_w acting tangential to the surface and in the direction of the flow and (b) normal stress or pressure (P_w) acting normal to the surface.

Figure 1.1 schematically illustrates the origin of shear stress in a two-dimensional boundary layer. It can be seen that a flow with a uniform velocity develops a non-uniform velocity profile in the vicinity of the wall. If $y = 0$ represents the wall, the velocity at $y = 0$ is equal to zero, to satisfy the no-slip boundary condition. The velocity reaches the freestream value of U at some distance from the wall, known as the boundary layer thickness. Hence a non-uniform velocity profile is set-up near the wall. The magnitude of the wall shear stress (in the X-direction) is proportional to the gradient of the flow velocity at the wall and can be written as (for a Newtonian fluid):

$$\tau_w = \mu\left(\frac{\partial U}{\partial y}\right)_{y=0} \tag{1.1}$$

where the constant of proportionality μ is the dynamic viscosity of the fluid and U is the streamwise (X-direction) velocity.

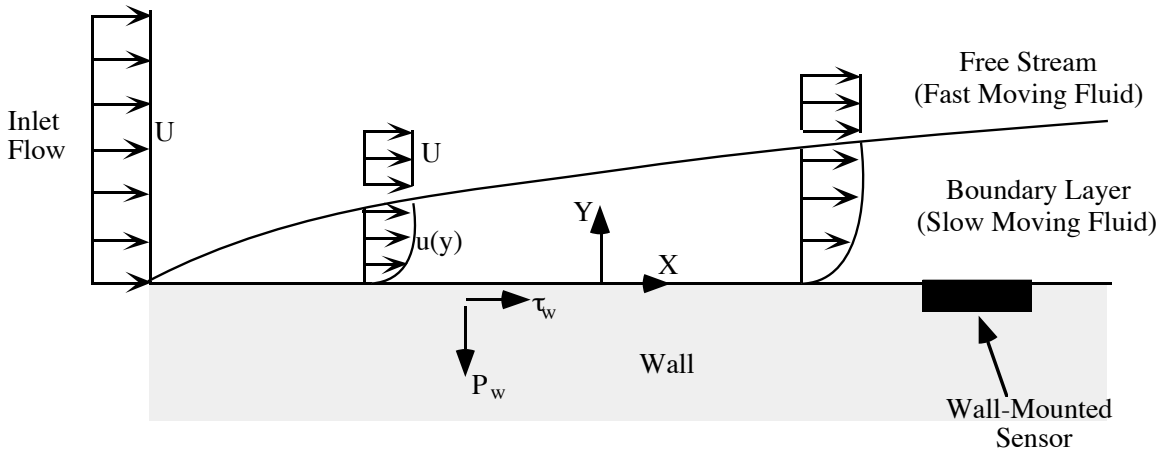

Fig. 1.1 Schematic diagram illustrating the origin of wall shear stress in a two-dimensional boundary layer

The physics of the origin of the wall shear stress can be understood from the typical molecular-motion picture in such a moving fluid. If a molecule moves from a region of low-velocity to a region of high-velocity, it tends to act as a drag in the high-velocity region and this resists the motion of the fluid in the high-velocity region. Similarly molecules moving from a region of high velocity to a region of low velocity tend to accelerate the flow. Therefore, there is a net transfer of *X*-direction momentum due to the molecular motion. The wall shear stress is a consequence of this momentum transfer and is equal to the ratio of the net rate of change in X-direction momentum and the surface area of the plate.

1.2 Motivation For Shear-Stress Measurements and Sensor Specifications

Most of the flows occurring in nature and in engineering applications are turbulent. In order to estimate the various parameters associated with such flows and to develop a physical model for turbulence, it is necessary that we have a good understanding of the characteristics of the turbulence process. Though a considerable amount of theoretical modeling and simulation of turbulent flows has been done, there is a lack of good experimental data at length and time scales that are most critical. Presently, accurate quantitative predictions in turbulence rely considerably on simulation results/empirical data, and significant future advances in turbulence depends on the availability of flow data at turbulent length and time scales. The rapidly growing results from computer simulations have given experimentalists a new incentive to make measurements of fundamental quantities in turbulent flows more precisely than might have been considered acceptable before [2]. In the customary description of turbulence there are always more unknowns than equations. This is known as the closure problem. At present this gap is closed using

Flow Situation	Typical value of the Shear Stress
Dolphin moving at a speed of 1.5 mph (0.6 m/s)	0.6 Pa
Automobile traveling at 60 mph	1 Pa
Airplane cruising at speed of 250 mph	2 Pa
Ship traveling at 20 mph	40 Pa
Polymer extrusion process (typical velocity ~ 1-3m/s)	1 kPa - 100 kPa

Table 1 Typical values of shear stress (on the surface) in different flow situations. For all the estimates (except the polymer extrusion case) it is assumed that the bodies are sufficiently streamlined and hence-skin-friction is the dominant form of drag.

turbulence models that are usually empirical and many times rely on ad hoc assumptions. In order to develop a formal theory of turbulence, it is necessary to have sophisticated models that have been validated by experiments. The measurement of flow parameters in the immediate vicinity of the wall will provide the necessary experimental information required for turbulence modeling and also for various types of flow and heat transfer predictions [2]. One such flow parameter that can be used to provide this information is the wall shear stress. Shear-stress probes are useful for studying the structure of turbulent boundary layers and can be incorporated in sensor-actuator systems used for active control in turbulent boundary layers [1].

The magnitude of the shear stress (to be measured) depends on the flow situation. Table 1 lists the typical values of shear stresses encountered in some common flow situations. The shear stress numbers for some of the examples are based on the listed values of the drag (or skin-friction) coefficient [3]. For complex bodies (ex: airplane, automobile, pasenger train etc) the drag was obtained by treating the body as a collection of parts. For example, the drag on an airplane can be approximated by adding the drag produced by its various components--the wings, fuselage, tail section, and so on. Such an approximation provides reasonable order-of-magnitude (and not exact) estimates of the wall drag. This thesis focuses on the development of sensors and sensor arrays for

measurements of low-magnitude (τ_w ~ 0-100 Pa) shear stresses in laminar and turbulent aerodynamic flows.

The sensor requirements depend on the flow environment. In laminar flows the sensors must be capable of measuring the average shear stress. In a turbulent boundary layer the wall shear stress has a mean shear component $\overline{\tau_w}$ and a fluctuating shear component τ_w'. The mean shear stress is related to the overall state of the flow and can be used to determine average properties like drag on surfaces. The fluctuating component of the shear is a footprint of the individual unsteady flow-structures that transfer momentum to the wall and is a good indicator of the turbulence activity within the flow. It is desirable that the sensor designed to measure wall shear stress in a turbulent boundary layer be capable of measuring both these components accurately. In order to understand the requirements for sensors designed to measure the wall shear stress in a turbulent boundary layer, it is useful to know the various parameters of interest in such a flow. Table 2 lists the analytical expressions [4] and the typical values of the various parameters in a turbulent boundary layer in the low-speed wind tunnel at MIT. It can be seen from Table 2 that the sensors need to operate in a high Reynolds number environment. The typical characteristic length scale (ℓ) and time scale (t) in such an environment are equal to 30 μm and 58 μs, respectively. In order to make accurate measurements in a turbulent boundary layer the minimum sensor size must be 4ℓ or 120 μm [1] and this sensor must have a temporal resolution of 58 μs (or bandwidth of 17 kHz). This sensor size and bandwidth will minimize any spatial and temporal averaging of the measured shear stress. A number of researchers have made measurements of fluctuating wall shear stress in a flat-plate boundary layer and in channel/pipe flows. These measurements show a large scatter in the measured fluctuating shear stress, in many cases, using the same devices under the same flow conditions [2]. This is because these sensors do not possess the desired spatial and temporal resolution and hence average the measured fluctuating shear stress to different extents (depending upon their size).

The sensors that possess the desired spatial and temporal resolution (sensor size = 120 μm and bandwidth = 17 kHz) are also useful for the active control of turbulent flows. Real time control of turbulent flows requires detection and actuation at the above-described length and time scales [1]. A practical control application would require the distributed measurement of wall shear stress using an array of sensors. A detailed description of the requirements on the shear-stress sensor arrays for such a control application are presented in section 2.10.2 of the sensor design chapter.

Parameter	Analytical expression	Typical value in the low-speed and low-turbulence wind tunnel at MIT
Freestream velocity, u_∞	u_∞	15 m/s
Reynolds number based on streamwise distance, Re_x	$Re_x = \frac{u_\infty x}{\upsilon}$	1.2×10^6
Boundary layer thickness, δ	$\delta(x) = 0.37\ x\ Re_x^{-0.2}$	2.7 cm
Displacement thickness, δ^*	$\delta^* \approx \frac{\delta}{8}$	0.34 cm
Momentum thickness, θ	$\theta \approx \frac{7\delta}{72}$	1.6 cm
Reynolds number based on momentum thickness, Re_θ	$Re_\theta = \frac{u_\infty \theta}{\upsilon}$	16000
Wall shear stress, τ_w	$\tau_w \approx \frac{0.03\ \rho\ U^2}{(Re_x)^{0.2}}$	0.48 Pa
Friction velocity, u_τ	$u_\tau = \sqrt{\frac{\tau_w}{\rho}}$	0.6 m/s
Characteristic length-scale, ℓ	$\ell = \frac{\nu}{u_\tau} = 9\ Re_\theta^{1/8}\ \frac{\upsilon}{u_\infty}$	30 μm
Characteristic time-scale, t	$t = \frac{\nu}{u_\tau^2} = 78\ Re_\theta^{1/4}\ \frac{\upsilon}{u_\infty^2}$	58 μs

Table 2 List of parameters for flat-plate turbulent boundary layer [4]. The calculated values in this table are based on x = 120 cm, which is the location at whicg our shear-stress sensor was mounted

The most important issue associated with the design of sensors for low-magnitude shear-stress measurements in laminar and turbulent air flows is the ability to develop a transduction mechanism that allows the measurement of the mean and fluctuating components. The next section presents an overview of the existing measurement techniques and explains why existing sensors are incapable of measuring such a small wall shear stress, with the above-mentioned spatial and temporal resolution.

1.3 Shear-Stress Measurement Techniques

The wall shear stress can be measured by different methods depending upon the application under consideration. The required size and bandwidth of the sensors are also application-specific. Figure 1.2 illustrates the various available shear stress measurement techniques. The measurement

techniques can be broadly classified as direct or indirect methods, depending upon whether they directly measure the wall shear stress or infer it from other measured properties. The number of available techniques is enormous and hence it is not possible to discuss each technique and the measurement results in this thesis. We will therefore discuss only the principal categories of shear-stress measurement and their usefulness for the present application. This section is divided into: a) conventional shear-stress measurement techniques; and b) micromachined shear-stress measurement techniques.

1.3.1 Conventional Shear-Stress Measurement Techniques

In this thesis, the term conventional techniques refers to methods that employ sensors that are not micromachined in silicon. There are several review papers that discuss in detail the merits and drawbacks of these devices in a variety of flow situations and for a wide range of applications [5, 6, 7, 8]. Table 3 provides a summary of these papers. The conventional sensing schemes can be broadly categorized into direct and indirect types, as shown in Fig. 1.2.

Indirect Techniques

The indirect conventional techniques can be the following:

a) Surface-obstacle type devices [9, 10, 11, 12]:
- Stanton tube/razor blade
- Preston tube
- uni- and bi-directional fences

b) Sensors based on heat and mass transfer analogies [13, 14, 15, 16, 17]:
- hot films
- hot wires
- electrochemical techniques - surface films based on evaporation/sublimation

c) Sensors that infer the shear stress from the near-wall velocity profile [18, 19]:
- use of Clauser charts
- law of the wall sensors

The surface-obstacle type devices measure the shear-stress by creating a separated flow field in front of the obstacle that is embedded in the boundary layer. From a momentum balance it can be shown that there is an increase in the pressure at the front face of the obstacle, over the static pressure in the boundary layer. The calibration of the device is governed by a relationship between the non-dimensional pressure rise and the non-dimensional shear-stress [8]. The nature of this calibration in a turbulent boundary layer is sensitive to the size and geometry of the obstacle. In addition, the calibration also depends on the location of the probe relative to the boundary layer

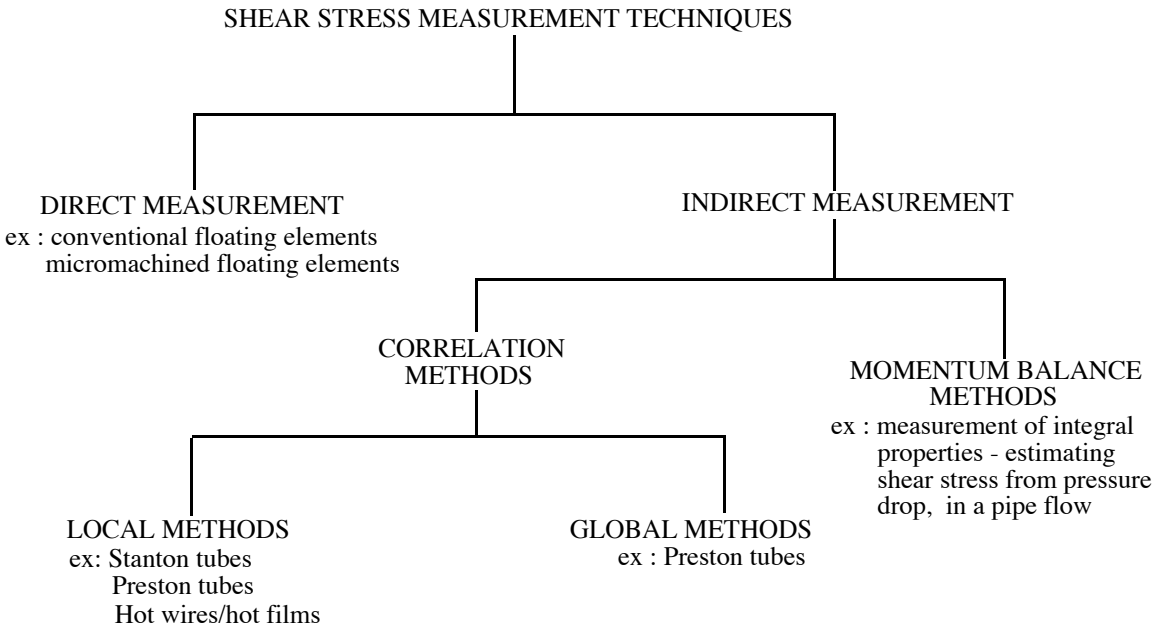

Fig. 1.2 Shear-stress measurement techniques

Author	Year of Publication [reference]	Comments
K. G. Winter	1977 [5]	Comprehensive review of the available conventional measurement technqiues (except methods based on heat and mass transfer) upto 1977. Good discussion of issues associated with measurements in turbulent boundary layers.
T. J. Hanratty & J. A. Campbell	1983 [6]	Good discusion of experimental issues associated with using the various shear stress sensors.
J. H. Haritonidis	1989 [7]	Comprehensive review of all conventional technqiues and the original micromachined sensor. Good discussion of sources of error associated with each technique during measurements in turbulent boundary layers.
R. J. Hakkinen	1991 [8]	Recent survey of all the conventional measurement technqiues. Good summary of the merits and drawbacks of the various methods. Extensive list of references.

Table 3 Summary of review papers on conventional shear-stress measurement techniques

velocity profile. Another drawback of these devices is that proper care must be exercised in employing them in any flow situation where the assumptions underlying the calibration

relationships are violated (examples: flow separation, accelerated or non-equilibrium flows). Also, the calibration of these devices depends on the boundary layer velocity profile, and they are essentially steady-state devices with very limited usefulness in fluctuating shear-stress environments.

The sensors based on heat and mass transfer analogies can be used to estimate the wall shear-stress based on the heat and mass flux exchange between the device and the flow. The attractive features of this technique are its small size, high-sensitivity in low-shear environments, non-intrusive mounting, ability to operate in high pressure gradients and high-frequency response. Hence these devices seem suitable for measurements of low-magnitude fluctuating shear stress. In practical applications, however, they have suffered from calibration and repeatability problems due to substrate conductivity. In particular, measurements in high-frequency fluctuating flows have presented uncertainties (example: heat transfer to the substrate) [8]. Another drawback of this technique is that it depends on correlations (heat/mass to momentum transfer analogies) to relate the measured flow properties to the wall shear stress. Hence the accuracy of the measured shear stress depends on the accuracy and the validity of the empirical and semi-empirical correlations.

The wall shear stress can also be estimated from a measurement of the near-wall velocity profile [18]. This may require measurements by invasive probes. The use of optical techniques (which is a non-invasive measurement) is practically limited only to sufficiently thick boundary layers. The use of the optical technique in thin boundary layers makes the measurement process very complex. The most widely used inference technique uses the matching of the near-wall velocity profile with the logarithmic law-of-the-wall (widely known as the Clauser plot) [19]. This technique is useful only if the logarithmic region of the velocity profile can be identified and measured, which is particularly difficult in flows with large pressure gradients. Some of the indirect measurement techniques are schematically illustrated in Figs. 1.3a, 1.3b and 1.3c.

Direct Techniques

The direct measurement techniques measure the local wall shear using a plate or floating-element type structure, which is flush-mounted on the wall bounding the flow (Fig. 1.3d). The floating-element displaces under the action of the wall shear stress, and this motion is then directly measured. This method has been extensively used for wind tunnel measurements since the early1950's [20, 21, 22, 23, 24, 25]. In addition to the obvious advantage of direct shear-stress measurement, these devices have been used to calibrate the various indirect measurement techniques. There are, however, some problems associated with making measurements with these type of devices. We will discuss each of these problems in more detail since the performance of the floating-element type sensors is critically dependent on them. Table 4 compares the conventional

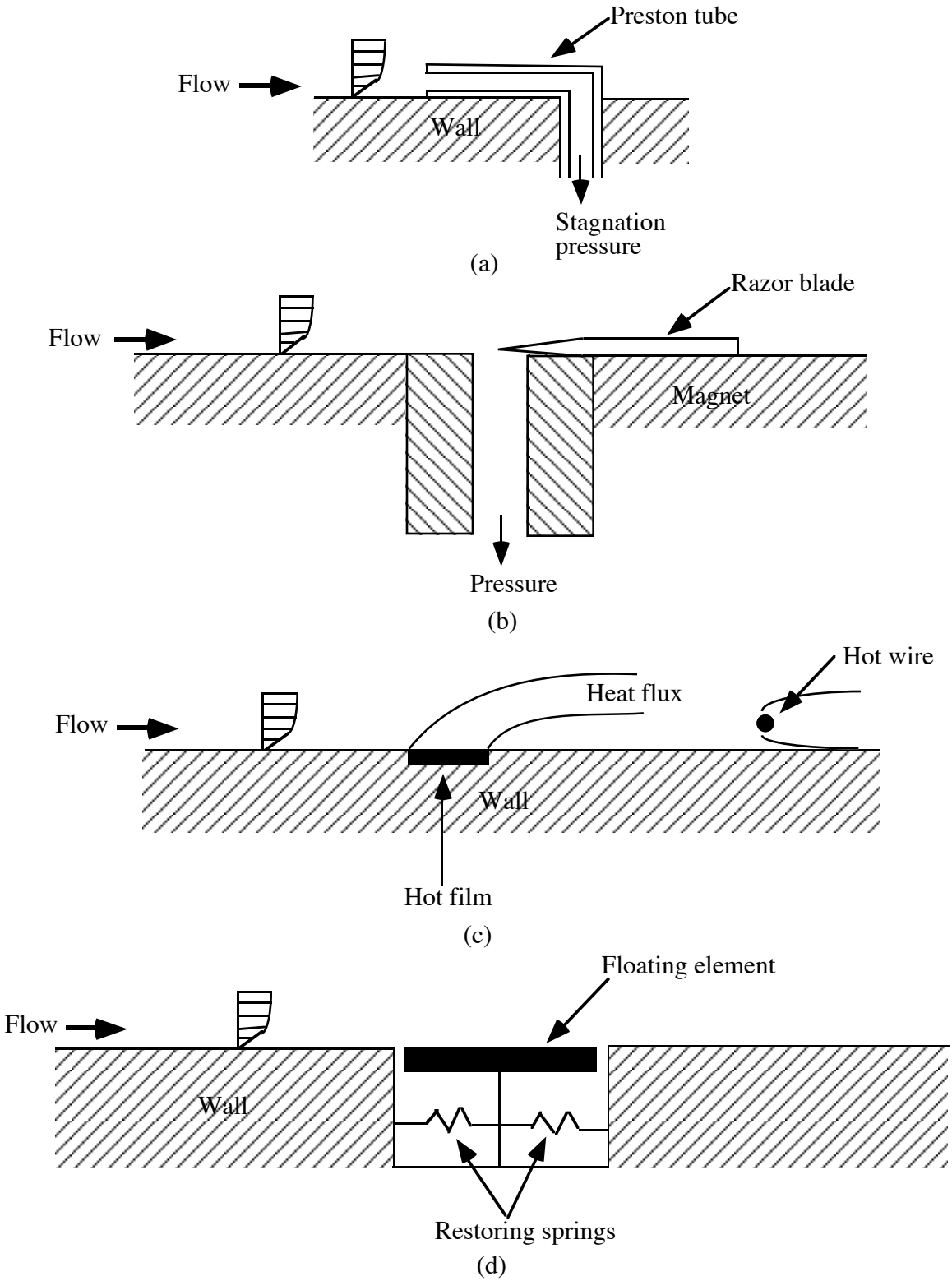

Fig. 1.3: a) Side view of a Preston tube; b) side view of a razor blade (Stanton tube); c) illustration of sensors based on heat-momentum transfer analogies; d) floating-element balance

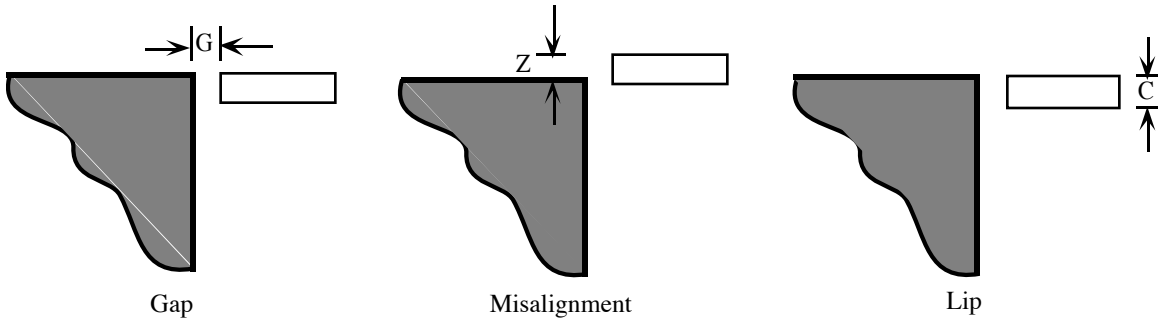

Fig. 1.4 Various parameters that affect the performance of floating-element sensors

and micromachined floating-element sensors in the context of each of these problems. Figure 1.4 schematically illustrates the various paramaters of interest in a floating-element type sensor. The problems associated with floating-element sensors are:

1) *Effects of the gaps around the element.* The use of a floating-element type sensing structure necessitates the presence of gaps around the element. The presence of these gaps and cavities affects the sensor performance. This effect has been investigated in detail by Allen [26]. The presence of gaps causes a perturbation of the flow field. If the gap size is less than a few viscous length-scales ℓ ($\ell = \nu/u_\tau$), it will not disturb the flow [27]. For measurements in the low-speed wind tunnel at MIT, $\ell = 30$ μm (from Table 2) and hence gap sizes smaller than this value will not result in errors in the measured values. The presence of gaps also results in flow around the element, in the presence of a pressure gradient. This is significant only in large pressure gradient flows.

2) *Effects of misalignment of the floating-element.* The sensor response is also affected by the lack of perfect "flushness" of the element with the wall. A misaligned (protruded or recessed) element results in a perturbed flow field around the sensor, as shown in Fig. 1.5. The resulting pressure force acting on the element can lead to errors in the measured shear stress. Allen [26] reports that the sensor is more sensitive to the misalignment at small gap sizes. Also, for a given gap size, $Z > 0$ and $Z < 0$ result in errors of similar magnitudes. Hence the widely held belief that a recessed element is better, is not correct. The magnitude of the effective shear stress acting on a misaligned floating-element has been derived to be [1.28]:

$$\tau_{w,eff} = \left[1 + \frac{1}{3} \frac{\rho x^3}{\mu^2 L_e^2} \tau_w \right] \tau_w \tag{1.2}$$

where x is the misalignment of the element, L_e is the length of the floating-element and ρ and μ are the density and viscosity of the fluid, respectively. The second term in the bracket of equation (1.2)

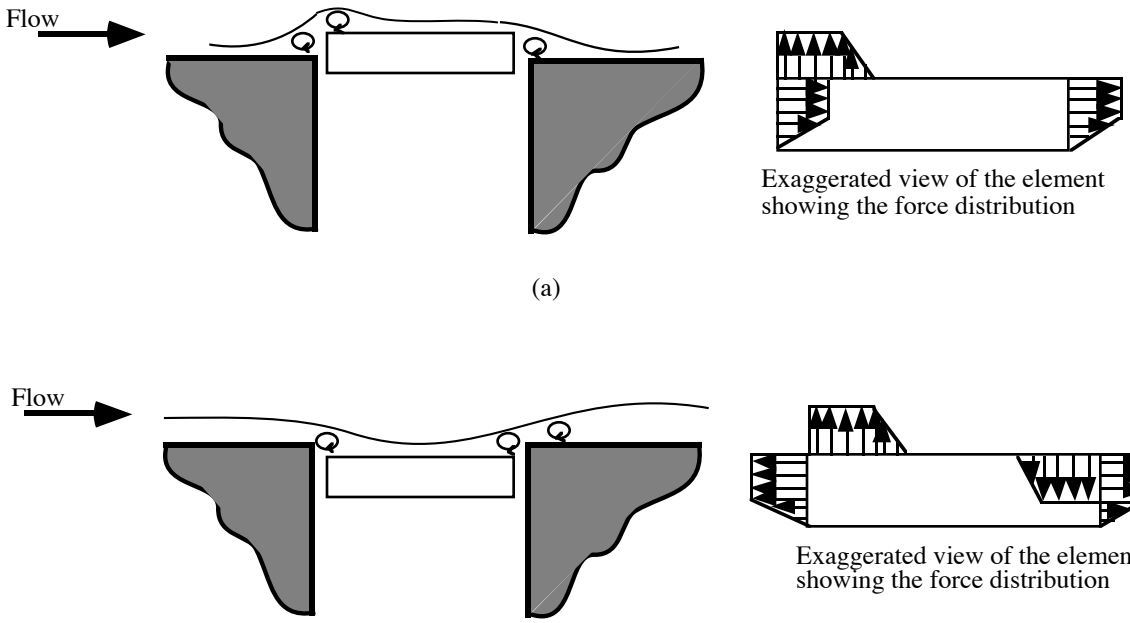

Fig. 1.5: (a) Schematic diagram illustrating the effect of a protruded floating-element and the resulting force distribution on the element; (b) effect of a recessed floating-element (adapted from [5])

is the net error contribution due to the misalignment. For a floating-element misaligned by x = 3 μm, the magnitude of the misalignment error for a conventional floating-element (L_e = 1) cm is 3 x 10^{-4}%, during the measurement of wall shear stress of 1 Pa in air. For a typical micromachined floating-element (L_e = 120 μm), the error is 0.025%. Hence the magnitude of the error is negligible (for both cases) for typically expected misalignments of few microns.

3) *Effect of pressure gradients*. The effect of pressure gradients is illustrated schematically in Fig. 1.6. There are two sources of error arising due to pressure gradients. The first one is the lip force, which is the net pressure force acting on the lip (this is equal to the product of the differential pressure and the cross-sectional area of the element). The second source of error is due to the flow beneath the element caused by the pressure gradient. This results in a shear stress τ_g acting on the bottom face of the element, as shown in Fig. 1.6. The magnitude of the effective shear stress acting on the element in the presence of a pressure gradient has been derived to be equal to [28]:

$$\tau_{w,eff} = \left[1 + \frac{g}{h} + \frac{2t}{h}\right] \tau_w \qquad (1.3)$$

where t is the lip size (element thickness), g is the depth of the cavity under the element and h is the height of the channel. The second and third terms in the bracket of equation (1.3) contribute to the

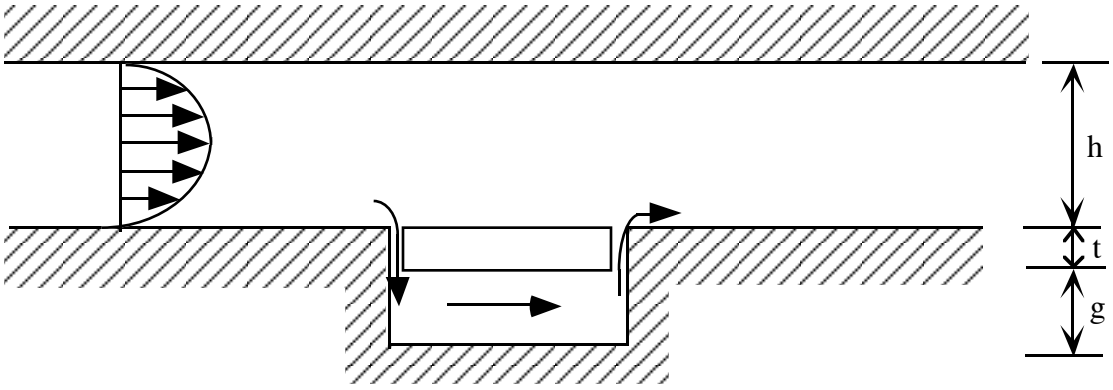

h = channel height, t = floating-element thickness, g = cavity depth

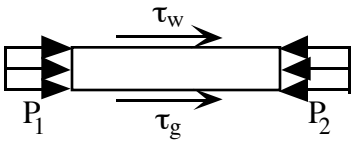

Fig. 1.6 Schematic diagram illustrating the forces acting on the floating-element in a pressurized channel flow

error in the measured shear stress. It must be noted that the error is independent of the streamwise extent of the element, L_e. It has been shown that the percentage of this error can be as high as 50% in large pressure gradient flows [8]. It is the large magnitude of this error that has resulted in floating-element sensors being relegated to use on flat or cylindrical surfaces with small pressure gradients. The magnitude of this error can, however, be considerably reduced by the use of a thin floating-element, which is suspended over a shallow cavity, as is the case in micromachined floating sensors. For measurements in a channel of height h = 508 μm (this is the channel height used for experiments in this thesis for sensor calibration in the range $0 \le \tau_w \le 1$ Pa) the total error is equal to 2% for a micromachined floating-element and as high as 1100 % for a conventional floating-element (Table 4). The pressure gradient induced error can also be minimized by using the gap-sealing technique proposed by Frei and Thormann [29]. The cavity beneath the floating-element is filled with a high surface tension liquid like glycerine. In such a back-filled sensor, the pressure differential results only in a change in the shape of the meniscus of the cavity fluid and has no effect on the pressure acting on the lip of the floating-element. Hence the effect of a pressure gradient can be effectively reduced to a net surface tension component reflecting in the difference of the meniscus contact angles in the gaps. This technique has been successfully applied by Frei and Thormann in the calibration of a floating-element balance in the presence of a pressure gradient.

The main drawback of this method is in the ability to retain fluids in the gap under high pressure differentials and in the ability to operate at high temperatures [29].

Parameter	Comments	
	Conventional floating-element sensor	Micromachined floating-element sensor
Effect of gaps	Typical gap sizes are O(mm) and can cause flow perturbation since this is greater than a few viscous length scales in a turbulent boundary layer.	Typical gap sizes are O(μm) and will not cause flow perturbation since this is smaller than a few viscous length scales in a turbulent boundary layer.
Error due to a misalignment of x = 3 μm (shear = 1 Pa) (using equation (1.2))	3 x 10^{-4} %	0.025 %
Effect of pressure gradients for measurements in a channel of height, h = 508 μm (using equation (1.3))	1100 % (for a cavity depth of 1 mm)	2 % (for a cavity depth of 1 μm)
Equivalent shear stress due to *one-g* acceleration	196 Pa	0.16 Pa
Acoustic frequency corresponding to wavelength = element size	34 kHz	2.93 MHz

Table 4 Comparison of the magnitudes of the errors (due to various sources) for the conventional and micromachined floating-element sensors. The calculated values are based on typical conventional floating-element sensors (manufactured in steel) of size = 1 cm x 1 cm x 0.25 cm and a silicon micromachined sensor of size = 120 μm x 120 μm x 7 μm

4) *Effects of acceleration.* The acceleration sensitivity is a problem for a sensor that is used in a moving system. For a given acceleration, we can define an equivalent wall shear stress as:

$$\tau_{eff,\,accn} = \frac{Equivalent\ shear\ force}{Area\ of\ the\ element} = \frac{mg}{A_e} = \rho t g \tag{1.4}$$

where ρ is the density of the element and t is the element thickness. For a conventional floating-element made of steel, the equivalent shear stress for *one-g* of acceleration is 196 Pa, as shown in Table 4. For a silicon micromachined floating-element, the equivalent shear stress for *one-g* of acceleration is 0.16 Pa. The acceleration sensitivity of a floating-element sensor can be considerably minimized by employing a novel design [5]. In this design a counterweight is placed under the element such that the center of gravity of the system for lateral acceleration is at the pivot point.

5) *Effect of the normal pressure*. During measurements in a turbulent boundary layer, the sensor will be subjected to normal pressure fluctuations. The normal pressure could be due to the acoustic pressure waves or due to the transfer of vertical momentum between the turbulent eddies and the

floating-element. If the size of the floating-element is smaller than the characteristic length-scale associated with the pressure fluctuations, the effect of the pressure fluctuations will be felt uniformly across the element (it will then contribute to a common-mode signal in a differential sensing scheme and will not result in any error). The characteristic length-scale could either be the wavelength of the acoustic pressure wave or the size of the smallest eddy. The acoustic pressure waves will have a wavelength depending upon the speed of sound in air, c (340 m/s, at room temperature) and the acoustic frequency, f. The acoustic wavelength λ is given as $\lambda = c/f$. For a conventional floating-element, this corresponds to a frequency of 34 kHz. This could be a problem in a turbulent boundary layer. For a micromachined floating-element, this corresponds to a frequency of 2.83 MHz. This is much higher than any frequency that is likely to be encountered in a turbulent boundary layer, and hence acoustic pressure fluctuations should not be a problem for micromachined floating-element sensors.

6) *Effects of temperature changes*. This effect is important when the floating-element, the substrate and the anchor that connects the element to the substrate, are made from different materials. The different thermal expansion coefficients of each material will result in different strains in each member due to an imposed temperature change. Since the members are connected, there will be non-uniform expansion effects that could result in out-of-plane deformation and torsion of the element.

The summary of the above-described error sources is that the magnitude of the error (due to each source) is typically smaller for a micromachined floating-element sensor compared with a conventional floating-element sensor, as shown in Table 4.

The main drawback of the conventional (not micromachined) floating-element type sensors is that they have poor spatial and temporal resolution for low-magnitude shear stress measurement. In order to obtain a measurable output signal in a low-shear environment, a large sensing element is required. This results in a loss of spatial resolution. Similarly, the need for a compliant structure to accurately transduce low-magnitude shear stresses results in a loss of bandwidth. Hence it is not possible to simultaneously achieve a high sensitivity and high bandwidth, as illustrated schematically in Fig. 1.7. The next section discusses how the use of silicon micromachined floating-element sensors has pushed this sensitivity-bandwidth horizon upwards, thereby permitting measurements in low-shear turbulent boundary layers.

Another type of direct measurement technique has been recently developed [30]. It involves the measurement of the torque acting on a small cylindrical body placed above the wall deep in the viscous sublayer. The magnitude of the torque produced is directly proportional to the wall shear stress. The angular displacement of the cylinder (is proportional to the torque acting on it) is

directly measured. This scheme uses an invasive sensor and was designed for measurements of

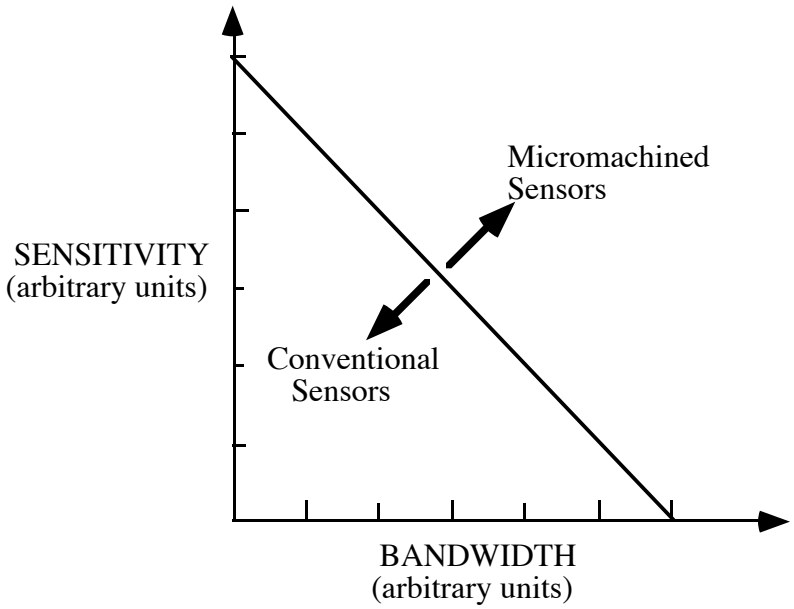

Fig. 1.7 Sensitivity-bandwidth tradeoff in shear-stress sensors

shear stress in the range of 100 Pa. The sensor had an operating bandwidth of 500 Hz which is inadequate for the present application. In addition to the above described direct and indirect techniques, there are some hybrid approaches to shear-stress measurement [31, 32]. These devices do not possess the sensitivity or bandwidth to make unsteady measurements in a turbulent boundary layer.

1.3.2 Micromachined Shear-Stress Sensors

In this sub-section we first present an overview of micromachining. The different micromachined shear-stress sensors that have been previously developed, is presented next.

Overview of Micromachining

Silicon has become synonymous with integrated circuit technology thanks to its spectacular electronic properties. Silicon integrated circuit technology has been responsible for creating whole new industries in electronics and for revolutionizing the field of information processing. It is only recently (in the last 15 years) that its equally impressive mechanical properties have been exploited for the manufacture of miniature mechanical devices and mechanical systems. Silicon has an elastic modulus comparable to that of stainless steel ($E_{Si,(100)}$ = 190 GPa, E_{steel} = 210 GPa) and a yield strength that is about two times that of steel ($\sigma_{y,steel}$ = 4200 MPa, $\sigma_{y,silicon}$ = 7000 MPa). It surpasses

aluminum in strength to weight ratio and the lack of hysteresis in single crystal silicon makes it a perfect material for making micromechanical devices, viz., sensors, actuators and microsystems [33]. The structural engineering of silicon has permitted the fabrication of micron-sized mechanical devices alongside integrated circuits on the same silicon wafer. These microsystems provide the much needed interface between the physical world and the electronic world, thereby allowing electronic systems to sense and control physical quantities like velocity, light, force, sound etc. This discipline of combining miniaturized electronic and mechanical systems on the same substrate is called microelectromechanical systems (MEMS) and is widely known as micromachining. It must be noted that quite often MEMS stands for microfabricated electromechanical systems as opposed to microelectromechanical systems. This is because in many cases microsystems may be called MEMS due to the fact that they are manufactured using a microfabrication technology and not because they are of micron-dimensions. An excellent introduction to MEMS and an overview of the different MEMS technologies can be found in [34, 35, 36].

MEMS devices are fabricated using manufacturing processes that are similar to those used for fabricating integrated circuits (ICs). However, there are several process technologies that have been developed specifically for MEMS applications. Some of these commonly used processes are: anisotropic etching of silicon, fabrication of high-aspect ratio microstructures, anodic bonding of silicon to glass, to name a few [36]. It must be noted that throughout this thesis, the term microfabrication technology refers to a combination of IC-fabrication technology and MEMS-specific technologies that are used to fabricate microelectromechanical systems. There are several inherent advantages associated with the manufacture of sensors using microfabrication technology: i) high volume and low cost manufacture; ii) sensor arrays can be fabricated on a single chip; and iii) electronics associated with the sensor can be incorporated on the same chip, providing for a compact measurement system.

The rest of this sub-section presents a brief summary of the most widely used microfabrication technologies. The processing technologies can be broadly classified as: (a) bulk micromachining; (b) surface micromachining; (c) micromolding or LIGA process; and (d) wafer-bonding or sealed-cavity process;. We will briefly describe (a), (b) and (c) in this sub-section. A detailed description of the wafer-bonding technology is presented in section 3.2 of the sensor fabrication chapter.

Micromachining Process-Technologies

1) *Bulk Micromachining*. This is the most mature and oldest of the various micromachining technologies and has been widely used to fabricate pressure sensors [36]. Figure 1.8a shows an example of a simple device fabricated using a bulk micromachining process. By using a photolithography step, a pattern is defined on a silicon dioxide or silicon nitride masking layer on

the backside of the wafer. The wafer bulk (and hence the name bulk micromachining) is then

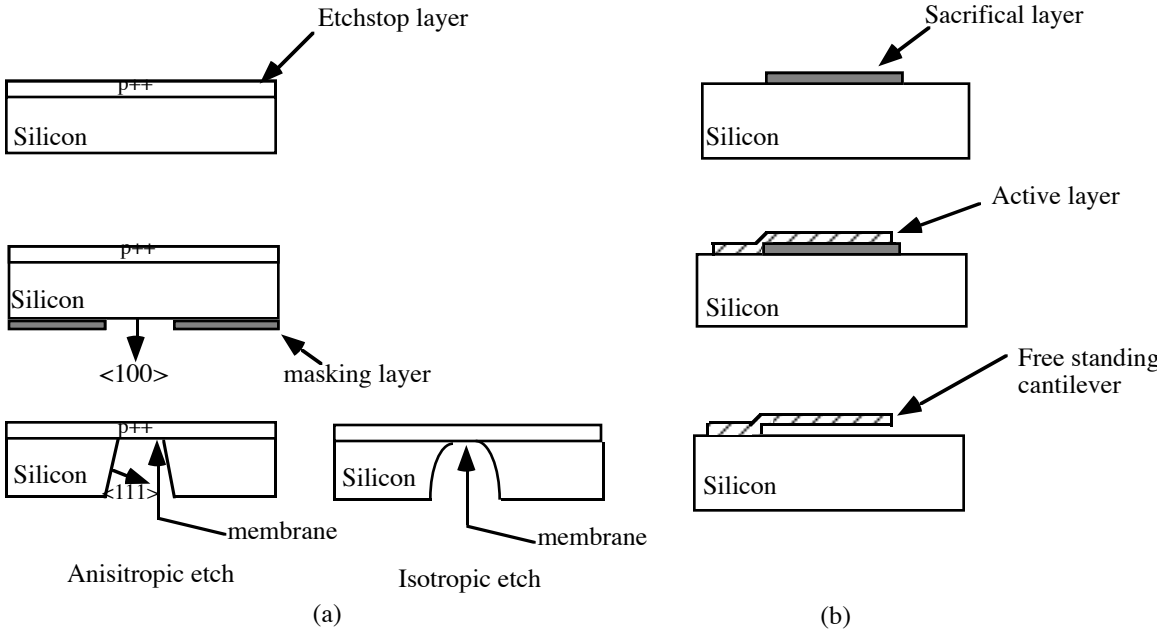

Fig. 1.8: a) Schematic illustration of the key steps in a bulk micromaching process; b) schematic illustration of the key steps in a surface micromachining process

isotropically/anisotropically etched. The thickness of the active layer (beam/diaphragm) is defined by the etch-stop technique, that is, the etching process stops on a layer whose thickness is equal to that of the desired thickness of the beam or diaphragm. The etching can be terminated using a diffused boron etch-stop, buried boron etch-stop or an electrochemical etch stop [36]. The most widely used isotropic etchant is the hydrofluoric/acetic/nitirc acid system. The anisotropic etch is typically carried out in a solution of either potassium hydroxide (KOH), cesium hydroxide (CsOH), ethylene diamine pyrocatechol (EDP) or hydrazine. These chemicals attack the <100> crystallographic planes of silicon much faster than the <111> planes. This difference in the etch rates gives rise to a 54.7° side wall angle.

One of the drawbacks of bulk micromachining is that the geometries of devices are controlled by the aspect ratios inherent in the various anisotropic etching techniques that are used. The devices are hence larger than those fabricated using other micromachining technologies. It must, however, be noted that a variation of the traditional bulk micromachining process known as the dissolved-wafer process, pioneered at the University of Michigan, allows the fabrication of smaller devices [35].

2) *Surface Micromachining*. This technique is one of the most widely used forms of micromachining today. This technology, as the name suggests, involves the fabrication of devices on the surface of a handle wafer. Figure 1.8b illustrates a simple example of a device (cantilever) fabricated using the surface micromachining process. A good review of this technology can be found in [37].

The first step in the process involves the growth or deposition of a sacrificial layer on a silicon handle wafer. The sacrificial layers that are typically used are silicon dioxide (thermal or deposited), photoresist and a silicon epitaxial layer. The sacrificial layer is then patterned and etched in locations where the mechanical structure (active layer) will be attached to the handle wafer. The active layer is deposited on the patterned sacrificial layer. The active layer materials that are typically used are polysilicon, silicon nitride, silicon dioxide, aluminum, polyimide, tungsten, and single crystal silicon. The active layer is then patterned. The final step involves the selective etching of the sacrificial layer to release the microstructure, resulting in a free-standing cantilever as shown in Fig. 1.8b. In order to fabricate more complex structures, additional sacrificial and active layers can be used. Some examples of the devices that have been fabricated using this technology are micromotors by MIT [38], micromirror arrays by Texas Instruments Inc [39] and integrated accelerometers by Analog Devices [40].

The main attractiveness of the surface micromachining technology compared with traditional bulk micromachining, is in the ability to fabricate smaller devices, achieve better dimensional control and also in its ability to use materials other than silicon. Some of the drawbacks of surface micromachining are: i) polysilicon, which is the material of choice for surface micromachining, has considerable as-deposited film stress [36]. The magnitude and sign of this stress is strongly dependent on the deposition conditions. Even though a high temperature anneal helps to minimize this stress, micromechanical structures may undergo changes in dimensions (elongation or contraction) due to relaxation of the residual stress when the structure is released; ii) the thickness of microstructures that can be fabricated by surface micromachining is limited to a few microns. This limitation is dictated by the deposition techniques that are used to put down the thin films; iii) the final step in the surface micromachining process typically involves a wet etching process to release the devices. This leads to the problem of stiction, which is sticking of the active layer to the substrate. This problem of stiction can lead to significant reductions in the yield of the process [39].

3) *LIGA Process*. LIGA is an acronym that stands for lithography, electroforming and micromolding (in German, lithographe, galvanoformung, abformung). It is a micromachining process that allows the fabrication of 3-D, high-aspect ratio (thickness to width) microstructures. A

LIGA process, which uses a sacrificial layer to fabricate a suspended microstructure, is called the SLIGA process. A good description of both of these technologies can be found in [36, 41].

The first step in the process involves the deposition and patterning of a sacrificial layer on a substrate wafer. The widely used sacrificial layer material is polyimide. A titanium/nickel film is then sputtered on top of the sacrificial layer. This Ti/Ni film acts as a seed layer for the electroplating of the active layer material. The wafer is then coated with a thick layer of photoresist (typically 300-400 μm thick PMMA). The PMMA layer is then patterned using X-rays generated by a synchrotron source. Because of the short wavelength of X-rays and a thick PMMA layer, a high aspect ratio (300-400:1) can be achieved. After patterning the PMMA layer is developed, resulting in a micromold. This micromold is then electroplated with the active layer material, viz., nickel. The final step is similar to surface micromachining and involves the selective etching of the sacrificial layer, resulting in a suspended microstructure (a clamped-clamped beam in this example).

This technology has been used to fabricate high aspect ratio microactuators [42]. The main disadvantage of this technology lies in the need for expensive synchrotron sources for the X-rays.

Micromachined Shear-Stress Sensors (Indirect and Direct Methods)

There are several micromachined sensors that are already available for shear stress measurements. Table 5 lists the published work to date, with a brief description of each device. The techniques can again be classified as indirect and direct methods.

1) *Indirect Methods*. The indirect micromachined sensors that have been developed are either hot wires or hot films [47, 48, 49, 50, 52]. We will not discuss each of these devices in detail. A brief summary of each technique is provided in Table 5. Even though some of these sensors [49, 50, 52] possess the desired spatial and temporal resolution for measurements in turbulent boundary layers, they suffer from the same problems as the conventional hot wires and hot films. They depend on empirical correlations to relate the measure property to the wall shear stress, and significant errors in measurements can occur due to substrate conduction.

2) *Direct Methods*. In this sub-section we will describe the floating-element type micromachined sensors. A brief decsription of each of the available sensors is provided in Table 5. The original micromachined floating-element sensor was developed at MIT by Schmidt [28, 43] in 1988. This sensor was designed for operation in low-speed turbulent boundary layers. The floating-element sensors employed a differential capacitive sensing scheme. A schematic diagram of the sensor is shown in Fig. 1.9a. The sensor comprised of a floating-element (500 μm x 500 μm x 32 μm) suspended by four tethers. The sensors were designed to have a bandwidth of 20 kHz and a shear

stress resolution of 0.1 Pa. The polyimide floating-element with an embedded conductor formed

Author, Year [reference]	Type of Sensor	Brief Description & Comments
Oudheusen, 1988 [47]	Thermal	The sensing principle is based on a thermopile (with directional sensitivity). The sensor area was 4 mm x 3 mm and was fabricated in silicon. The sensor was tested in a turbulent boundary layer over a range of 0-2 Pa. The frequency response (< 1 Hz) was poor due to substrate conduction.
Liu, 1994 [48]	Thermal	This sensor is a hot wire anemometer of size 200 μm x 200 μm, fabricated in polysilicon. The sensor was wind tunnel tested in the constant current mode and demonstrated a sensitivity of 15 V/kPa (over a range of 0-1.4 Pa). The sensor has a bandwidth of 500 Hz.
Jiang, 1994 [49]	Thermal	This sensor is a hot wire anemometer of size 10-160 μm x 1 μm, fabricated in polysilicon. The sensor was wind tunnel tested and only the velocity data is presented. The sensor has a bandwidth of 500 kHz (in constant current mode).
Kalvesten, 1995 [50]	Thermal	This sensor is a direction-sensitive hot film anemometer of size 300 μm x 60 μm, fabricated in polysilicon. The sensor was used to measure wall shear-stress spectra in a turbulent boundary layer. The sensor bandwidth was observed to be 40 kHz in a constant temperature mode of operation.
Jiang, 1996 [52]	Thermal	This is a hot wire sensor array (25 sensors of pitch = 300 μm) of size 150 μm x 3 μm, fabricated in polysilicon. The sensor was tested extensively in turbulent boundary layers and was able to detect a "streak" structure and provide instantaneous wall shear stress distributions. The sensor bandwidth = 30 kHz.
Schmidt, 1988 [43]	Floating Element	This is a floating-element sensor of size 500 μm x 500 μm, fabricated in polyimide. The sensing principle is based on differential capacitive sensing. The sensor was tested in a laminar channel flow upto a shear stress of 1 Pa. The sensors showed drift and EMI problems during wind tunnel tests. The sensor bandwdth ~ 10 kHz.
Ng, 1991 [45]	Floating Element	This is a floating-element sensor of size 120 μm x 140 μm, fabricated in silicon. The sensor operates on a piezoresistive transduction scheme. The sensor was designed for operation in the shear stress range of 1kPa - 100 KPa, for polymer extrusion applications.
Goldberg, 1994 [46]	Floating Element	This sensor operates on the same principle as Ng [45] and was developed for the same application. The floating-element size is 500 μm x 500 μm, fabricated in silicon. The sensors have backside electrical contacts, to facilitate the packaging of these devices.
Pan, 1995 [44]	Floating Element	This is a capacitive floating element sensor of size 100 μm x 100 μm, fabricated in polysilicon. It has been tested in laminar channel flows upto a shear stress of ~ 10 Pa. No measured bandwidth reported.
Padmanabhan, 1996 [51]	Floating Element	This is a floating element sensor based on an optical position sensing scheme. The sensor size is 120 μm x 120 μm, fabricated in silicon. The sensor was able to measure shear stresses of 0.005 Pa in a laminar boundary layer. The theoretical bandwidth = 52 kHz.

Table 5 Progress in micromachined shear-stress sensor technology

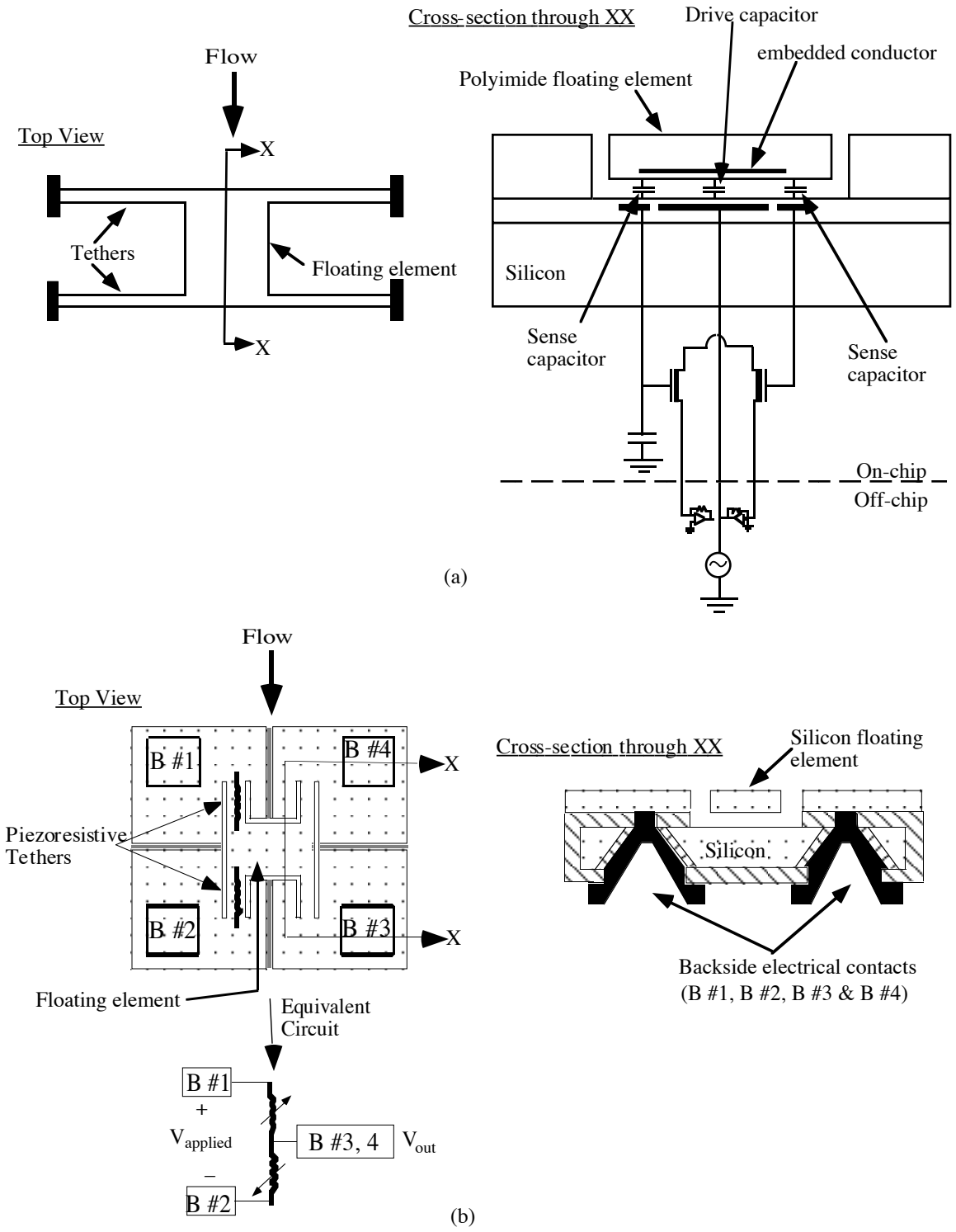

Fig. 1.9: a) Floating-element shear-stress sensor based on a capacitive transduction scheme [43]; b) floating-element sensor based on a piezoresistive transduction scheme (taken from [46])

the top plate of a parallel plate capacitor. An embedded conductor in the bottom silicon layer formed the bottom plate of the capacitor. The wall shear-stress induced deflection of the floating element was detected using an integrated differential capacitive readout scheme. The sensors were able to measure a shear stress of 1 Pa in a laminar channel flow. However, they showed sensitivity to electromagnetic interference (due to the high-impedance capacitive readout) and drift problems (due to the absorption of humidity by the polyimide) during continuous wind tunnel testing. In addition, the need to have the first-stage amplification on-chip (to detect the small signals) made the design and fabrication process for this scheme more complex. Another disadvantage inherent to all capacitive sensing schemes is that their use is limited to non-conductive fluids.Since the original micromachined device, floating-element sensors based on capacitive [44] and piezoresistive transduction schemes [45, 46] have been developed. The capacitive floating-element sensor [44] was a force-rebalance device designed for making measurements in a wind tunnel. This device has been tested only in a laminar channel flow and the dynamic response of this device has not been reported. This device was fabricated in polysilicon using a surface micromachining process and suffers from the drawbacks associated with this technology (see surface micromaching description in the previous section). The residual stresses associated with polysilicon can result in a non-planar floating-element structure.

The piezoresistive device was developed for measurements of wall shear stress during polymer extrusion [46]. These sensors comprised of a silicon floating-element (500 μm x 500 μm x 5 μm) suspended by four tethers. The sensing scheme uses the piezoresistive property of the silicon tethers to transduce the displacement of the floating-element, as illustrated in Fig. 1.9b. These sensors were designed for operation in a high shear stress ($1kPa \le \tau_w \le 100\,kPa$), high pressure (~40 MPa) and high temperature (300ºC) environment. The measurement of low-magnitude shear stress requires extremely high sensitivity to detect small forces (*O(nN)*) and corresponding small displacements (*O(Å)*). In such a low shear-stress environment the percentage change in resistance ($\frac{\Delta R}{R}$) of piezoresistive sensors is very small and typically is below the threshold level that can be effectively measured. Hence these devices are inadequate for the present application.

The summary of this section is that there is a need to develop a new sensing scheme for the measurement of wall low-magnitude shear stresses in aerodynamic flows. In this thesis we have developed a new micromachined sensor based on an optical position sensing technique (this makes it an inherently low-impedance device), which has the sensitivity and bandwidth required for the measurements of mean and fluctuating shear stress. The sensors were fabricated in single-crystal silicon using a wafer-bonding technology. The next section presents the outline of this thesis.

1.4 Outline of Thesis

Chapter 2 will describe the operating principle and the various aspects of the design of the first-generation optical shear-stress sensor. The mechanical analysis (static and dynamic) of the sensor structure and the design of the sensor layout will be presented. Finally, the improved sensing scheme developed for the second-generation sensors and the issues associated with the design of sensor arrays will be discussed.

Chapter 3 presents the mask design and the chip layout for the first and second-generation sensors. An overview of wafer-bonding technology (the process technology used for the sensors described in this thesis) for the fabrication of microsensors and microactuators is presented. A detailed step-by-step description of the actual fabrication process is then presented.

Chapter 4 describes the package for the individual sensors and sensor arrays. The issues associated with the design of the measurement circuit and the laminar-calibration flow cell are also presented. Finally, the test results for the individual sensors and sensor arrays are described. The tests include, electrical characterization, sensor static-calibration and measurements in a custom-designed laminar-calibration flow cell, sensor dynamic-calibration in a custom-designed plane wave tube, measurements in a laminar boundary layer and stochastic calibration in a turbulent boundary layer.

Chapter 5 summarizes the results and conclusions from this work.

Chapter 2. SENSOR DESIGN

This chapter presents the design of the new optical shear stress microsensor. The various aspects of the design for the first-generation stand-alone sensors and second-generation sensor arrays are presented. The first nine sections discuss the design for the first-generation sensors. The last section presents the design of the second-generation sensors.

The chapter begins with a description of the sensor operating principle. The second section presents a brief review of photodiode theory. The third section is a detailed description of the design of the photodiode. The next few sections describe the noise sources in photodiode-based detection systems and detailed mechanical analysis (static and dynamic) of the sensor structure. This is followed by a discussion of the theoretical minimum and maximum shear stress which can be measured using the sensor. The next section presents the design of the sensor layout. The final section is a discussion of the design of the second-generation sensors, pointing out the features that are different from the first-generation sensors.

2.1 Detection Principle - Optical Position Sensing

The sensing principle for the optical shear-stress sensor is based on a floating-element optical shutter and integrated photodiodes as shown in Fig. 2.1. The sensor is comprised of a floating-element structure, which is suspended by four tethers, as shown in the top view in Fig. 2.1a. A pair of photodiodes are located under the floating-element on the leading and trailing edge, as shown in the cross-sectional view (Fig. 2.1b). The sensor is subjected to uniform illumination from a laser source located above the floating-element. In the absence of any fluid flow, the exposed area of the two photodiodes (to the incident light) are the same (the photocurrents are also the same) and hence the differential photocurrent ΔI_{photo} is zero. In the presence of a flow, the floating-element deflects under the action of the wall shear stress. This results in an increase in the exposed area on the leading-edge diode and a decrease in area on the trailing-edge diode. The resulting differential photocurrent is proportional to the *magnitude* and *sign* of the wall shear stress. That is

$$\Delta I_{photo} \propto \tau_w \,. \tag{2.1}$$

It must be noted that for equation (2.1) to be valid, the incident light intensity for the two photodiodes must be the same and a differential photocurrent output must be solely due to the change in the exposed areas of the two photodiodes (and not due to any variations in the incident intensity). In a high-speed turbulent flow (*Mach number* > 0.5) or if the flow is heated (or cooled), the spatial variation in density of the flow-field might result in a spatial variation in

the refractive index of the medium. This could cause the diffraction of the incident light and

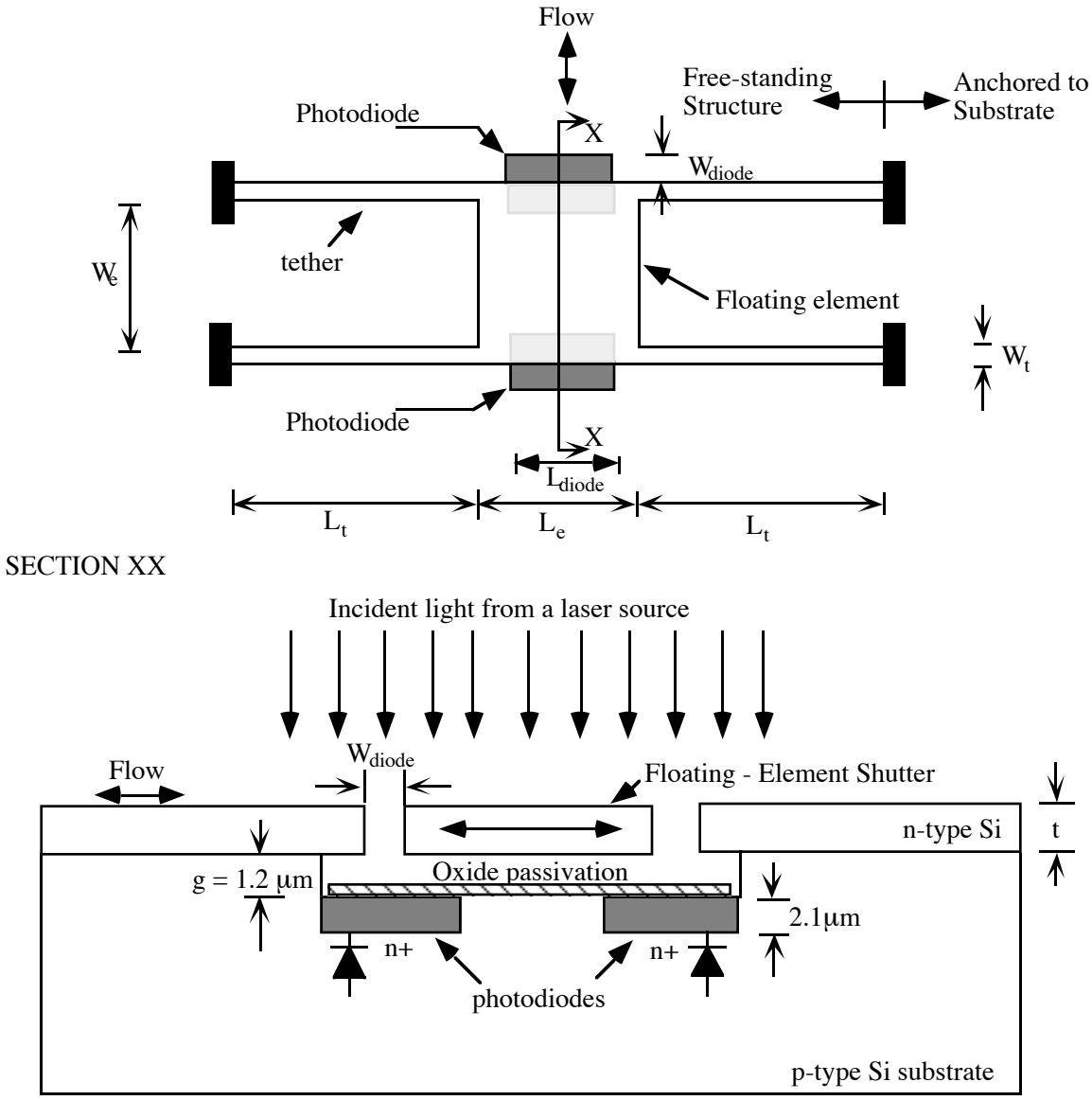

Fig. 2.1 Schematic diagram illustrating the sensing principle. Electrical leads and other structures adjacent to the sensor are not shown in this figure.

may result in a non-uniform incident illumination. This is not an issue for our current experiments since all the data presented in this thesis are based on experiments in low-speed flows that are at ambient temperature. Also, since the spacing between the photodiodes is small (spacing = 450 μm for the first-generation sensors and 70 μm for the second-generation sensors), the effect of the diffraction of the light on the performance of the sensor would be minimal.

The interest in microfabricated optical choppers (modulators/shutters) has increased considerably in recent times due to the ability to integrate optical choppers and displays. The literature in the field of micromachined light modulators is vast and beyond the scope of this thesis. A good description of the different aspects of this technology can be found in [53, 54, 55]. In this section we present a brief discussion of some of the devices that have a design similar to our sensor.

Micromachined sensors based on an optical shutter and photo-detector have been developed by other groups for various applications, viz., accelerometer [56], angular position-sensing in a micromotor [57] and infrared (IR) sensors [58]. The novel accelerometer [56] is based on a *p-i-n* photodiode and an optical shutter supported by cantilever beams. The shutter (with slits etched in it) forms the proof-mass of the accelerometer. When the sensor is subjected to an acceleration, the proof-mass moves and the displacement of the proof-mass controls the exposed areas of the photo-detector to the incident illumination. The output of the photo-detector is proportional to the proof-mass displacement and hence the acceleration. This sensor is comprised of three parts: *p-i-n* photodiodes, an optical shutter and a LED source. Each of these was fabricated independently and then assembled (using epoxy) to form the final device. This is different from our sensor where the optical shutter and photodiode are fabricated simultaneously on the same structure, and hence there is no need for any assembly. Therefore, our design does not have the problem of alignment errors that may be associated with assembly.

Micromotors with integrated photodiodes beneath the rotor have been used to make continuous real-time measurement of rotor motion [57]. As the rotor moves under illumination, its shadow modulates a photocurrent through the underlying photodiodes. The resulting photocurrent is amplified and filtered by off-chip electronics before passing through an algorithm that extracts the rotor position in time.

The group at Toyota Central Research Laboratories has developed a micromachined optical chopper for IR radiation, based on an optical shutter (with slits etched in it) [58]. The shutter in this device is moved electrostatically using comb-drive actuators. The sensor is illuminated with IR radiation from above. In the undeflected position of the shutter, all the IR radiation is reflected. When the shutter is electrostatically moved, IR radiation goes through the slits and is transmitted through the silicon substrate and can be detected by an IR sensor underneath the silicon wafer. The silicon substrate acts as an IR filter that cuts off radiation below a wavelength of 1 μm.

2.2 Photodiode Theory

A photodiode is a device that converts an incident light signal into an output electrical signal. The simplest photodiode consists of a *p-n* junction as shown in Fig. 2.2a. In a *p-n*

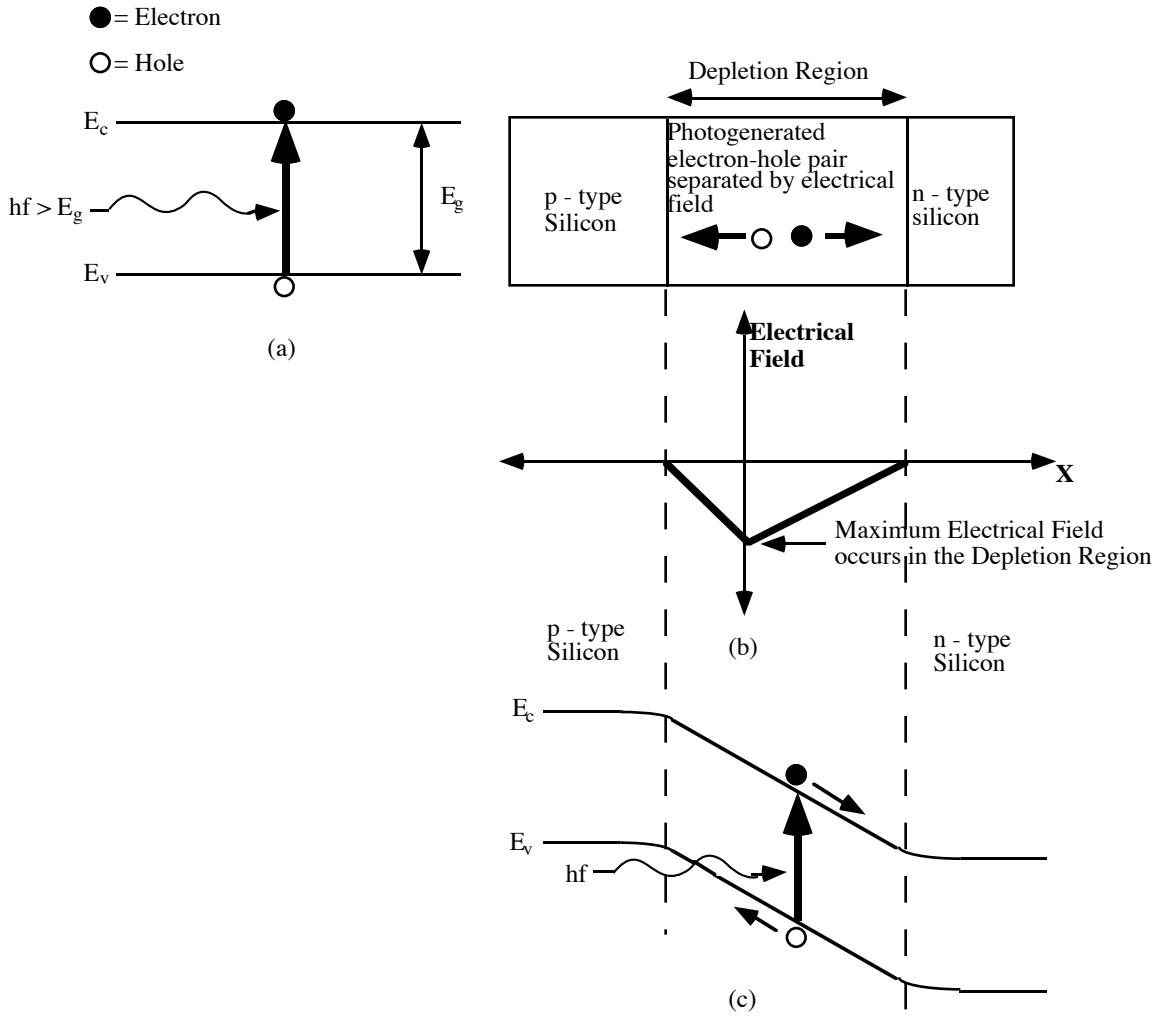

Fig. 2.2: a) Creation of electron-hole pairs by an incident photon having energy greater than E_g; b) electric field distribution in the depletion-region of the *p-n* junction; c) energy band diagram illustrating the photogeneration process

junction at thermal equilibrium ($V_{applied}$ = 0 and no incident illumination) a depletion region or space-charge layer is created on either side of the metallurgical junction [59]. The electrical field distribution in the depletion region and bulk material is shown in Fig. 2.2b. It can be seen from Fig. 2.2b that the electric field has a maximum value in the depletion region and a zero value in the bulk *p* or *n*-type material. Such an electric field distribution has the effect of stopping the majority carriers crossing the junction in the opposite direction to the field. However the large

electrical field in the depletion region accelerates the minority carriers from both sides of the junction, resulting in a leakage current flow in the external circuit. An incident photon that has an energy greater than E_g, the band gap of silicon, will excite an electron into the conduction band, leaving behind a hole in the valence band. This process by which an incident photon creates an electron-hole pair is known as photogeneration and is shown in Fig. 2.2c. In order to achieve maximum sensitivity and efficiency of the photodiode, majority of the incident photons must be absorbed in the depletion region. This is because the large electric field in the depletion region separates and sweeps (large drift velocity of the electrons and holes due to the large electrical field) the electron-hole pairs that are created, thereby resulting in a photocurrent in the external circuit. The photons that are absorbed in the bulk material create electron-hole pairs that have a higher probability of recombining and hence do not contribute significantly to a current in the external circuit. The photocurrent output due to the motion of photogenerated electron-hole pairs is similar to the drift motion of minority carriers in a *p-n* junction at thermal equilibrium and hence adds on to the drift current. A more detailed description of other photodiode designs and details of photodiode operation can be found in [59, 60, 61, 62].

The magnitude of the photocurrent that is generated as a result of the incident light intensityJ_{flux}(W/m^2) is proportional to the incident light intensity and the area of the photodiode that is exposed to that light intensity and is given as [63]:

$$I_{photo} = \frac{J_{flux}\, q\, (1 \pm r)\, \{1 \pm e^{\pm \alpha_o w}\}}{h\, c\, /\, \lambda}\, A_{diode} \tag{2.2}$$

where q is the electronic charge, α_o is the absorption coefficient (m^{-1}), w the width of the absorbing region (designed to be the depletion region width), h is Planck's constant, λ is the wavelength of the incident photons, c is the speed of light in air, r is reflectivity of the diode surface and A_{diode} is the area of the diode exposed to the incident photon flux. The reciprocal of the absorption coefficient is the penetration depth of the light. The absorption coefficient is a function of the wavelength of the incident light as shown in Fig. 2.3 (reproduced from [63]). The wavelength of the illumination source must be chosen so as to achieve maximum absorption at the desired depth, viz., in the depletion region. Equation (2.2) assumes that the incident photons are collected over a region from the surface of the photodiodes to a depth equal to the depletion-region width.

It must be noted that photodiodes can be operated in either the photovoltaic mode ($V_{applied} = 0$) or the photoconductive mode ($V_{applied} < 0$). For simplicity, all the experiments in this thesis were performed with the photodiodes being operated in the photovoltaic mode. This mode of operation was found to be more than adequate for our application.

2.3 Photodiode Design and Parameters

This section describes the design of the photodiode. The various parameters that are discussed are: a) metallurgical junction depth; b) choice of implant parameters for fabrication; c) depletion-region width; d) quantum efficiency; and e) response speed.

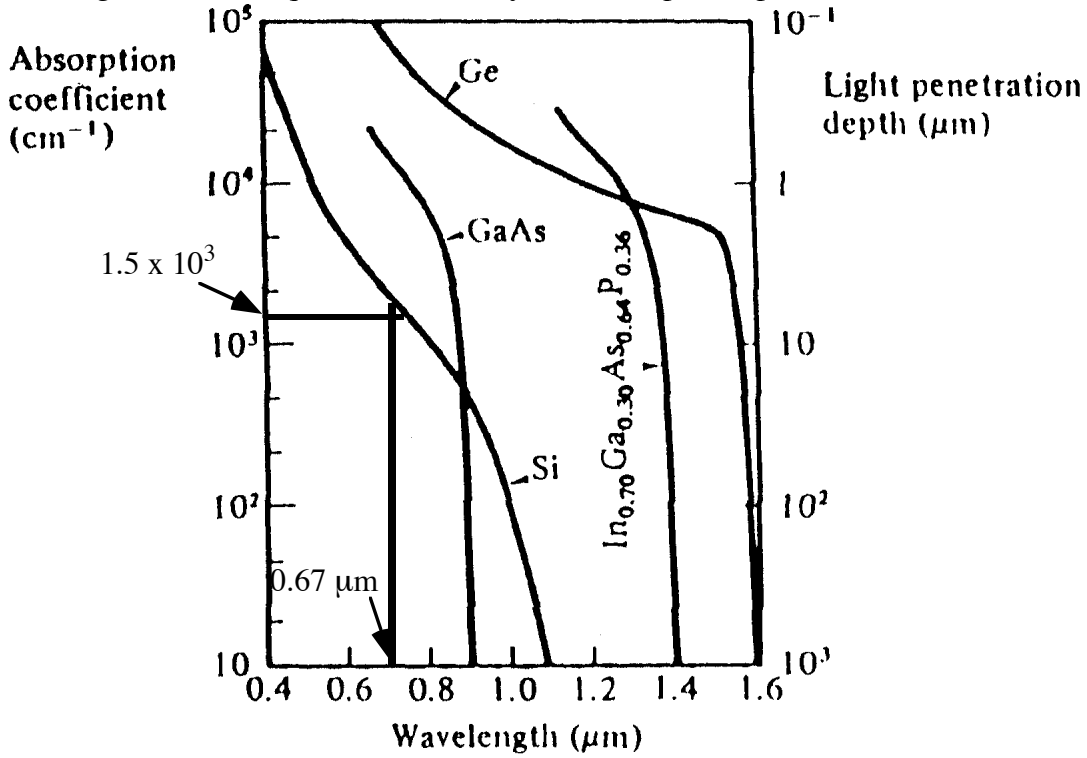

Fig. 2.3 Absorption coefficient of radiation in silicon as a function of the wavelength of the incident radiation [63]

a) *Metallurgical Junction Depth*. As described in section 2.2 the junction depth must be such that most of the incident light is absorbed in the depletion region of the *p-n* junction. All the tests in this thesis were performed using a commercially available 670 nm solid-state laser. The value of α_o for this wavelength is 1.5 x 10^3 cm^{-1} (from Fig. 2.3). In order to obtain the maximum absorption efficiency, the metallurgical junction depth was designed to be located at a depth of 2 μm. This results in a depletion-zone encompassing a region on either side of the metallurgical junction. This choice of junction depth results in 90% absorption of the incident power in the depletion region. (Note: the fraction of the incident power that is absorbed at a depth x is given as $e^{\pm\alpha_o x}$. By integrating across the length of the depletion-region we can calculate the fraction of the incident power that is absorbed in that region).

b) *Implant Parameters*. The implant parameters (species, dose and energy) were chosen based on SUPREM [64] simulation results, so as to yield a metallurgical junction depth of 2 μm after the drive-in and other thermal steps. The SUPREM program file that was used for the simulations can be found in Appendix A. The results of the simulations are also shown in Appendix A. The following implant parameters were chosen based on the simulations:

i) species = phosphorus
ii) dose = 5 x 10^{15} cm^{-2}
iii) energy = 90 keV.

The actual junction-depth on the wafers was measured using sheet resistance analysis to be 2.1 μm, which is in good agreement with the designed value (see Appendix A for the measured values).

c) *Built-in Potential*. In thermal equilibrium, the diffusion of carriers across the metallurgical junction results in an electric field (as shown in Fig. 2.2) and hence a potential difference. This is called the built-in potential V_{bi} and for a step-junction the expression for V_{bi} is given as [59]:

$$V_{bi} = \frac{KT}{q} \ln \left[\frac{N_D N_A}{n_i^2}\right] \tag{2.3}$$

where N_D, N_A and n_i are the donor, acceptor and intrinsic carrier densities, respectively. Using values of KT = 0.026 eV (at room temperature), q = 1.6 x 10^{-19} C, N_D = 4 x 10^{19} cm^{-3}, N_A = 7 x 10^{14} cm^{-3} and n_i = 10^{10} cm^{-3}, we get V_{bi} = 0.86 V. The values of N_D and N_A are obtained from SUPREM simulations. These values are in good agreement with the actual dopant concentrations measured on the wafers using a sheet resistance analysis (see Appendix A).

d) *Depletion-region Width*. The expression for the depletion-region width w for a linearly-graded junction (a junction where the dopants are ion-implanted into the semiconductor) is given as [2.7]:

$$w = \left[\frac{12\, K_{Si}\, \varepsilon_0}{q\, a} (V_{bi} \pm V_{applied})\right]^{1/3} \tag{2.4}$$

where $K_{Si}\varepsilon_0$ is the product of the dielectric constant of silicon and permittivity of vacuum and is equal to 1.045 x 10^{-12} F/cm, a is the slope of the plot of $|N_D \pm N_A|$ versus the depth into the wafer. From the SUPREM simulation results (which agree well with the measured dopant concentrations) the value of a is calculated to be equal to 8.4 x 10^{18} cm^{-4}. Using V_{bi} = 0.86 V and $V_{applied}$ = 0, we get w = 1.9 μm.

e) *Quantum Efficiency*. The quantum efficiency η is defined as the ratio of the number of carriers generated to the number of incident photons and is given as:

$$\eta = \frac{number\ of\ carrier\ pairs\ generated}{number\ of\ incident\ photons} = \frac{I_{photo}/q}{P\lambda/hc}$$

where $P = J_{flux}\, A_{diode}$ is the incident optical power. Substituting for I_{photo} from equation (2.2) we get

$$\eta = (1 \pm r)\,(1 \pm e^{\pm \alpha_o w})\,. \tag{2.5}$$

Using w = 1.9 μm and α_o = 1.5 x 10^3 cm^{-1} (for an incident wavelength of 670 nm) and $r \approx 0$, we get $\eta = 62$ % at 670 nm. It must be noted that the quantum efficiency is a function of the wavelength of the incident radiation and is always quoted at a specific wavelength.

f) *Depletion Capacitance*. The expression for the capacitance of the depletion region (at thermal equilibrium) is given as [59]:

$$C = \frac{K_{Si}\, \varepsilon_o\, A}{w} \tag{2.6}$$

where A is the junction area of the depletion region. Substituting for the different parameters we get C = 1.6 pF, for our design.

g) *Response Speed*. The response speed of a photodiode detection system depends on the time constants associated with the different aspects of the detection process: i) the *RC* time constant of the measurement circuit, including the photodiode capacitances (diffusion and depletion capacitance); ii) the time constant associated with the carrier diffusion outside the depletion region; and iii) the transit time of the photogenerated carriers in the depletion zone. The dominant time constant controls the response speed of the system. The *RC* time constant of our off-chip measurement circuit (see chapter 4) is of the order of 10 μs. The typical hole diffusion times are on the order of 40 ns through 10 μm [63]. This time is much faster than the time constant of the off-chip measurement circuit. The third factor is the drift transit time of the carriers in the depletion region. It must be noted that the need for a thick depletion region to maximize the absorption efficiency is traded off with the need for a thin depletion region to reduce the carrier drift times. The typical carrier velocities in the depletion region are of the order of 10^7 cm/s [63], which yields a transit time of 20 ps for a 1.9 μm depletion-region width. Hence the response speed of the detection process is controlled by the speed of the off-chip measurement electronics.

2.4 Noise Sources and Signal to Noise Ratio (SNR) for Detection System

The ultimate performance limits of a photosensor system are set by the noise fluctuations that are present at the various stages of the detection system (photodetector, the electrical connection between the photodetector and first-stage amplifier and the current amplifier). Figure 2.4 schematically shows the various sources of noise in the present detection system. This sub-section describes each of these noise sources.

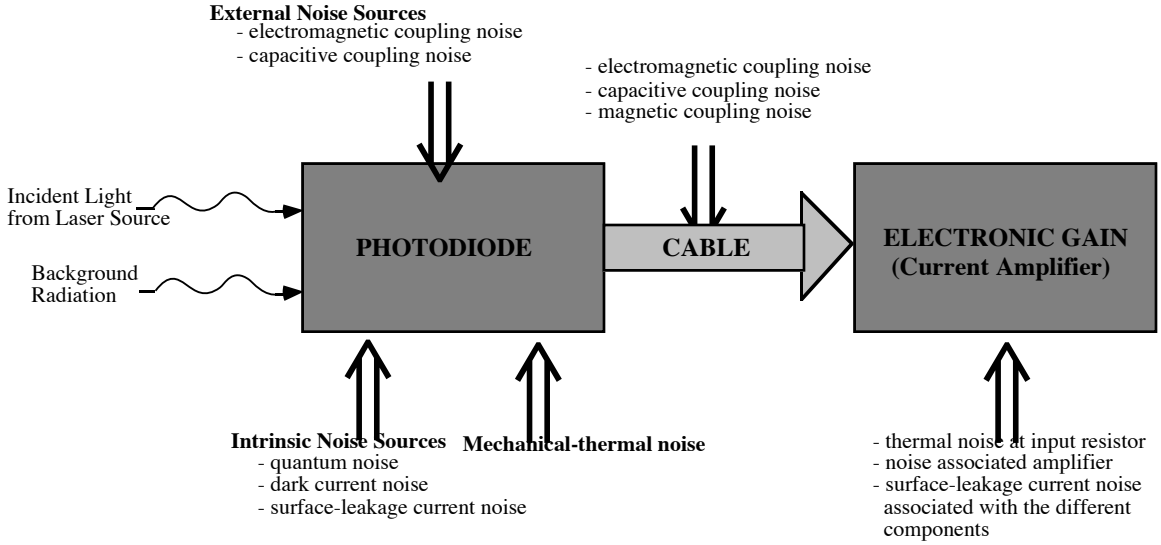

Fig. 2.4 Schematic illustration of the noise sources present at the different stages of the detection system

2.4.1 Photodiode Noise Sources

The intrinsic noise fluctuations present at the input to the photodiode can be classified as [65, 66]: a) dark current noise; b) quantum or shot noise; and c) surface leakage current noise. The next few paragraphs present a brief description of each of these three noise types and the expressions that can be used to estimate the noise current contribution due to each source:

a) *Dark Current Noise*. This is also sometimes referred to as background radiation noise. Even when there is no optical power incident on the photodiodes, there is a small reverse leakage current that flows across its terminals (due to the thermal generation of carriers and due to any background light that may be incident on the photodiode). This dark current contributes to random fluctuations about the average photocurrent. It manifests itself as a shot noise on the photocurrent. The mean square value of the dark current noise $\overline{i_d^2}$ is given by [65]:

$$\overline{i_d^2} = 2\, q\, B\, I_d \tag{2.7}$$

where q is the electronic charge, B is the measurement bandwidth and I_d is the dark current. The magnitude of the dark current noise can be reduced by careful design and fabrication of the photodiode.

The maximum measurement bandwidth B for the system is given as $B = 1/(2\pi RC)$ where R is the load resistance and C is photodiode capacitance (since the amplifier input capacitance is small). For our system, R = 1 MΩ and C (depletion capacitance) = 1.6 pF, we get B = 100 kHz. Using a typical value of the dark current I_d = 100 pA (see chapter 4 for the measured values), we get $\overline{i_d^2} = 3.2 \; x \; 10^{\pm 24} \; A^2$.

b) *Quantum or Shot Noise*. The detection of light by a photodiode is a discrete process since an electron-hole pair is created by the absorption of a photon and hence the output signal of the photodiode is dictated by the statistics of the incident photons. The quantum noise arises due to the intrinsic fluctuations associated with this process of photoexcitation of carriers. It manifests itself as a shot noise. The quantum noise current on the photocurrent I_{photo} is given as [65]

$$\overline{i_{shot}^2} = 2 \; q \; B \; I_{photo} \; . \tag{2.8}$$

The magnitude of the shot noise current can be estimated using the typical value of the photocurrent of I_{photo} = 100 nA (see chapter 4 for the measured values) and B = 100 kHz as $\overline{i_{shot}^2} = 3.2 \; x \; 10^{\pm 21} \; A^2$.

c) *Surface Leakage Current Noise*. This noise current arises due to the presence of unterminated surface states on the surface of the silicon. These unterminated states contribute to energy levels in the center of the band gap region of silicon. These mid-band gap energy states act as sites for recombination-generation (R-G) and are thus responsible for increased leakage current (the R-G centers are also sometimes referred to as traps). This leakage current can be considerably reduced by passivating the surface using a thermal oxide. It has been found that the thermal oxide reduces the surface leakage current by several orders of magnitude [3.10]. The details of the passivation process that was used for the present sensor can be found in section 3.3 of the fabrication chapter. For this analysis it is assumed that the surface leakage noise current is small.

2.4.2 Mechanical-Thermal Noise

Microfabricated sensors are often associated with miniature moving parts (the floating-element in this case) that are susceptible to mechanical noise resulting from molecular agitation

[67]. In our case the floating-element sensor is designed for measurements of small-signals. The mechanical-thermal noise could set the limit on the lowest measurable displacement of the floating-element. The mechanical-thermal noise arises due to the Brownian motion of the particles in the surrounding medium, that is, agitation of the floating-element structure due to collisions from the particles in the surrounding gas. The collision-induced displacement sets the limit on the smallest shear-stress-induced displacement which can be detected by the sensor. The magnitude of this noise depends on mass, lateral resonant frequency and the damping ratios of the floating-element structure. This noise displacement magnitude has been estimated for a second order system as [67]: $Z = \sqrt{(4kT)/(\omega_r m Q)}\ \ [m\sqrt{Hz}]$, where k is the Boltzmann constant (1.38 x 10^{-23} J/K), T is the absolute temperature, ω_r, m and Q are the lateral resonant frequency, mass of the floating-element and quality factor, respectively. The equivalent noise current can be estimated from the noise displacement magnitude and equation (2.12) as

$$i_{mech\pm therm} = \frac{2\,Z\,I_{photo}}{W_{diode}}\,. \tag{2.9}$$

Using typical values for our sensor (floating-element size = 500 μm x 500 μm) ofω_r = 16 kHz, m = 4.1x10^{-9} Kg, Q = 100, we get Z = 5.077 x 10^{-12} m, for a measurement bandwidth of 100 kHz. The mechanical-thermal noise current can be calculated using equation (2.9) (with Z = 5.077 x 10^{-15} m, I_{photo} = 100 nA and W_{diode} = 7 μm) as 1.45 x 10^{-13} A.

2.4.3 Noise inputs between photodetector and amplifier

The photodiode outputs are connected to the first-stage amplifier by cables. This could result in noise introduced into the detection system by means of the cable; for example, field-coupled noise and movement-induced triboelectric and microphony noise [66]. To minimize this noise contribution, the first-stage amplifier should be placed as close to the sensor as possible, and the amplifier should have sufficient gain such that the noise from all sources entering the signal path later may be ignored. It can be seen from the calculations in the following paragraph that this is the dominant noise source for our system.

The field-coupled noise could be due to: a) electromagnetic coupling; b) magnetic (mutual inductance) coupling; c) electric (capacitive coupling). For our system we used coaxial cables to connect the sensor to the amplifier, as described in the measurement circuit section of the sensor testing chapter. The coaxial cable provides excellent electric field shielding when the shield on the cable is properly grounded. A coaxial cable with only one shield connection to ground will provide no magnetic field shielding [66]. In order to achieve good shielding from

magnetic coupling noise, either a triaxial cable or a shielded twisted pair is preferred [66]. Hence the main source of noise contamination between the sensor and amplifier is due to magnetically coupled noise. Common sources of this noise are power-line transformers and electric motors, where the fields and induced currents are at the line frequency of 60 Hz. The field from brush motors will also contain some high frequency components as a result of arcing. The amplitude of magnetically coupled noise current can be estimated using the following equation [66]:

$$i_{mag} = 2\pi f B_o A/R \tag{2.10}$$

where B_o is the flux density and A is the loop-area over which the current is induced. Using typical values for a power-line: $f = 60$ Hz, $B = 1\text{mWb/m}^2$, $R = 1$ MΩ and $A = 0.0182$ m^2 (this value is based on the area of a single circular loop formed by the cable. By coiling the cable more than once, this area can be minimized), we get $i_{mag} = 6.9 \times 10^{-9}$ A. It must be noted that any field-coupling directly into the sensor chip is minimized by using a frontside electric shield, as described in section 2.8.3.

2.4.4 Load Resistor and Amplifier Noise

The major source of noise in the resistor is thermal (or Johnson) noise. The mean square noise current is equal to $4kTB/R$ where k is the Boltzmann constant,T is the absolute temperature and R is the resistance in ohms.

A commonly used index of noise performance for an amplifier is the noise figure, F [66]. The noise figure is the fractional increase in noise (from the amplifier) over the unavoidable thermal noise from the resistor. For our circuit we used a low noise amplifier (AD 712 KN), which has a small noise figure. The noise figure of the amplifier was (from the amplifier specification sheet) 3 db. The sum of the noise contributions due to the load resistor and the amplifier can be written as $4KTBF/R$ [65]. For our amplifier, noise figure = 3db or 10 $\log_{10}2$ and hence $F = 2$.

2.4.5 SNR for the Detection System

The SNR for the entire detection system (shown in Fig. 2.4) can therefore be written as ratio of the mean square signal amplitude to the mean square noise amplitude as

$$SNR = \frac{I_{photo}^2}{2qB\,(I_d + I_{photo}) + i_{mech\pm therm}^2 + i_{mag}^2 + 4kTBF/R}\,. \tag{2.11}$$

Since the various noise sources are statistically independent, the total mean square value of the noise amplitude is the sum of the mean square values from each noise source [68].

For our system, R = 1 MΩ and C (depletion capacitance) = 1.6 pF, we get B = 100 kHz. Using I_d = 100 pA, I_{photo} = 100 nA (for values of I_d and I_{photo} see testing chapter) and F = 2 and B = 100 kHz, the SNR can be calculated to be equal to 211. The measured values of the *SNR* for the detection system are presented in section 4.5.4 of the sensor testing chapter.

2.5 Sensitivity, Sensor Dimensions and Illumination Source

2.5.1 Sensitivity

The sensitivity of the sensor is defined as the fractional change in the photocurrent for a given applied shear stress. It is expressed as %/Pa. Using equation (2.2), the differential photocurrent normalized by the average photocurrent, when the floating-element deflects, can be shown to be equal to:

$$\frac{\Delta I_{photo}}{I_{photo}} = \frac{2\,\delta}{W_{diode}} \quad (for\ \delta \le W_{diode}) \tag{2.12a}$$

$$\text{and hence } sensitivity = \frac{\Delta I_{photo}}{I_{photo}\tau_w} = \frac{2\,\delta}{W_{diode}\tau_w} \quad (for\ \delta \le W_{diode}) \tag{2.12b}$$

where δ is the in-plane deflection of the floating-element, W_{diode} is the exposed width of the photodiode (as shown in Fig. 2.1) and I_{photo} is the average of the photocurrents from the two photodiodes when $\tau_w = 0$. The derivation of equation (2.11) is presented in Appendix B. It can be seen from equation (2.12) that the sensitivity of the photodiode is proportional to the deflection of the floating-element and is inversely proportional to the exposed width. It must be noted that the smallest value of W_{diode} that can be achieved is limited by the fabrication process. The value of W_{diode} for the present sensor is 7 μm. In order to estimate the sensitivity using equation (2.12) the relationship between the deflection δ of the floating-element and the applied shear stress must be known. This relationship is discussed in section 2.6.

2.5.2 Sensor Dimensions

The floating-element area is fixed from the desired spatial and temporal resolution of the sensor, as discussed in chapter 1. Process considerations impose dimensions of t = 7μm, W_{diode} = 7μm for the sensors. The length L_t and width W_t of the tethers were chosen such that the sensor response at the lowest shear stress can be effectively measured using off-chip

electronics. For all the devices L_t = 500 μm and W_t = 10 μm. In order to achieve a measurement range of 10 Pa and a bandwidth of 17 kHz (or better) required for testing in low-shear environments, sensors of two different floating-element sizes - 120 μm x 120 μm and 500 μm x 500 μm - were fabricated (see section 1.2 of chapter 1 for a detailed description of the choice of the sensor dimensions).

2.5.3 Illumination Source

All the experimental results presented in this thesis are based on tests carried out with a 7mW, 670 nm solid-state laser. The wavelength of the incident light source was chosen so as to maximize the absorption of photons at the depth of the depletion region of the photodiodes. Also, the wavelength is such that the 7 μm thick floating-element acts as a shutter for the light and that light strikes the diodes only through the exposed areas in the device wafer.

A typical solid-state laser (SPMT 670-10) has a non-uniform (Gaussian) intensity distribution across the spot [69]. To overcome this problem (for our initial experiments), the spot size was made much larger (~ 1 cm diameter) relative to the floating-element size. This provided a uniform intensity distribution over the central 500 μm region of the spot. The spot was then aligned relative to the floating-element to obtain $\Delta I_{photo}/I_{photo} = 0$, in the absence of any flow. For the second-generation sensors we implemented a three-photodiode sensing scheme, which reduced the sensitivity to a non-uniform incident beam and made the task of alignment of the laser spot easier (see section 2.10.1). In addition, in subsequent tests we used a new laser (ACMT 670-10) of the same wavelength, which was fitted with suitable optics to obtain a spot with a uniform intensity distribution [69].

2.6 Mechanical Analysis - Static and Dynamic

2.6.1. Stiffness

The stiffness k of the sensors can be estimated from a mechanical modeling of the sensor structure. The tethers can be modeled as clamped-clamped beams of length $2L_t$, subjected to a distributed load (per unit length) D and a central point load P [28], as shown in Fig. 2.5. We have assumed that the floating-element moves rigidly under of the applied shear stress. The distributed load (per unit length) is the direct shear on the tethers, and is given as $D = \tau_w W_t$. The point load is the effect of the resultant force (due to the wall shear) on the floating-element and is equal to $P = \tau_w W_e L_e/2$ (the factor of half is because there are a pair of

clamped-clamped beams). For a beam under such loading conditions (Fig. 2.5), the total deflection can be obtained from the principle of superposition as [70]:

$$\delta = \frac{P\,(8\,L_t^3)}{192\,E\,I} + \frac{D\,(16\,L_t^4)}{384\,E\,I} \tag{2.13}$$

where I is the moment of inertia of the beam. Substituting for P and D, equation (2.8) can be simplified to yield the force-deflection (F - δ) relationship as follows:

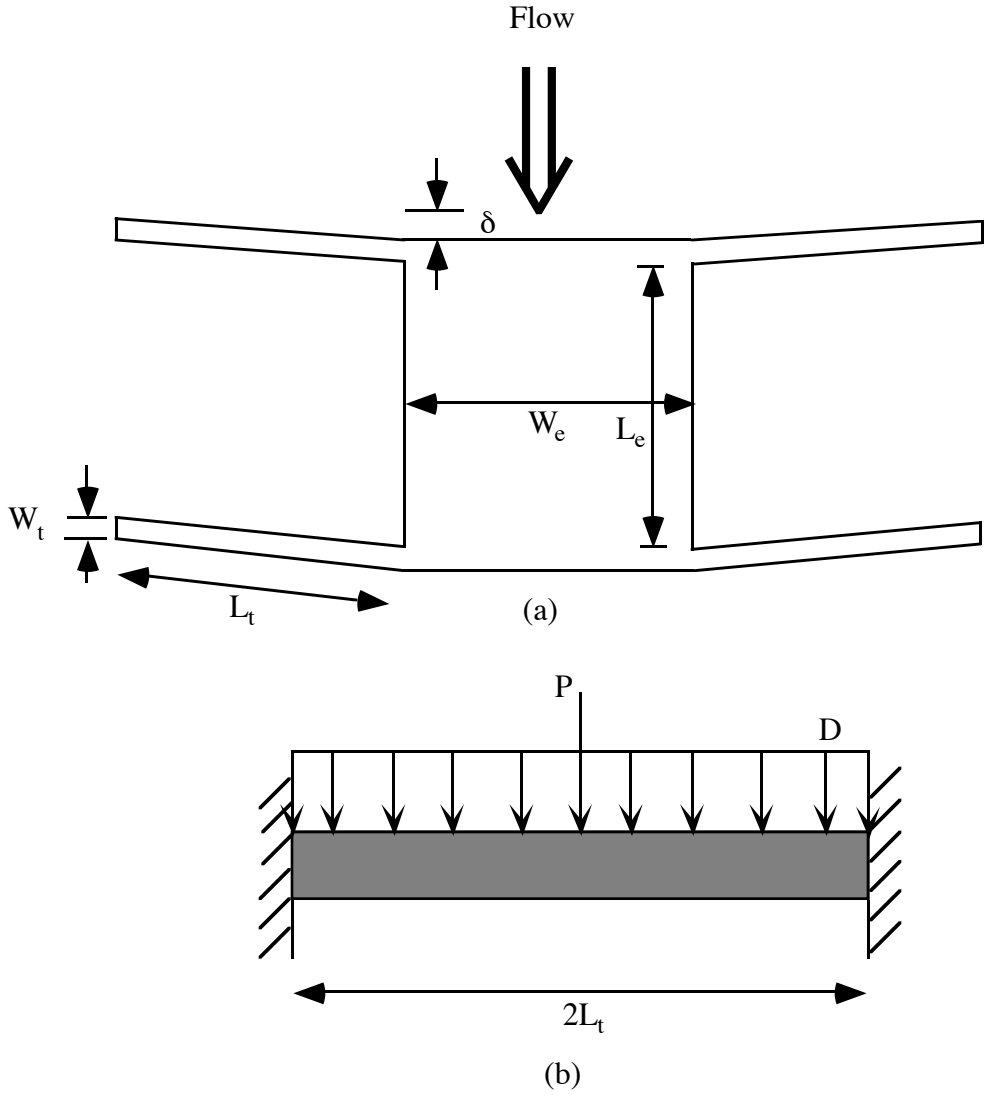

Fig. 2.5: a) Deflected floating-element structure in the presence of a flow; b) modeling of the loading as the sum of a distributed load D and a point load P acting on a clamped-clamped beam

$$k = \frac{F}{\delta} = \frac{4\,E_{si}\,t}{(L_t/W_t)^3\left\{1 + 2\,\frac{L_t\,W_t}{L_e W_e}\right\}} \tag{2.14}$$

where $F = \tau_w W_e L_e$, where E_{si} is elastic modulus of silicon (E_{si} = 190 GPa), L_t, W_t and t are the length, width and thickness of the tethers, respectively and L_e and W_e are the length and width of the floating-element, respectively. The calculated stiffness values for the two sensor sizes are shown in Table 6.

Using equations (2.11) and (2.12), the sensitivities for the two different plate sizes were estimated. For a shear stress of 1 Pa the percentage change in the photocurrent is 0.0183% for the 120 μm x 120 μm sensor and 0.195% for the 500 μm x 500 μm sensor. Hence the sensitivities of the sensors are 0.0183 %/Pa for the 120 μm x 120 μm sensor and 0.195 %/Pa for the 500 μm x 500 μm sensor.

2.6.2 Resonance Frequency

The mechanical resonant frequency (for lateral motions) of the sensor can be estimated by modeling the sensor element and the tethers as a spring-dashpot system (single degree of freedom and second order system). The governing equation of motion for such a system can be shown to be:

$$m\frac{d^2x}{dt^2} + c\,\frac{dx}{dt} + kx = F \tag{2.15}$$

where x is the displacement, m is the mass, c is the damping coefficient, k the spring constant and F is the forcing term, which in this case is the wall shear force. Equation (6) can be solved to obtain the lateral resonance frequency f_r of this system as

$$f_r = \frac{1}{2\pi}\sqrt{\frac{k}{m}}\ . \tag{2.16}$$

It must be noted that equation (2.16) assumes that the damping ratio is small and hence the damped natural frequency of the system is approximately equal to the undamped natural frequency. It will be shown in section 2.6.4 that the damping ratio for lateral (or in-plane) oscillations is much smaller than one. The mechanical resonance frequencies for the two different floating-element sizes can be estimated from equation (2.16) by substituting for the spring constant k from equation (2.14) and using $m = \rho_{si}\,L_e\,W_e\,t$, where ρ_{si} is the density of silicon. The mechanical resonance frequencies for the 120 μm sensor and 500 μm sensor are calculated as 52 kHz and 16 kHz, respectively.

The acoustic resonance frequency of the sensor can be obtained by modeling the sensor cavity as a Helmholtz resonator. The acoustic resonance frequency is given as [71]:

$$f_{acoustic} = \frac{1}{2}\sqrt{\frac{c^2 S}{t V}} \tag{2.17}$$

where c is the velocity of sound in air, S is the cross-sectional area of the sensor cavity opening, t is the depth of the opening and V is volume of the cavity. Substituting for the different parameters, gives $f_{acoustic} > 100$ kHz for all the different sensor designs. Hence the maximum frequency of sensor operation is controlled by the mechanical resonance frequency, for all the sensors.

2.6.3 Quality Factor

The quality factor Q of resonance for this system is given as:

$$Q = \frac{1}{2\xi} \tag{2.18}$$

where ξ is the damping ratio and is defined as the ratio of the damping coefficient c of the system to the critical damping coefficient c_c. The critical damping coefficient for such a second-order system is given as $c_c = 2\sqrt{km}$ [72].

2.6.4 Damping Ratio for in-plane Oscillations

The damping coefficient c for *in-plane oscillations* of the floating-element can be estimated using a slide-film damping model. The flow in the gap under the plate can be modeled as a Couette flow. In such a system, for small values of gap g, the damping coefficient can be shown to be [72]

$$c_{in\pm plane} = \frac{\mu_{air} (L_e W_e)}{g} . \tag{2.19}$$

The value of g for the present design is 1.2 μm, as shown in Fig.2.6a. It must be noted that the damping generated by the ambient fluid above the floating-element is small at low and moderate frequencies ($\leq 15\ kHz$) [73]. Using L_t = 500 μm, W_t = 10 μm, t = 7 μm and the material properties of silicon, the quality factor Q and the damping ratio $\xi_{in\pm plane}$ ($= c_{in\text{-}plane}/c_c$) for the two plate sizes can be obtained. Table 6 lists these values. It can be seen that the sensor response for in-plane oscillations is underdamped ($\xi_{in\pm plane} < 1$). Accurate estimation of $c_{in\text{-}plane}$ may require the modeling of the flow in the gap as Stokes flow [73]. However, it has been shown that for a thin air film (g < 2 μm), the energy dissipation behavior of a Couette-type damper becomes identical to that of a Stokes-type damper [73]. It must also be noted that the above described analysis typically underestimates the value of $c_{in\text{-}plane}$ and hence $\xi_{in\pm plane}$.

This is because of a zero pressure gradient assumption in the gap and also since fluid loading and edge effects have been neglected. Moreover, since the gap size is small, the mean free path of the air molecules becomes significant with respect to the gap thickness. Under such conditions a slip flow exists at the boundaries [74]. This will also affect the calculated value of $\xi_{in\pm plane}$, and has not been accounted for in this analysis.

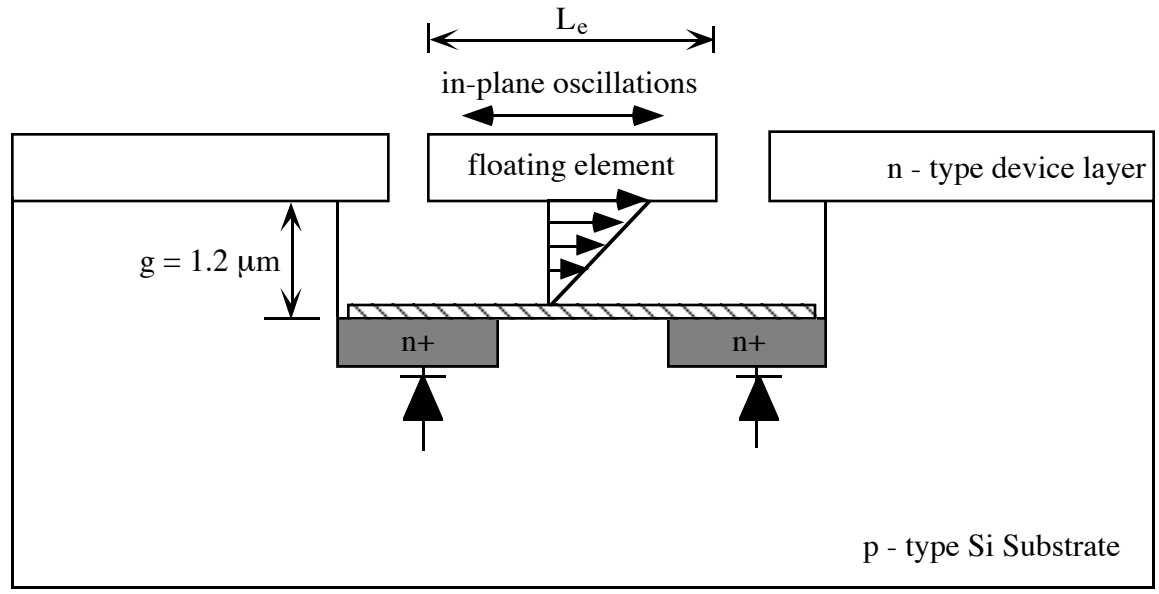

(a)

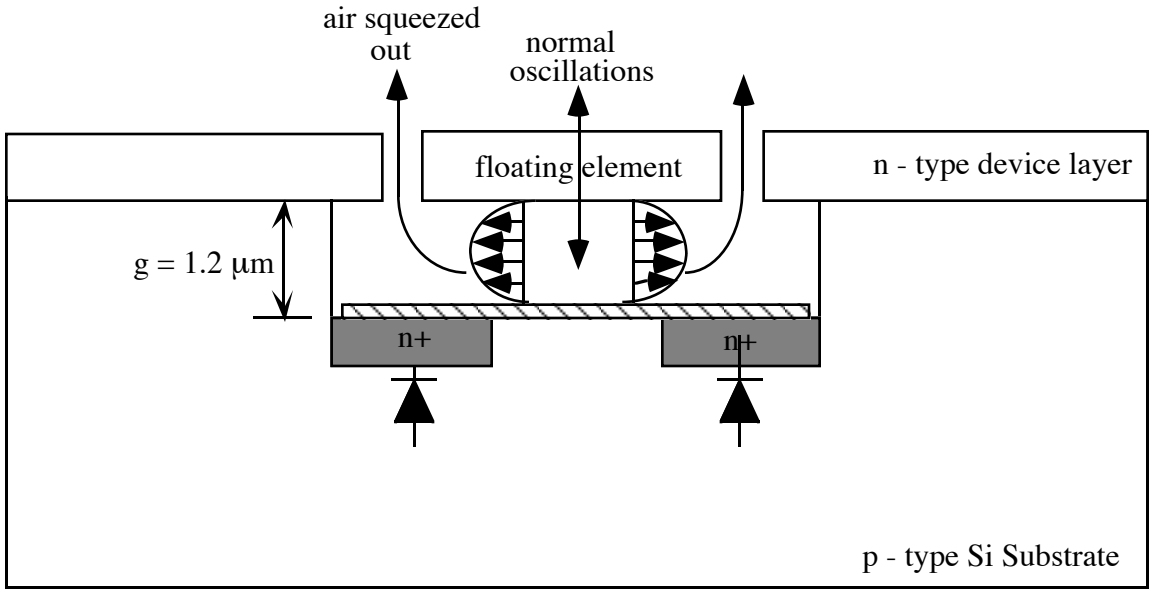

(b)

Fig. 2.6: a) Illustration of the slide-film damping model, for in-plane oscillations of the floating-element. The pressure gradient in the gap is assumed to be zero for this analysis and hence the velocity profile is linear; b) illustration of the squeeze -film damping model, for normal oscillations of the floating element

QUANTITY	120 μm SENSOR	500 μm SENSOR
Floating element size (length, width, thickness)	120 μm x 120 μm x 7 μm	500 μm x 500 μm x 7 μm
Tether dimensions (length, width, thickness)	500 μm x 10 μm x 7 μm	500 μm x 10 μm x 7 μm
Stiffness, k	22.5 N/m	33.6 N/m
Resonant Frequency, f_r	52 kHz	16 kHz
Current Sensitivity, $\frac{\Delta I_{photo}/I_{photo}}{\tau_w}$ (first-generation sensors)	0.0183 %/Pa	0.195 %/Pa
Damping ratio for in-plane oscillations, $\xi_{in-plane}$	1.5×10^{-3}	5×10^{-3}
Damping ratio for normal oscillations, ξ_{normal}	6.5×10^{4}	1.8×10^{6}

Table 6 Summary of all the calculated sensor characteristics

2.6.5 Damping Ratio for Normal Oscillations

For *normal oscillations* of the floating-element, the damping coefficient c can be estimated using a squeeze-film model for the fluid in the gap, as shown in Fig. 2.6b. It can be shown that the damping coefficient for such oscillations is given as [75]

$$c_{normal} = 8.35\ \mu_{air} \sqrt{L_e} \left[\frac{\sqrt{\pi}\, L_e}{g}\right]^3 . \tag{2.20}$$

Substituting values for different parameters, the values of ξ_{normal} (= c_{normal}/c_c) for both the plate sizes is obtained as shown in Table 6. The normal oscillations are highly overdamped ($\xi_{normal} >> 1$). Therefore, unsteady pressure fluctuations (which, to first order, produce a common-mode signal) are not likely to cause resonance of the sensor structure. The above analysis for c_{normal} assumes the fluid in the gap to be incompressible. It has been shown that for squeeze numbers ($\sigma = (12\ \mu_{air}\ \omega\ {L_e}^2)/\ (g^2\ P_a)$, where ω is the plate oscillation frequency and P_a is the ambient pressure) less than 0.2 the fluid in the gap behaves like an incompressible fluid [76]. For the present case $\sigma = 0.137$ for the 120 μm sensor and $\sigma = 2$ for

the 500 μm sensor at 1 kHz plate oscillation frequency. Hence the incompressible assumption is valid for the 120 μm sensor and not for the 500 μm sensor at 1 kHz oscillation frequency. It must also be noted that this analysis overestimates the value of ξ_{normal} since slip flow conditions existing at the boundaries have been neglected. Table 6 summarizes all the theoretical sensor parameters calculated in this section.

2.7 Theoretical Minimum and Maximum Shear Stress

The lowest measurable shear stress is limited by the quantum noise due to the intrinsic fluctuations of the charge carriers in the photodiodes. From equation (2.8) the smallest differential photocurrent that can be detected is $\Delta I_{photo} = i_{shot,rms}$ and is equal to 10^{-13}A at a typical photocurrent of 1 μA. This corresponds to a wall shear stress of 10^{-4} Pa for the 120 μm sensor and 10^{-5} Pa for the 500 μm sensor (using equations (2.12) and & (2.14)). The lowest shear stress that we have measured is 0.0014 Pa for the 500 μm sensor and 0.0115 Pa for the 120 μm sensor. This was limited by the resolution of the differential pressure transducer that we used, as discussed in the testing chapter.

The maximum shear stress that can be measured is limited by the theoretical maximum allowable floating-element deflection. This is equal to the size of the gap between the floating-element and the substrate and is 7 μm for all devices. This results in a maximum measurable shear stress of 1 kPa for the 500 μm sensor and 10 kPa for the 120 μm sensor (using equation (2.14)). The maximum shear stress that we have measured is 133 Pa for both the sensors. This is limited by the maximum shear stress we were able to generate in our laminar flow channels, as described in section 4.6 of the testing chapter. It must be noted that over the entire measurement range, the stresses on the sensor element and supporting tethers are in the elastic regime (maximum deflection = 7 μm and maximum strain ~ 10^{-8}) and hence the force-deflection relationship should be linear (given by equation (2.14)).

2.8 Design of Sensor Layout

2.8.1 Location of bond Pads

The electrical access to the sensor chip was made through frontside wire bonds. Hence to minimize the perturbation of the flow field in the vicinity of the floating-element, the bond pads were located sufficiently downstream of the flow. The exact location of the bond pads was calculated by modeling the flow past the wire bonds, as illustrated in Fig. 2.7. For all the devices a low-profile gold ball-bond was used to electrically connect the chip to the package.

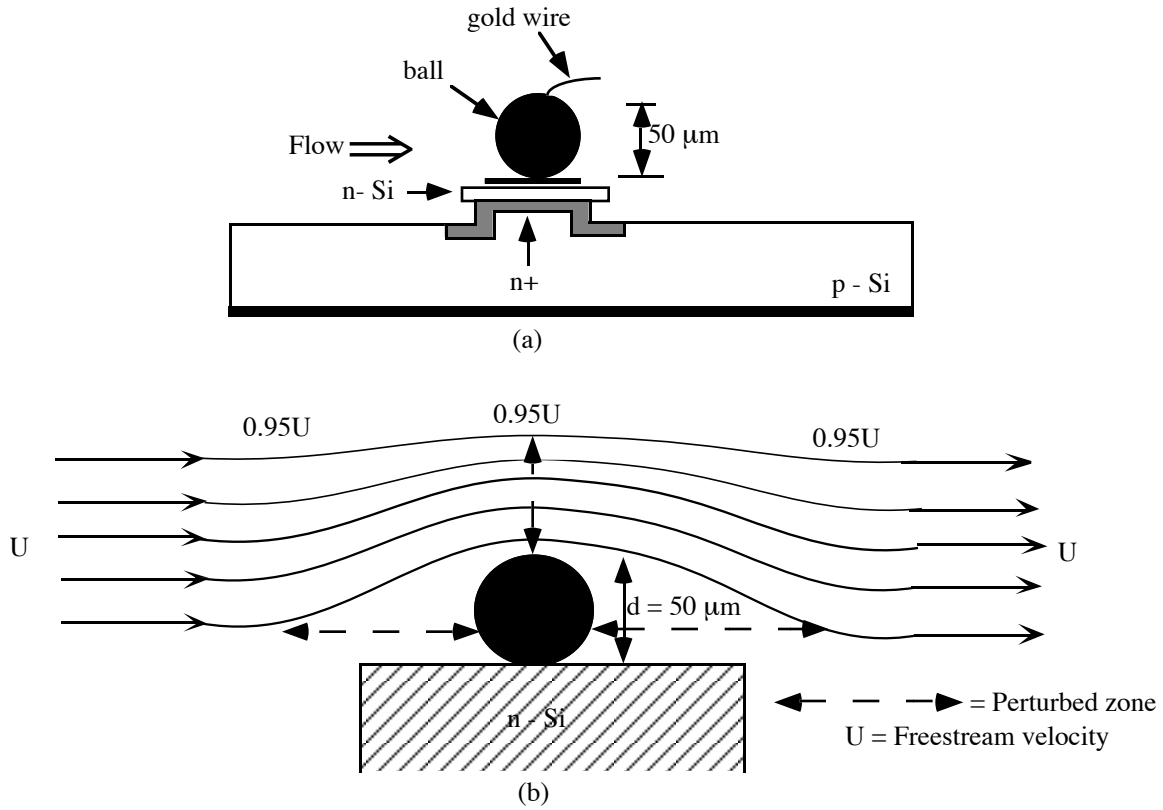

Fig. 2.7: a) Schematic diagram illustrating the flow past the ball-bond; b) exploded view of the flow past the ball-bond, modeled as flow past a sphere of diameter = 50 μm

The flow past the ball-bond was modeled as flow past a sphere of diameter = 50 μm. The typical air velocities encountered during testing are in the range 1 - 45 m/s. The Reynolds number based on the ball diameter *d* is in the range of 2 to 90. For Reynolds numbers close to one, the velocity distribution around the ball-bond can be obtained from the Stoke's solution for an immersed sphere [77]. For this velocity field around the bond, the radial and tangential velocities reach 95% of their freestream value at a distance of *10d* upstream of the bond. This corresponds to a perturbed zone size of 500 μm for our sensors. At the higher Reynolds numbers, the size of the upstream perturbed zone is smaller than for the low Reynolds number case [77]. In all the devices the bond pads were located at a minimum distance of 2500 μm, which is about five times the maximum size of the perturbed zone.

2.8.2 Matching of Output Lead-Lengths

Figure 2.8 illustrates the top and cross-sectional views of the junction-isolated lead from the floating-element to the bonding pad. This junction-isolated lead electrically isolates the

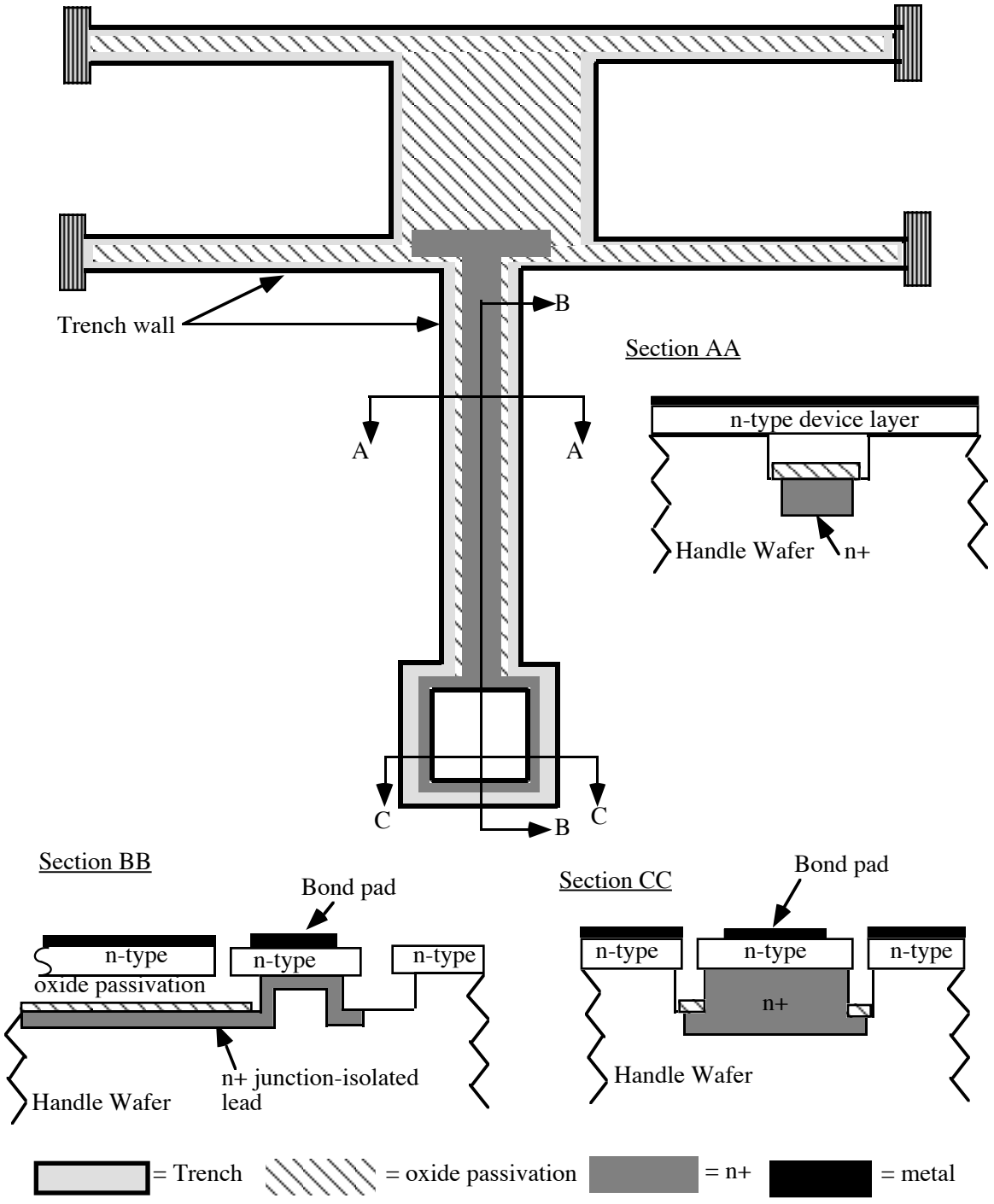

Fig. 2.8 Schematic diagram illustrating the readout scheme (only one junction-isolated lead is shown in this drawing). It must be noted that the top view shows only the handle wafer, while the cross-sectional views show both the handle wafer and the *n*-type device layer

sensor from the rest of the wafer substrate. The lead lengths from the two photodiodes were matched, so that the leakage currents from the two photodiodes would be equal. This is necessary to avoid any differential photocurrent output arising solely due to a mismatch in the leakage currents from the two photodiodes.

2.8.3 Frontside Sensor Shield

The purpose of shielding was to reduce the electric and electromagnetic field strengths by the use of a conducting layer. The shield helps to reduce the strength of fields in the vicinity of a susceptible device (the photodiode in this case). A thin metal layer was deposited on the frontside (during the sensor fabrication process) to define the frontside shield. This shield was connected to ground during measurements. Hence any noise current generated due to field-coupling is simply shunted to ground.

2.9 Different Sensor Designs and Test Structures

The different types of sensor layouts that were designed are described below -

2.9.1 *Diffused-Lead Sensor*. This sensor is comprised of two n^+ junction-isolated leads that connect the photodiodes to the bond pads, as described in section 2.8.2. The n^+ lead is defined on the handle wafer and runs continuously between the photodiode and the bond pad, as shown in Fig. 2.8.

2.9.2 *Airbridge Sensor*. This sensor is similar to the diffused-lead device except that the n^+ lead is not continuous between the photodiode and the bond pad, as shown in the top view and cross-sectional views of Fig. 2.9. The electrical connection between two disconnected n^+ regions is made through the *n*-type device layer, which is bonded on top of the handle wafer. The device layer looks like a "bridge," which is held at the silicon islands on the handle wafer and hence the name airbridge sensor. The two main reasons for developing this design were: 1) reduction of the total leakage current of the photodiode (due to reduced n^+ diffusion area). The measured leakage currents in this device were lower than that for the diffused-lead device ($I_{leakage,airbridge} \sim 75$ pA and $I_{leakage,diffused\text{-}lead} \sim 100$ pA). The n^+ diffusion area of the airbridge sensor was 30 % lower than that of diffused-lead device; 2) placement of the bond pads much more downstream of the floating-element than in the diffused-lead device due to the long lead-lengths in this device. For these sensors the passivation oxide is not present around the bond pads. This could explain the proportionately higher observed leakage current compared with the diffused-lead device.

2.9.3 *Other Designs*. In addition, we have also developed other design variants. A sensor with a mechanical handle attached to the floating-element was also designed, as illustrated in the

.

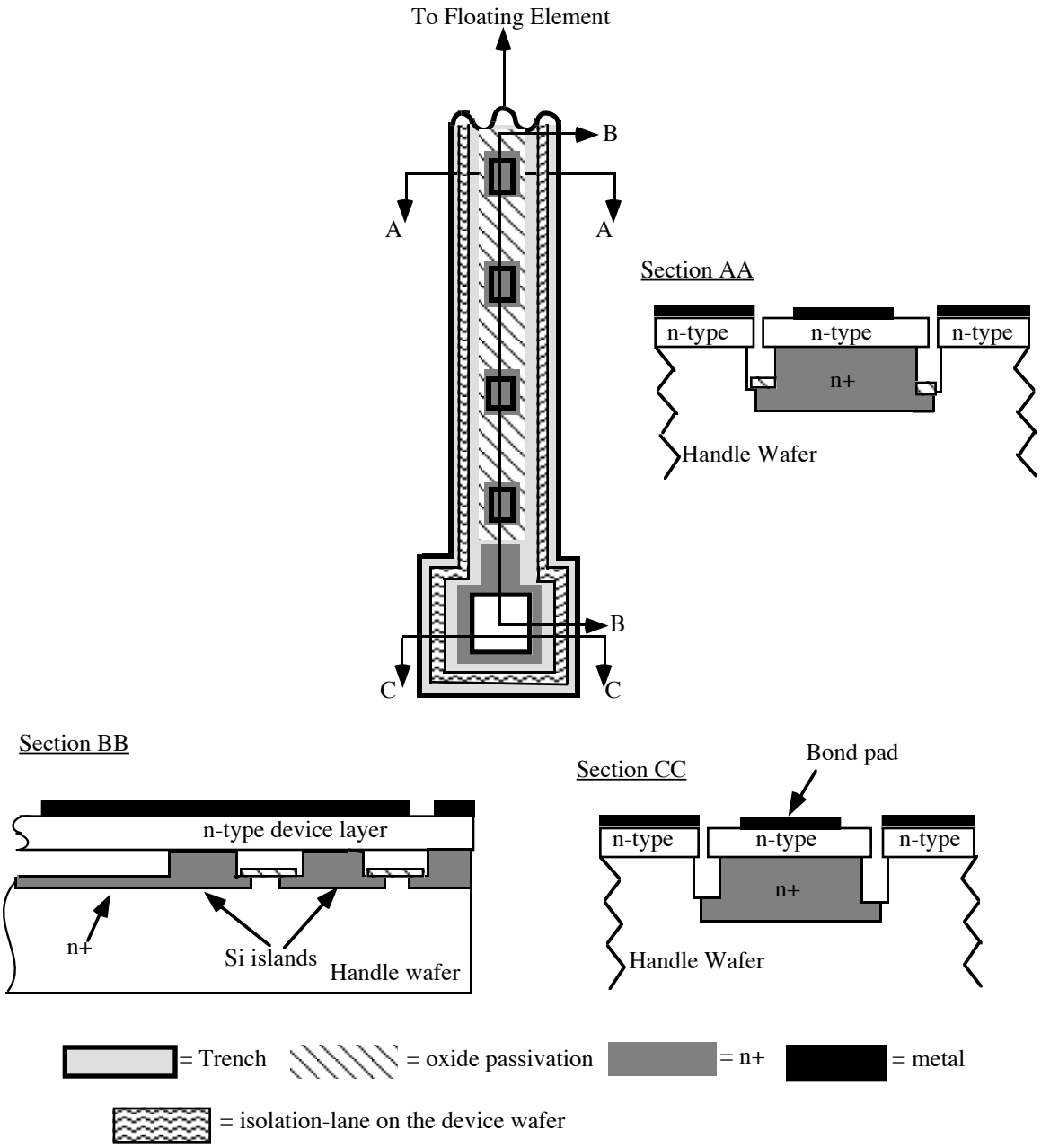

Fig. 2.9 Schematic diagram illustrating an airbridge sensor lead. It must be noted that the top view shows the features on the handle wafer and the isolation-lane on the device layer.

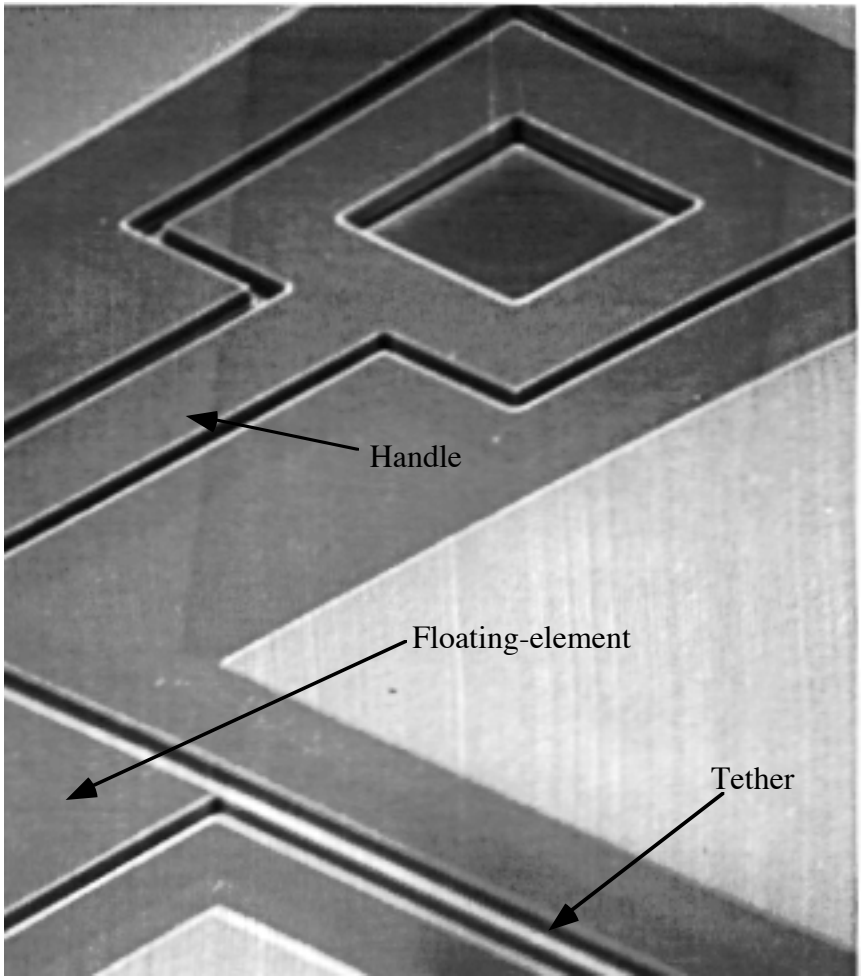

Fig. 2.10 Scanning electron photograph of floating-element sensor with a handle. Parts of the floating-element and the tethers have been cut off to clearly show the handle structure

photograph (Fig. 2.10). The floating-element structure can be moved by pulling the handle, thereby displacing the element without any flow. This sensor was designed to test the device performance on a wafer-inspection station, without any flow.

We have also developed a floating-element sensor with an interdigitated finger structure. The floating-element (which is the moving electrode) can be moved by applying a bias between the stationary electrode (this is fixed to the substrate) and the moving electrode. The sensor is designed for operation in the force-rebalance mode, i.e., the floating-element displaces under the action of the flow and can be brought back to its null-deflection position by applying a suitable bias. The output of the sensor is the applied bias, which is proportional to the wall shear stress. This sensor exploits the advantages of null-deflection devices, viz., better frequency-response (due to closed-loop operation) and reduced gap size around the floating-

element resulting in smaller measurement errors (see chapter 1 for errors caused by gaps around floating-element devices). A good overview of the operating principles of comb-drive devices can be found in [44, 78].

2.9.4 *Test Structures***.** Two kinds of test structures were designed: mechanical test structures and diode test structures. The mechanical test structures are arrays of cantilevers and fixed-fixed beams of different dimensions, which were designed to extract the Young's modulus and residual stress of the bonded and etched-back silicon layer (using electrostatic pull-in tests). Such tests have been performed on similar structures by other researchers at MIT. The modulus determined from these measurements was found to be consistent with published values, and the residual stress in the thinned-back silicon layer was measured to be zero to within the measurement resolution of 100 kPa ($strain < 10^{-6}$) [79]. For the purpose of this thesis, we used the published values of Young's modulus (E_{si} = 190 GPa) and residual stress (negligible), since the measured values were in good agreement with the published values.

The diode test structures are diodes of different shapes and sizes, i.e., diodes of different area-to-perimeter ratios. These were designed to electrically characterize the various diode parameters (ex: ideality factors, leakage currents and breakdown voltages) and also to study the effect of area-to-perimeter ratios on the different diode characteristics. We did not extensively study the effect of area-to-perimeter ratios, since the measured performance characteristics of the these diodes were found to meet or exceed the requirements of our application, as described in section 4.1 of the sensor testing chapter.

2.10 Second-Generation Sensors

The aim of fabricating the second generation sensors was to: a) develop an improved design for the photodiodes that would make them less sensitive to non-uniformities in the incident illumination; and b) to fabricate arrays of floating-element sensors. All the other aspects of the design of the second-generation sensors are similar to the first-generation devices. In this section we will discuss only those aspects of the design that are unique to the second-generation devices.

2.10.1 Design Improvements in the Second-Generation Sensors

As described in section 2.4.3, the original laser source had a non-uniform intensity distribution across the spot. This meant that the laser spot had to be precisely aligned relative to the sensor, to ensure that $\Delta I_{photo}/I_{photo} = 0$ with no flow. In order to minimize the sensitivity of the devices to light intensity variation the following two design changes were implemented:

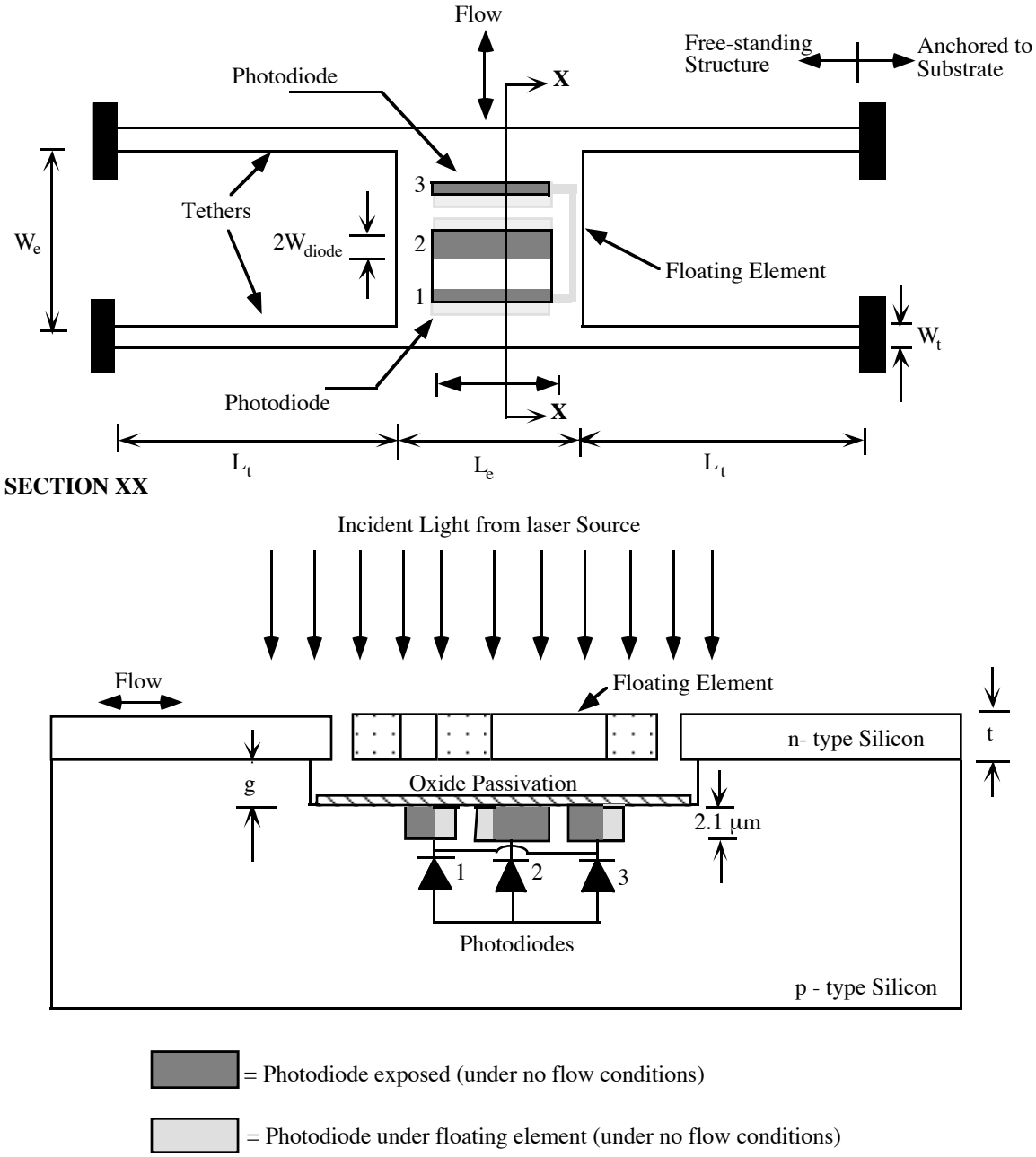

Fig. 2.11 Top and cross-sectional views showing the three-photodiode sensing scheme

a) *Reduced Photodiode Spacing*. The photodiodes were moved closer. They were located under the floating-element as opposed to the edges of the floating-element structure. A schematic diagram of the new design is shown in Fig. 2.11. This helps in minimizing the sensitivity of the devices to intensity variations because the non-uniformity in intensity across a shorter distance is lower and hence the photodiodes are subjected to a smaller intensity variation.

b) *Three-photodiode Scheme*. A three-photodiode scheme was implemented instead of the original two-photodiode scheme. This helps to eliminate the effect of linear intensity gradients that exist in the *Y*-direction. The new structure is illustrated in Fig. 2.11. The top diode (1) and the bottom diode (3) are electrically connected to form photodiode # 1 and the middle diode (2) forms photodiode # 2. The three diodes are equispaced and the exposed areas (in the no flow condition) of the top and bottom diodes (A) are half that of the middle diode (2A). The expression for the sensitivity of a sensor employing such a three-photodiode scheme is derived in Appendix B.

Let us consider the following example to illustrate how the three-photodiode scheme helps to null out a linear gradient in the *Y*-direction. Let the intensity at the location of the bottom photodiode be zero (arbitrary units), at the middle diode be five (arbitrary units) and at the top diode be ten (arbitrary units). The output photocurrent of a photodiode is proportional to the product of the incident intensity and exposed area (equation (2.2)). Hence for this example the output currents of the top, middle and bottom diodes are 10A, 10 A and zero, respectively. The constant of proportionality is the same for all three diodes. Since the top and middle diodes are electrically connected (and hence their photocurrents add), the differential output of the system is equal to $\Delta I = 10A - 10A = 0$. It can therefore be seen that a 1-D linear gradient in intensity can be nulled out using this design. Since the dimension of the diodes in the *X*-direction is large, any gradient in intensity in this direction is averaged out by each of the diodes. A theoretical estimate of the reduction in sensitivity that can be obtained by using the three-photodiode design shows a 78% reduction in sensitivity to intensity variations as compared with the earlier deisgn (see Appendix C for the calculations). The measured performance improvement obtained using the three-photodiode design, is presented in section 4.12 of the sensor testing chapter.

2.10.2. Sensor Arrays

The main motivation for fabricating sensor arrays was to develop a tool for fundamental and applied research in turbulence. Sensor arrays can be used to estimate the spanwise spacing and streamwise orientation of coherent structures in a turbulent flow [80]. Such estimates can be obtained from cross-correlation measurements using an array of wall-mounted shear stress sensors [81]. The asymmetry of the coherent structures, which is an essential aspect of the turbulence-generation process, can also be detected by an array of wall-mounted shear-stress sensors [82].

Applied research includes the active control of turbulent flows. This could either be the control of laminar-turbulent transition [83] or active turbulence control [81]. An important aspect of the existence of coherent structures in a turbulent flow environment, is the possibility

of controlling turbulence by interacting with these structures, as pointed out by [84]. Interaction with coherent structures is the basis for localized active control in turbulent flows. Shear-stress sensor arrays (of the desired size and spacing) can be used as part of a system of sensors and actuators for the control of turbulence. Sensors located upstream and downstream of the actuators observe the passage of coherent structures. Once a structure has been detected by the sensors, the information can be used by the actuator to optimally counteract the detected structure, in order to accomplish the control task. A good discussion of the issues associated with the use of sensor arrays for active control of turbulent flows can be found in [52, 82, 84]. The biggest problem facing the practical implementation of active control is the unavailability of miniature sensors and actuators. In order to accomplish the control task, the sensors must have sufficient spatial and temporal resolution to accurately identify: 1) the emergence of the coherent structure; and 2) the spanwise orientation of this structure. The next sub-section discusses the choice of sensor size and spacing that are desired for the above-described applications.

2.10.3 Array Parameters

It has been suggested that the desired sensor size and spacing is of the order 50ℓ or lower, where ℓ is a viscous length scale [1]. The desired temporal resolution for this application, is of the order of a few t^*, where t^* is the viscous time scale [1]. Using typical values for the low-speed wind tunnel at MIT, $Re_\theta = 16000$ and $U = 15$ m/s, $\ell = 30$ μm and $t^* = 58$ μs [see Table 2, chapter 1]. Hence we need sensors whose size and spacing are of the order of 1000 μm or lower and with a bandwidth of 17 kHz or better.

We have designed and fabricated the following two types of sensor arrays: 1) two-sensor array, which is an orthogonal pair of sensors (Fig. 2.12). Such a pair could be used to detect the emergence and orientation of coherent structures; 2) eight-sensor array as shown in Fig. 2.13. This array can be used to obtain the spanwise distribution of the streamwise shear stress or by rotating the array by 90°, the streamwise distribution of the spanwise shear stress. In a turbulent boundary layer such an array can be used to obtain shear-stress correlation measurements that provide the desired information about the coherent structures. Table 7 lists all the dimensions of the two-sensor and eight-sensor array. The design of the layout for the arrays is the same as that for the first-generation sensors. These sensors were tested using the new laser source, which had a more uniform incident intensity, as described in the testing chapter.

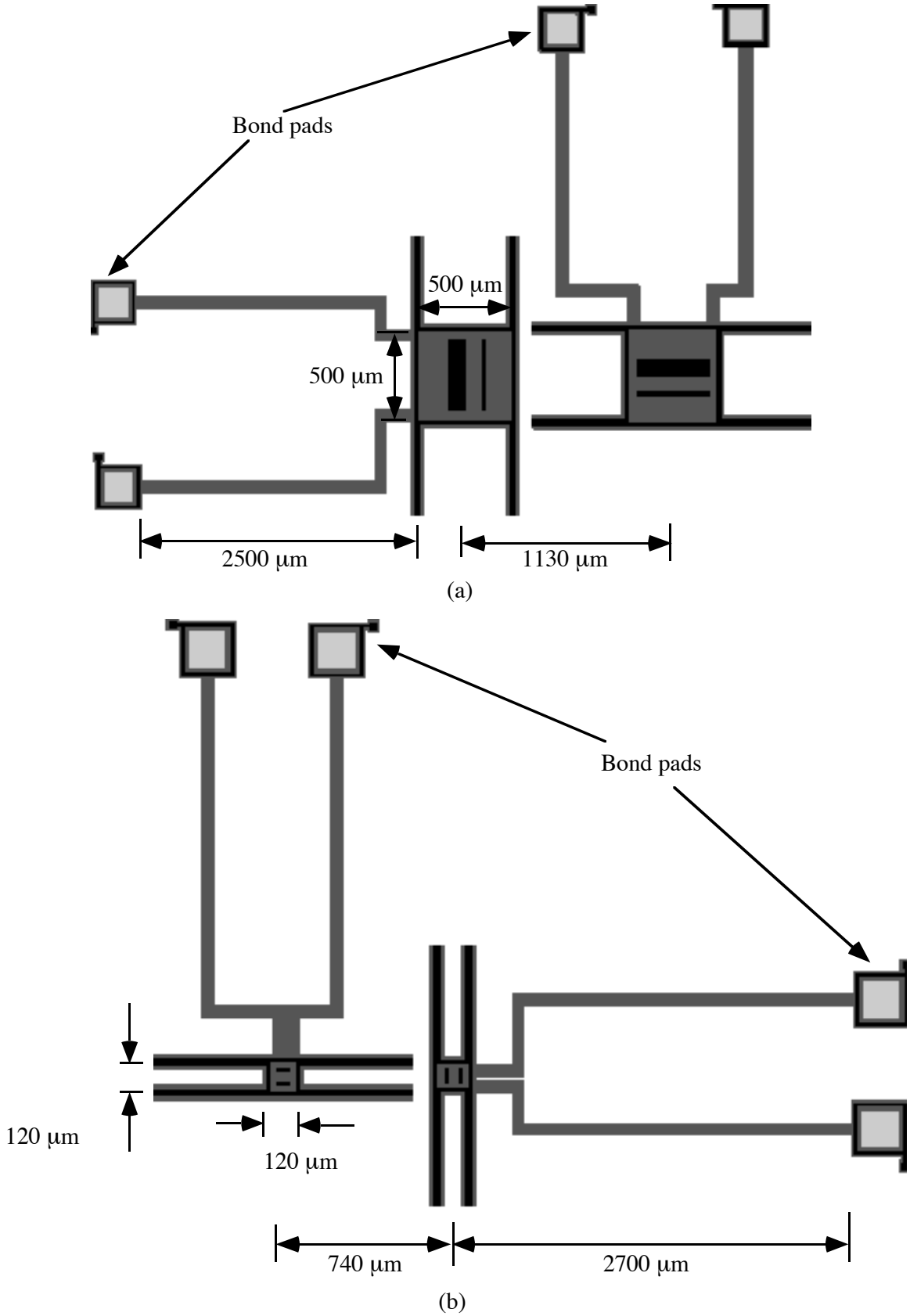

Fig. 2.12: a) Two sensor (500 µm) array; two sensor (120 µm) array

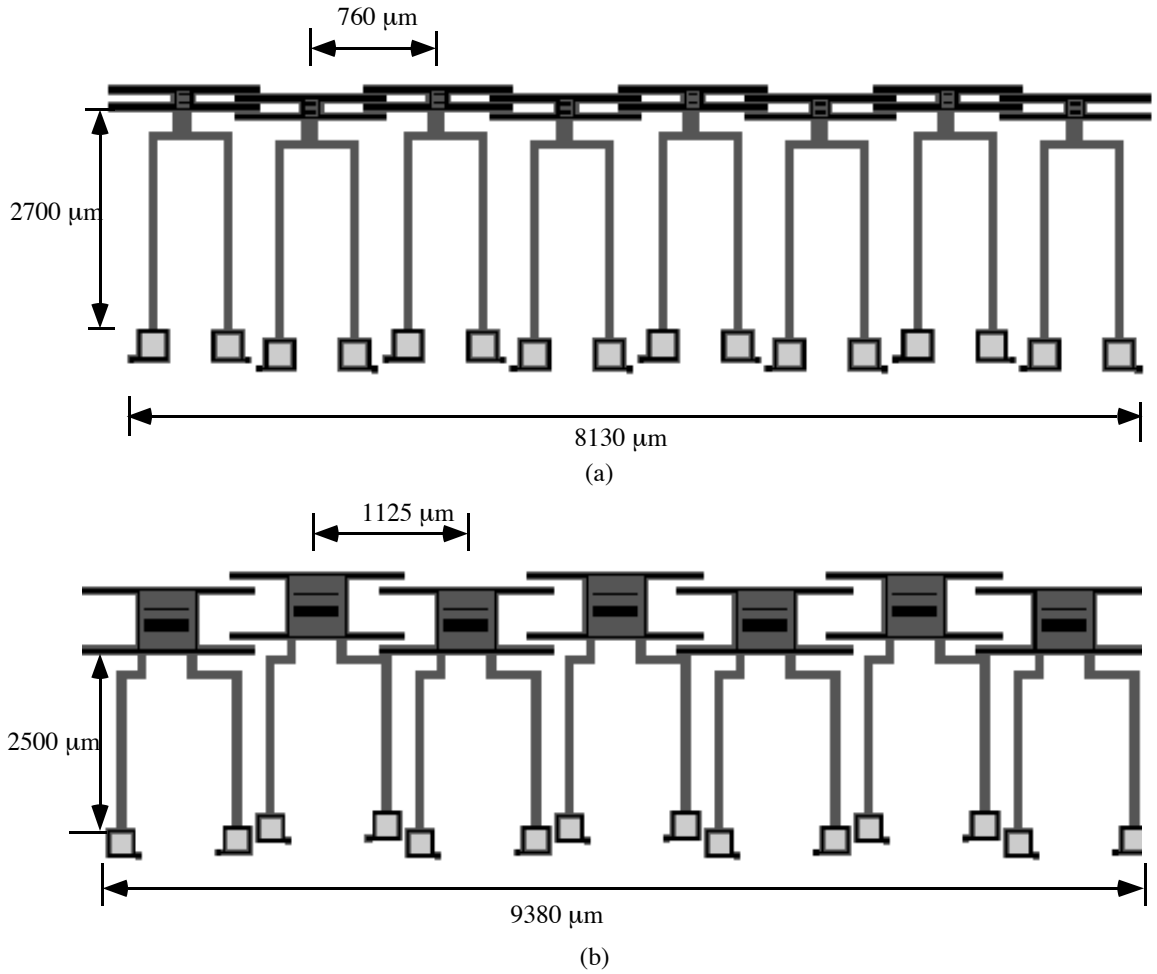

Fig. 2.13: a) One-dimensional array of 120 μm sensors; b) one-dimensional array of 500 μm sensors

Array type	Floating element size (length, width, thickness)	Floating element size in L^*	Center-to-center spacing of floating elements in L^*	Bandwidth
Two sensor array - 120 μm	120 μm x 120 μm x 7 μm	4	25	52 kHz
Two sensor array - 200 μm	200 μm x 200 μm x 7 μm	6.7	27	34 kHz
Two sensor array - 500 μm	500 μm x 500 μm x 7 μm	16.7	37	16 kHz
Eight sensor array - 120 μm	120 μm x 120 μm x 7 μm	4	31	52 kHz
Seven sensor array - 500 μm	500 μm x 500 μm x 7 μm	16.7	42	16 KHz

Table 7 Dimensions of sensor arrays. For all the sensors the tether width and thickness are 10 μm and 7 μm, respectively. The viscous length scale is equal to 30 μm at $Re_\theta = 16000$ and $U = 15$ m/s (typical conditions in the low-turbulence wind tunnel at MIT)

Chapter 3. SENSOR FABRICATION

This chapter presents a detailed description of the shear stress sensor fabrication process. The chapter begins with a discussion of the masks used in the fabrication process and the layout of the sensor dies. The sensors were fabricated using a sealed-cavity fusion-bonding process, similar to [85]. The second section presents a brief overview of fusion-bonding and a generic sealed-cavity sensor fabrication process. The rest of this chapter discusses the actual fabrication process itself, with the aid of schematic cross-section drawings. At each stage the following three aspects of the process are presented: i) the description of that step; ii) process development issues; iii) any other issues associated with process optimization. A detailed process flow that lists all the process parameters, the equipment and laboratories (MIT Labs) in which the steps were performed, is given in Appendix D. It must be noted that the process flow used to fabricate the first-generation stand-alone sensors and second-generation sensor arrays are almost the same. The only difference in the process for the two generations is in the starting material that is used for the device wafers, as pointed out in the device wafer processing section.

3.1 Mask Design

The sensor fabrication process is an eight mask process. This section describes: i) the function of each of the mask layers (the details of the photolithographic steps that are performed using these mask layers is presented in section 3.3); ii) the overall layout of the sensor chip. All the masks were generated using the KIC CAD layout tool [86].

3.1.1 Mask Layers

Mask # 1 (Dark Field Mask). This mask is used to define the trenches on the frontside of the handle wafer. It must be noted that all the subsequent mask layers align to this layer.

Mask # 2 (Dark Field Mask). This mask defines the photodiode implant (n+ implant) regions. The n^+ leads from the photodiode to the bond pads run within the trenches. The design rule for this layer is such that the n^+ region (after all the thermal steps) is 20 μm away from the trench walls (see Fig. 2.8).

Mask # 3 (Clear Field Mask). This mask is used to pattern the oxide layer on the handle wafer so that the oxide can be selectively etched from the field-region, leaving it behind in the trenches. The design rule for this layer is such that the oxide that is left behind in the trench is 10 μm away from the trench walls on both sides (see Fig. 2.8). This design rule ensures that the oxide layer is cleared from the vertical trench walls and the regions where the wall meets the top surface of the wafer.

Mask # 4 (Dark Field Mask). This layer is used to transfer the alignment marks on the handle wafer to the top surface of the device wafer. This mask was used only for the second-generation sensors.
Mask # 5 (Clear Field Mask). This layer is used to protect the floating-element structure during the high dose and high energy implant of the top surface of the device layer. The design rule for this layer is such that the mask protects the floating-element and a region 15 μm around the floating-element.
Mask # 6 (Clear Field Mask). This layer patterns the metal on the top surface of the device wafer.
Mask # 7 (Dark Field Mask). This layer is used to define the regions for the vent-hole etch.
Mask # 8 (Dark Field Mask). This layer is used for the final release (using a plasma etch) of the microstructures. Since a vertical overetch (which is required to ensure the release of all the microstructures on the wafer) produces some degree of lateral overetch, the patterns on this mask layer are designed to be smaller (by 1 μm) than the desired opening on the structure. The choice of 1 μm is based on the amount of lateral etch that occurs during the final plasma etch.

3.1.2 Chip Layout

The first-generation sensor wafer is comprised of two dies (die # 1, die # 2) stepped across the wafer, as shown in Fig. 3.1. The layout of the dies are shown in Figs. 3.2 and 3.3. In both cases the die is separated into three zones. Figure 3.3 shows die # 1, which comprises of 4 sensors. The first zone on the left is a 500 μm airbridge sensor, the second zone comprises of the 120 μm and 500 μm diffused-lead sensor and the third zone on the right has a 500 μm airbridge sensor. The diode test structures are located on the left edge of this die. Figure 3.4 shows die # 2, which comprises of 4 sensors. The first zone on the left has two sensors - 500 μm diffused-lead sensor with handle and with comb-drives, the middle zone has a 120 μm airbridge sensor and the third zone on the right has a 500 μm airbridge sensor with comb-drive. The mechanical test structures are located on the left edge of the die (For a description of the different devices please section 2.9, of the sensor design chapter). The chip layout for the second-generation sensors is shown in Fig. 3.4. The 120 μm and 500 μm sensor arrays are located on the top and bottom of the chip, respectively.

3.2 Wafer-Bonding (Fusion-Bonding) Technology for Microsensor Fabrication

Sensors and actuators can be manufactured using a silicon-to-silicon direct wafer bonding or a sealed-cavity process. In this section we present a brief description of the physics of the wafer-bonding process. A simple example of a generic sealed-cavity process that can be used to fabricate a microstructure is then presented in the next sub-section. This simple

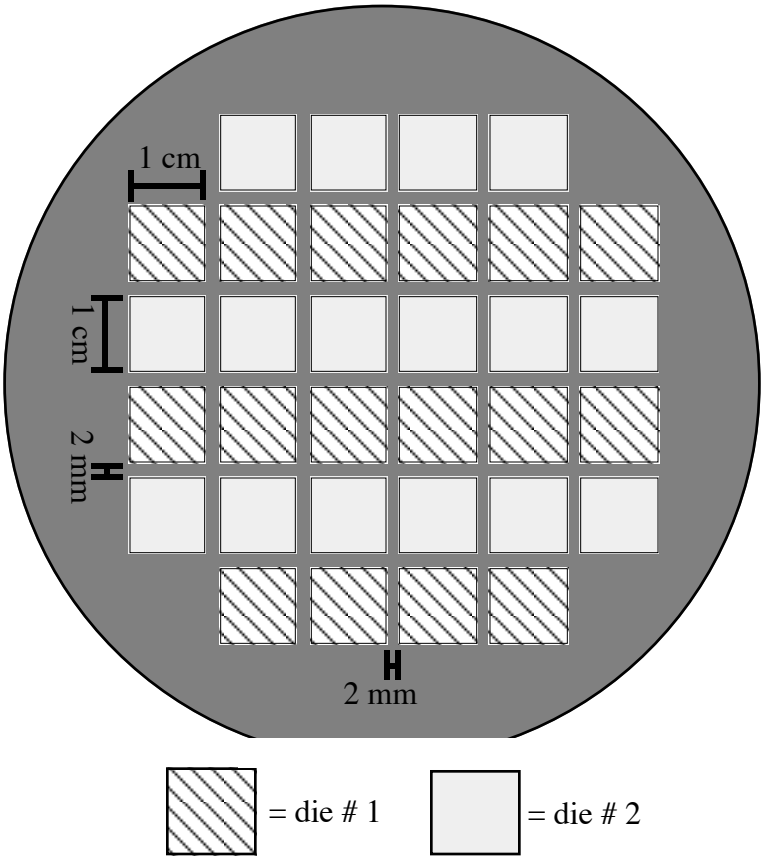

Fig. 3.1 Layout of sensor chips on the wafer. The chip size is 1 cm x 1cm and the chip-to-chip spacing is 2 mm.

example will help the reader in better understanding the actual shear stress sensor fabrication process, presented in section 3.3. An excellent overview of wafer bonding can be found in [36, 87]. A good review of the application of the wafer-bonding technology for the fabrication for micromechanical devices can be found in [36, 88].

3.2.1 The Physics of Wafer-Bonding

Silicon wafer-bonding technology is a technique of fusing together two silicon wafers by heat. The process of fusion-bonding of silicon involves two steps - 1) contacting a pair of specularly clean wafers (which have been treated in an appropriate chemical solution) at room temperature; 2) annealing the wafers at a high temperature to form a permanent bond. The success of silicon to silicon fusion bonding depends greatly on the quality of the silicon surface prior to bonding. Both the physical and chemical state of the surface are critical to the bonding process: Physical state - the surfaces should be mirror polished and free of any contamination; Chemical state - the normal (stable) state of silicon has a thin native oxide (40 - 50 Å) on the

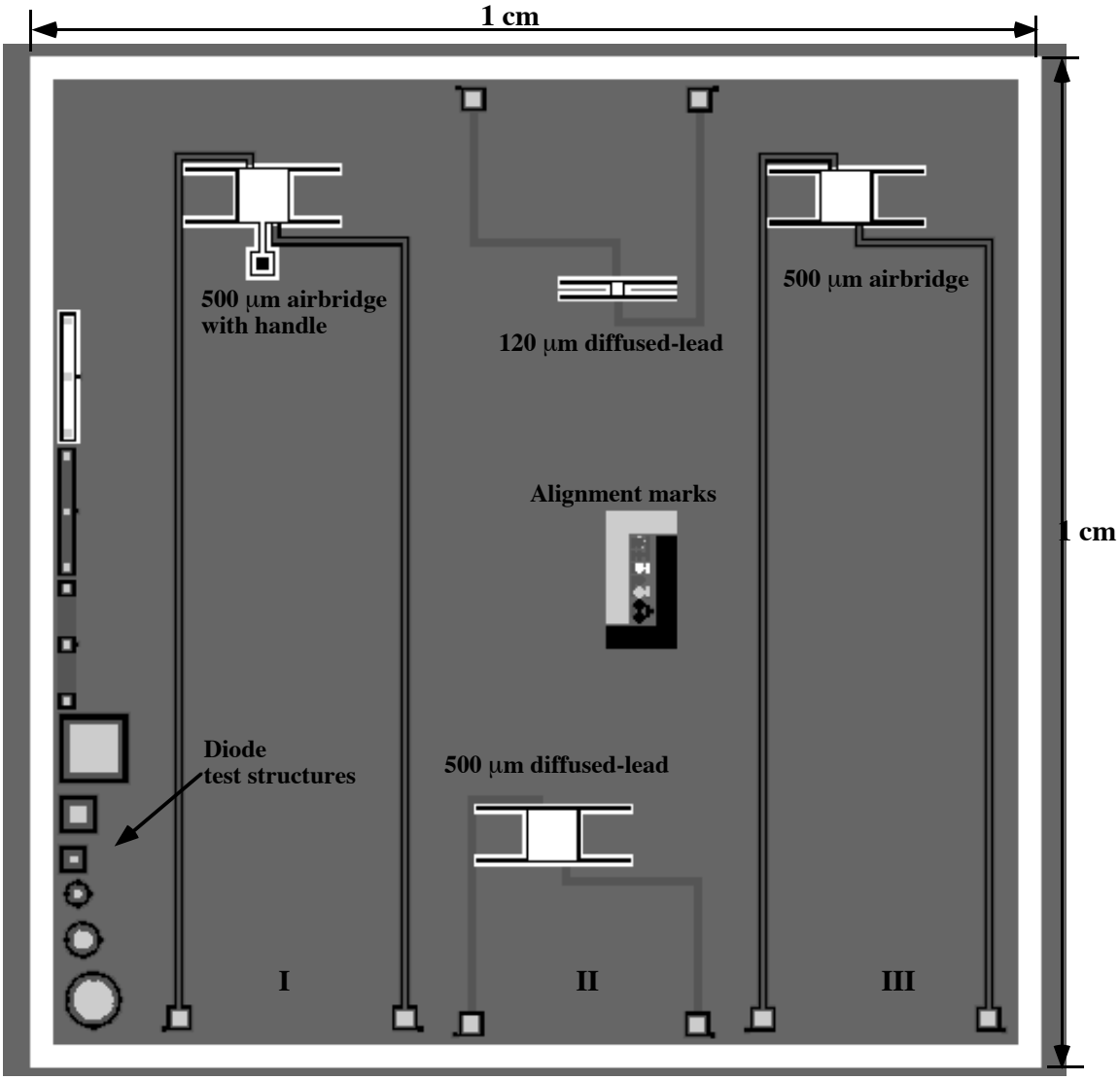

Fig. 3.2 KIC plot of the chip layout for die # 1 (first-generation sensors)

surface and the surface is said to be *hydrophilic*. A hydrophilic silicon surface state can be created using a RCA cleaning procedure (See Appendix D for a description of the RCA cleaning procedure). A study of hydrophilic surfaces has shown an abundance of *OH* groups attached to the dangling bonds on the wafer surface [89]. When two wafers that have *OH* groups on their surface are brought into intimate contact, a weak attractive electrostatic force results between the two wafers that helps to keep the contacted wafers together. This weak force is believed to be due to the formation of hydrogen bonds between the OH groups [90]. It should be pointed out that this room temperature contacting process is reversible, and at this stage the wafers can still be separated. A permanent bond occurs only after the high temperature anneal step.

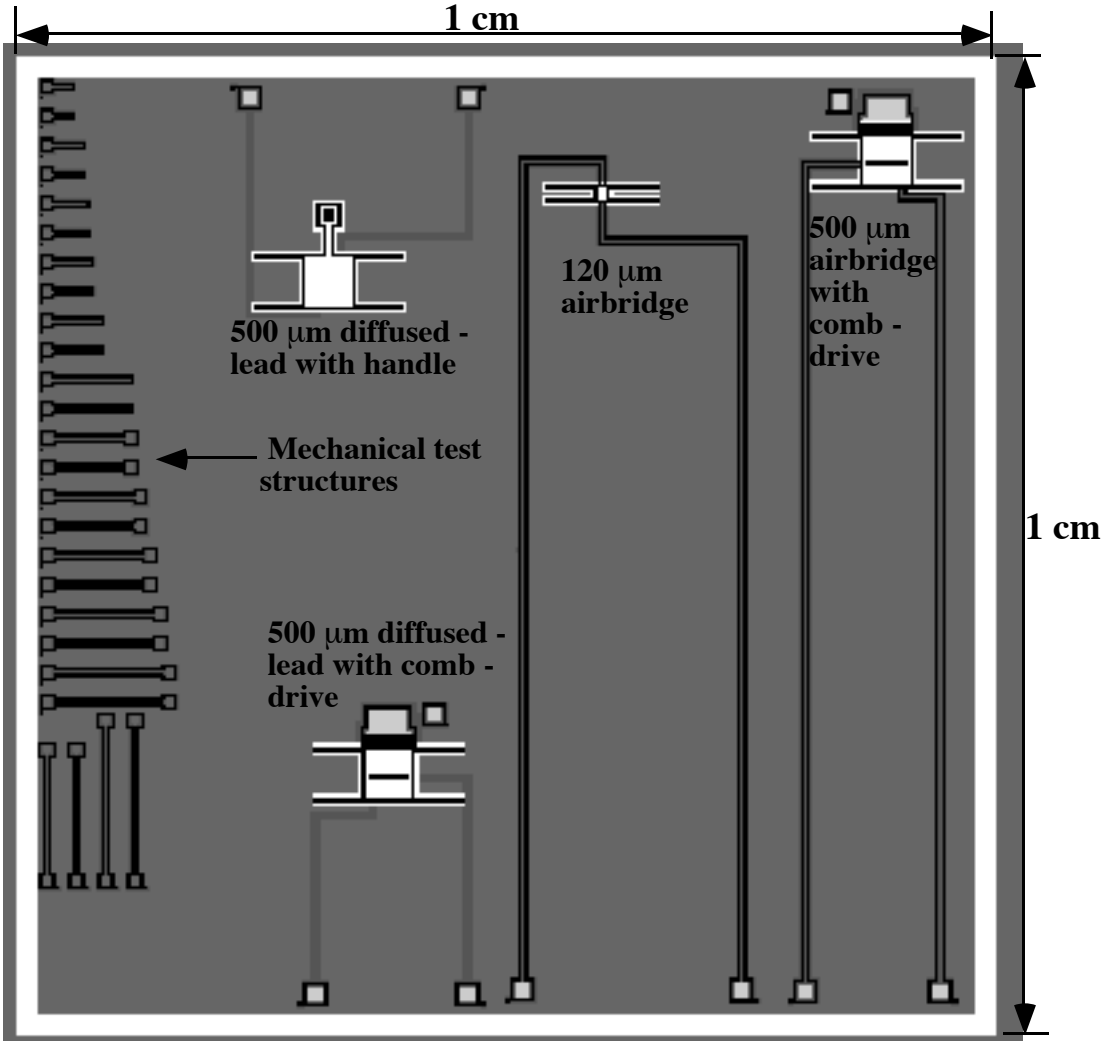

Fig. 3.3 KIC plot of the chip layout for die # 2 (first-generation sensors)

In the second step, the contacted wafers are subjected to a high temperature anneal. Typically wafers are annealed in an O_2 or N_2 environment at temperatures greater than 600^{O}C. When the wafers reach temperatures of about 200^{O}C, dehydration of the *OH* groups begins and the hydrogen bonds between the OH groups are converted to siloxane (*Si-O-Si*) bonds and water. At even higher temperatures, typically around 400 C, the *Si-O-Si* bonds are converted into a very strong covalent *Si-Si* bond and the resulting oxygen diffuses into the substrate. Following the anneal, a permanent bond has formed between the two wafers and the wafers cannot be separated without fracturing the silicon substrates. The strength of the bond is a function of the annealing temperature and is typically specified in terms of the surface energy (erg/cm^2) required to separate the wafers. Typical low-temperature (< 600^{o}C) *Si-Si* bond strengths are of the order of 500 erg/cm^2 and high-temperature (> 1000^{o}C) bond strengths are of the order of 1000 erg/cm^2 [36].

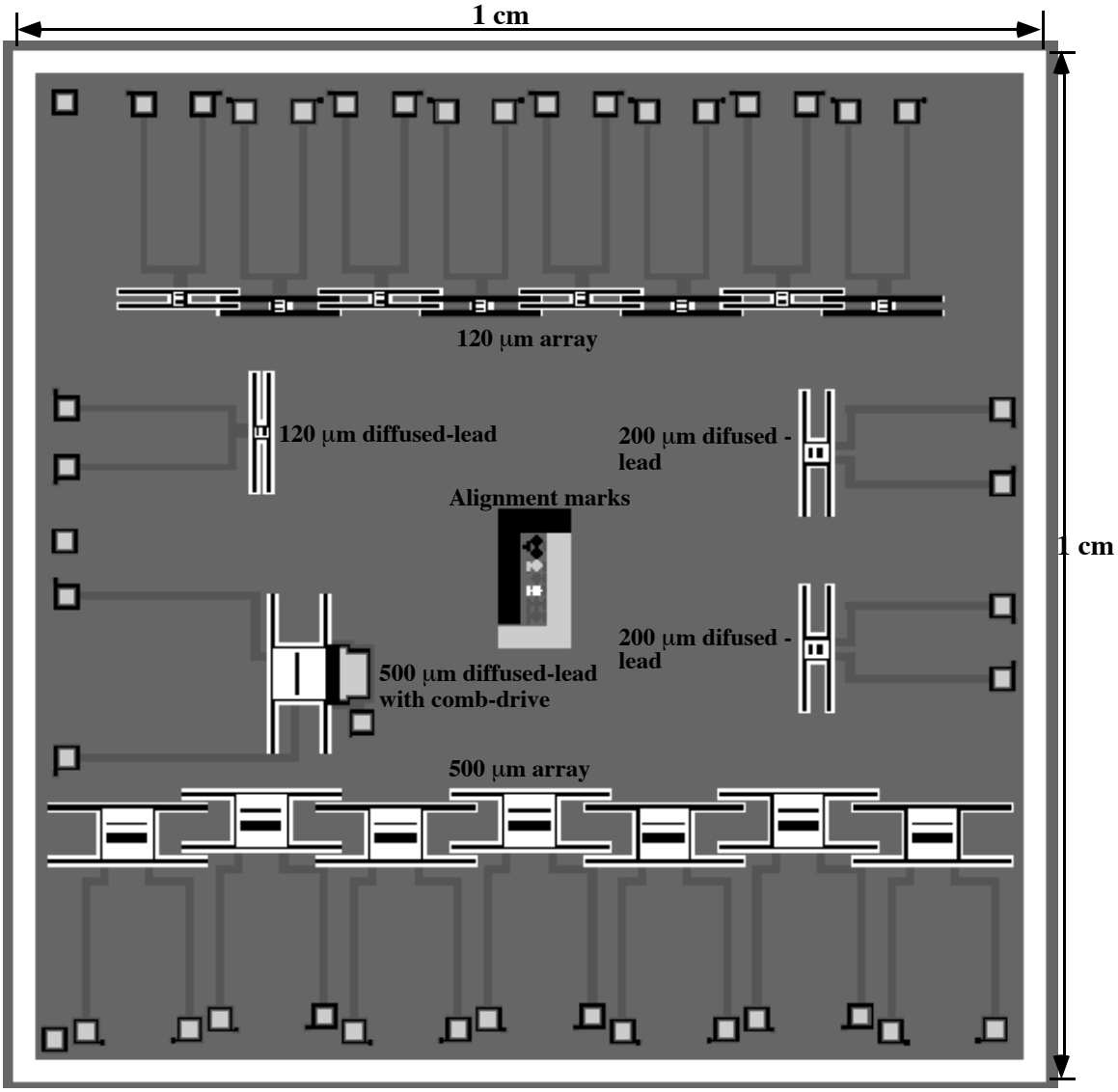

Fig. 3.4 KIC plot of the chip layout for the second-generation sensors

The above description of the bonding process is for a hydrophilic surface (surface with a native oxide). This is the most commonly used form of fusion bonding. It must be noted that a silicon-to-silicon fusion bond can also be achieved between two hydrophobic surfaces (surface where the native oxide has been stripped in *HF* solution, prior to bonding). The physics of the bonding process for these surfaces is different than that for hydrophilic surfaces. The details of this process can be found in [87].

3.2.2 Bond Evaluation

The integrity of the surface of the two wafers controls the final quality of the bond. A poor surface quality results in voids in the interface region of the bonded pair. Voids in the

interface can arise due to - trapped gases, particulates, surface contaminants and insufficient wafer flatness. The most common cause of bonding voids is due to particulates and trapped air at the interface.

There are several methods by which the bonded interface can be inspected for voids. Some of the techniques are - infrared (IR) imaging, X-ray and ultrasonic imaging. Each of these techniques has a different level of resolution in detecting interface voids. The IR inspection system is typically used for coarse inspection while ultrasonic imaging is used for imaging very small voids. Figure 3.5 shows a schematic diagram of a simple IR inspection system developed by our group at MIT. The system comprises of a wafer holder, an incandescent bulb that acts as an IR source, a CCD camera fitted with a visible light filter and a video monitor. Voids appear as either dark regions or as a series of concentric interference fringes on the video monitor. The wafers are typically inspected after the "contacting" process and before the anneal. If the bonded pair has an unacceptable number of voids, it can be separated by inserting a teflon tweezer between the two wafers. The wafers should then be cleaned and the bonding process can be attempted again.

3.2.3 Generic Sealed-Cavity Process

The sealed-cavity process starts on two wafers: a handle wafer and a device wafer. The handle wafer provides the cavities, which allow the fabrication of suspended microstructures. The microstructure (ex: beam/diaphragm) itself is fabricated on the device wafer.

The first step in the fabrication process involves the etching of cavities in the handle wafer. The device wafer is then contacted with the handle wafer in a controlled ambient and annealed in a high-temperature ambient (1150°C), to produce a sealed-cavity (and hence the name sealed-cavity process). The controlled ambient (typically a ratio of N_2 and O_2) contacting process helps to control the residual pressure in the sealed-cavity after the high-temperature anneal step. During the anneal step, most of the oxygen in the cavity is consumed to form a thin SiO_2 layer and the pressure in the cavity after the anneal is equal to the original partial pressure of nitrogen. The device wafer is then thinned back. It must be noted that in order to successfully exploit this technology to fabricate micromechanical devices, the controlled thinning of the device wafers is very critical. The thin-back process controls the final surface roughness and dimensional tolerance of the device layer, both of which are important parameters for the final device performance. The final step in the process involves plasma etching the device wafer to release the microstructure.

The procedure that is employed for the thin-back process depends upon the type of etch-stop that is used to define the device layer thickness. The following etch stop techniques are commonly used: i) diffused boron etch-stop; ii) electrochemical etch-stop; iii) oxide etch-

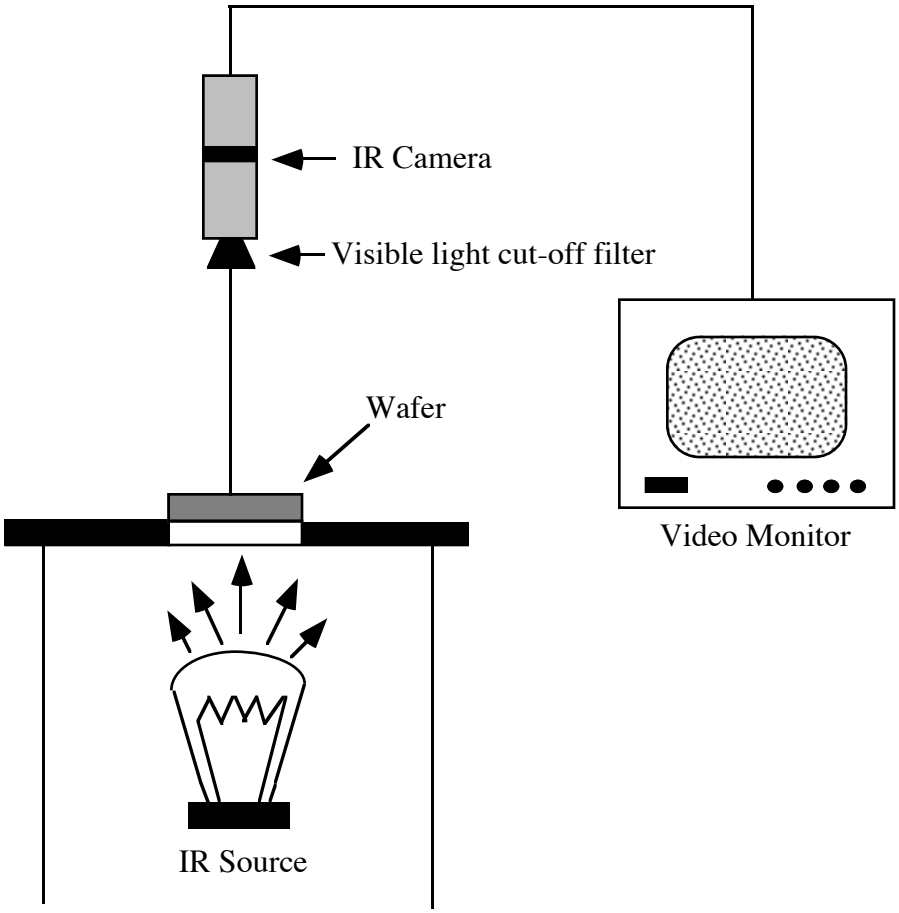

Fig. 3.5 Schematic diagram of an IR bonding-void inspection system

stop. An example of a device fabricated using the boron etch-stop technique can be found in [91]. In this thesis devices have been fabricated using etch-stops ii) and iii). In all the three cases wafers are typically thinned in an alkaline solution (ex: *KOH*/*CsOH* solution). The details of the fabrication steps for the thin-back process using etch stops b) or c) can be found in the next section.

After the thin-back process the membrane or diaphragm is deflected downwards due to the differential pressure load ($P_{atmosphere}$-P_{cavity}) acting on them. The amount of downward deflection can be estimated from the elastic load-deflection equations [92]. It must be noted that the low pressure in the cavity prevents the rupturing of the thin membranes during any high-temperature or low-pressure step that are carried out after the thin-back process and prior to the microstructure release step.

The advantages of the fusion-bonding process over the conventional surface micromachining process are:

1) Microstructures are fabricated in single-crystal silicon and hence they have better mechanical properties. Moreover, this silicon device layer has no residual stress.

2) The final microstructure release step is performed using a dry (plasma etching) process as opposed to a wet process that is used in surface micromachining processes. The dry release process helps to overcome the problem of stiction of the released structure to the substrate [85].

3.3 Optical Shear Stress Sensor Fabrication Process

This section describes (in sequence) the details of the various process steps involved in the fabrication of the sensor. The process starts on two wafers: a handle wafer and a device wafer. Each of these wafers are procesed separately up to the wafer bonding step, after which they are processed together. It must be noted that in the following process description the step numbers refer to the numbers in the process traveler (Appendix D).

3.3.1 Handle Wafer Processing - Upto Wafer Bonding

Starting Material

The handle wafer starting material is:

<100> Boron doped (0.5 - 20 ohm-cm) double-side polished 4" silicon wafers (500-550 μm thick).

Backside electrode formation (steps 1- 2.5)

The first step in the process is the growth of a thermal screening oxide layer that is 450 Å thick. The next step involves a high dose and high energy blanket boron implant (species = boron, dose = 5 x 10^{15} cm^{-2}, energy = 100 KeV, 7 degree tilt) and drive-in (temperature = 1150°C, time = 2 hrs, N_2 ambient) of the backside of the handle wafer. This provides an ohmic contact for the backside metallization for the photodiode contact and also ensures a good electrical contact during the electrochemical etch (ECE) that is used to thin-back the device wafer. The screening oxide helps to minimize implant channeling and prevent out-diffusion of the implanted species during the drive-in process. The screening oxide was grown for all the subsequent implant steps. The SUPREM process simulation software was used to determine the surface concentration and the sheet resistivity in the implanted layer. The concentration profile after all the thermal steps seen by this layer, is shown in Appendix D. The SUPREM output file that gives the electrical characteristics of this layer is also included in Appendix D.

Frontside trench etch (steps 4.1-4.4)

The wafer is first coated with a 1 μm photoresist. Before being coated with photoresist the wafers are primed in an automatic HMDS (hexamethyldisilazane) vapor prime oven. HMDS is widely used in the semiconductor industry to improve photoresist adhesion to oxides. The HMDS reacts with the oxide surface forming a strong bond to the surface. At the

same time free bonds are left that readily react with the photoresist, enhancing the photoresist adhesion. The stable state of silicon always has a thin layer of native oxide on the surface and hence the use of HMDS improves the adhesion of the photoresist. This HMDS coating process is assumed for all subsequent photo steps. The wafers are then patterned in a KarlSuss Model MA 4 contact aligner (note: all the subsequent photolithography steps were performed on the contact aligner). This layer is aligned to the major flat on the wafer. All the subsequent mask layers align to this layer.

The next step involves the plasma etching of 1.2 μm trenches in the handle wafer, as shown in Fig. 3.6A. The plasma etching is carried out in a LAM 480 etcher using the etch parameters given in Appendix D. The etching chemistry is based on a SF_6/CCl_4 based plasma. The etch rate of silicon using this chemistry was highly geometry-dependent, 50 Å/s for large geometries and 27 Å/s for the smaller ones. This is referred to as the "loading effect". Typically, much higher etch rates were observed in larger areas. The etch rates varied by almost an order of magnitude as the pattern size was changed by an order of magnitude. This made it difficult to achieve uniform trench depths across different pattern sizes. The wafers were rotated halfway through the etch in order to achieve better uniformity in the etch depth across the wafer. The measured trench depths on the wafer were in the range 1.1-1.2 μm.

The bottom of the trenches were found to be quite rough when the standard SF_6/CCl_4 plasma (SF_6 = 95 sccm; CCL_4 = 3 sccm; sccm = standard cubic centimeter per minute) chemistry was used. We believe this was due to the "micromasking" effect of the photoresist, which is "sputtered" from the top surface of the wafer into the bottom of the trenches. This problem was overcome by increasing the flow rate of CCl_4 from 3 sccm to 10 sccm. This considerably minimized the surface roughness on the bottom of the trenches but did provide a small curvature to the trenches (center to edge etch depth of 500-750 Å). This small curvature is acceptable for the final device structure. The reduced surface roughness is due to the increased etch rate of the photoresist. The increased CCl_4 flow rate resulted in a small increase in the resist removal rate and small decrease in the silicon etch rate, thereby reducing the overall silicon to photoresist selectivity (original selectivity- 6:1; new selectivity- 4.5:1). The initial photoresist thickness of 1 μm was hence more than sufficient to etch a depth of 1.2 μm. After the etch the photoresist was stripped in a piranha solution.

Photodiode implant (steps 5.2-6.4)

The first step is to grow a 450 Å of screening oxide. The wafers are then blanket boron implanted (species = boron, dose = 8 x 10^{11} cm^{-2}, energy = 70 KeV, 7 degree tilt). This implant helps to increase the surface boron concentration, thereby increasing the threshold

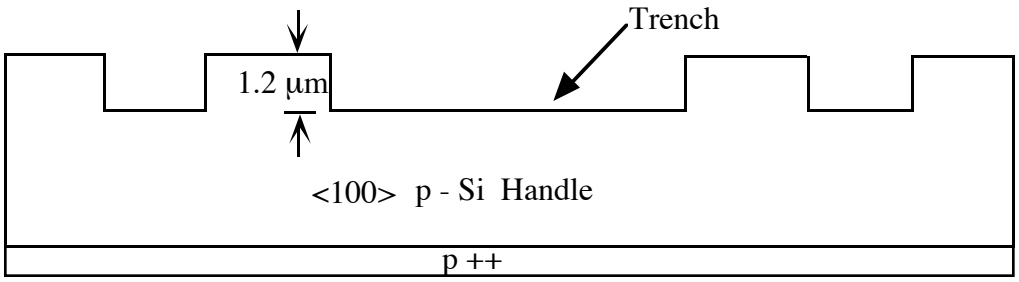

(A)

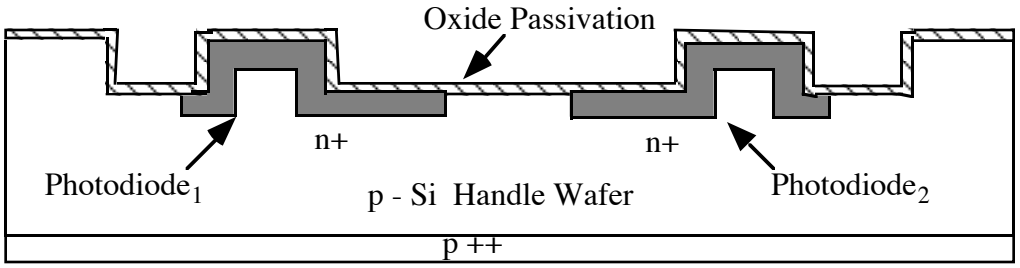

(B)

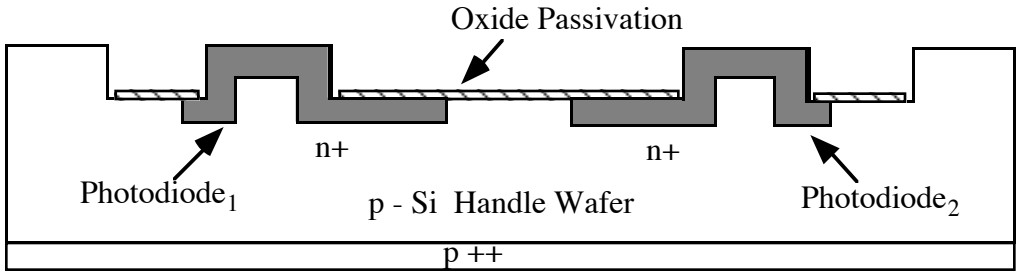

(C)

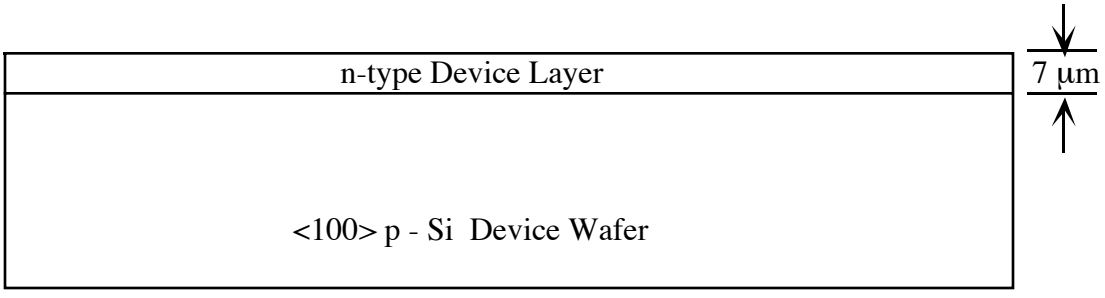

(D)

Fig. 3.6 Sensor fabrication sequence

voltage for surface inversion. This helps to prevent "cross-talk" between the two photodiodes through the substrate (see next sub-section for more discussion).

A 1 μm photoresist layer is then patterned using the photodiode mask. The wafers are then phosphorus implanted (dose = 5 x 10^{15} cm^{-2}, energy = 90 keV, 7 degree tilt). All parameters for the implant, the species, dose, energy and drive-in time were obtained from SUPREM simulations, as described in section 2.3 of the sensor design chapter. It must be noted that the parameters were chosen to obtain a junction depth of 2 μm. The drive-in for this implant is the same as the bonding-anneal step (step # 10.3). The resulting structure is shown in Fig. 3.6B.

Electrical passivation and patterning the passivation oxide (steps 7.1-7.6)

A note on electrical passivation. Surface electrical passivation is the process of reducing the surface state density of silicon by tying up the "dangling" bonds (or unterminated surface states). The presence of dangling bonds that are not tied up results in leakage currents. This is because these unterminated surface states contribute to energy levels in the center of the band gap region of silicon (donors and acceptors contribute to energy levels towards the edges of the band gap). These mid-band gap energy states act as sites for recombination-generation (*R-G*) and are thus responsible for increased leakage current (the *R-G* centers are also sometimes referred to as traps). Thermal oxides (and not deposited oxides) have been shown to considerably reduce the charge density (or surface trap density) at the Si-SiO_2 interface, thereby reducing the leakage currents. It has been found that when a thin layer of SiO_2 is grown on the surface of silicon where a *p-n* junction intercepts the surface, the leakage current of the junction was reduced by an order of magnitude[93]. This is because the oxide reduces and stabilizes interface traps.

The process steps 7.1-7.6 provide electrical passivation of the trench surfaces, thereby preventing diode cross-talk or surface leakage current that can cause the shorting of the two photodidoes. In addition, the electrical passivation also helps to minimize the individual *p-n* junction leakage currents. The plasma etching process that is used to etch the trenches, leaves behind dangling bonds on the surface. These unterminated surface states provide sites for carriers (electrons and holes) to "hop" from photodiode #1 to photodiode # 2 resulting in diode cross-talk. This problem can be overcome by "terminating" these bonds with a thermally grown oxide layer, as described above. The oxide layer reduces both the surface leakage current and the device (*p-n* diode) leakage current.

The screening oxide grown in step 5.2 is left behind in the trenches and performs the task of electrical passivation of the silicon surfaces. In addition, a 2400 Å layer of LTO is deposited on this screening oxide layer. This is to ensure that there is a thick protective oxide

layer on the photodiodes during the final stage of the process when a plasma etch is used to release the microsensor structure. As described in step # 6, there is some non-uniformity in the etch rate across a wafer during the plasma etching process. Hence the wafers are typically overetched to ensure that structures are released all around the wafer. This could mean that in some of the devices on the wafer (those which were released first) the plasma could attack the underlying photodiodes. The presence of a thick oxide layer permits a large overetch time, with the underlying photodiodes being unaffected.

After the LTO has been deposited, this layer is patterned using a 1 μm photoresist layer. The pattern ensures that (after BOE oxide etch step) the screening oxide and LTO layer is left behind only in the trenches and is completely removed from the field regions. In order for the wafer bonding step to be successful, the oxide layer must be completely removed from the field regions of the wafer and be left only in the trenches. Any oxide particle in the field regions will translate to bonding voids and a dielectric isolation of the device layer from the handle wafer. In addition, any misalignment of this pattern could also result in oxide being left behind in the field regions and the above mentioned problems. The main concern for this photolithography step is to eliminate any photoresist from the field regions. Any photoresist in the field regions would correspond to oxide in the field after the BOE etch, thereby resulting in bonding defects (voids/debond regions). The following steps were therefore taken to thoroughly clear the field regions of any photoresist. First, this mask layer was designed to be tolerant to misalignments of the order of 10 μm. Second, two 10X emulsion plates were generated from the same KIC file. Each of the emulsions was then stepped out to generate its own 1X chrome contact mask, which was then used in the photolithography process. Each wafer is exposed using both the chrome masks. This "double exposure" procedure helps eliminate any photoresist from the field regions that may arise due to mask imperfections. The probability of two independently generated chrome masks to have imperfections at the same location is small. Hence any resist left behind in the field region of the wafer due to an imperfection in one of the masks will be exposed away during one of the two exposures. Third, a "ring" mask (which blocks the central regions of the wafer and exposes a ring-region about 1 cm from the wafer edge) was used to expose the edges of the wafer, a region where resist tends to accumulate and thicken during the coating process. While the edge-bead removal solvent removes most of this photoresist, it does not completely remove it. The "ring" mask is used to expose this photoresist layer. Typically, a very long exposure and development time is used to completely remove any photoresist from the edges of the wafer. This third step was found to help considerably in improving the quality of the wafer bonds between the device and handle wafers. The resulting structure is shown in Fig. 3.6C.

3.3.2 Device Wafer Processing (Upto Wafer Bonding Step)

Starting Material

The device wafers are one of the following:

1) *junction etch-stop wafers*:

<100> Boron doped (0.5 - 20 ohm-cm) double-side polished 4" silicon wafers (500-550 μm thick). These wafers were thinned-back using the electrochemical etch-stop (ECE) technique. These wafers were used for the first-generation of stand-alone sensors.

2) *oxide etch-stop (SOI) wafers*

4" silicon-on-insulator (SOI) wafers supplied by Motorola [94] of thickness equal to 7 μm (± 0.2 μm) with a *n*-type <100> silicon device layer on top of a 4000 Å buried oxide (BOX) layer which is on top of a 385 μm thick *n*-type silicon substrate. The typical resistivity of the 7 μm device layer is 1-10 ohm-cm. These wafers were thinned-back using a KOH etch. The SOI wafers were used for the second-generation sensors. It must be noted that if SOI wafers are used, the device wafers require no further processing before the wafer bonding step (step # 10.2).

Etch-stop definition (steps 8-9.6)

The processing steps (8-9.6) are required only for non-SOI wafers that are thinned-back using an electrochemical etch-stop technique. The first step is to grow a screening oxide on the wafers. The frontside is then blanket implanted with phosphorus (dose = 1.4 x$10^{13}$$cm^{-2}$, energy = 180 Kev, 7 degree tilt) and annealed (time = 21 hrs, temperature = 1150ºC, N_2 ambient) to obtain a 7 μm *n*-type junction on a *p*-type substrate. The SUPREM simulation package was used to determine the dose, energy, drive-in time and drive-in temperature. The output from the simulation is plotted in Appendix D. A 0.25" ring-region (from the edge) of the wafer is then patterned and plasma etched to a depth of 2 μm. The wafer is held along the 0.25" ring-region during the implant and hence is not implanted in this region. For the electrochemical etch (step # 11.3) to work, this *p*-type region should not be in contact with the handle wafer after the wafer-bonding step. The 2 μm etch prevents the ring-region of the device wafer from being in contact with the handle wafer. This completes the device wafer processing steps for non-SOI device wafers. The resulting structure is shown in Fig. 3.6D.

3.3.3 Bonding of Handle and Device Wafers

Wafer bonding (steps 10.1-10.3)

The processed handle wafers and the device wafers (junction etch-stop or oxide etch-stop wafers) are first RCA cleaned to hydrate their surfaces. The wafers are then loaded into a spin-bonder, which allows the frontsides of the two wafers to be brought into intimate contact.

The ambient in the spin-bonder can be controlled to be pure oxygen, pure nitrogen or a mixture of both. The initial bonding of the two wafers is made possible by two factors that result in successful hydrophilic bonds (see section 3.2.1): i) mirror smoothness of the wafer surfaces; ii) the presence of OH groups on their surfaces, introduced during the RCA cleaning procedure. In the present case, the wafers were contacted in a pure oxygen (100 % O_2) ambient, and hence this is the ambient within the sealed cavity that is formed between the handle and device wafers. The spinning process has been found to considerably improve the quality of the bond in wafers that have cavities in them. This is because the spinning action helps to clear the cavities of any particles or trapped gases both of which can lead to bonding voids, as described in section 3.2.2. Figure 3.7a shows the interface of a bonded wafer imaged using the IR inspection system. It can be seen that the interface is free of any voids. It must be noted that the absence of voids in the output of an IR imager does not mean that the interface is completely free of voids. The same interface (Fig. 3.7b) now imaged using an ultrasonic imaging system shows some voids on the wafer periphery. Since the voids are on the edge (and not in the active device area), this wafer is acceptable for subsequent processing.

The contacting process is followed by a high-temperature anneal for 70 minutes at 1150ºC in a nitrogen ambient. During the annealing process most of the oxygen that is trapped in the sealed-cavity is consumed to form a thin layer of silicon dioxide, which coats the walls of the sealed-cavity. The consumption of the trapped oxygen reduces the pressure in the sealed cavity. The low pressure in the cavity, typically 0.05 atm or lower [92], prevents the rupturing of the thin membranes during any high-temperature or low-pressure step that is carried out after the thin-back process and prior to the microstructure release. It must be noted that during the annealing process it is preferable to have the temperature gradually increased from the furnace idling temperature of 800ºC to 1150ºC, and similarly to gradually decrease it from 1150ºC to the furnace idling temperature. This is to ensure that at no time does a large temperature gradient exist between the wafers and the furnace. The presence of large temperature differences could result in large thermally induced stresses in the bonded pair. The annealing step results in a permanent bond between the two wafers, as shown in Fig. 3.6E. This annealing step is used to drive-in the photodiode implant of step # 6.3.

3.3.4 Bonded Wafer Processing

Thin-back of device wafer (steps 11.1-11.8)

The first step in the thin-back process involves the mechanical grinding and polishing of the device wafer surface of the bonded pair. Typically, about 450 μm of silicon is removed from the junction etch-stop device wafer leaving behind a 90 μm thick layer. In the case of SOI wafers, typically about 300 μm of silicon is removed from the device wafer leaving behind a

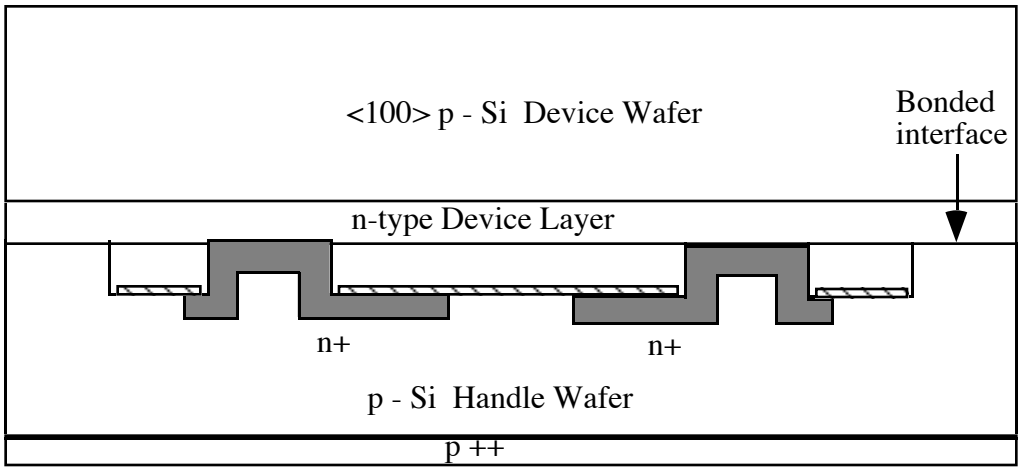

(E)

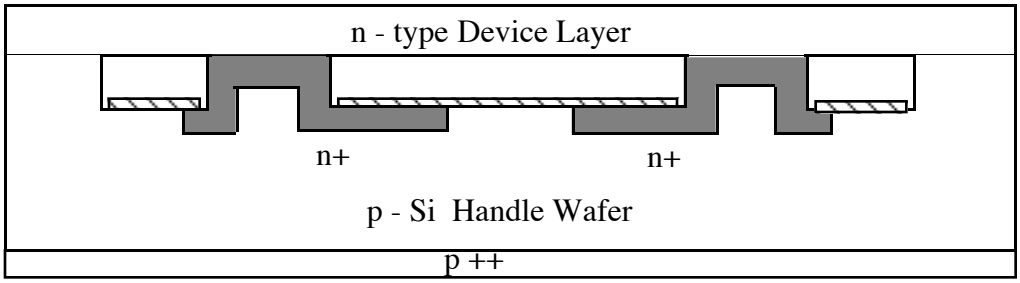

(F)

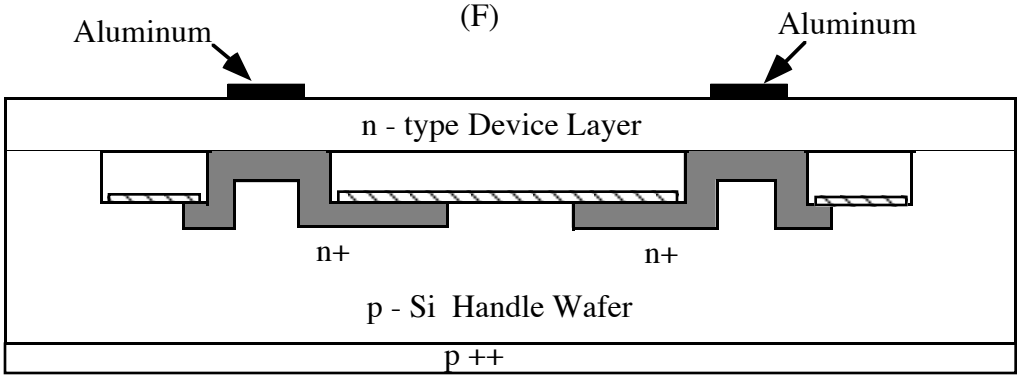

(G)

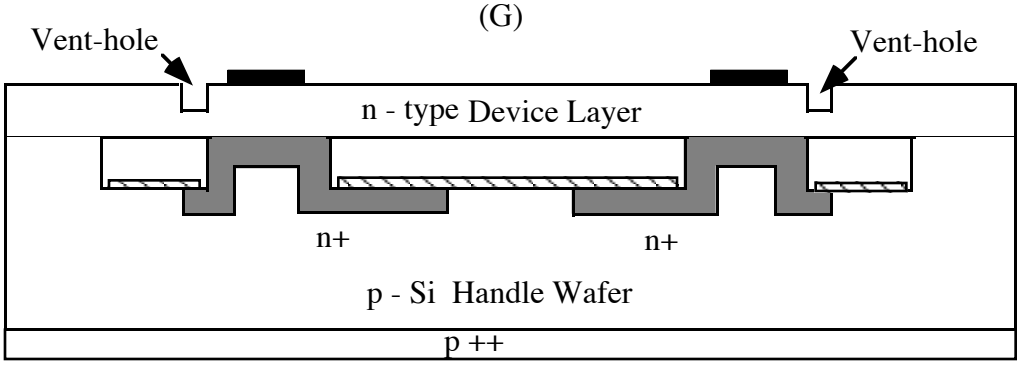

(H)

Fig. 3.6 Sensor fabrication sequence - Continued

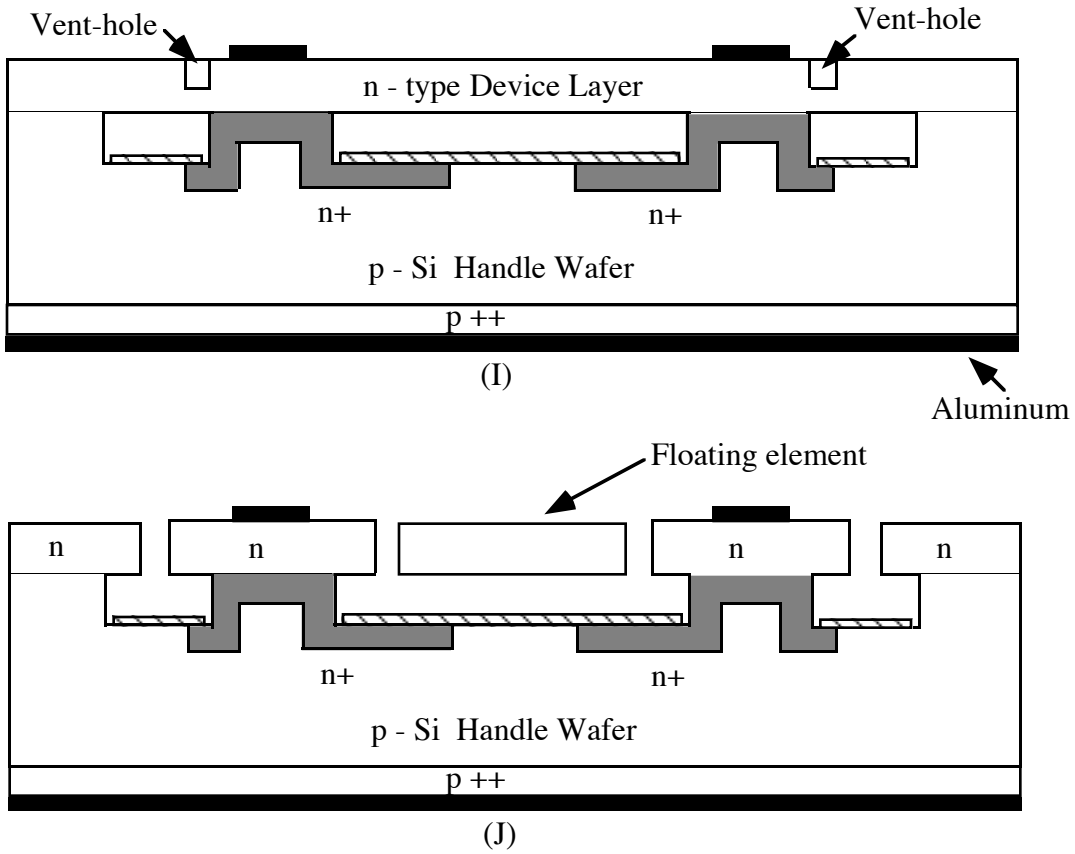

Fig. 3.6 Sensor fabrication sequence - Continued

80 μm thick layer (note that the starting thickness of the SOI wafers are 380 μm). The mechanical grinding and polishing is performed to minimize the etch time during step # 11.3.

Electrochemical etch (ECE)

The next step in the thin-back process of the junction-isolated wafers is the electrochemical etch to remove the rest of the device wafer leaving behind a 7 μm device layer. Figure 3.9a shows the configuration of the wafer during the electrochemical etch. It can be seen that the wafer is comprised of two *p-n* junctions in a *p-n-p* configuration. The two *p-n* junctions are labeled diode1 and diode2, respectively. The device wafer is selectively thinned back to diode1 using a procedure described below.

The electrochemical etch is carried out in a polypropylene tub filled with 3 liters of water and 750 g of *KOH* pellets (20 % by weight $KOH:H_2O$ solution). The tub is placed in a water bath and heated to a temperature of 95ºC (± 0.5ºC). To reduce the surface roughness of the final surface, a fluorochemical surfactant (FC-129, 3M Corporation) is added to the $KOH:H_2O$ solution. Typically about four drops of surfactant per liter of solution are added. The electrochemical potentials are applied and the resulting currents are monitored using a

computer-controlled EG&G Princeton Applied Research Corporation Model 273 Potentiostat/Galvanostat. All the applied potentials are referenced to a double junction $Ag/AgCl$ reference electrode (model # 13-620-273, Fischer Scientific). A platinum foil is used as a counter electrode. The bonded wafer pair is first dipped in BOE solution to remove the native SiO_2. The wafer is then rinsed in DI H_2O and dried using N_2. The wafer is then loaded on to a one-sided teflon etch jig. The etch jig exposes the frontside of the wafer to the etchant, while the backside is protected (Fig. 3.8a). The wafer is held in place by a vacuum O-ring seal, which protects most of the backside (about 1/4" from the wafer edges are exposed) of the wafer from the etching solution. The backside of the wafer is in contact with a platinum mesh on the top surface of the jig. This platinum mesh provides electrical contacts to the backside of the bonded wafer. After the wafer is loaded on the etch jig, the jig is then placed in the KOH:H_2O etching solution under a constant applied voltage bias for about 1 hr. The wafers are typically etched at an applied bias of 0 V. This results in diode1 being forward biased and diode2 being reverse biased and hence no current flow through the wafer. This causes the potential of the *p*-type layer (which is in contact with the KOH solution) to "float" [95]. Hence the *p*-type silicon will etch until the *n*-type layer is reached. At this point the *p*-*n* junction that remains (diode1) is forward biased. This results in a current flow (and hence holes are supplied), and the top surface of the *n*-type silicon will be passivated due to the formation of an anodic oxide. This causes the etch to terminate. A good description of the physics of the electrochemical etch-stop technique can be found in [95].

The progress of the etch is monitored through the potentiostat. When the current reaches a peak passivation value and then drops down to a plateau, the etch has self-terminated due to the formation of an anodic oxide on the top surface of the 7 μm device layer (see Fig. 3.9). At this point the applied voltage is turned off and the wafer is pulled out of the etching solution. It must be noted that once the applied bias is removed, the wafer must be immediately pulled out of the etching solution. This is because the removal of the bias will result in the anodic oxide being etched and the etching solution will start attacking the underlying 7 μm silicon device layer.

In the case of the oxide etch-stop, the wafers are etched in a 20 % by weight KOH:H_2O solution using the same procedure described above but without any applied bias (Fig. 3.8b). In this case the *n*-type silicon in contact with the KOH solution will be completely etched away and the etch terminates once the buried oxide layer is reached. The thinned-back wafer is shown in Fig. 3.6F.

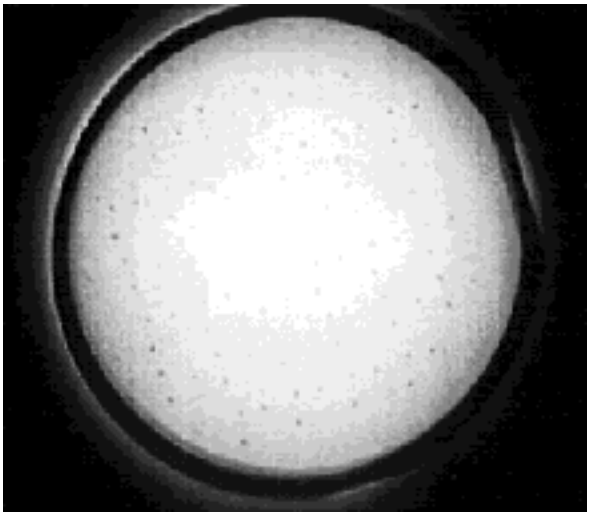

(a)

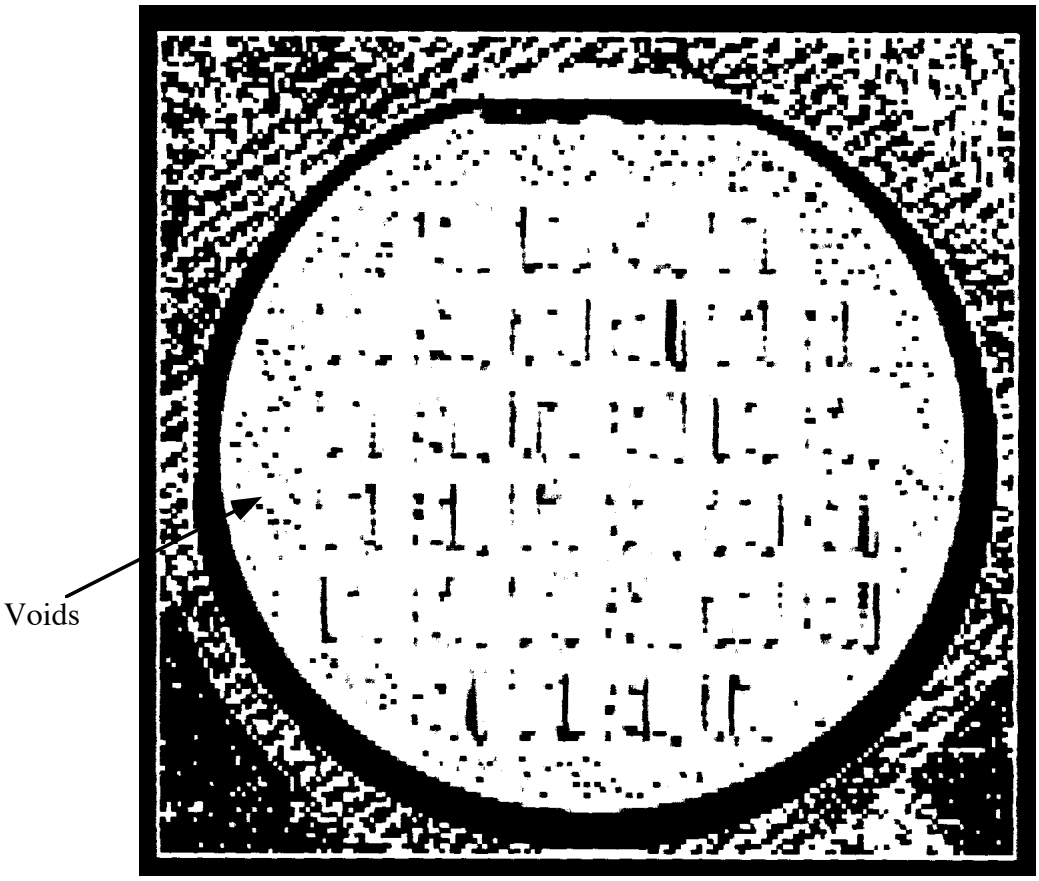

(b)

Fig. 3.7: a) Infrared image of the bonded wafer pair with no voids; b) image of the same interface in an ultrasonic imaging system showing some small voids on the wafer periphery (courtesy of Motorola [94])

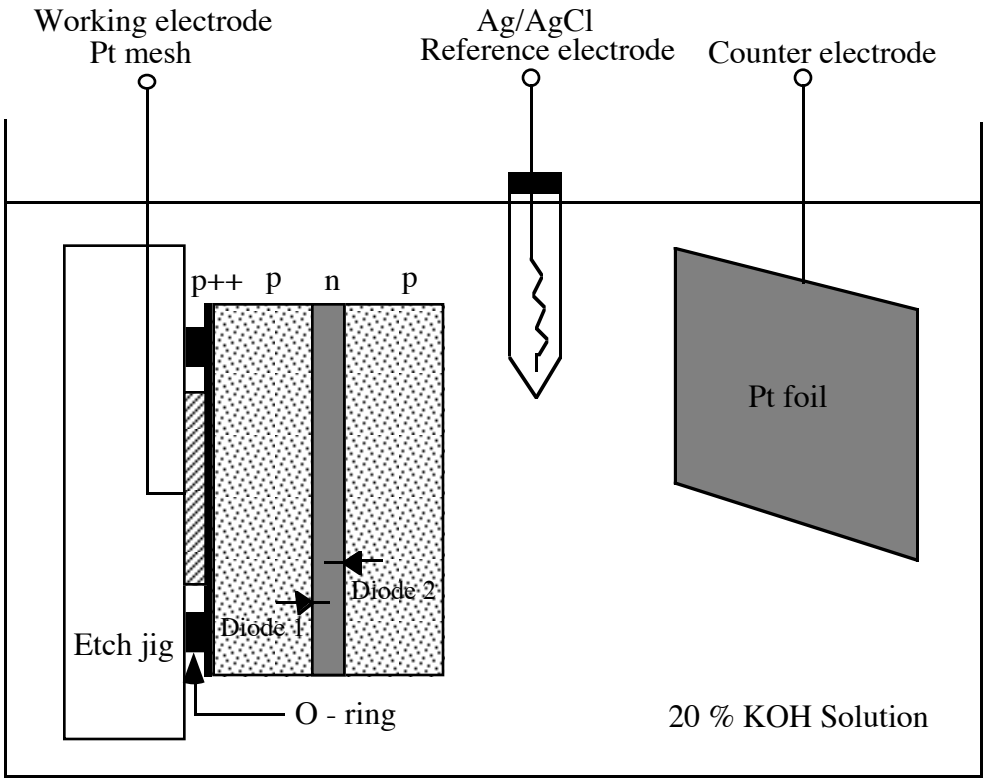

(a)

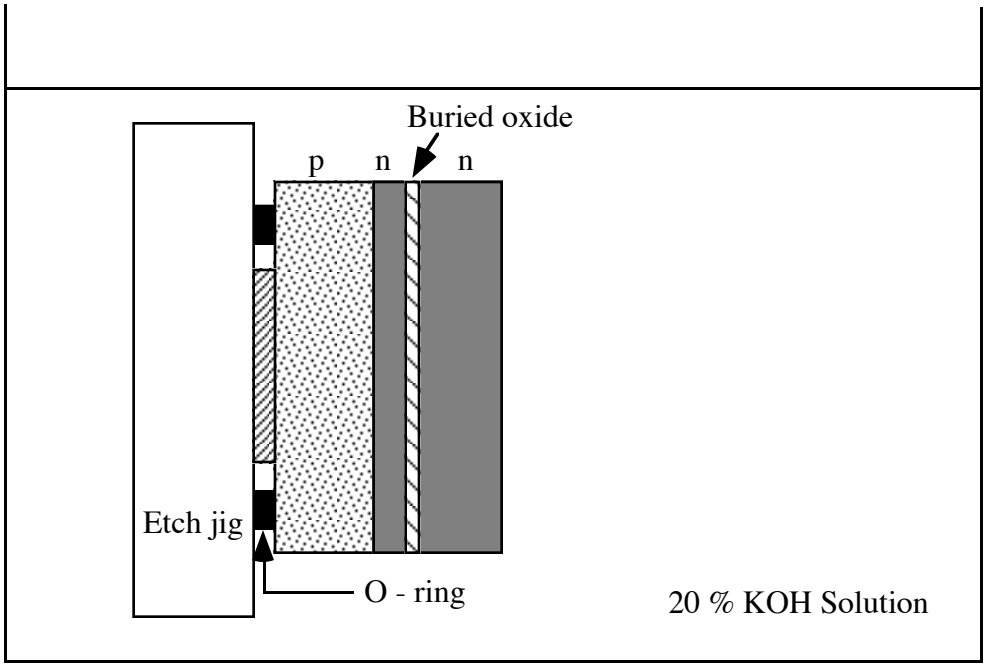

(b)

Fig. 3.8 Configuration of the bonded wafers during the electrochemical etch. Figure (a) shows a *p-n-p* wafer and Fig. (b) shows a SOI wafer

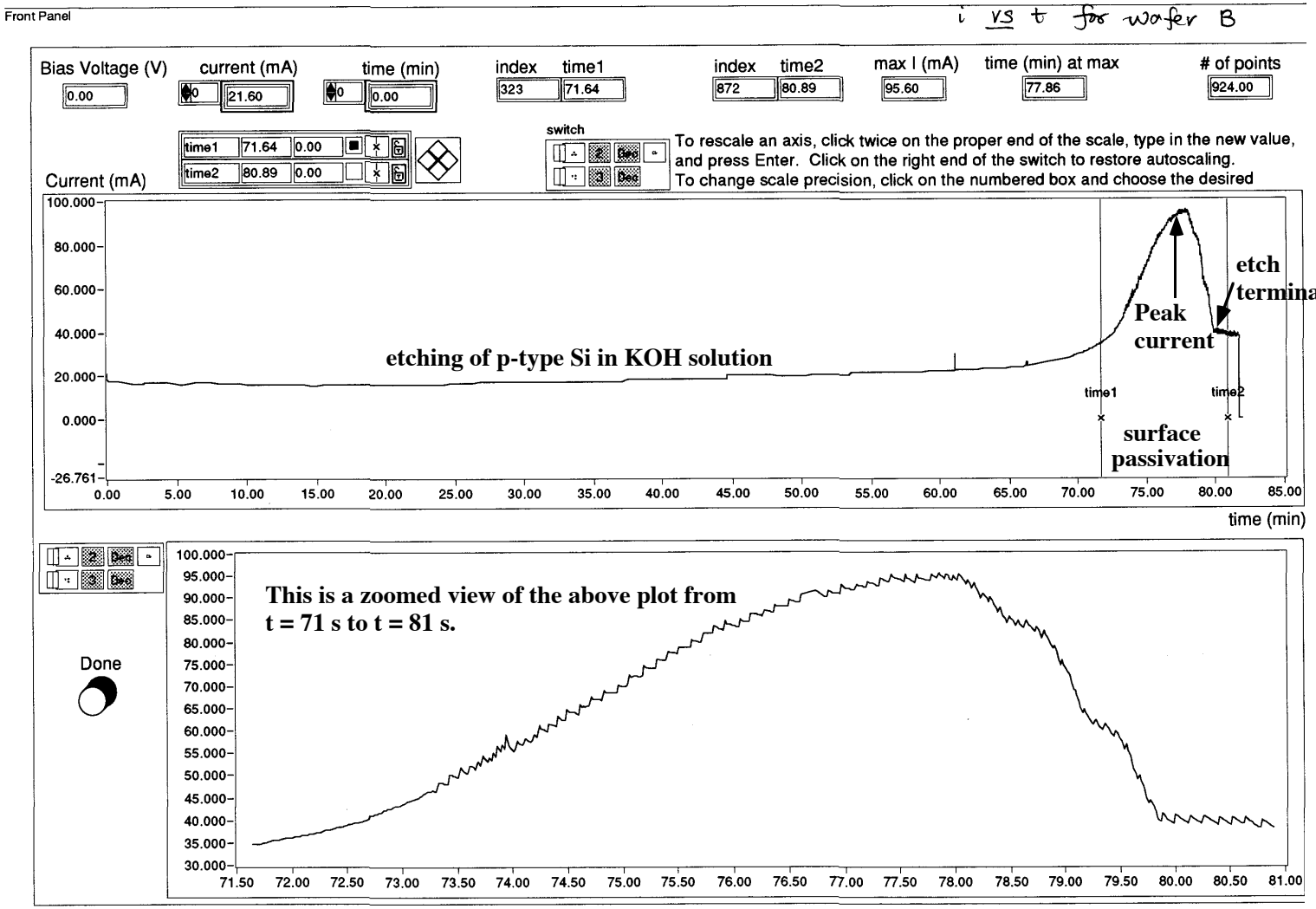

Fig. 3.9 Current versus time plot during the electrochemical etch showing: i) etching of p-type silicon; ii) passivation of the surface due to anodic oxide formation; iii) etch-termination

The final step in the thin-back process is the post-*KOH*-etch cleaning procedure. This cleaning procedure permits the re-introduction of the wafers into the IC fabrication line. The cleaning procedure is as follows: 1) wafers are first rinsed in DI water for 10 mins; 2) piranha clean followed by a 10 min rinse in DI water; 3) oxide etch in 50:1 DI H_2O:*HF* solution followed by 10 min rinse in DI water; 4) RCA clean.

Transfer alignment marks (step 11.9, only for second-generation sensors)

This step is used to transfer the alignment marks from the sealed-cavities of the handle wafer on to the top surface of the device wafer. This procedure eliminates the need to use IR alignment for all the subsequent photolithographic steps. The transfer allows all the subsequent photolithographic steps to be aligned to the patterns in the sealed cavities in the handle wafer. The alignment for this step is done using an infrared (IR) alignment procedure. The IR radiation (which is transmitted through the thickness of silicon) illuminates the backside of the handle wafer and the transmitted beam is picked up by an IR imaging CCD camera. The image can be viewed on a TV monitor. Hence the alignment marks in the sealed cavity can now be viewed on the TV monitor. The alignment marks on the alignment-marks-mask are then aligned to the original alignment marks seen on the TV monitor. The patterned frontside is then plasma etched (depth ~ 0.6 μm) and this completes the process of transfer of alignment marks from the sealed-cavities to the top surface of the device wafer.

Note: this transfer process was done only for the second-generation sensors. For the first-generation sensors all the photolithography steps after the thin-back were performed using an IR alignment procedure.

Surface-replenish implant (steps 12.1-12.8)

The process steps 12.1-12.8 are used to increase the surface phosphorus concentration of the frontside (device layer side) of the thinned-back wafer (note that after the thin-back process the frontside is the 7 μm n-type layer). This implant ensures an ohmic contact after the frontside metallization (step # 13.1).

The first step is to grow 450 Å of screening oxide. The device wafer is then patterned and implanted (species = phosphorus, energy = 180 KeV, dose = 5 x 10^{15} cm^{-2}, 7 deg tilt). The device layer is implanted everywhere except for the regions where the floating-element structure will be fabricated. The reason for doing this is because the high dose and high energy implant (followed by the anneal step) introduces a steep concentration profile of the dopants and hence a large gradient of stress across the thickness of the 7 μm device layer (note: the flatter the concentration profile over the thickness of the device layer, the smaller the stress gradient). Any variation in stress across the thickness results in an internal bending moment,

whose magnitude is equal to the integral of the stress (integrated across the 7 μm thickness). This bending moment will cause the floating-element structure to warp (curl out of the plane) resulting in a non-planar device when the microstructure is released.

After the implant the resist is stripped by ashing in an O_2 plasma followed by a piranha clean. It must be noted that the sequence is important. The high dose, high energy implant "polymerizes" the photoresist converting it into a hard plastic-like film. The O_2 plasma attacks this hardened photoresist layer loosening the bonds which hold the polymer chains together. The loosened layer can then be removed by a piranha solution.

The final step involves an anneal at 800^{O}C for four hours in a nitrogen ambient. This step helps to drive-in the implanted species and results in the desired surface concentration of phosphorus, as shown in the SUPREM simulation in Appendix D.The screening oxide is then stripped in BOE solution.

Frontside metallization (steps 13.1-13.4)

The first step for the frontside metallization process is to pattern a 1.4 μm layer of image reversal photoresist AZ 5214-E. The process of producing negative images from a positive resist is referred to as image reversal. The main reason for using AZ 5214-E for this lift-off process is due to its ability to produce a negative slope (that is an angle greater than 90^{o} with the substrate) on the sidewall. The exact angle of the negative profile can be controlled by adjusting the exposure time. Typically a lower exposure time gives a more negative profile. The negative slope of the photoresist sidewall is desirable for the lift-off process as it prevents good coverage of the walls with aluminum during the evaporation process, thereby facilitating the easy lift-off of aluminum.

The wafers are then subjected to a 2 min descum in an O_2 plasma. This is to make sure that the areas that are supposed to be clear of any photoresist are completely free of any resist. Any remaining photoresist in the clear regions will affect the quality of electrical contact of the metal to the underlying silicon. In addition, the adhesion of the metal to the substrate will be poor and the metal in these regions will tend to lift-off. The wafers are dipped in a solution of BOE to strip the native oxide layer, immediately before the metal deposition step. A 5000 Å layer of aluminum is e-beam evaporated on the wafers. The planetary rotation of the wafers is turned off during the evaporation process. The planetary rotation is typically used to achieve a uniform thickness of metal across all the wafers and to provide a good step-coverage of the metal. Since in this case we were going to do a lift-off of the metal, a good step-coverage was not desirable.

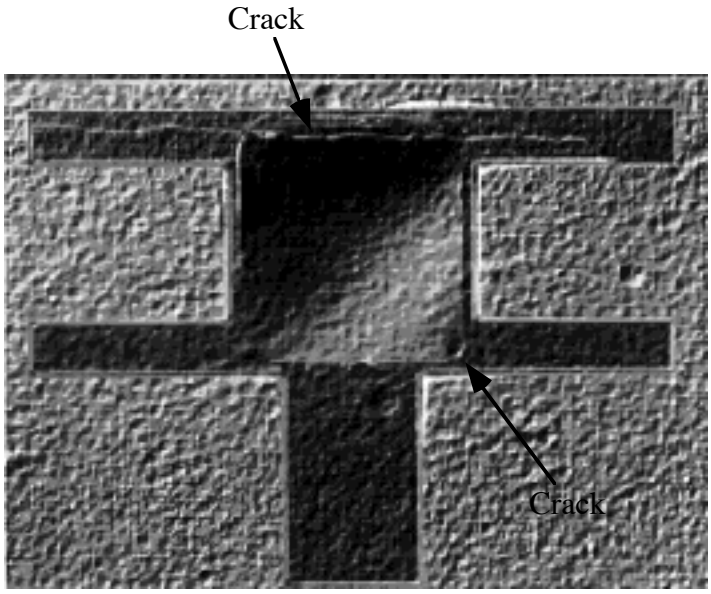

Fig. 3.10 Optical photograph showing cracks on the edges of the floating-element, caused by ultrasonic agigation during the metal lift-off process

The lift-off of the metal was accomplished by immersing the wafers in acetone. An important observation regarding the lift-off process should be mentioned here. The wafers were not subjected to any ultrasonic agitation, a process that is commonly used to facilitate the lift-off of metal. The reason for not using ultrasonic agitation is because this was found to be responsible for crack initiation and crack growth at membrane-corners (regions of stress concentration). Figure 3.10 shows a membrane that was subjected to ultrasonic agitation (note the cracks at the edges). The lift-off process (without ultrasonic agitation) was successful but took more time to be completed (approximately three hours).

The final step in the lift-off process is to perform a 3 min nanostrip (diluted piranha) clean of the wafers. This is to remove any remaining traces of photoresist from the wafer. The resulting structure is shown in Fig. 3.6G.

Vent-hole etch (steps 14.1-14.5)

This step is used to pattern and etch vent-holes. The vent-holes help to *vent* the sealed-cavities to atmosphere (before the floating-element structure is released) during the final structure release step. The reason for doing this is as follows: during the plasma etching process (step # 17.1), which is used to release the microstructure, all the membranes on the wafers are subjected to a pressure load that is equal to the difference of the pressure in the sealed-cavities, P_{cavity} and the pressure in the etching chamber, $P_{chamber}$. In our case P_{cavity} = 0.05 atm = 38000 mTorr and $P_{chamber}$ = 200 mTorr. Since P_{cavity}-$P_{chamber}$ is positive the membranes

are subjected to an upward pressure load. The upward force is equal the product of the upward pressure and the membrane area on which this pressure acts. Hence larger the membrane area the larger the upward force. During the final moments of the structure-release etch the amount of silicon remaining in the etch-areas is small. If a large upward force acts on this remaining silicon, it could cause a catastrophic rupture resulting in a broken floating-element. To avoid this problem the sealed cavities are vented much before the final structure is going to be released. This is to ensure that at the time of the microstructure release, the pressure on either side of the membrane has equalized and there is no danger of rupturing the membrane. The vent-hole is located far away from the floating-element structure. Hence any catastrophic event when the vent-hole is being punched-through will not affect any of the devices on the wafers.

The first step is to pattern the vent-holes. The patterned wafer was then etched in a SF_6/CCl_4 plasma for about 12 mins. This resulted in 3.5 μm deep vent-holes (Fig. 3.6H). It must be noted that the etch depth of 3.5 μm is half the thickness of the device wafer. Hence during the final structure-release step (which also etches the pre-etched vent-holes) the vent-holes are punched through in about half the time it takes for the microstructure to be released. This ensures pressure equalization across the microstructures during the release step. After the etch the photoresist is stripped in an O_2 plasma and the wafers are cleaned in nanostrip for 2 mins. The nanostrip removes any residual photoresist from the wafer.

Patterning for structure-release etch (steps 15.1-15.2)

The wafers are patterned using the structure release mask. The exposure and development times for this photolithography step are chosen so as to under-expose and under-develop the patterns. This is done in addition to biasing the mask by 1 μm (section 3.1.1, Mask # 8). Both these steps help to compensate for the lateral etching of patterns during the structure-release etch (step # 17.1).

The patterning for this step was done using an IR alignment procedure, for the first-generation sensors. Hence this step is performed before the backside metallization (the backside metal would not permit IR alignment). It must be noted that if the wafers are patterned using a normal frontside alignment (as in the case of the second-generation sensors), the preferred process sequence would be: backside metallization, sintering of metal, patterning for structure-release etch and finally the structure-release etch.

Backside metallization (steps 16.1-16.2)

This step was used to put down aluminum (e-beam evaporation with planetary rotation) on the backside of the wafers (Fig. 3.6I). This metal layer is the common ground for all the devices on the wafer.

Structure-release etch (step 17.1-17.2)

This step is used to release the floating-element structure using a dry plasma etching process. The etch depth was 7 μm, which is the thickness of the desired floating-element. The plasma chemistry is based SF_6/CCl_4 (95 sccm:10 sccm). This is the same chemistry that was used for the trench etch (step # 4.3). This silicon etch chemistry resulted in 86° vertical side walls for all the released structures, which is adequate for our application. The etch lasted for about 43 mins, including 5 mins of overetch time. Since there was some variation in the etch rate across the wafer, 5 mins of overetch was necessary to ensure the release of all the devices on the wafer. The resulting structure is shown in Fig. 3.6J. After the etch, the wafers are ashed in an O_2 plasma for 1 hour to remove the remaining photoresist.

Sintering of metal (step 17.3)

The sintering step (performed in forming gas at 400ºC) helps to achieve an ohmic contact between the metal layer and the underlying silicon substrate. A scanning electron photograph of the final device is shown in Fig. 3.11.

3.4 Measured Dopant Concentrations (Spreading Resistance Analysis)

The actual dopant concentrations that were obtained on the wafers were measured using a spreading resistance analysis (SRA) measurement on monitor wafers. The monitor wafers were subjected to the same thermal steps as the real sensor wafers. All the results are included in Appendix A, only a summary of the results is presented in this section. All the measurements were done at Solecon Laboratories [96].

SRA determines the resistivity-depth profile in silicon. Using published values of carrier mobility, a majority carrier concentration-depth profile can be calculated. Going one step further, a dopant profile can be calculated (by solving Poisson's equation) by accounting for the space-charge distribution under the bevel used for the spreading resistance profile. The calculated dopant distributions are good representations of the actual dopant distribuiton in the wafer.

The summary of the measurements are as follows: i) the measured junction depth of 2.1 μm compares well with the theoretically designed junction depth of 2.2 μm; ii) the measured dose for the photodiode implant (step # 6.3) was 3.2 x 10^{15} cm^{-2}. This is lower than the implanted dose of 5 x 10^{15} cm^{-2}, due to the loss of some dopant atoms due to segregation into the screening oxide layer; iii) the surface boron concentration (due to the blanket boron implant of step # 9) was measured to be 7 x 10^{15} cm^{-3}. This is an order of magnitude greater than the substrate boron concentration. This surface concentration is adequate to prevent surface

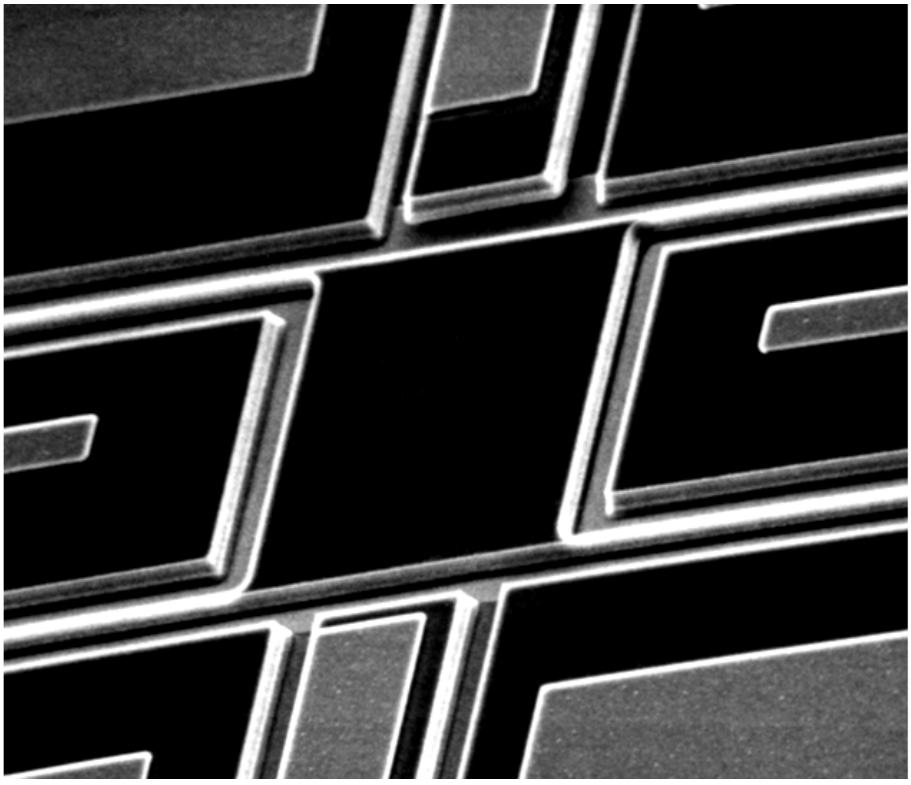

Fig. 3.11 Scanning electron photograph of a 120 μm x 120 μm x 7 μm floating-element sensor. The tether ends have been cropped to clearly show the details of the floating-element structure.

inversion; iv) the measured sheet resistances for all the implants are in good agreement with the values predicted by SUPREM.

3.5 Discussion

The die yield (on a wafer) for the fabrication process was typically 75%. The main factors that affected the final yield of devices were:

1) Inability to achieve good adhesion of the metal to the silicon surface, resulting in the metal bond pads lifting-off from some areas of the wafer surface during the metal lift-off process in acetone (step # 13.4). The yield of the final devices was further reduced by some of the bond pads breaking off during electrical probing and wire bonding. This problem can be overcome by using a plasma etching process to pattern the metal layer.

2) The plasma etching chemistry that was for used (for the first fabrication run) for the structure release step (step # 17.1) resulted in considerable lateral etching of the tethers. On some of the devices the tethers were very thin (1-2 μm instead of the designed 10 μm) and broke easily during testing. This problem was overcome in subsequent process runs by adjusting the plasma etch chemistry (ratio of SF_6 to CCl_4) to obtain a more anisotropic etch.

The fabrication process developed for the optical shear stress sensor lends itself to the integration of read-out electronics on the same chip as the sensor. After the thin-back process (step # 11.3) the electronics can be fabricated on the top surface of the device wafer, before the silicon floating-element structures are released. It must be noted that all IC processing is done after the fusion bonding step, which is a high temperature process. This process-technology has been successfully demonstrated in the fabrication of integrated pressure sensors [97]. In addition, the present process (with minor modifications) can be used to implement backside electrical contacts for the sensors. This backside electrical contacts' technology has already been demonstrated on piezoresistive shear stress sensors [46, 98] and can be easily adapted to the optical shear stress sensors.

Chapter 4. SENSOR TESTING

The goal of this chapter is to describe the tests that were performed to verify and characterize the sensor performance. The first ten sections present the results for the first-generation sensors. The final three sections discuss the test results from the second-generation sensors.

The testing of the sensors can be divided into the following categories: 1) electrical functionality; 2) light-response tests; 3) sensor calibration and measurements in the laminar-calibration flow cell; 4) measurements in a laminar boundary layer in a wind tunnel; 5) dynamic calibration: frequency-response studies; and 6) stochastic calibration in a turbulent boundary layer.

4.1 Electrical Functionality (First-Generation Sensors)

The sensors and diode test-structures were first tested to evaluate the electrical characteristics of the photodiodes. All the electrical functionality tests were performed at the wafer-level (before the sensors were diced and packaged) on a Hewlett Packard semiconductor parameter analyzer (HP 4145). The three photodiode parameters of interest that were measured are: (i) ideality factor; (ii) reverse leakage current; (iii) reverse breakdown voltage.

4.1.1 Ideality Factor

The ideality factor is a measure of the closeness in operating behavior between an ideal diode and a real diode. The ideality factor n (not to be confused with the n in p-n diode) of the p-n junction photodiode can be determined from the forward biased i-v characteristic. The total photodiode current (in the absence of any incident light) is given as [59]:

$$i = I_{leakage}\,(e^{qV/nkT} \pm 1) \tag{4.1}$$

where $I_{leakage}$ is the reverse leakage current, V is the applied voltage, k is the Boltzmann constant (1.38×10^{-23} J/K), T is the absolute temperature and n is the ideality factor. For forward bias voltages greater than the thermal voltage of KT/q = 25 mV, the exponential term in equation (4.1) is much greater than unity and hence the equation can be approximated as

$$i \approx I_{leakage}\, e^{qV/nkT}\,. \tag{4.2}$$

Taking the natural logarithm of both sides of equation (4.2) we get

$$\ln i = \ln I_{leakage} + \frac{qV}{nkT}\,. \tag{4.3}$$

When equation (4.3) is plotted on a semilog scale with V as the abcissa, the ideality factor can be calculated from the slope. The intercept gives the value of the reverse leakage current. The configuration of the diode structure for the sensors is shown in Fig. 4.1. It must be noted that the diode structure is not planar, as in conventional CMOS diodes. The non-planar diode structure

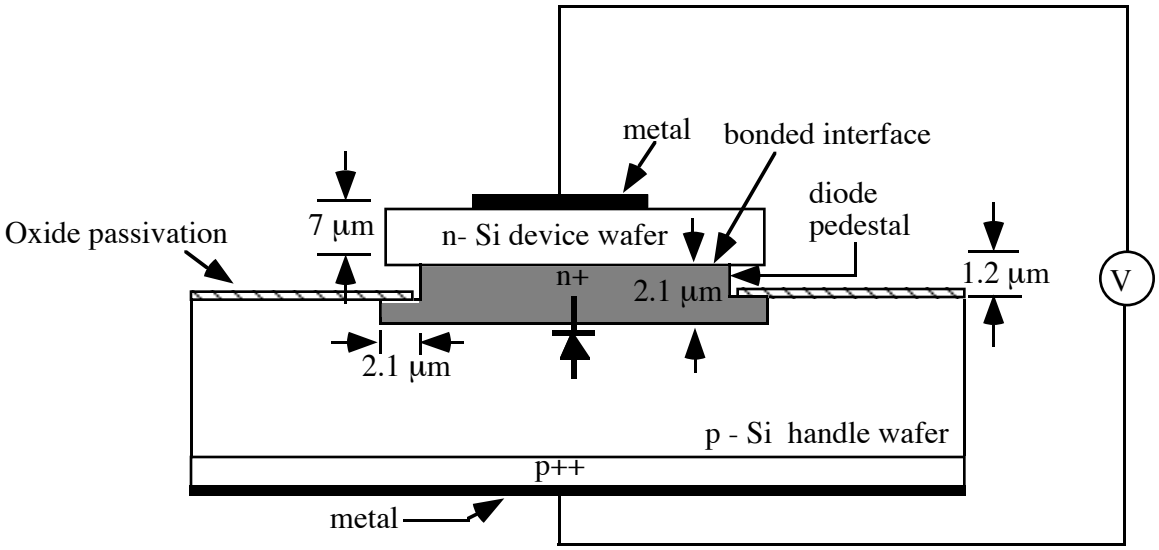

Fig. 4.1 Schematic diagram illustrating the configuration of the diode structure

results in some variation in the performance of these diodes (as compared with CMOS diodes), as described in the next two sub-sections.

A typical forward bias characteristic (on a semilog plot) of these diodes is shown in Fig. 4.2. The measured slope is 16.9/V, which corresponds to an ideality factor of 1.00. For all the fabricated photodiodes the ideality factors were measured to be in the range of 1.00 - 1.04.

4.1.2 Reverse Leakage Current

The reverse leakage current is defined as the constant current that flows across an ideal reverse-biased *p-n* junction. This current has a constant value for an ideal diode for reverse-bias voltages less than the breakdown voltage. In real diodes the reverse leakage current may not be a constant as a function of the applied bias.

The reverse leakage current for the photodidoes was measured to be in the range of 40 - 100 pA, for diodes with a junction depth of 2.1 μm and total junction area in the range 43350-111100 μm^2. All of the implant parameters for the photodiode (see sensor design chapter) and for the blanket boron implant (to prevent surface inversion) were values similar to that used for the MIT twin-well CMOS process [99]. The typical value for the leakage current density for the MIT twin-well CMOS process is 0.0009 $pA/\mu m^2$ at -50 mV of applied bias. This current density multiplied by the complete junction area yields the reverse leakage current. The total junction area for the present case is the sum of: i) floor surface area = length times the width of the n^+ junction lead; and ii) sidewall surface area = length times the *p-n* junction depth. For the diodes in the sensors which were flow tested, the total junction area was 43350 μm^2. Hence the estimated

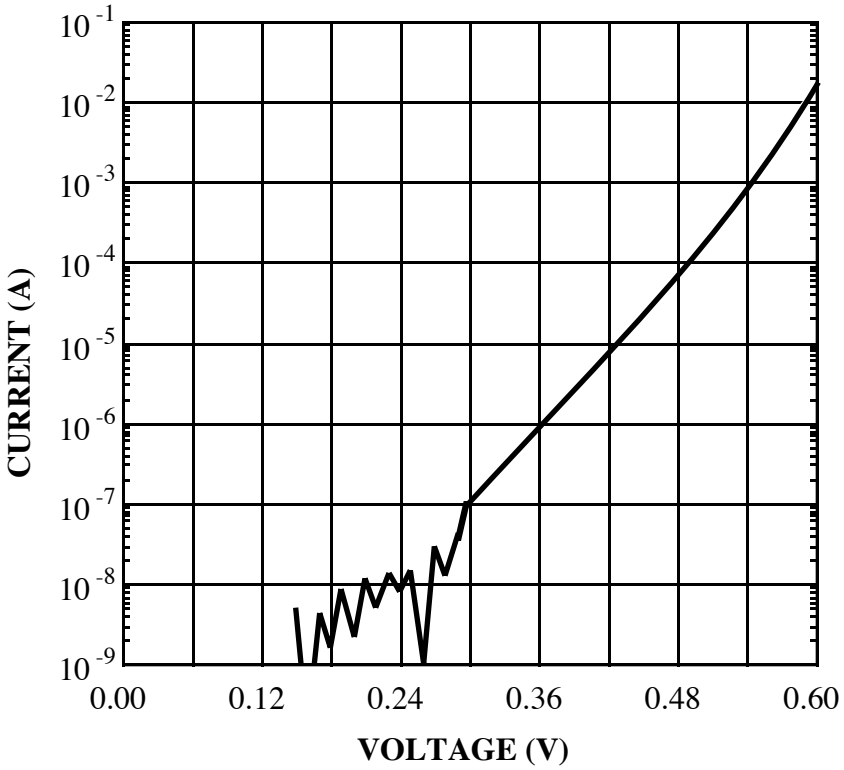

Fig. 4.2 Forward biased *i-v* characteristics of a photodiode (under no illumination). The measured slope is 16.9/V which yields an ideality factor of $n = 1$

reverse leakage current is equal 39 pA, which is smaller than the measured value. We believe that the two main factors for the higher measured leakage current are: i) imperfections (traps) at the *Si-Si* bonded interface; ii) dangling bonds located on the diode pedestal interface, contributing to an increased surface leakage current (Fig. 4.1). It must be noted that the measured leakage current is several orders of magnitude smaller than the typical value of the photocurrent (10's of nA - μA).

4.1.3 Reverse Breakdown Voltage

The reverse breakdown voltage V_{br} is the value of the reverse-bias voltage at which the magnitude of the current suddenly becomes very large. The expression for the reverse breakdown voltage for a linearly-graded *p-n* junction is given as [60]:

$$V_{br} = \pm \frac{4\, E_{critical}^{3/2}}{3} \left(\frac{2\varepsilon_{si}}{q} \right) a^{\pm 1/2} \tag{4.4}$$

where $E_{critical}$ is the critical breakdown field in silicon, ε_{Si} is the permeability of silicon, q is the electronic charge and a is the impurity gradient. The critical breakdown field is a physical constant for a given semiconductor material and is almost independent of doping.

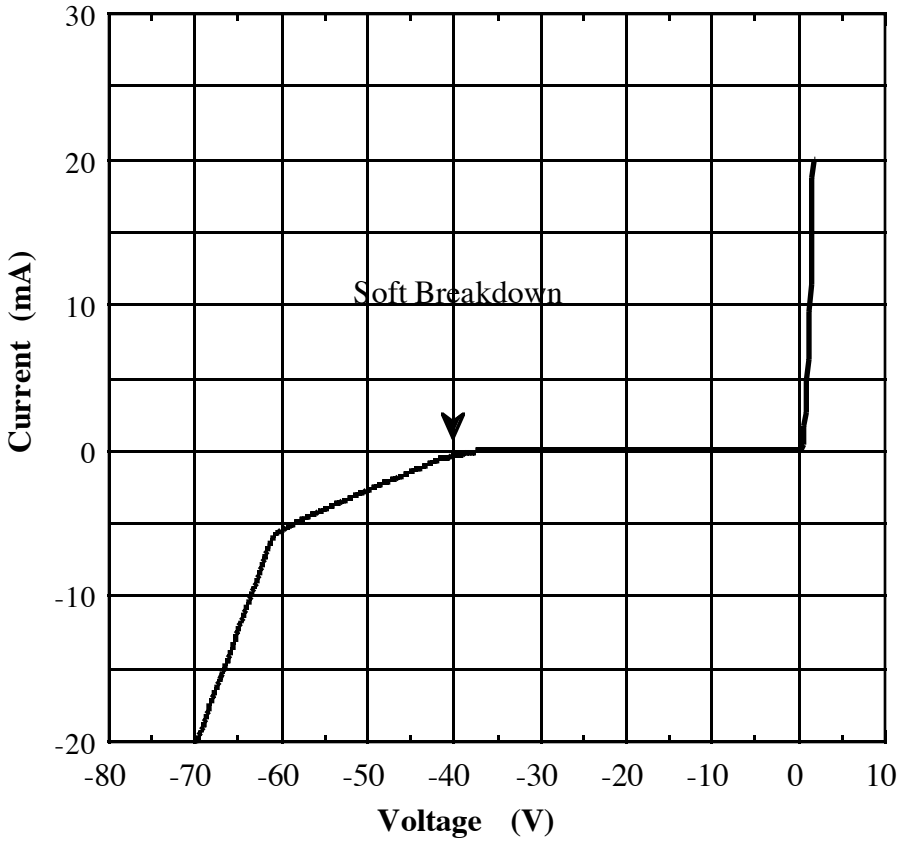

Fig. 4.3 Reverse biased *i-v* characteristic of an unilluminated photodiode. The breakdown voltage is approximately equal to -40 V

Using the value of the critical breakdown field in silicon to be equal to 3 x 10^5 V/cm [60], the reverse breakdown voltage is calculated to be equal to -125 V. The typical measured value of the breakdown voltage was -40 V, as shown in Fig. 4.3. It can be seen from Fig. 4.3 that the measured breakdown voltage is lower than the value predicted by equation (4.4). We believe that this is due to the presence of imperfections (traps) at the silicon-silicon bonded interface.

It can also be seen from Fig. 4.3 that the diodes exhibited a "soft" breakdown, i.e., there is no voltage at which the reverse-bias current increased dramatically. The reverse current increased steadily as the reverse-bias was increased. The "soft" breakdown in the case of the airbridge sensors could be the premature breakdown of the junction due to the absence of passivation oxide around the bond pads.

4.2 Light-Response Tests (First-Generation Sensors)

The aim of the light-response tests was to study the following two aspects of the photodiode performance. The first test was to measure the amount of photocurrent generated by the

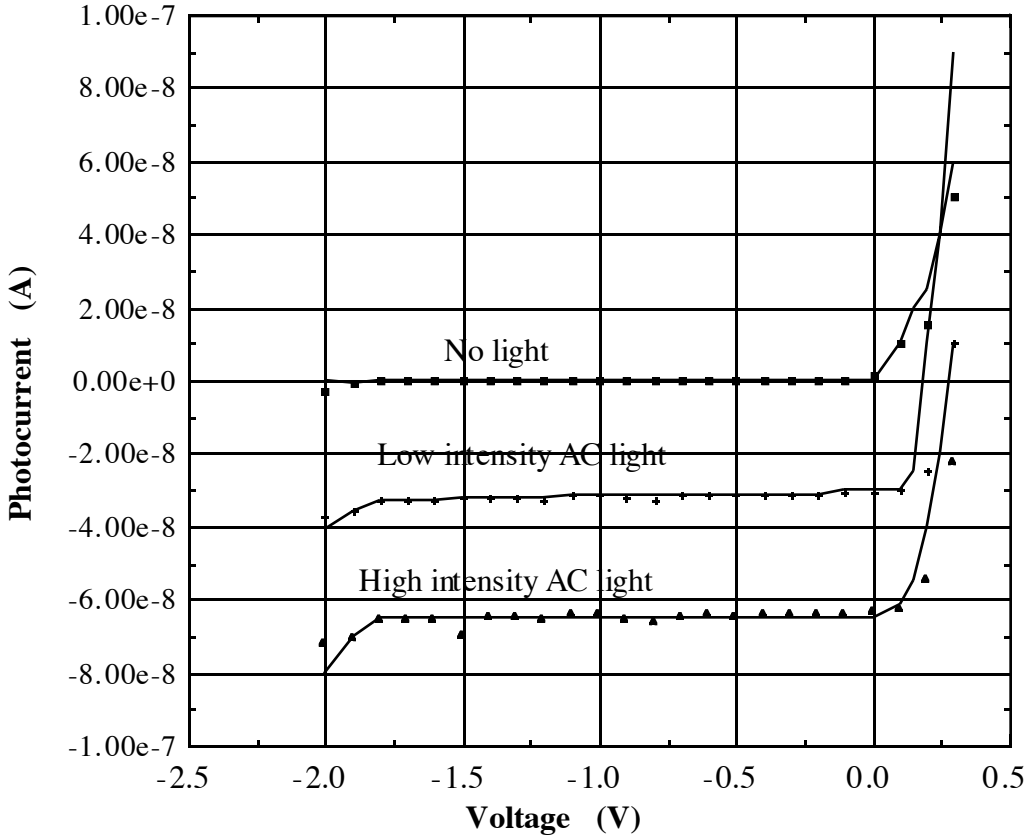

Fig. 4.4 Photodiode *i-v* response under incandescent AC light illumination. The AC light is used to observe the response of the photodiodes under dark, low intensity and high intensity conditions

diodes and the second test was to study how well the photocurrent response of the two diodes were matched. All the tests described in this sub-section were performed on a HP 4145, using either the incandescent AC light source of the microscope or using a DC light source.

4.2.1 Intensity Response

Figure 4.4 shows the response of the photodiode to increasing light intensity (incandescent AC light illumination), in the absence of any flow. It can be seen that the photocurrent increases with increasing light intensity and the magnitude of the current is of the order of tens of nA. It must be noted that all the flow test results presented in this thesis are based on measurements using a 7 mW, 670 nm laser source. The output photocurrent obtained using a 7 mW, 670 nm laser source was of the order of 1 μA, for the same photodiode area. The increased magnitude in the value of the current is due to the increased incident light intensity (W/m^2).

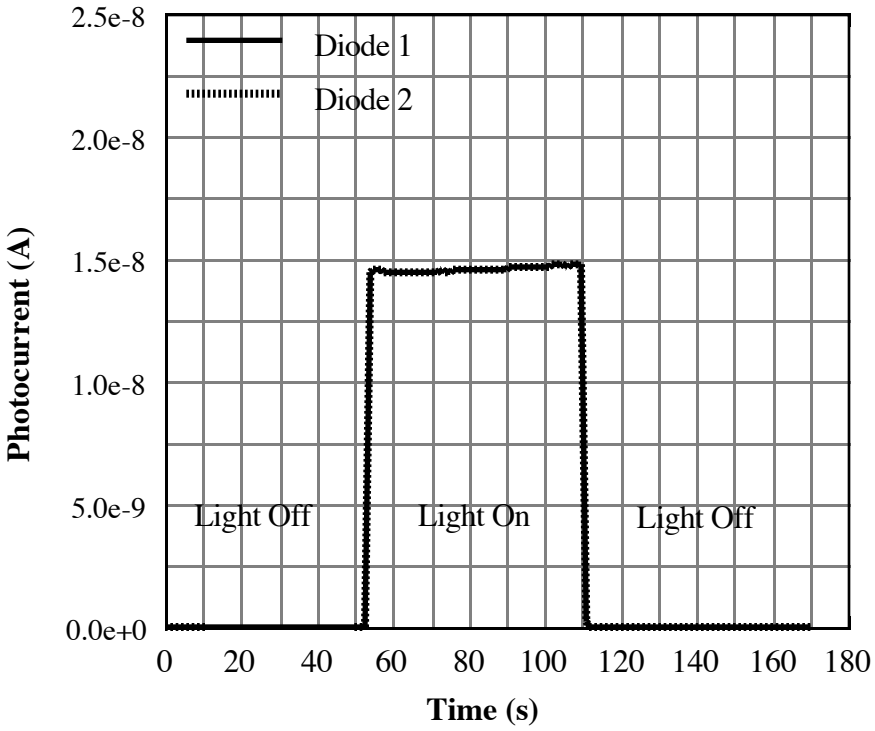

Fig. 4.5 Response of the two photodiodes to DC light illumination. The response shows the output photocurrent as a function of time when subjected to a 50 second light-off period followed by a 50 second light-on period and a final 50 second light-off period.

4.2.2 Light-Matching Tests

The aim of this test was to check the degree of match of the response of the photocurrents from the two diodes, without any flow. Figure 4.5 shows the response of the two photodiodes to incident light from a DC light source. The figure shows an initial 50 second "light off-period," followed by a 50 second "light on-period" and a final 50 second "light off-period." It can be seen that the response of the two photodiodes are matched at all times.

The sensors on one of the wafers showed a small difference in the output currents of the two photodiodes, when subjected to uniform incident illumination. We believe that this is due to a difference in the exposed photodiode area (in the undeflected position of the floating-element) caused by misalignments (~ 1 μm) of the mask that was used to release the microstructures. This degree of misalignment results in a 4 % change in the exposed area of the photodiodes. It can be shown (using equation (2.2)) that this can result in a constant, non-zero value of differential photocurrent of approximately 30 nA, in the undeflected position of the floating-element. This value is in good agreement with the measured differential photocurrent output of 45 nA. The

difference in the predicted and the measured values could be due to the error in estimating the exact value of the miaslignment. For all measurements made with these sensors, the measurement circuit (described in section 4.5.3) was designed to null out the resulting differential voltage.

4.3 Sensor Package

This section describes the sensor package (for both the first-generation and second - generation sensors) that was used for calibration of the sensors in the laminar-calibration flow cell and for testing in the wind tunnel. The main requirements on the sensor package are:

a) Flush-mounting of the sensor chip to the package and the package to the wall of the test facility. The effect of protruded or recessed floating-element was explained in chapter 1 (Fig. 1.5). It can be seen from Fig. 1.5 that a protruded or recessed floating-element results in perturbation of the streamlines around the element and hence a disturbed pressure-field around the sensor. This can change the effective shear stress that is imposed on the floating-element. The sensor chip cannot protrude (or be recessed) by more than a few percent of the channel height. During testing in the wind tunnel, the chip and package must be flush-mounted to within a few wall units (1 wall unit = 30 μm at $Re_\theta = 16000$ and $U = 15$ m/s, in the low-speed wind tunnel at MIT). For measurements in the flow cell, the maximum deviation from flushness (~ 1 μm) was measured to be 1% of the minimum channel height, and hence the error contribution due to this was negligible. For measurements in the wind tunnel the sensor was mounted flush to within one wall unit.

b) Minimization of any protrusions caused by the frontside electrical access to the chips. The wire bonds (which provide the electrical interface between the chip and the read-out electronics) must have a small loop-height as illustrated in Fig. 2.7 of the sensor design chapter. It must be noted that the wire bonds were located sufficiently downstream of the floating-element, and hence any flow perturbation caused by the them would not be felt at the floating-element (see section 2.8.1).

c) Minimization of any gaps between the sensor chip and the package and between the package and the wall of the test facility. As described in chapter 1, gaps around the floating-element structure can cause errors in the shear stress measurement by disturbing the flow field around the sensor. The gaps around the floating-element were designed to be as small as possible (7μm in this case), within the constraints of our fabrication process. Also, all gaps between the sensor chip and the package were filled with moulding clay.

4.3.1 First-Generation Sensors

The sensors were packaged in a 25 mm diameter acrylic (PMMA) plug similar to [1.31]. PMMA was chosen because it is electrically insulating and is easy to machine. The plug comprises of a square recess (1.2 cm x 1.2 cm x 790 μm) on the top surface and three through-holes (for three copper wires) downstream of the recess. The copper wires are 1/16" in diameter and are mounted such that the top surface of the wires are flush with the top surface of the plug. A complete dimensioned drawing of the plug can be found in Appendix E. The sensor chip (1cm (length) x 1cm (width) x 550 μm (thickness)) was mounted in the recess and the gaps around the chip were filled with moulding clay. A flat (slip gage quality) and smooth (< 2 μm surface roughness) aluminum block was used to press on the edges of the chip to ensure flushness of the chip to the top surface of the plug. Wire bonds were made from the bond pads on the chip to the top surface of the three copper wires (the three wires correspond to diode #1, diode #2 and the frontside ground shield). Electrical access to the backside (common ground) was achieved by using silver epoxy (BIPAX® TRA-DUCT BA-2902 manufactured by Tra-Con, Inc.) to attach a 1/16" copper wire to the backside of the chip. The four copper wires (3 frontside and 1 backside) form the output leads from the sensor. A schematic illustration and scanned photograph of the sensor plug with the mounted chip are shown in Fig. 4.6. The four output leads from the sensor can be seen in Fig. 4.6b.

4.3.2 Second-Generation Sensors

For the second-generation sensor arrays, a PC-board type package was used, as shown in the schematic illustration of Fig. 4.7a (a similar PC-board type design has been used to package thermal shear-stress sensors by [52]). The PC-board was manufactured by an outside vendor [100]. The custom-made PC-board (1.4"x 1.4" x 3/32") comprises of a central square chip-recess (1.2 cm x 1.2 cm x 790 μm). A layer of gold was deposited and patterned to form the bond pads and output leads on the frontside of the PC-board. These outputs were connected to a 20-pin dual-inline connector (3M 3421-6620). The connector was mounted and soldered in place from the backside of the board. The pins were made flush with the frontside of the board. The entire backside of the PC-board was coated with gold to form the common ground plane. The sensor chip (1cm x 1cm x 520 μm) was mounted in the square recess using the same procedure used for the first-generation sensors. Electrical access to the chip was made by wire bonding from the bond pads on the chip to the pads on the frontside of the PC-board. There were sixteen wirebonds on the frontside (2 wire bonds per sensor times 8 sensors). Electrical access to the backside was achieved by using silver epoxy to attach a copper wire from the backside of the chip to the common backside ground plane. The ground plane was electrically connected to the pins on the twenty pin connector.

This PC-board was mounted on a 2" diameter PMMA plug which has a central square recess (1.4"x 1.4" x 0.095") such that the board was flush with the top surface of the plug. All the small gaps around the board were filled with moulding clay and made flush with the top surface of

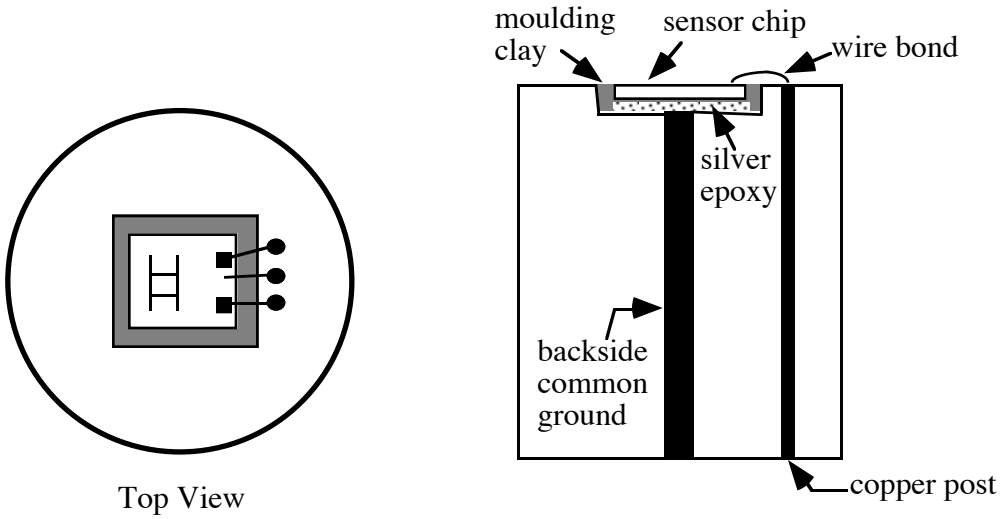

(a)

(b)

Fig. 4.6: a) Schematic diagram showing the top and cross-sectional views of the first-generation

sensor package . It must be noted that the loop on the wire bond has been exaggerated in this drawing; b) photograph of the first-generation sensor package. The four output leads from the sensor can be seen in this picture

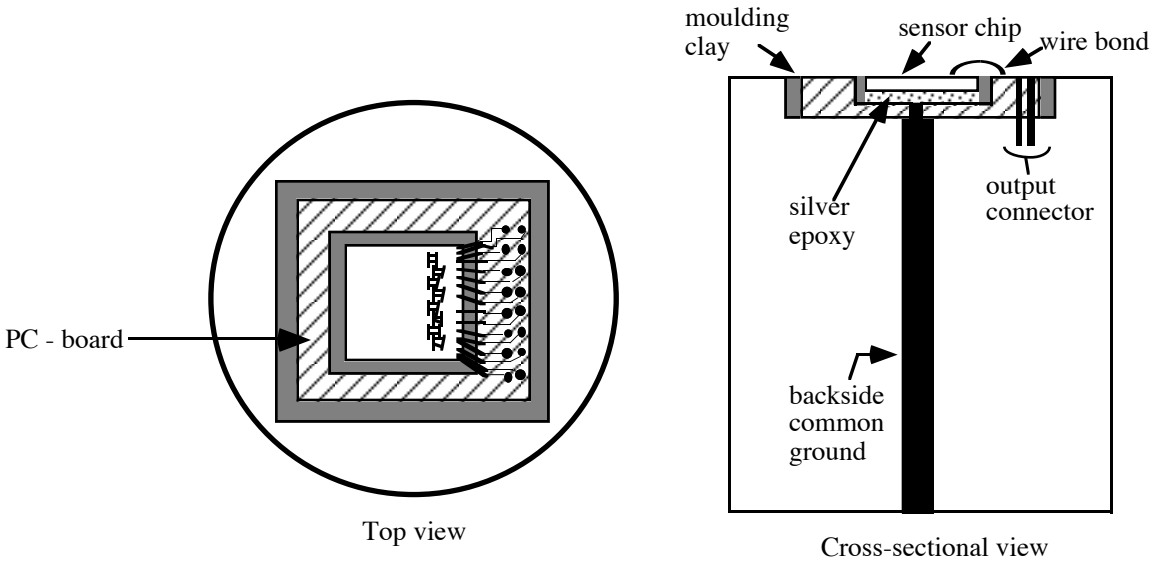

(a)

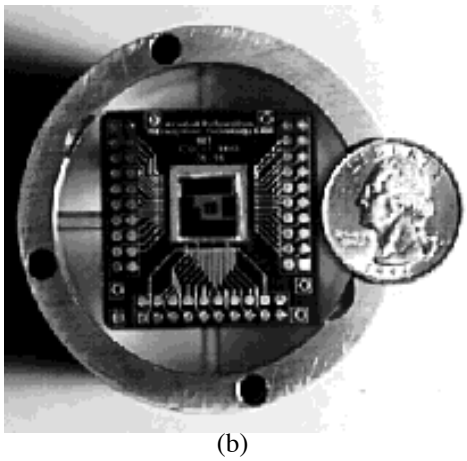

(b)

Fig. 4.7: a) Schematic illustration of the second-generation sensor package. Note that the wire bonds have been exaggerated in this drawing; b) photograph of the second-generation package

the plug. The package was interfaced with the measurement circuit using a twenty-connector shielded ribbon cable (3M 3659/20). The dimensioned drawings the PMMA plug can be found in Appendix E. A photograph of the packaged sensor is shown in Fig. 4.7b.

4.4 Laminar-Calibration Flow Cell Design

The sensors were calibrated in a specially designed laminar-calibration flow cell as shown in Fig. 4.8. The flow cell is comprised of a bottom aluminum plate (with six static pressure taps machined in it) and a top optical glass plate. The channel height is defined using a brass shim

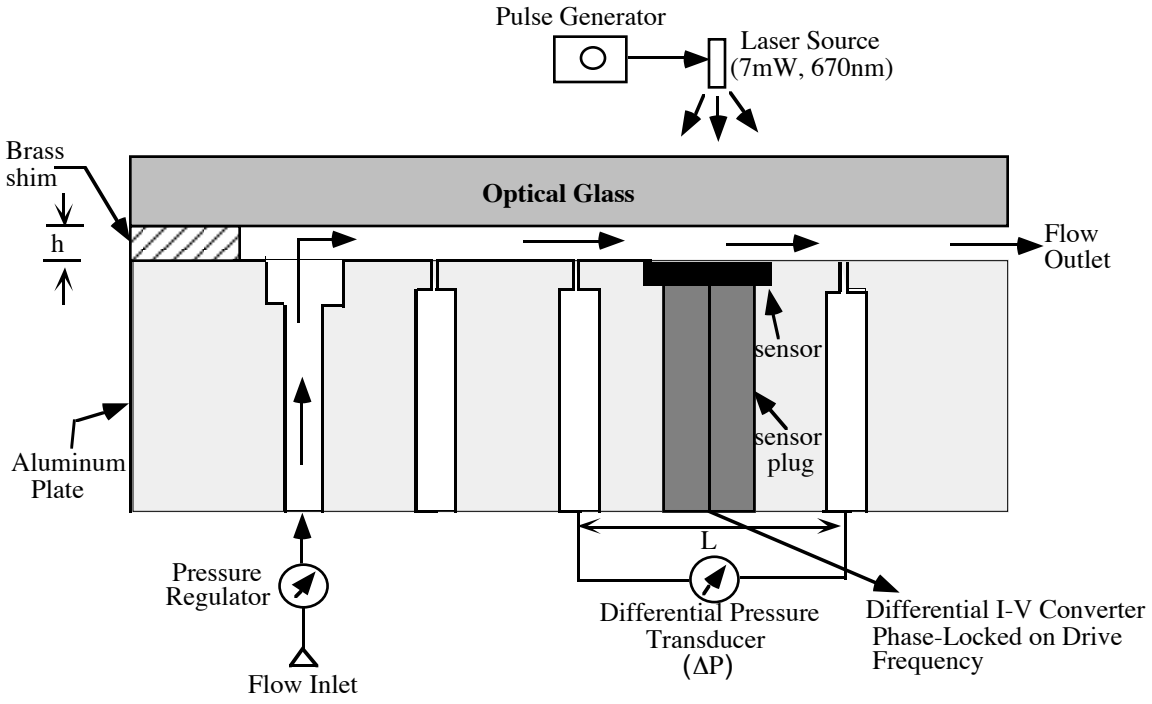

Fig. 4.8 Laminar-calibration flow cell

stock. Shim stocks of different thickness were used to obtain different channel heights. The channel was 27.7 cm long and 12.7 cm wide. The width of the channel was designed to be much larger than the maximum channel height and hence the flow in the cell is two-dimensional in nature. The diameter of the static pressure taps was designed to be 100 μm, so as to minimize thecurvature of the streamlines in the vicinity of the taps and hence minimize the error in the static pressure measurement [101]. A photograph of the different components of the flow cell and the assembled flow cell are shown in Fig. 4.9. A detailed drawing of this laminar-calibration flow cell can be found in Appendix E.

Dry compressed air is introduced into the channel through a pressure regulator. By adjusting the pressure regulator, different values of inlet pressures were obtained. The pressure distribution in the flow cell is obtained by measuring the pressure at pressure tap # 1 using a Honeywell-microswitch 160 series pressure transducer [102]. The differential pressure between any two pressure taps was measured using Setra systems model 206 and 264 series differential pressure transducers [103]. These measurements provide the complete pressure distribution *P(x)* in

the flow cell. The wall shear stress in the flow cell for a fully-developed laminar channel flow can be evaluated from a momentum balance as [3]:

$$\tau_w = \frac{h}{2} \left. \frac{dP(x)}{dx} \right|_{x = x_{sensor}} \tag{4.5}$$

where h is the channel height and $dP(x)/dx$ is the gradient of the pressure measured at a location x. The Reynolds number based on the channel height is defined as $Re_h = uh/\nu$, where u is the average velocity in the channel and ν is the kinematic viscosity of air. For all our experiments $Re_h < 1500$, and hence the flow in the channel is always in the laminar regime.

For all the tests, care was taken to provide a "smooth" inlet of the flow into the channel and to minimize any entrance effects. The maximum entrance length for the entire calibration range was calculated, and all the static pressure taps were located beyond this maximum entrance length. Hence the pressure (and therefore shear stress) measurements were made in a fully-developed laminar channel flow. The sensor response was measured using an off-chip measurement circuit. The details of the measurement circuit are described in the next section.

4.5 Measurement Circuit

The low magnitude photocurrent from the sensor is converted into an output voltage using a differential *I-V* converter employing an amplitude modulation scheme. The next sub-section describes the design of the circuit.

4.5.1 Circuit Design for Small-Current Detection

The differential photocurrent output from the transducer is small in magnitude. Therefore, this signal needs to be amplified before detection. Any noise in the system (between the transducer and first-stage amplification) will also be amplified along with the sensor signal. Hence the measurement circuit must be designed to be immune to any interfering noise input. The noise sources can be classified as: i) low-frequency noise - examples of this type of noise include 60 Hz noise that originates from AC power distribution systems, and DC noise that originates from offset voltages in the circuit components. Another dominant source of low-frequency noise is *1/f* noise generated due to surface leakage in transistors and semiconductor diodes, which are significant only below 1 kHz; ii) high-frequency noise - examples of this type of noise include white noise (noise that has the same energy at all frequencies) from resistors and diodes (shot noise). Our measurement circuit was designed to pick out the desired signal and reject all forms of noise. A detailed description of all the different noise sources and the theoretical SNR for the detection system, can be found in section 2.4 of the sensor design chapter.

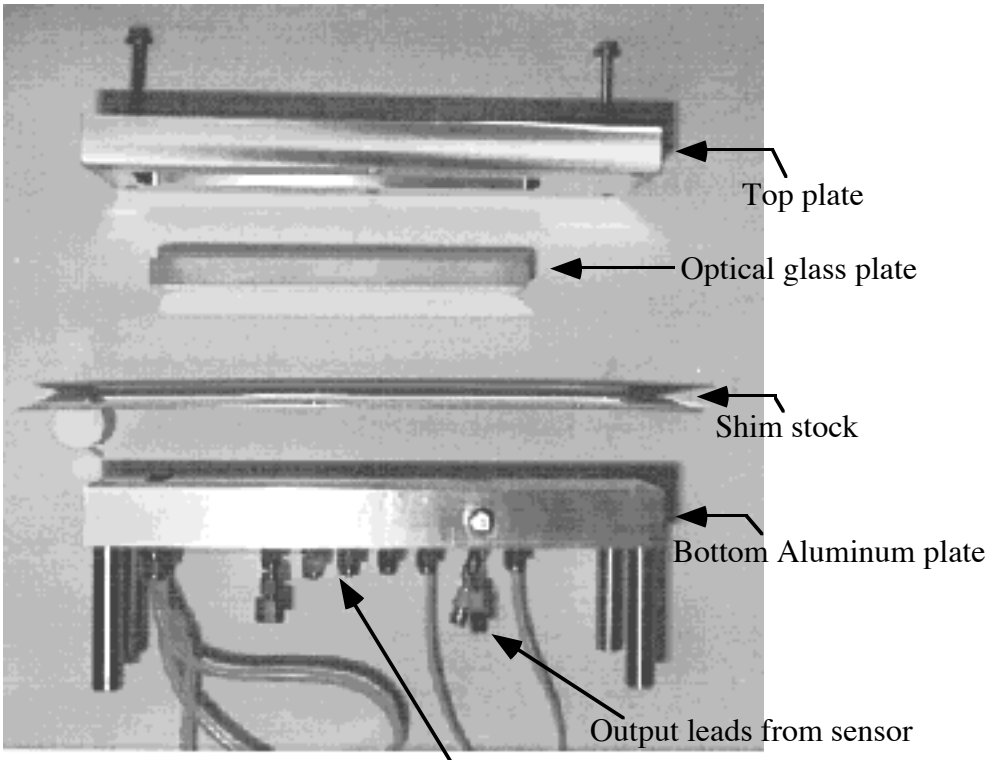

(a)

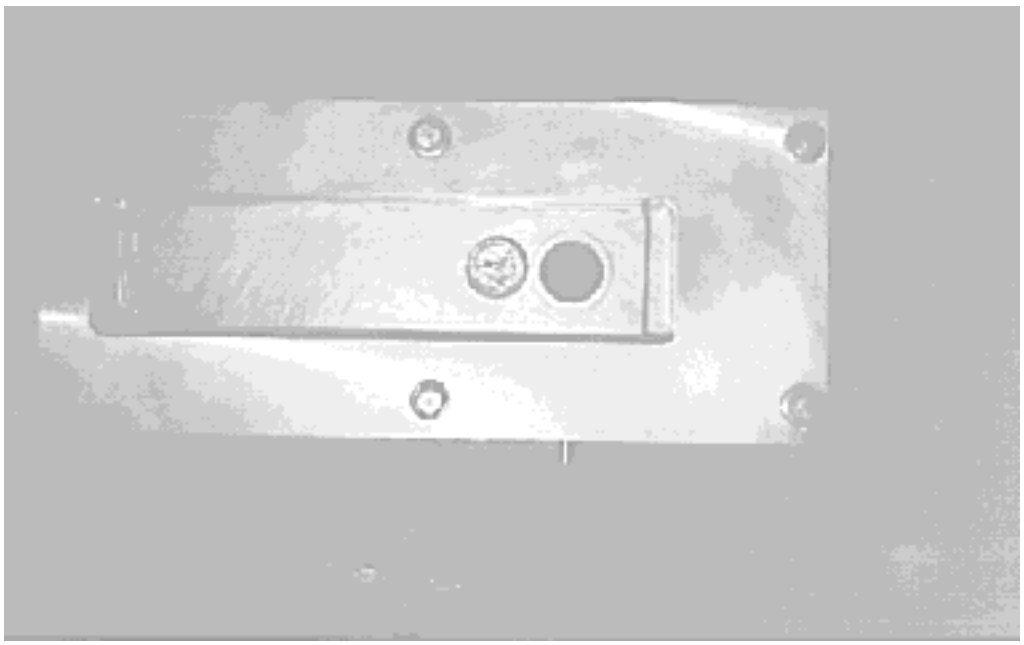

(b)

Fig. 4.9: a) Photograph showing the different components of the laminar-calibration flow cell; b) photograph showing the assembled flow cell

A schematic diagram of the measurement scheme is shown in Fig. 4.10. A detailed layout of this circuit can be found in Appendix F. The laser output is modulated using a square carrier wave from a function generator. Since the laser source is modulated at a high frequency (5 kHz), the sensor output signal is also modulated at this high frequency. The differential photocurrent from the sensor is converted to a voltage using a differential *I-V* converter. The differential

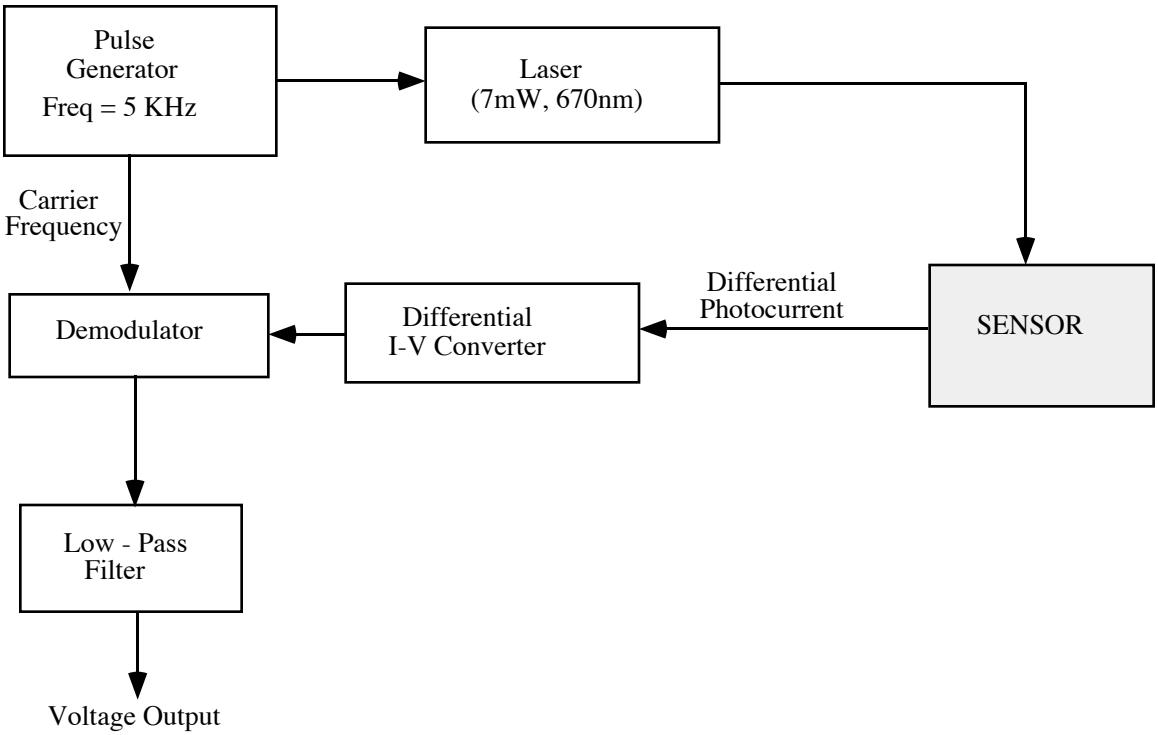

Fig. 4.10 Schematic diagram of the measurement scheme

amplifier amplifies both the signal and noise. However, some of the common-mode noise is rejected due to the high common mode rejection ratio (CMRR) of the differential amplifier. This modulation process (which frequency-shifts the output signal), helps to get away from the *1/f* and 60 Hz noise sources. By bandwidth limiting the output signal, the white noise can also be minimized. The signal is then demodulated and low-pass filtered to retrieve the original sensor output. The above technique is known as amplitude modulation/demodulation. Another motivation to use the amplitude modulation/demodulation process is to be able to measure DC signals using AC amplifiers. To measure small signals we require a very-high-gain amplifier. Because of drift problems, a high-gain amplifier is easier to build as an AC rather than a DC unit. An AC amplifier, however, does not amplify DC signals (due to a roll-off in its gain at low-frequencies). By frequency-shifting the signal, the AC amplifier can be employed to amplify it. A good description of the above technique can be found in [104]. We only present a brief summary here:

1) Drive the laser source at a high frequency, greater than the *1/f* noise corner frequency (~ 1 kHz). For the measurements presented in this thesis the laser source was driven at 5 kHz. For making measurements of fluctuating wall shear stress, the laser must be driven at a frequency that is at least twice the maximum frequency at which we wish to measure the wall shear stress (Nyquist criterion).
2) Amplify both the noise signal and desired signal using a differential amplifier.
3) Demodulate the amplified output with a carrier signal that has the same frequency as the laser drive frequency.
4) Select the DC portion of this signal by using a low-pass filter with a low cut-off frequency (in the present case f_{corner} = 100 Hz). For measurements of fluctuating wall shear stress, this low-pass filtering step is bypassed.

The output of the low-pass filter is a DC voltage whose magnitude is a measure of the magnitude of the desired signal and the signals' phase difference with respect to the carrier signal [104]. Since all the lead lengths were designed to be equal, the phase difference for the present case is zero. Hence the output voltage of the circuit is proportional to the magnitude of the desired signal.

The above described circuit was used for our initial experiments. In subsequent tests we used two SR 570 low-noise current preamplifiers [105] instead of the measurement circuit. The SR 570 has adjustable gain and allowed the low-pass filtering of the signal at different cut-off frequencies. It duplicated all the features of our measurement circuit.

4.5.2 Other Circuit Design Issues

This sub-section presents some of the other circuit design features that had to be implemented in order to make accurate off-chip measurements of low-level photocurents. They are:
a) All voltages in the circuit were measured with respect to ground. Since the ground plane itself has some resistance, different points on the ground plane could have different potentials. This could lead to errors in the measured voltages. A method by which we minimized the problem was by using one common ground bus on the circuit. All the voltages were measured with respect to this common ground bus.
b) The cable that connects the sensor to the first stage *I-V* converter is the "weak link" in the whole measurement system. Any noise input into the system at this stage will get amplified along with the desired signal. The noise interference into the system can be considerably minimized by using a coaxial cable, which is as short as possible and is also well shielded (see section 2.4.2). It must be noted that the shield on the coaxial cable must be connected to the above described common ground. For our circuit we used a coaxial cable which was one foot long with C = 31 pF/ft and impedance = 50 Ω.

c) In order to minimize any electromagnetic coupling between the circuit components and any external energy sources, the entire circuit board was enclosed in a metallic box, which was connected to the common ground. The physics of the reduction in EMI, which can be achieved by using metallic shields, is discussed in [106]. An excellent discussion of grounding and shielding techniques for small-signal measurements can be found in [107].

d) As explained earlier, any phase difference between the carrier frequency and the amplified sensor signal will result in an output voltage that carries this phase difference information. One way of reducing this error is to design all the cables to be of the same length.

e) All the resistors used for the gain stages must be well matched. For our circuit we used 1% metal-film resistors.

4.5.3 Nulling of Nominal Signal

As described in section 4.2.2 some of the sensors have a nominal output signal, i.e., a constant non-zero output voltage when there is no applied shear stress. This signal is not desired because it adds on to all the output readings obtained in a flow environment. To obtain the real output voltage in the presence of a flow, this nominal value will have to be accounted for. In order to simplify the data collection process, this nominal output voltage was eliminated by adding an offset adjustment stage between the first and second stages, as shown in Appendix F. The offset stage subtracts out this nominal voltage, thereby making the zero shear stress output of the circuit equal to zero.

4.5.4 Noise-Floor of Measurement Circuit

The noise-floor for the circuit (at a gain of 10^7 V/A) was measured to be 10 mV. This corresponds to a wall shear stress of 3.6 x 10^{-4} Pa for the 500 μm sensor and 3.4 x 10^{-3} Pa for the 120 μm sensor. The signal-to-noise ratio was equal to 4 at the lowest shear stress for the 500 μm sensor and 3.38 for the 120 μm sensor (see next section for the lowest measured shear stress).

4.6 Testing in Laminar-Calibration Flow Cell

4.6.1 Sensor Calibration

This sub-section presents the results from the calibration of the sensors over a wide range of wall shear stress: 0.001 Pa to 100 Pa. The experiments can be divided into two categories: A) low shear stress regime, $0.001 \text{ Pa} \le \tau_w \le 1 \text{ Pa}$; B) high shear-stress regime, $1 \text{ Pa} \le \tau_w \le 133 \text{ Pa}$. We will first derive the expressions for the shear stress in the two regimes. As shown in equation (4.5) the wall shear stress for a fully-developed channel flow is given as

$$\tau_w = \frac{h}{2} \left. \frac{dP(x)}{dx} \right|_{x = x_{sensor}} .$$

For small pressure ratios (P_{inlet} / $P_{outlet} \leq 1.1$), the pressure distribution in the channel (excluding the *entrance* region) should be linear for a fully-developed laminar flow (which is incompressible). For a linear pressure distribution in the flow cell, equation (4.5) reduces to:

$$\tau_w = \frac{h}{2} \frac{\Delta P}{L} \tag{4.6}$$

where ΔP is the pressure drop across the sensor and is measured across a length of L. Hence the theoretical wall shear stress in the flow cell can be calculated from a differential pressure measurement across the sensor.

For large pressure ratios ($P_{inlet}/P_{outlet} \geq 1.1$), the flow in the channel becomes compressible and the pressure distribution is no longer linear [74]. The square of the non-dimensional pressure ($\prod$) is proportional to the non-dimensional distance (X) along the channel, and can be expressed as $\prod^2 = aX + b$ where $\prod$ is the ratio of the pressure $P(x)$ at any location x to the outlet pressure P_{outlet} , X is the ratio of the distance x to the total length of the channel L_c, and a and b are the slope and intercept of the plot of $\prod^2$ versus X. This relationship between the non-dimensional pressure and distance is valid when the flow in the channel is steady, two-dimensional and isothermal. All these assumptions are valid for our experiments. The expression for the wall shear stress for large pressure ratios can then be derived from equation (4.5) as described below.

Derivation of expression for τ_w for a non-linear pressure distribution in the flow cell

Equation (4.5) can be re-written as follows

$$\tau_w = \frac{h}{2} \frac{d\frac{P(x)}{P_{outlet}}}{d\frac{x}{L}} \frac{P_{outlet}}{L_c} . \tag{4.7}$$

The above equation can be simplified using the substitution, $\prod = P(x)/P_{outlet}$, $X = x/L_c$ as follows

$$\tau_w = \frac{h}{2} \frac{P_{outlet}}{L_c} \left. \frac{d\Pi}{dX} \right|_{X = X_{sensor}} . \tag{4.8}$$

Differentiating $\prod^2 = aX + b$ we get

$$2\ \Pi(X) \frac{d\Pi}{dX} = a . \tag{4.9}$$

which can be written as

$$\left. \frac{d\Pi}{dX} \right|_{X = X_{sensor}} = \left. \frac{a}{2\ \Pi(X)} \right|_{X = X_{sensor}} . \tag{4.10}$$

Substituting for $d\prod/dX$ from equation (4.10) in equation (4.8) we get

$$\tau_w = \frac{h}{2}\frac{P_{outlet}}{L_c}\frac{a}{2\Pi(X)}. \tag{4.11}$$

Using $\Pi = \sqrt{aX + b}$ in equation (4.11) the final expression for the wall shear stress can be written as

$$\tau_w = \frac{h}{2}\frac{P_{outlet}}{L_c}\frac{a}{2\sqrt{aX_{sensor} + b}}. \tag{4.12}$$

The theoretical value of the wall shear stress in the flow cell can then be calculated using equation (4.12). The values of h, L_c and X_{sensor} for our channel are known. The pressure at the channel outlet P_{outlet} and the pressure at various x-locations along the channel $P(x)$ were measured. The constants a and b are evaluated from a plot of Π^2 and X.

A. Measurements in the Low Shear-Stress Regime (Linear Pressure Distribution)

All measurements in this regime are based on $P_{inlet} / P_{outlet} \leq 1.1$. The pressure drop along the channel was confirmed to be linear by measuring the pressure using six pressure taps (all six are not shown in Fig. 4.9) located along the length of the channel. Figure 4.11 shows the measured pressure distribution in the flow cell, plotted as a function of the distance x. The data points represent the measured values and the solid lines are the theoretically predicted pressure values. The expression for the theoretical pressure distribution for a laminar, incompressible flow is given as [3]:

$$P(x) = P_{inlet} \pm \frac{3\mu Q}{2h^3 W}x \tag{4.13}$$

where P_{inlet} is the pressure at the inlet to the channel, μ is viscosity of air, Q is the volumetric flow rate and W is the width of the channel. It can be seen from Fig. 4.11, that the measured pressure distribution is linear and the measured values are in good agreement with the theory. It must be noted that for measurements in this regime, $Re_{h,max} = 369$.

In order to obtain a range of wall shear stress in the flow cell, channels of different heights (different shim stock thickness) were used. The experiments in this regime were done using shims of thickness' 127 μm, 254 μm and 508 μm. Figures 4.12 and 4.13 are the composite plots of the sensor output voltage plotted as function of the wall shear stress for the 500 μm and 120 μm sensor, respectively. It can be seen that for both the sensors, the response is linear over four orders of wall shear stress. The measured sensitivity is in good agreement with the theoretically predicted sensitivity.

The lowest measured shear stress was 0.0014 Pa for the 500 μm sensor and 0.0115 Pa for the 120 μm sensor. The lowest measured value was limited by the smallest differential pressure

that could be measured by the differential pressure transducer and not by the smallest signal which could be measured by the circuit.

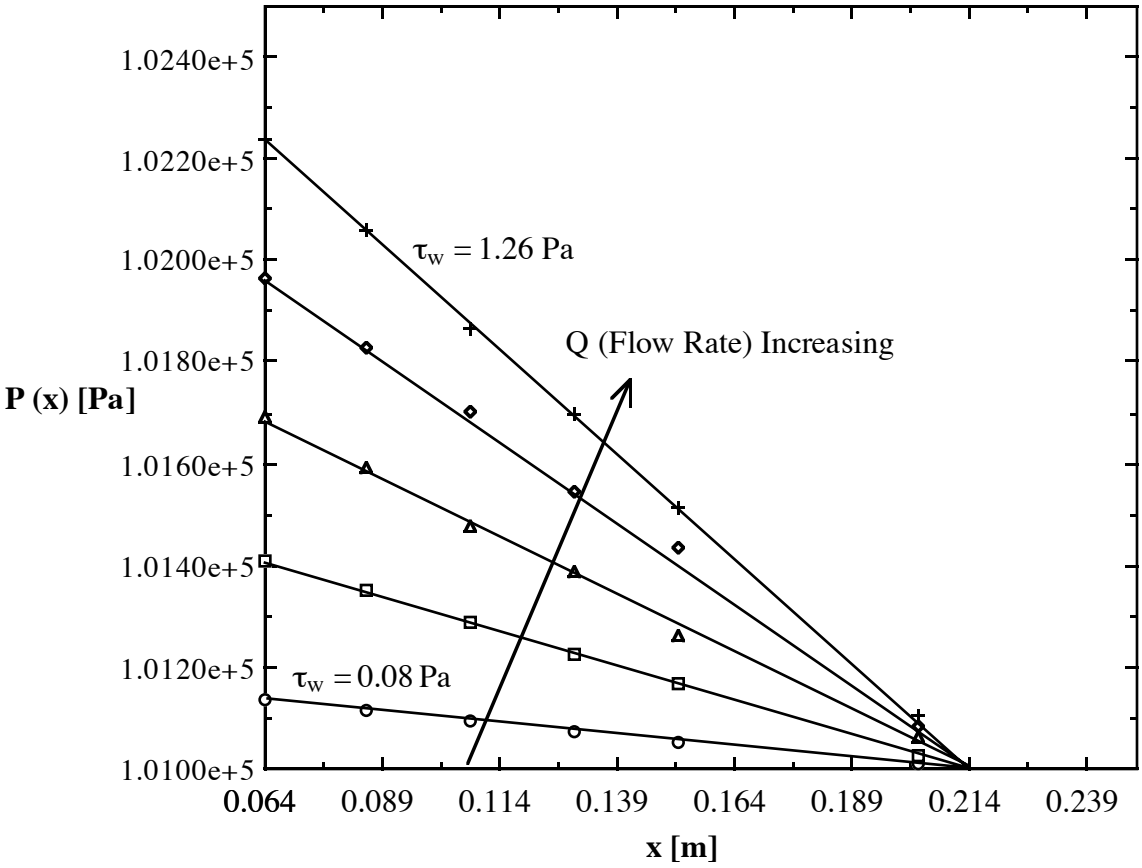

Fig. 4.11 Plot showing the linear pressure distribution in the laminar-calibration flow cell in the low shear-stress regime

B. Measurements in the High Shear-Stress Regime (Non-Linear Pressure Distribution)

All measurements in this regime are based on $P_{inlet}/P_{outlet} \geq 1.1$. A large magnitude shear stress can be obtained in the flow cell by adjusting both the channel height h and the pressure ratio P_{inlet}/P_{outlet}. All the tests in this regime were performed using shims of thickness 508 μm and 1016 μm. The maximum Reynolds number for this regime was $Re_{h,max} = 1500$.

The pressure distribution in the channel $P(x)$ was again measured using six pressure taps. The measured pressure at different x locations was normalized by the outlet pressure and plotted asa function of the non-dimensional channel length X ($=x/L_c$), as shown in Fig. 4.14. This plot of $\prod^2$ versus X is a universal pressure curve, which is independent of the channel height. The shear stress in the channel can be estimated from this plot, as described in the previous sub-section. Figures 4.15 and 4.16 show the response of the 500 μm and 120 μm sensors in the high-shear

regime. Again, the response is linear with the same sensitivity as in the low-shear regime. The

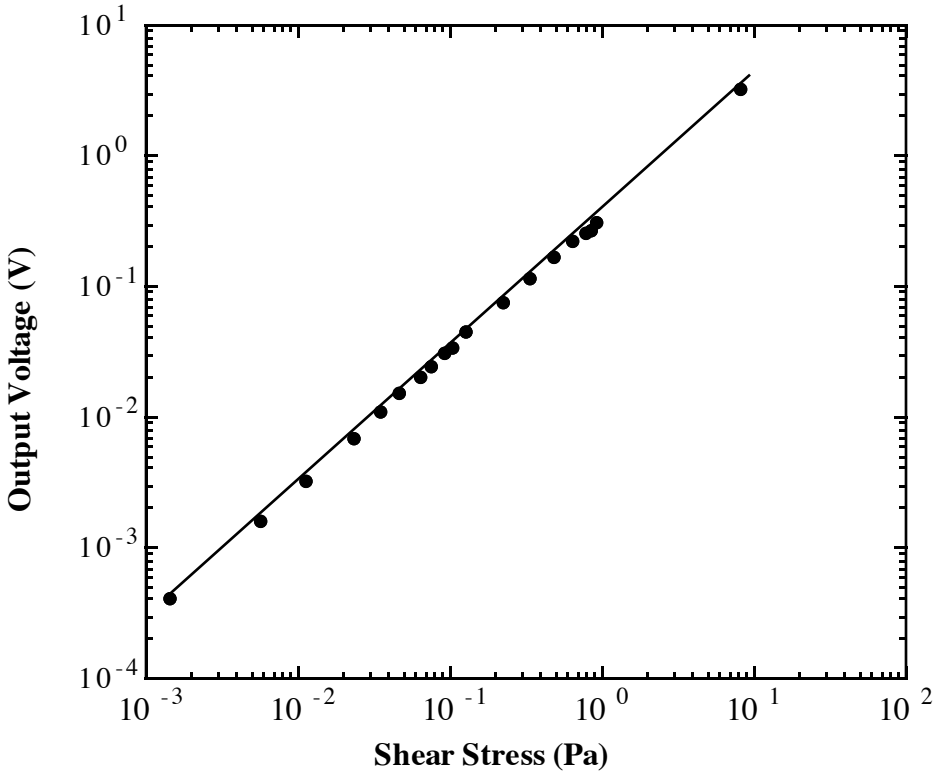

Fig. 4.12 Response of the 500 μm sensor in the low shear-stress regime

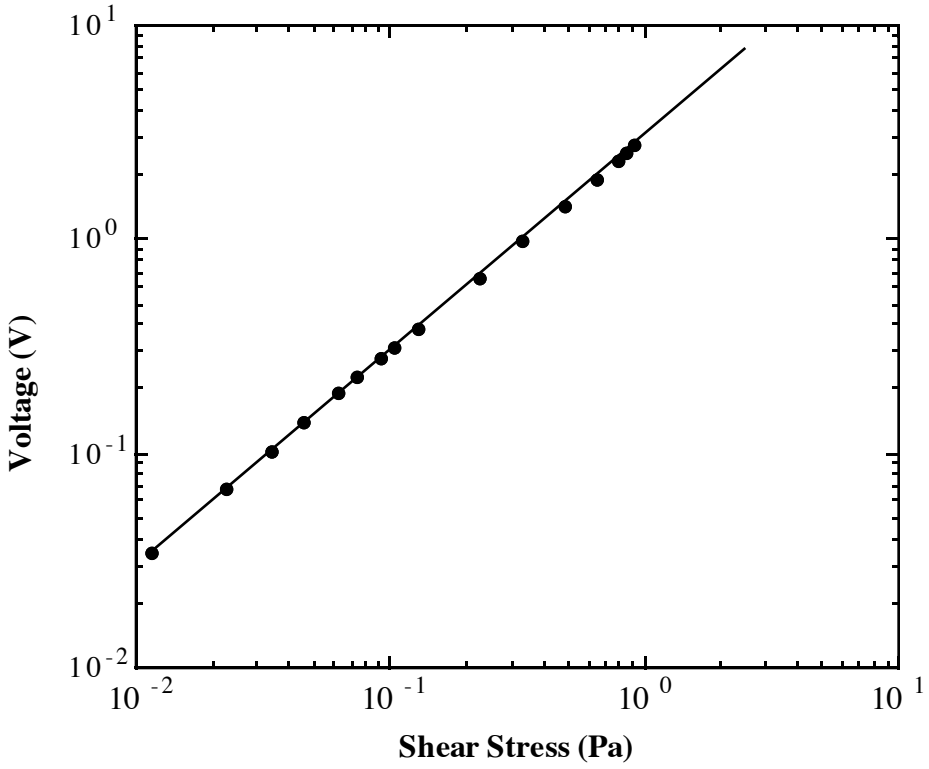

Fig. 4.13 Response of the 120 μm sensor in the low shear-stress regime

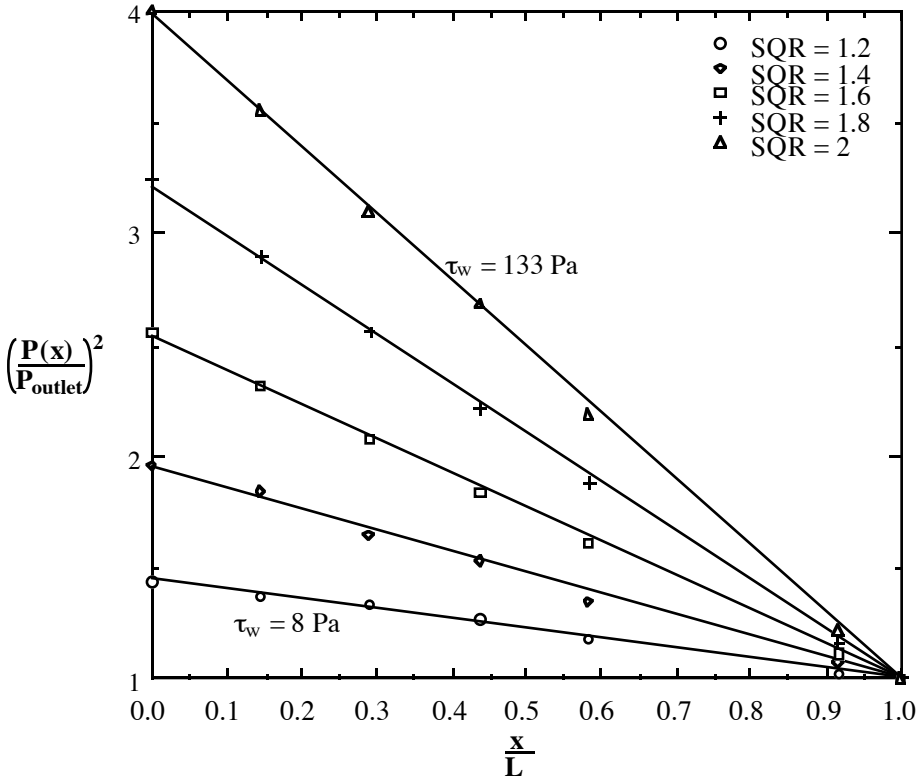

Fig. 4.14 Plot of the pressure distribution in the laminar-calibration flow cell in the high shear-stress regime. The square of the non-dimensional pressure shows a

linear dependence with the non-dimensional presure

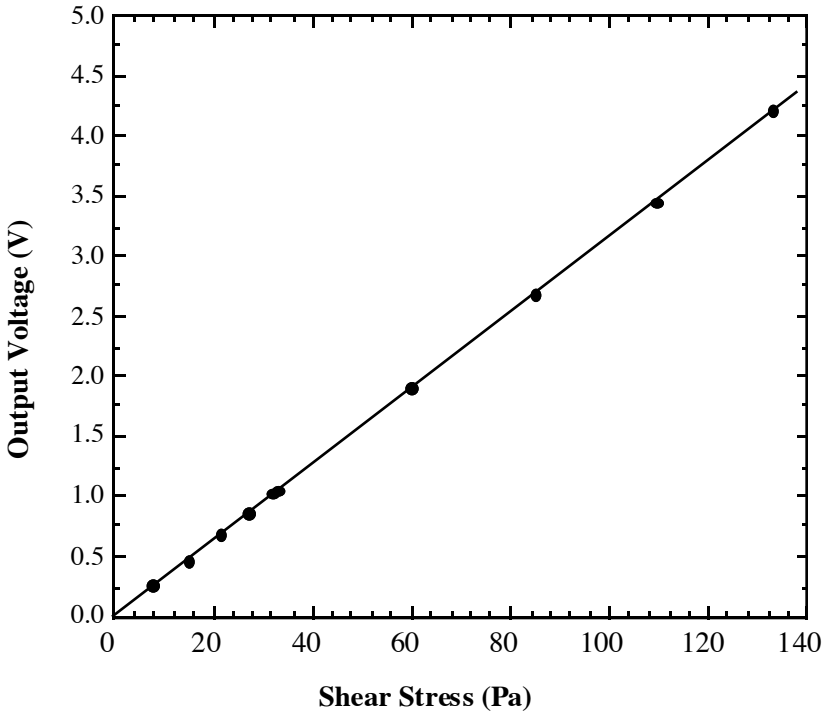

Fig. 4.15 Response of the 500 μm sensor in the high shear-stress regime

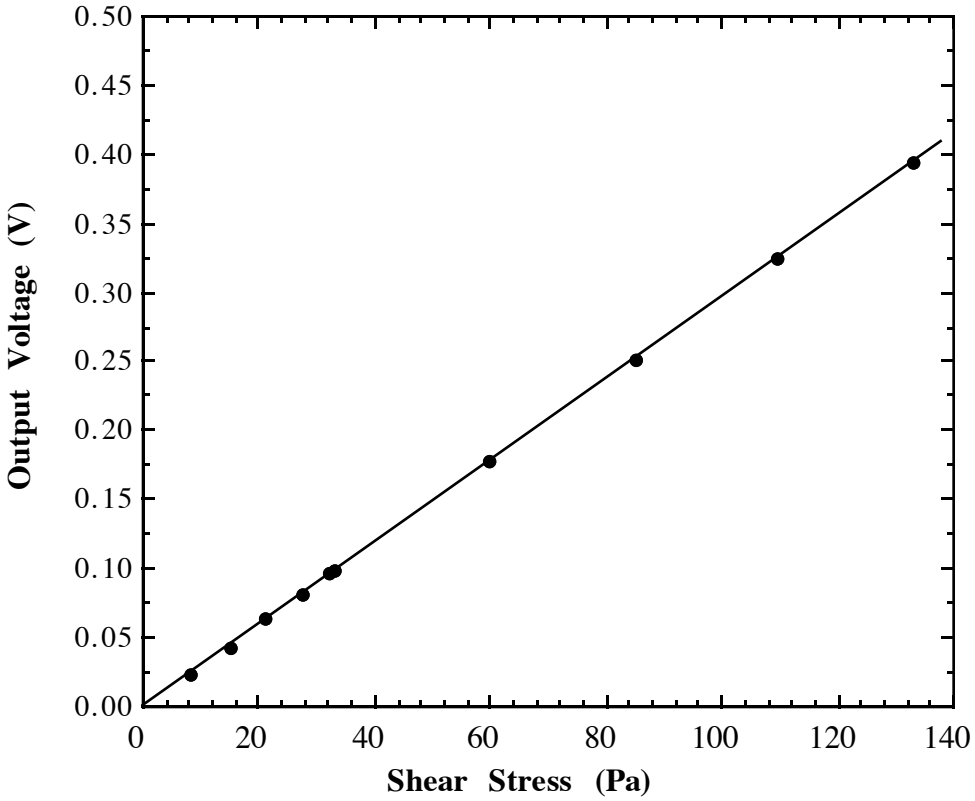

Fig. 4.16 Response of the 120 μm sensor in the high shear-stress regime

maximum measured shear stress was 133 Pa for both the sensors. This was limited by the maximum shear stress that we were able to generate in our channels, for a fully-developed laminar flow.

The linearity of the sensors (for both the regimes) can be expressed in the form "within ± ... % FSO" as the maximum deviation of any calibration voltage from the corresponding value on the "best-fit" line [108]. The "best-fit" line is defined such that the sum of the squares of the residuals is minimized. (The term *residual* refers to the deviation of the actual sensor output from the corresponding point on the calculated straight line). The expression for the linearity of the sensor is given as

$$Linearity = \frac{maximum\ deviation\ from\ the\ "best\pm fit"\ line}{full\pm scale\ output\ voltage}\ . \tag{4.14}$$

The measured linearity in the range $0.001\ \text{Pa} \le \tau_w \le 1\ \text{Pa}$ for both the sensor sizes was ≤ ± 1% FSO. The linearity in the range $1\ \text{Pa} \le \tau_w \le 133\ \text{Pa}$ for both the sensor sizes was ≤ ± 2% FSO.

4.7 Other Performance Criteria

4.7.1 Repeatability

Repeatability is the ability of a sensor to reproduce output readings when the same measurand (shear stress in this case) value is applied to it either consecutively or at different times, under the same experimental conditions and in the same direction. It is normally expressed as the maximum difference between the output readings at any measurand value within the range of interest and is stated as "within ...% of the full-scale output (FSO)" [108]. The expression for repeatability is given as

$$Repeatability = \frac{maximum\ value\ of\ the\ difference\ between\ sensor\ output\ voltages\ at\ a\ given\ wall\ shear\ stress}{full\pm scale\ output\ voltage}\ . \tag{4.15}$$

Several calibration cycles (a set of three loading and unloading cycles for each experiment) of the sensor performed at different times were used to calculate the repeatability of the sensor. The repeatability experiments were performed both in the low shear and in the high shear regime. The measured repeatability in the low-shear regime ($0.001\ \text{Pa} \le \tau_w \le 1\ \text{Pa}$) was within ± 3% FSO and in the high-shear regime ($1\ \text{Pa} \le \tau_w \le 133\ \text{Pa}$) was ± 1% FSO, for both the 120 μm and 500 μm sensors. We have tested one of the 500 μm floating-element sensors' several times over a period of

a year and half. The response of the sensor was found to be identical for each calibration-cycle during that period.

4.7.2 Drift

For the sensors in this thesis, drift is defined as the variation in the value of $\Delta I_{photo}/I_{photo}$ over time, in the absence of any flow. The expression for drift is given as

Drift = maximum shift in the value of $\Delta I_{photo}/I_{photo}$ *over a 2 hour interval measured by a HP 4145.* (4.16)

The measured long-term drift was found to be $\leq \pm$ 4 % change in the value of $\Delta I_{photo}/I_{photo}$ in a 2 hour measurement interval. The short-term drift (time < 30 mins) was less than 0.5 % and hence is acceptable for measurements of both DC and AC wall shear stress. We believe that the cause for the drift in the photocurrent is the laser-heating of the photodiodes (resulting in a thermal current). The magnitude of the drift should therefore be smaller in the presence of the flow (due to the cooling of the photodiodes).

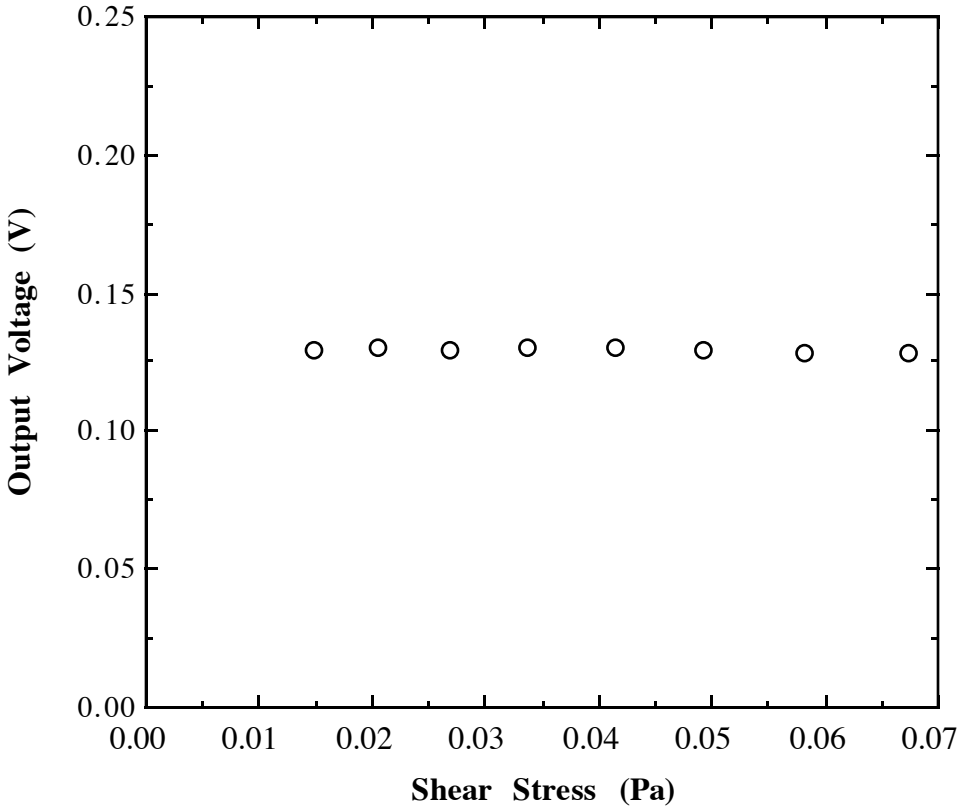

Fig. 4.17 Response of the 500 μm sensor in a laminar flow, with the tethers oriented parallel to the flow. The differential voltage output was deliberately set at a non-zero value (under no flow condition)

4.7.3 Cross-Axis Sensitivity

The shear stress sensors have been designed to be sensitive to wall shear in only one direction (transverse direction, i.e., flow direction perpendicular to the tethers). This is accomplished by making the stiffness of the sensor structure much larger for motions in the longitudinal direction (flow parallel to tethers) compared with the transverse direction. Cross-axis sensitivity is defined as the coupling into the primary sense axis of the sensor, of any longitudinal sensitivity. This can occur if the tethers are not perfectly perpendicular to the flow direction. This error can be minimized if the longitudinal sensitivity of the sensor is small. Figure 4.17 shows the sensor output voltage plotted as a function of the wall shear stress with the tethers parallel to the flow direction. This experiment was conducted in a laminar boundary layer, where the shear stress values were calculated for a Blasius boundary layer on the walls of the wind tunnel and using the free stream velocity measured by a Pitot tube. It can be seen that sensor response is almost flat, implying almost zero longitudinal sensitivity. The small deviation from a perfectly flat response is probably due to a misalignment of the tethers with the flow direction. This plot therefore indicates that the cross-axis sensitivity of the sensors, if any, is negligible.

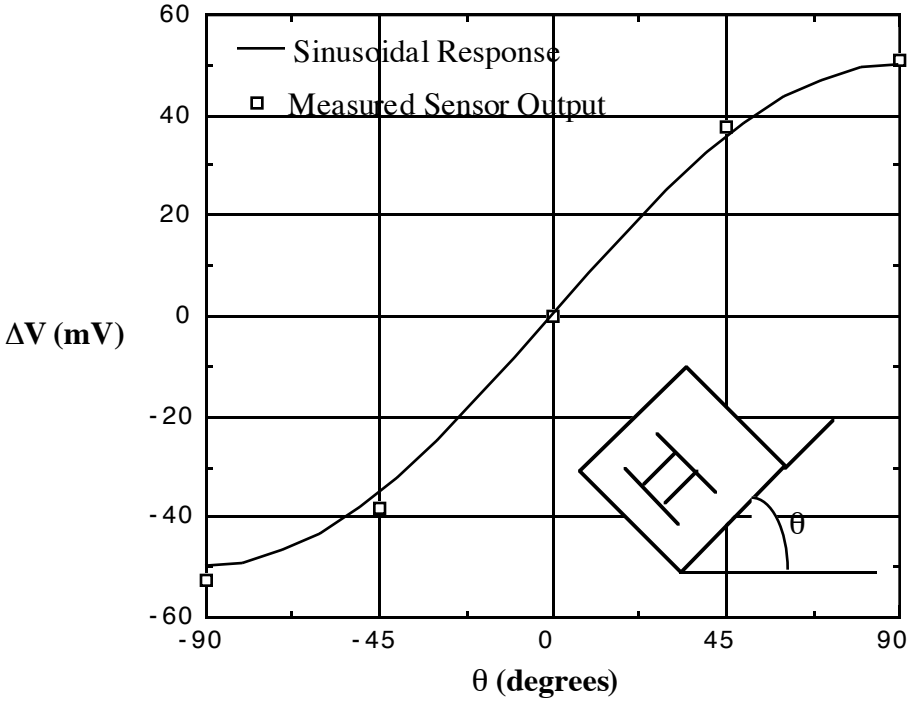

Fig. 4.18 Response of a 500 μm sensor as it is rotated through 180° in steps of 45°. The measured acceleration sensitivity is 50 mV/g

4.8 Acceleration Sensitivity of the Sensor

The acceleration sensitivity of the sensor can be estimated by considering the effect of an acceleration force in terms of an equivalent shear stress. The force acting on the floating-element due to an acceleration of *one-g* is given as $F = mg$ where m is the mass of the floating-element and is given as $m = \rho_{Si} L_e W_e t$. This force divided by the area of the floating-element is the equivalent shear stress and is given as

$$\tau_{w,\,equivalent} = \frac{\rho_{Si} L_e W_e t}{L_e W_e} = \rho_{Si} t g \,. \tag{4.17}$$

For our sensor t = 7 μm and using ρ_{Si} = 2328 Kg/m^3, the equivalent shear stress corresponding to *one-g* of acceleration is 0.16 Pa. Figure 4.18 shows the output voltage of the sensor plotted as a function of the angle, as the sensor is rotated through 180° in steps of 45°. The deviation from a perfectly sinusoidal response is due to the error in aligning the tethers parallel to the desired angular position.

4.9 Measurements in a Laminar Boundary Layer

The 500 μm x 500 μm sensor was tested in the low-speed, low- turbulence wind tunnel at MIT. The sensor plug was mounted on a circular port, which was in turn mounted on a circular window on the wall of the wind tunnel. The laser was located on a traverse, close to the opposite wall of the wind tunnel. The laser spot position relative to the sensor was adjusted by moving the computer-controlled traverse. The output leads from the sensor were connected to an A/D automated data acquisition system. A scanned photograph of the measurement set-up is shown in Fig. 4.19.

Figure 4.20 shows the sensor response in a laminar boundary layer plotted versus the calculated wall shear stress. This is the same sensor that was calibrated in the laminar-calibration flow cell, but with an additional gain of 100. The sensor response is linear over the entire measurement range. It can be seen from Fig. 4.21 (which is a composite plot of the data from the calibration cell in the range 0-1 Pa and the data from the laminar boundary layer) that the sensor has the same sensitivity in the wind tunnel as measured in the calibration cell.

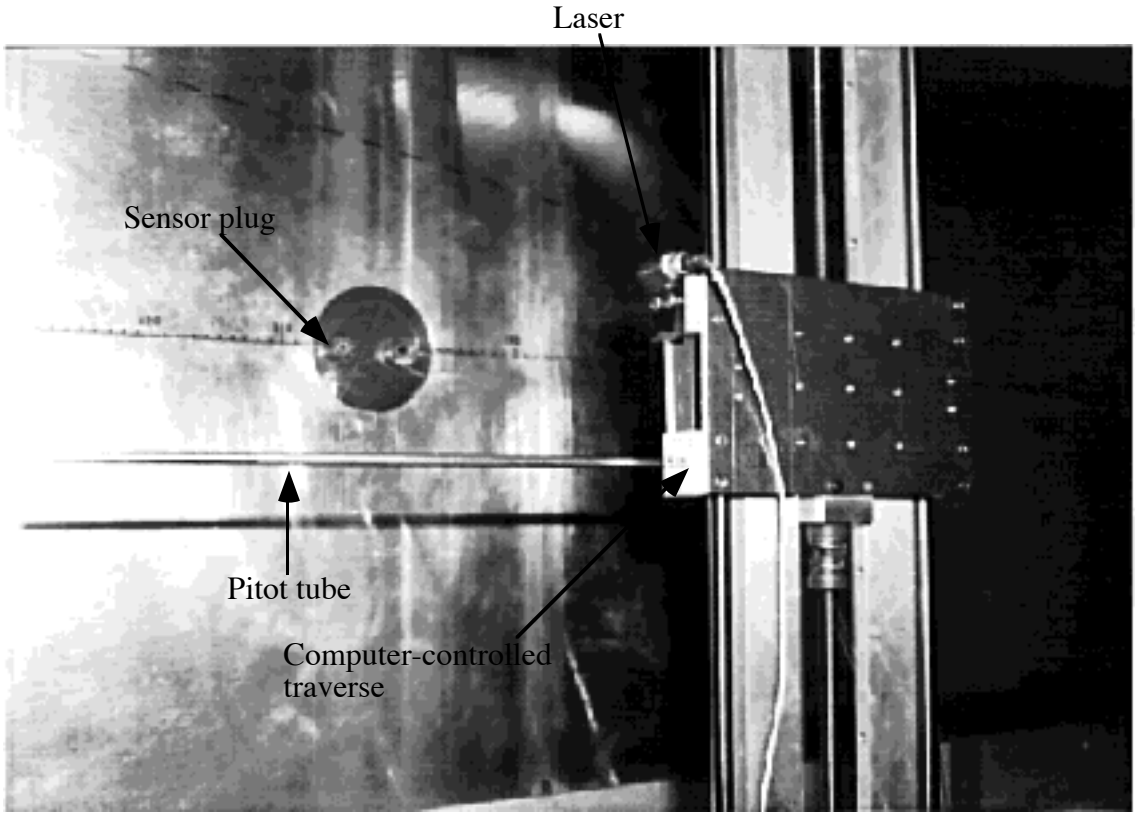

Fig. 4.19 Photograph showing the measurement set-up in the low-speed wind tunnel at MIT

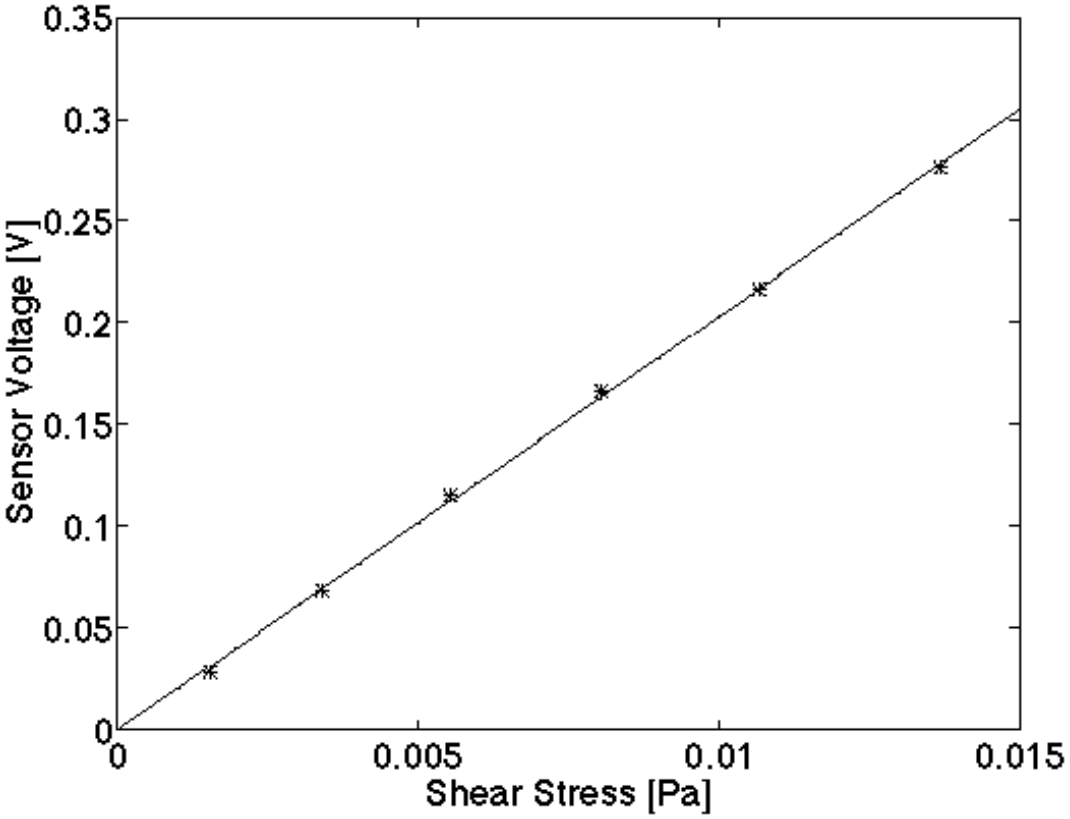

Fig. 4.20 Response of the 500 μm sensor in a laminar boundary layer

The sensor was able to transduce shear stresses of 0.01 Pa and lower, in a laminar boundary layer. This is three orders of magnitude lower than what we have measured before using micromachined sensors [28]. It must be noted that the shear stress values were calculated for a Blasius boundary layer (this was independently confirmed) on the walls of the wind tunnel and using the free stream velocity measured by a Pitot tube.

4.10 Dynamic Testing - Frequency-Response Studies

In order to make shear stress measurements in a turbulent flow, it is desirable that the sensor possess an optimally flat, unity gain and minimum phase frequency response function. Such characteristics are required for accurate correlation and spectral analysis during measurements in turbulent boundary layers. It is therefore necessary to characterize the frequency-response of the sensor. By frequency response we mean the steady state response of the sensor to a known sinusoidal input. The frequency of the input signal (oscillating wall shear stress in this case) is varied over a certain range and the resulting output of the sensor is studied.

The transfer function of the sensor can also be obtained from such frequency-response tests. A good description of frequency-response methods can be found in [109]. In order to obtain the frequency-response of the sensor, it is necessary to generate a known sinusoidal wall shear-

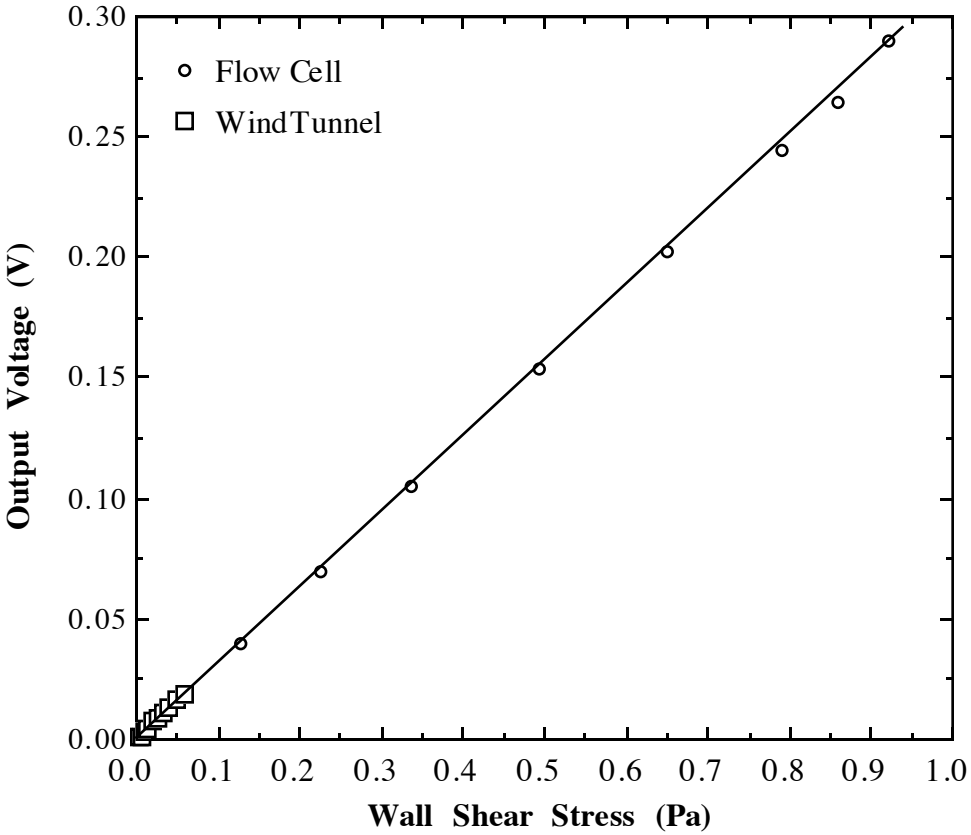

Fig. 4.21 Composite plot of the data from Fig. 4.20 and the data from Fig. 4.12 in the shear-stress range of 0-1 Pa

stress input. The generation of such a known shear stress is difficult in practice. However, an acoustic plane-wave excitation offers the capability of generating known oscillating shear stresses over a certain frequency range. The next three sub-sections discuss the basic theory of acoustic plane waves and the theory and experimental design of the set-up that was used to acoustically generate oscillating wall shear stresses of known magnitude and frequency.

4.10.1 Acoustic Plane Wave

An acoustic plane wave (or a sound wave) in air consists of sinusoidally oscillating planes of constant pressure and particle velocity (which is parallel to the direction of propagation of the sound wave). As the wave propagates, it disturbs the air from its mean rest-state. The properties of air (ex: pressure and density) change by a small percentage from their rest-state value and a

fluctuating pressure and density are established in the medium, superimposed over the mean rest-state pressure and density. The relationship between the rms value of this fluctuating pressure p at a given location in the medium and the local particle velocity u is given by:

$$p = Z\,u \tag{4.18}$$

where Z is the specific acoustic impedance of air and is equal to the product of the density and speed of sound in air [110]. The range of amplitudes of the fluctuating pressure that are commonly experienced in sound waves is great, and hence it is convenient to express the pressure fluctuation on a logarithmic scale. The level of sound pressure fluctuations can be expressed in decibels (db) as follows:

$$SPL\ in\ db = 20 \log_{10} \left(\frac{p}{2x\ 10^{\pm 5}\ N/m^2}\right) \tag{4.19}$$

where *SPL* stands for sound pressure level. The value of p in most commonly experienced sound waves is only a fraction of a percent of the atmospheric pressure.

4.10.2 Theory and Design of Plane Wave Tube (PWT)

Oscillating shear stresses of known magnitude and frequency can be generated using acoustic plane waves in a PWT. A PWT is widely used as a standard for measuring the performance of speaker drivers [111]. A schematic illustration of the set-up of a PWT is shown in Fig. 4.22a. The set-up is comprised of an acrylic tube with a speaker/compression driver on one end and a wedge-shaped end-termination on the other. The end-termination is designed to minimize the reflections of the sound waves from the end of the tube and thereby set-up a purely traveling wave in the tube. A signal generator and an amplifier drive the speaker to radiate sound at different intensities and frequencies. The sound waves very close to the speaker are not plane waves. The waves become planar at some distance X_{planar} downstream of the speaker. A condenser microphone, the shear-stress sensor and the laser are mounted on the PWT, downstream of the speaker and at the same downstream location, $X > X_{planar}$. The fluctuating pressure p in the PWT is measured using the microphone. The fluid mechanics problem in the PWT is a variation of the classic fluid dynamics problem of Stokes oscillating plate. The only difference is that instead of an oscillating wall and stationary fluid far away from the wall, we have a stationary wall and oscillating fluid molecules far away from the wall. The flow configuration is illustrated in the schematic diagram of Fig. 4.22b. The analytical expression for the wall shear stress in the PWT is derived below. A photograph of the plane wave tube set-up is shown in Fig. 4.23.

The stokes oscillating plate problem consists of a semi-infinite fluid initially at rest and bounded below by a solid infinite plane at $y = 0$ (note Y-direction is the coordinate normal to the plate). The problem is to find the velocity field in the fluid as the plate oscillates in its own plane.

Assuming a parallel flow and neglecting hydrostatic pressure variations in the fluid, the equation of motion for the fluid medium reduces to [77]:

$$\frac{\partial u}{\partial t} = \nu \frac{\partial u}{\partial y^2} \tag{4.20}$$

where u is the velocityof the fluid particles (equation (4.16) relates this to the pressure) and ν is the kinematic viscosity of air. It must be noted that for measurements in a tube (PWT in this case), it can be shown that$u$ represents the velocity-defect, that is, u is the difference between the particle velocity in the boundary layer and the freestream (the set-up is designed such that the boundary layers on the walls don't merge). The boundary conditions for the problem are as follows:

plate initially at rest $\Rightarrow u(y, t{=}0) = 0$;

fluid stationary far away from wall $\Rightarrow u(y \to \infty, t) = 0$;

oscillating plate $\Rightarrow u(y = 0, t) = U \cos(\omega t)$.

The steady-state solution to the problem yields the following expressions for the velocity distribution and boundary-layer thickness [77]:

$$u(y\ \ t) = U\, e^{\pm y\sqrt{\omega/2\nu}} \cos(\omega t \pm y\sqrt{\omega/2\nu}) \ ; \tag{4.21}$$

$$\delta(\omega) = 6.5\sqrt{\nu/\omega} \ . \tag{4.22}$$

Although the complete solution is the sum of both the steady-state and transient solutions, only the steady-state solution is needed to obtain a frequency-response. Hence the transient solution is not discussed here.

The governing equations for this problem are invariant under an unsteady transformation, allowing us to turn the problem around into one in which the wall is stationary and fluid particles far away are oscillating, as is the case in the PWT. This problem represents the near-wall behavior of a plane acoustic wave. The boundary conditions for our problem are as follows:

stationary wall $\Rightarrow u(y, t{=}0) = 0$;

oscillating fluid far away from wall $\Rightarrow u(y \to \infty, t) = U \cos(\omega t)$;

no-slip condition $\Rightarrow u(y = 0, t) = 0$.

The equation of motion for the particles can be solved in cylindrical coordinates, to yield the following expression for the wall shear stress [77]:

$$\tau(\omega, t) = \textit{Real part of} \left\{ U\sqrt{\rho\mu\omega}\ j^{3/2}\, e^{j\omega t}\, \frac{J_1(Rj^{3/2}\sqrt{\omega/\nu})}{J_0(Rj^{3/2}\sqrt{\omega/\nu})} \right\} \tag{4.23}$$

where R is the radius of the tube, J_0 and J_1 are Bessel functions of the zeroth and first order, respectively. It can be seen from equation (4.23) that the wall shear stress is proportional to the velocity of the particles (and hence the pressure) and to the square root of the frequency (rad/s).

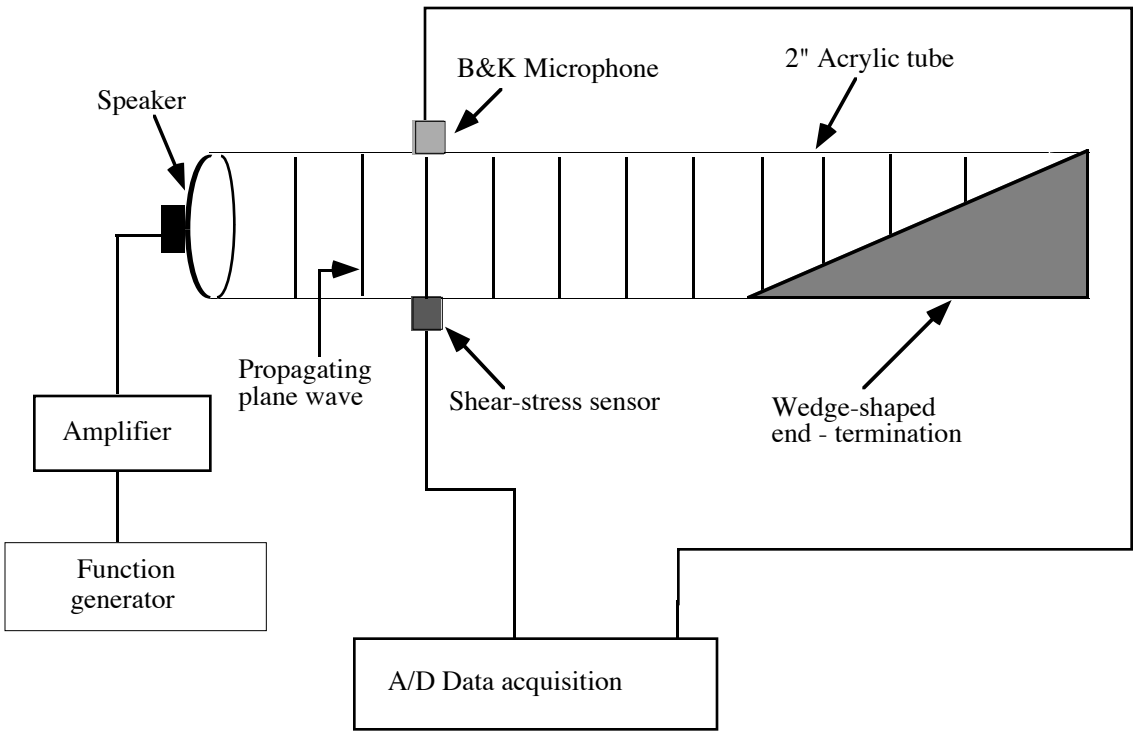

(a)

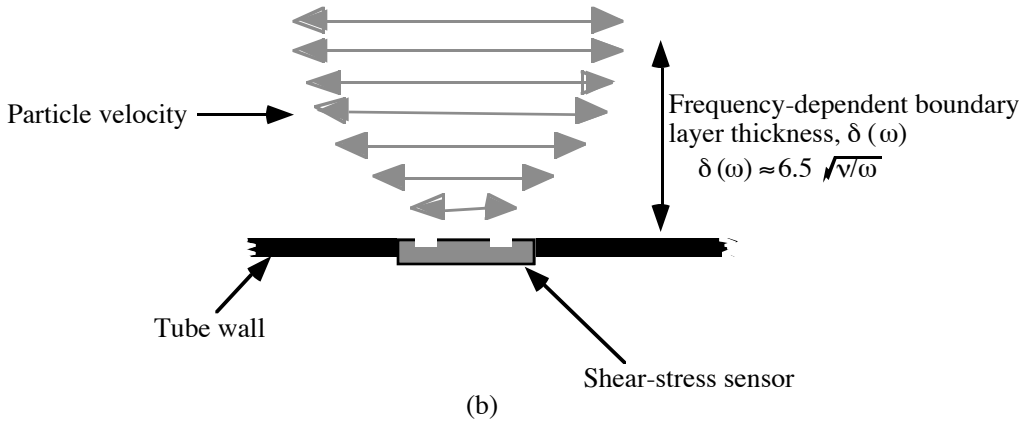

(b)

Fig. 4.22 : a) Schematic drawing of the plane wave tube set up. The laser source is mounted at the same axial location as the shear-stress sensor and microphone and is not shown in this figure; b) model for the near-wall flow behavior in the tube (stationary wall and oscillating fluid particles), resulting in a frequency-dependent boundary layer thickness. This results in a frequency-dependent wall shear stress

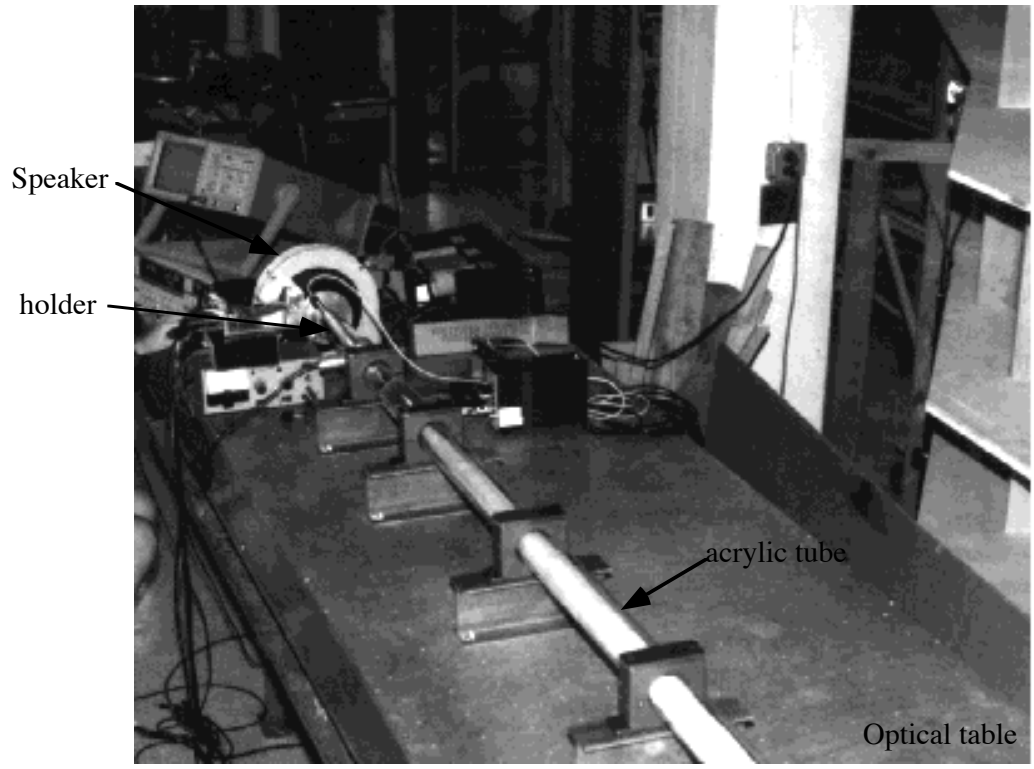

(a)

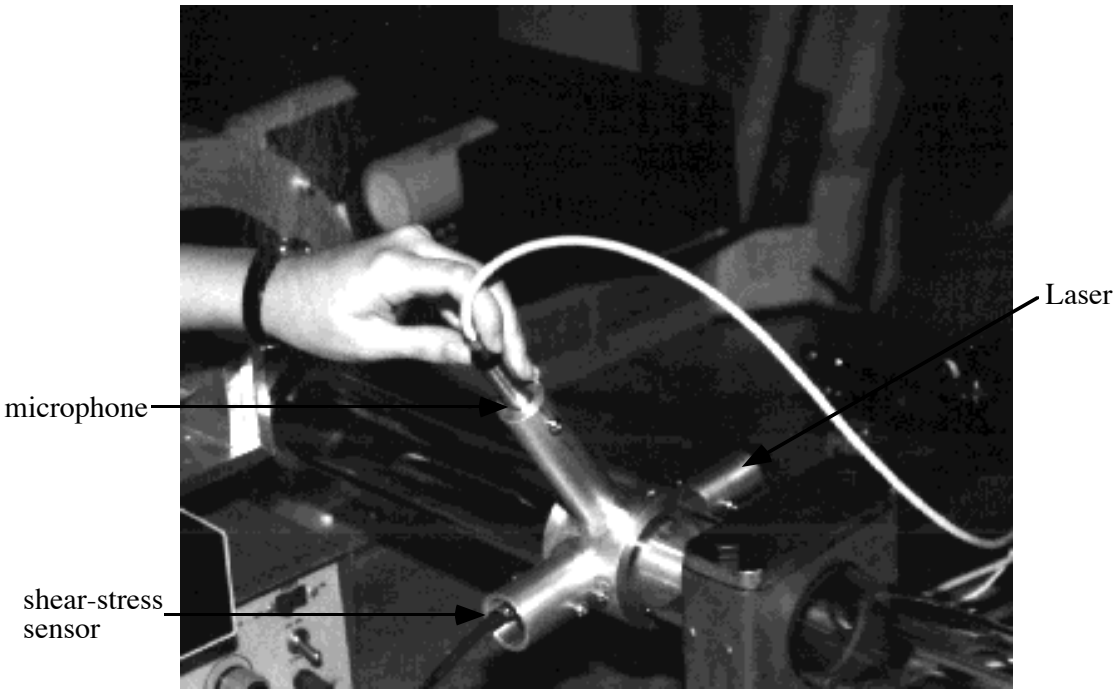

(b)

Fig. 4.23: a) Photograph of the plane wave tube set up; b) zoomed-in view of the holder for the microphone, laser and sensor (courtesy of Sarah Lee[112])

4.10.3 Experimental Design

This section discusses the issues associated with the design of the different components of the plane wave tube set-up: a) tube; b)speaker/compression driver; c) end-termination; and d) microphone.

a) *Tube*. The tube geometry imposes the low and high-frequency limits on the plane waves that it will support. The maximum frequency to which the sensor can be calibrated is determined by the onset of the first non-planar wave mode in the tube (since the analytical relations between pressure, velocity and shear stress described in the previous sections are valid only for a plane wave). This high-frequency cut-off is given as $f_{cut\text{-}off} = 0.5861\ c/d$, where d is the tube diameter and c is the speed of sound in air [110]. For our experiments we used an acrylic tube of 2" diameter and hence the high-frequency cut-off is $f_{cut\text{-}off} = 4$ kHz.

The length of the tube will determine the lowest frequency for which the wave envelope can be defined. The magnitude of the envelope is defined in a quarter wavelength of the traveling wave. Hence the low-frequency cut-off is given as $c/4l$ where l is the length of the tube. For our tube $l = 8$ feet and hence the low-frequency cut-off works out to 35 Hz. The lowest frequency to which our calibration is valid is actually 600 Hz and not 35 Hz. This is because of tube resonance caused by the propagating sound waves, during the experiments. The first resonance frequency of the tube vibrations was observed to be around 600 Hz (as seen from Fig. 4.24). Hence the low-frequency cut-off for our plane wave tube is 600 Hz.

b) *Speaker/compression Driver*. The radiation characteristics of the speaker will determine the magnitude and frequency range over which the sensor can be calibrated in the PWT. The wall shear stress in the tube is proportional to the velocity and the square root of the frequency. The velocity of the particles is proportional to the pressure and hence the SPL in the tube. For our experiments, the shear stress range was designed to be 0.01 Pa - 3 Pa and the frequency range was designed to be 100 Hz - 10 kHz. For this magnitude and frequency range, the desired SPL was found to be in the range of 130 db to 150 db [112]. Hence a 2-inch compression driver (JBL 2446J) was chosen, since it can generate SPL's between 130 db and 150 db and in the frequency range of 500 Hz to 10 kHz.

c) *End-termination*. The end-termination must be designed to absorb all the sound waves incident on it. Improper termination results in partial reflection of the incident wave, thereby setting-up a standing wave in the tube. A combination of standing and traveling waves in the PWT complicates the analytical relationships (described in section 4.8.1 and 4.8.2) between the pressure, velocity,

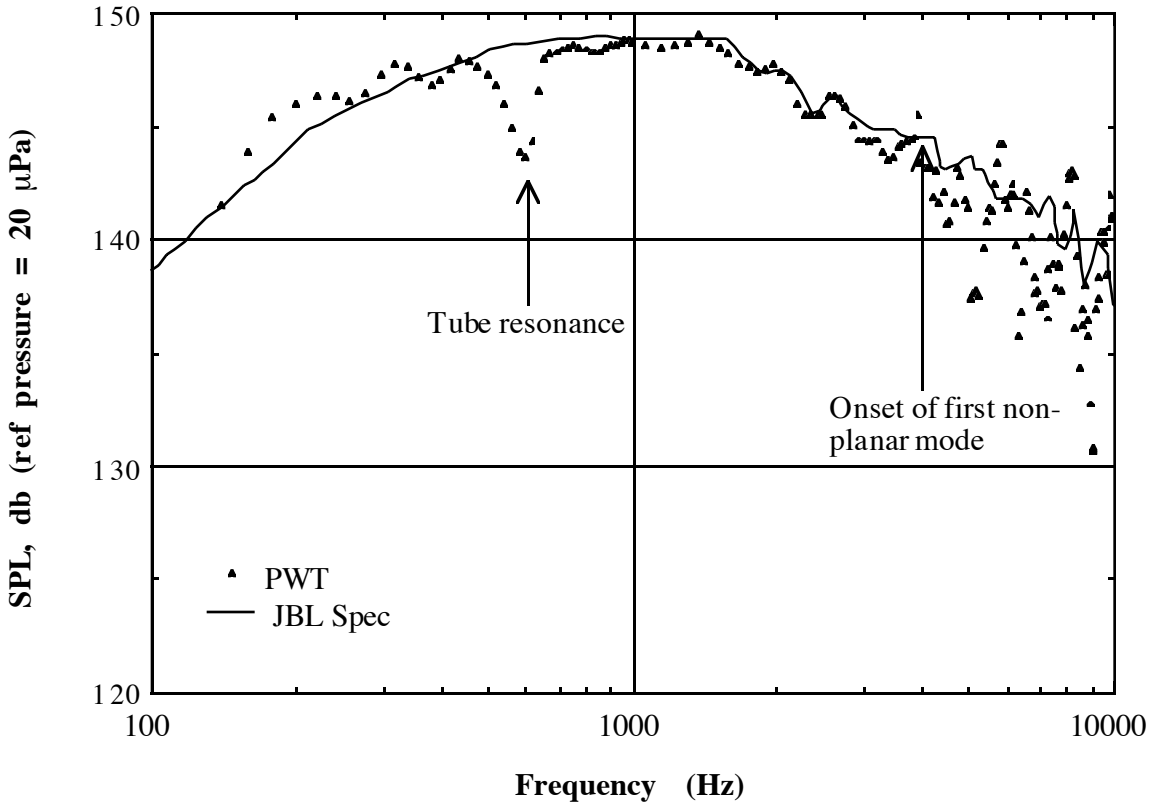

Fig. 4.24 Plot showing a comparison of the response of the plane wave tube and the manufacturers' calibration curve for the JBL speaker

shear stress and frequency and hence is not desirable. For our experiments we used a wedge-shaped insert filled with glass fibers. This has been shown to be able to absorb sound waves effectively [113].

d) *Microphone*. All pressure measurements in the tube were taken via a Brüel & Kjær (B&K) 4138 1/8" condenser microphone in conjunction with a B&K 2804 microphone power supply, a B&K 2639 preamplifier and a UA 0036 adaptor. The B&K 4231 sound level calibrator (with DP 0774 adaptor) was used for the microphone calibration.

4.10.4 Measurements in the PWT

The following three experiments were conducted to characterize the response of the sensor in the PWT: i) characterization of the PWT itself; ii) measurement of the output of the shear-stress sensor as a function of the frequency; and iii) measured transfer function of the sensor.

4.10.4.1 Characterization of the PWT

The first test was to characterize the performance of our plane wave tube. The speaker output was adjusted to a SPL of 150 db. The fluctuating pressure in the tube was measured using the B&K microphone, for different drive frequencies of the speaker. Figure 4.24 shows the output of the microphone (in decibels) plotted as a function of the frequency (the raw voltage output of the microphone is converted to a pressure using the sensitivity of the microphone and the pressure is then converted to a *db* value using equation (4.19)). The manufacturers' calibration curve for the JBL speaker [111] is also superimposed in Fig. 4.24. Our measurement shows a "spike" in the microphone output at 600 Hz. We believe that this corresponds to the first resonance frequency for the tube vibration. The first non-planar mode appears at 4 kHz, as described in the previous section. Hence the PWT data shown in Fig. 4.24, is accurate only upto 4 kHz. It can be seen that there is good agreement between the measured data and the manufacturers' curve for the speaker in the frequency range of 600 Hz - 4 kHz.

4.10.4.2 Oscillating Shear-Stress Measurement

Figure 4.25 shows the raw differential voltage output from the 500 μm sensor plotted as function of the frequency. As per equation (4.23) the shear stress varies with frequency as $\tau_w \sim \omega^{1/2}$. It can be seen from Fig. 4.25 that the sensor shows a $\omega^{1/2}$ dependence to 10 kHz, even though the analytical relationship (equation (4.23)) is valid only to 4 kHz.

The sensor output in the rotated position (the tethers parallel to the flow) was lower than in the original position by two orders of magnitude and did not show a $\omega^{1/2}$ dependence. The above two observations confirm that the sensor was accurately tracking the oscillating shear-stress input that was imposed on it.

4.10.4.3 Transfer Function of the Sensor

The transfer function is defined as the ratio of the shear stress measured by the sensor to the shear stress that is imposed on it (this is estimated from the microphone pressure measurement and equation (4.23)). Figure 4.26 shows the transfer function of a 500 μm sensor plotted as a function of the frequency. For an ideal dynamical system, the transfer function should be flat at zero db. For our sensor we observe a deviation of a few decibels (from zero) in the frequency range of 600 Hz - 4 kHz. We believe that the main factor responsible for this is the loss of some of the input energy due to tube vibration and due to viscous effects. Both these result in a lower measured pressure by the microphone and hence a positive decibel value for the transfer function.

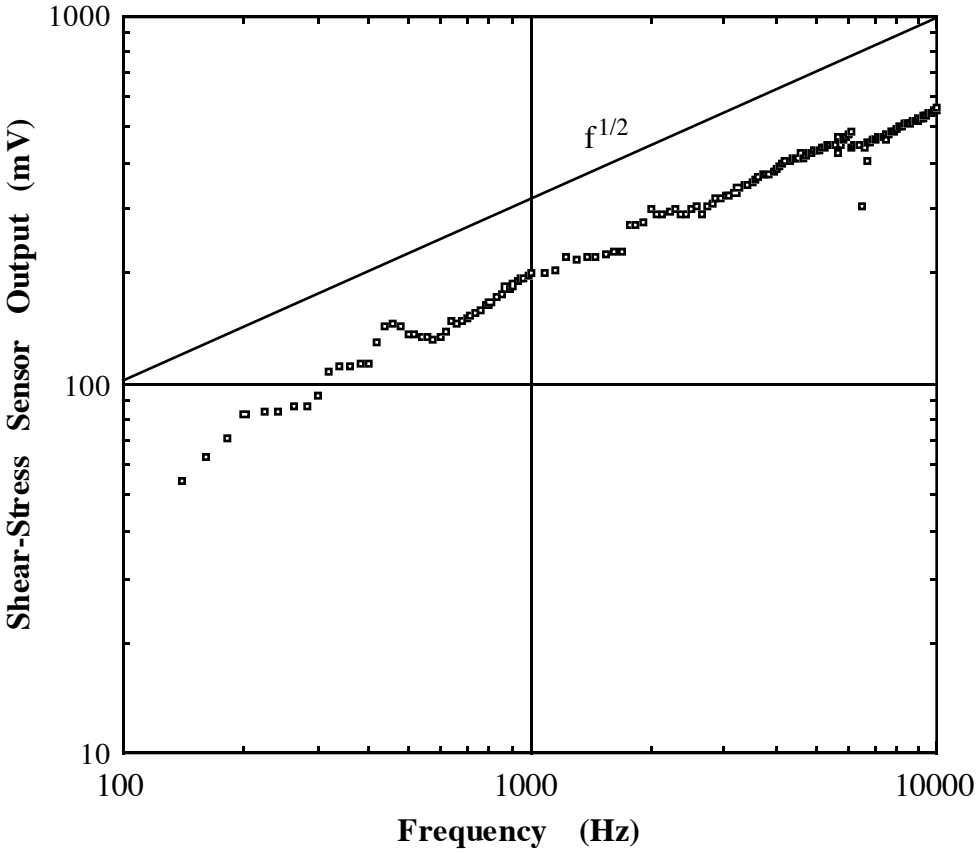

Fig. 4.25 Response of the 500 μm sensor to oscillating shear-stress inputs at different frequencies. The output shows a square-root of frequency dependence, as predicted by the analytical relationship

4.11 Calibration in a Turbulent Boundary Layer - Stochastic Calibration

In order to make measurements in a turbulent boundary layer, the sensor needs to be first calibrated in the turbulent environment. This can be accomplished by performing a stochastic calibration in a turbulent flow field. If the sensor response is linear over the complete calibration range, there is no need to perform a stochastic calibration for that sensor. This calibration technique is generally employed for devices with a non-linear response (ex: hot wires). This sub-section briefly outlines the calibration procedure. A more detailed description of the stochastic calibration method can be found in [4.22].

The time-dependent wall shear stress $\tau_w(t)$ in a turbulent boundary layer can be written as a function of the sensor output voltage V as:

$$\tau_w(t) = C_0 + C_1 V + C_2 V^2 + ... + C_N V^N \tag{4.24}$$

where C_i's are the calibration coefficients and N is the order of the calibration polynomial. At any instant (in a turbulent flow) both $\tau_w(t)$ and V can be written as a sum of a mean and fluctuating

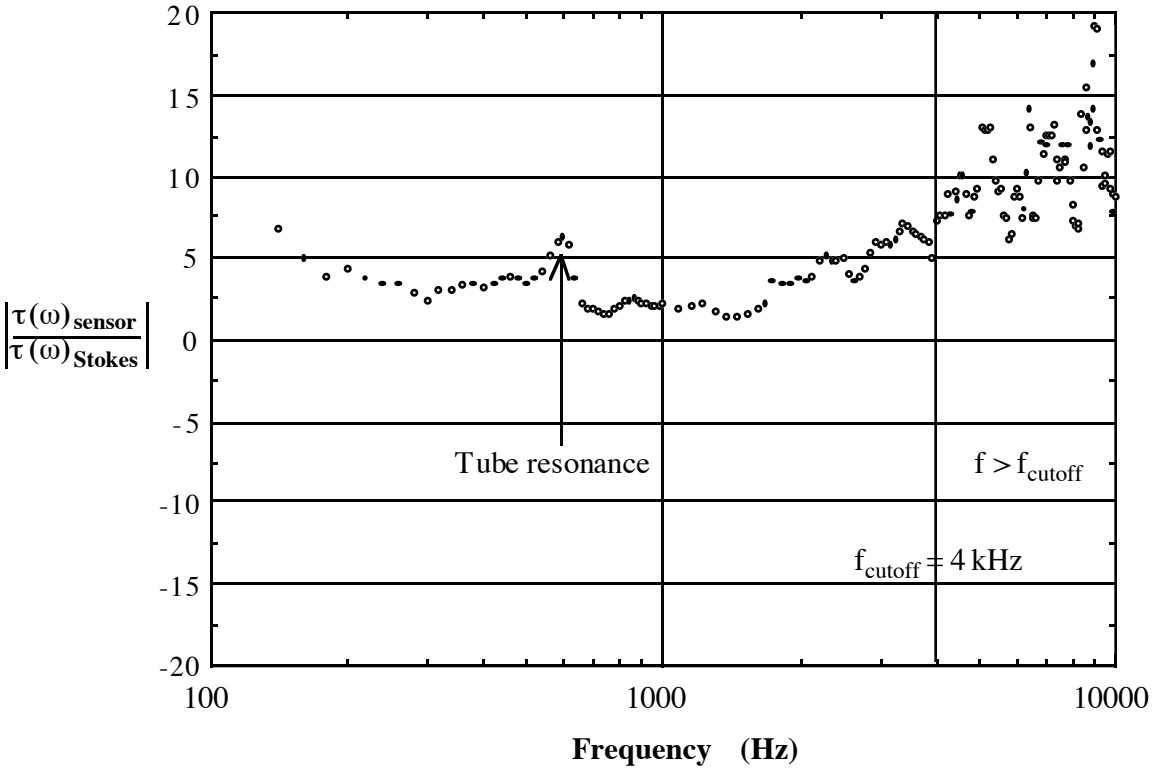

Fig. 4.26 Transfer function of the 500 μm sensor, as measured in the PWT

quantity. It must be noted that equation (4.24) assumes that the sensor transfer function (output voltage/wall shear stress) is flat over the range of frequencies over which the calibration is being performed. This is a good assumption for the sensors presented in this thesis, which have a high operating bandwidth.

Substituting for $\tau_w = \overline{\tau_w} + \tau_w'$ and $V = \bar{V} + V'$ in equation (4.24) we get

$$\overline{\tau_w} + \tau_w' = C_0 + C_1(V+V') + C_2(V+V')^2 + .. + C_N(V+V')^N \tag{4.25}$$

By averaging (time averaging) equation (4.25) we get

$$\overline{\tau_w} = \{C_0 + C_1\bar{V} + C_2\bar{V}^2 + ..\} + .. + \{C_2\overline{V'^2} + 3C_3\bar{V}\,\overline{V'^2} + ..\}\,. \tag{4.26}$$

It can be seen from equation (4.26) that at each calibration point both the average voltage $\bar{V}$ and the higher order statistics $\overline{V'^2}$ & $\overline{V'^3}$ need to be measured. In making measurements of $\bar{V}$, $\overline{V'^2}$ & $\overline{V'^3}$ care must be taken to ensure that all the statistics are fully converged for the calibration to be

accurate. The statistics for $\overline{V'^2}$converge slower than $\bar{v}$, and for $\overline{V'^3}$ slower than $\overline{V'^2}$, and so on. Hence longer averaging times must be used for higher order statistics.

It must be noted that if the sensor response is linear, there is no need to perform an elaborate stochastic calibration. This is because equation (4.26) then reduces to

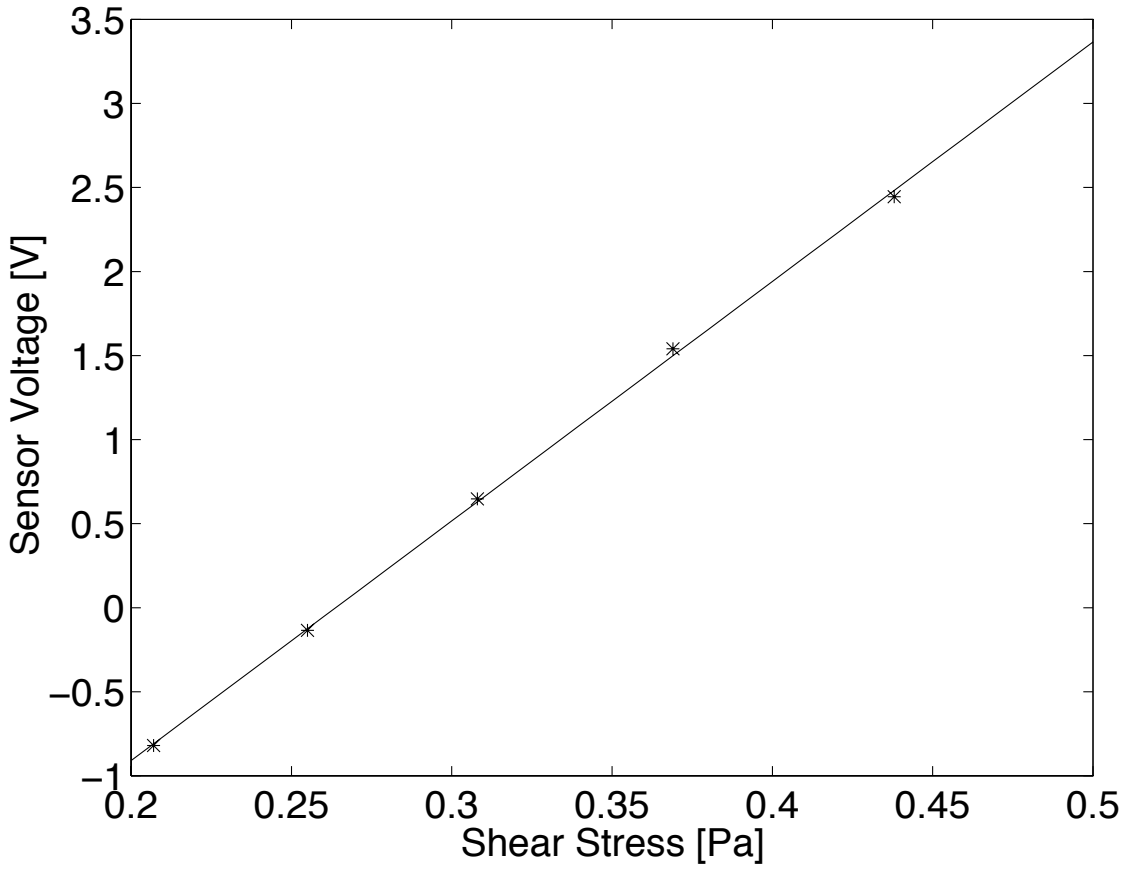

Fig. 4.27 Sensor response in a turbulent boundary layer. The freestream velocity range for this experiment was 8 m/s - 12 m/s. The value of $Re_\theta = 1500$ at 10 m/s. The shear stress was measured using a Preston tube

$$\overline{\tau_w} = C_0 + C_1 \bar{V} . \tag{4.27}$$

Hence at each calibration point only the mean shear stress and the mean output voltage need to be recorded.

The 500 μm x 500 μm sensor was calibrated (stochastically) over a velocity range of $8\ m/s \le u_\infty \le 12\ m/s$ in a turbulent boundary layer. The voltage output from the sensor is plotted as a function of the wall shear stress in Fig. 4.27 (The shear stress at different flow velocities was measured using a Preston tube). It can be seen that, even though not assumed, the sensor response

is linear over the complete velocity range and hence there is no need to perform a stochastic calibration for this sensor in the future.

4.12 Electrical Functionality (Second-Generation Sensors)

The sensors exhibited ideality factors in the range of 1-1.05, reverse breakdown voltages of 45 V and reverse saturation currents in the range 40 - 100 pA. All the measured values are similar to those obtained with the first generation sensors (section 4.1).This was expected since all the fabrication parameters for the photodiodes were identical for the two generations.

4.13 Light-Response Tests (Second-Generation Sensors)

The sensors exhibited performance characteristics similar to the first generation sensors, i.e., the response of the two photodiodes were well matched when subjected to illumination from a DC source.

Another test that was performed with the second-generation sensors was to evaluate the performance of the three-photodiode scheme in minimizing the sensitivity to intensity variations. As described in section 2.5.3 of the sensor design chapter, the output of the first generation sensors was very sensitive to the alignment of the laser spot relative to the two photodiodes. This was due to a non-uniform intensity distribution across the laser spot. The sensitivity of the sensor to variations in light intensity can be considerably reduced by either normalizing the photocurrent of the diodes against the output of a reference diode or by using a three-photodiode scheme (as described in section 2.10.1 of the sensor design chapter).

The laser spot (with non-uniform intensity) was scanned across the floating-element and the differential voltage normalized by the average voltage, $\Delta V/V$ was recorded for both the two-photodiode and three-photodiode sensors. Figure 4.28 shows the $\Delta V/V$ outputs (with no flow) for the two devices, as a function of the laser spot position. The two features to be noted from this figure are: i) the value of $\Delta V/V$ for the three-photodiode devices is lower at all spot positions. This implies that the new scheme is less sensitive to variations in light intensity. The new scheme showed 94% (average) reduction in sensitivity to variations in the light intensity (this was estimated by calculating the difference between the $\Delta V/V$ for the two schemes and normalizing by the original $\Delta V/V$). This is in agreement with the theoretical value predicted by the model described in Appendix C; ii) the "sweet-spot," i.e., region where $\Delta V/V = 0$ is much larger for the three-photodiode devices. This makes the task of aligning the spot relative to the floating-element much easier. It can be seen that the value of $\Delta V/V$ is non-zero at several spot positions even with the

three-photodiode scheme. We believe that this is due to the presence of non-linear gradients in intensity across the spot, which are not nulled out by this scheme.

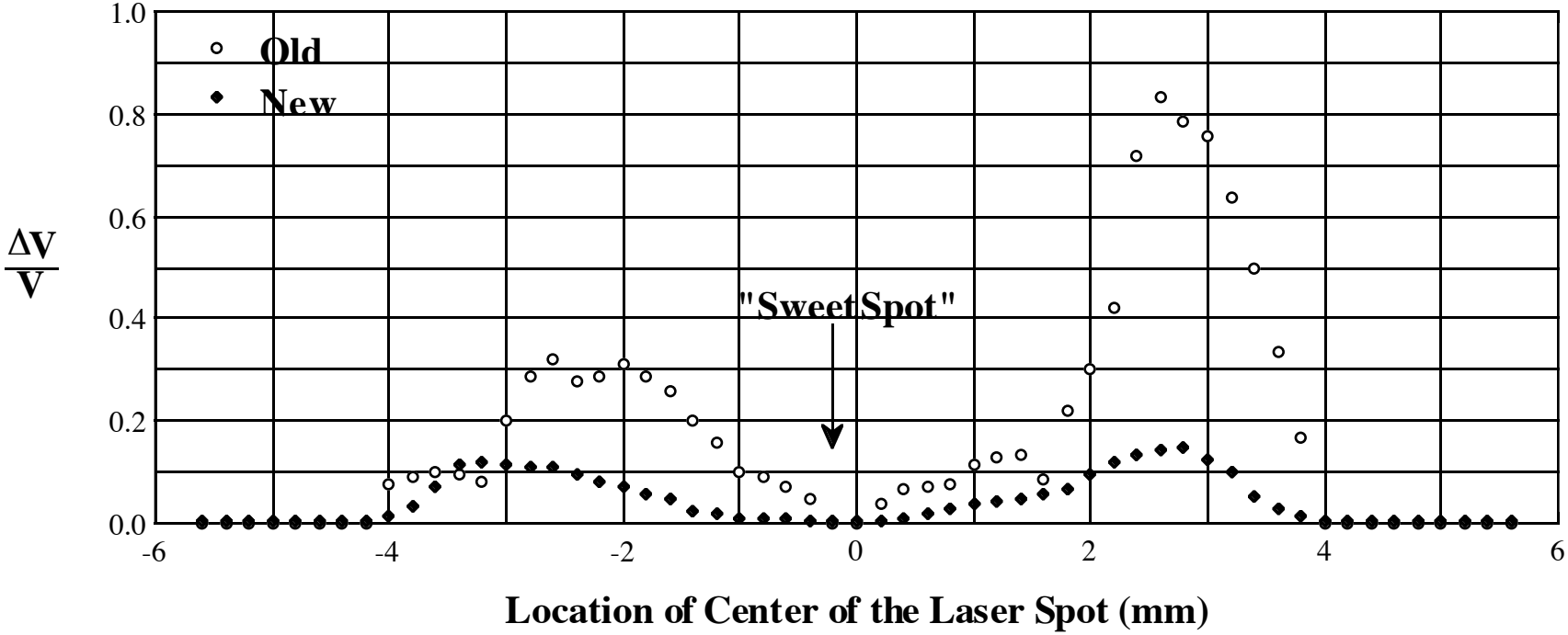

Fig. 4.28 Reponse of the old sensor (two-photodiode scheme) and the new sensor (three-photodiode scheme) as the laser spot is scanned across the floating element. The new sensor has a bigger sweet-spot compared to the old sensor.

4.14 Calibration of Sensor Arrays in Laminar-Calibration Flow Cell

The sensor arrays were packaged and calibrated in the laminar-calibration flow cell. The array was mounted such that the tethers were perpendicular to the flow direction. Such an array configuration provides the spanwise distribution of the streamwise shear stress. The response of each of the sensors was recorded as the shear stress in the flow cell was ramped-up from 0 to 1 Pa in steps of approximately 0.1 Pa. This experiment was performed at a channel height of 508 μm and maximum Reynolds number (based on the channel height) of 369. The pressure distribution in the channel was confirmed to be linear for the entire calibration range. The sensor arrays were tested with the new laser source, which was manufactured to have a uniform intensity distribution across the spot.

Figure 4.29 shows the response of the sensors in the 120 μm array. It can be seen that the sensors exhibit very similar sensitivities. This was expected since in a two-dimensional laminar channel flow there is no spanwise variation of the streamwise shear stress. The response is linear with a measured sensitivity of 0.097%/Pa. This compares well with the theoretical sensitivity of 0.102 %/Pa. The bond pads on one of the sensors' broke during wire bonding, and hence the data shows the output from seven (as opposed to eight) sensors.

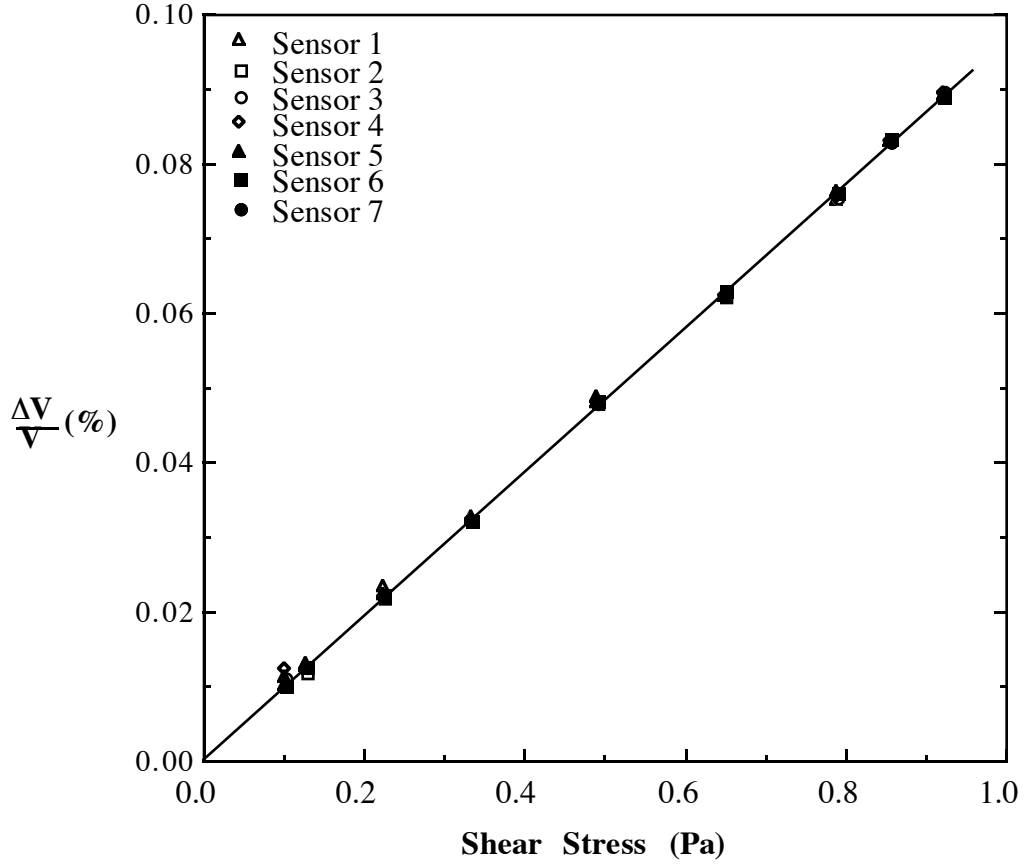

Fig. 4.29 Response of a 120 μm sensor array in a laminar channel flow

Chapter 5. CONCLUSIONS

The goal of this thesis was to design, fabricate and test a micromachined shear-stress sensor for operation in a low-speed turbulent boundary layer. There have been various accomplishments that have resulted from this research effort. We highlight the significant accomplishments in this chapter. The contributions of this work can be categorized into the following topics: development of a new transduction scheme based on optical position-sensing with integrated photodiodes, design of a readout scheme, design and development of a robust fabrication process, static-calibration of the sensors over five orders of wall shear stress, dynamic-calibration of the sensors upto 10 kHz, measurements in a laminar and turbulent boundary layer, design of an improved sensing scheme for the second-generation sensors, design and fabrication of sensor arrays and static-calibrations of sensor arrays. In the following sections we summarize the results and contributions in each of these areas.

New Transduction Scheme and Readout

Measurements of low-magnitude shear-stress (such as in low-speed turbulent boundary layers) require extremely high sensitivity to detect the small forces (O(nN)) and correspondingly small displacements (O(Å)). In addition, unsteady measurements in turbulent boundary layers require sensors with high operating bandwidth (~ 20 kHz). These requirements render most of the existing sensors inadequate for this application. In response to the limitations of the existing devices, we have developed a floating-element sensor based on a new transduction scheme (optical position-sensing by integrated photodiodes). The floating-element structure was designed to be compliant enough to detect the low-magnitude shear forces and at the same time have a large resonance frequency for lateral motions (and hence large operating bandwidth). A set of analytical expressions were developed to predict the static and dynamic response characteristics of the sensor. The new design was found to have the desired sensitivity and bandwidth to make measurements of mean and fluctuating wall shear stresses in a turbulent boundary layer. A summary of the features of the new sensors are:

- low-impedance device;
- mechanically robust structure;
- differential sensing results in twice the sensitivity and allows for common-mode signal rejection;
- the output ($\Delta V/V$) is insensitive to variations in light intensity (to first order).

The readout scheme was designed to allow for the off-chip measurements of the output signal from the sensor. In addition, the frontside electrical readout from the sensor chip had to be designed to minimize the flow perturbation and also keep the magnitude of the photodiode leakage

current to a minimum. The differential photodiode sensing scheme developed in this thesis can be applied to a broader range of sensors, in applications that require the measurement of small displacements of a proof-mass.

Fabrication Process

Although the fabrication process was an extension of a process that had been previously developed at MIT [85], the actual fabrication scheme and the resulting photodiode quality were different. We had to redesign the existing fabrication process to allow for the integration of photodiodes. The fabricated photodiodes exhibited excellent behavior, with ideality factors of unity in the forward direction and reverse breakdown voltages of 45V. It is perhaps the first time a photodiode of such a quality has been fabricated using a wafer-bonding process. This new process has utility in a wide variety of sensors beyond the shear-stress sensor.

Static Calibrations

The sensors were packaged and calibrated in a laminar flow environment. The calibration procedure depended on the ability to generate wall shear stresses of known magnitude in a repeatable manner. This was accomplished by testing the sensor in a custom-designed laminar-calibration flow cell. By adjusting the inlet pressure of air (and by maintaining the outlet at atmospheric pressure) shear stresses of different magnitudes were generated. The wall shear stress in the flow cell (under laminar flow conditions) is known from a measurement of the pressure drop along the length of the channel. The individual floating-element sensors have been calibrated in the laminar flow cell over a range of four orders of wall shear stress. The sensors have demonstrated a linear response over four orders of wall shear stress (0.003 Pa - 10 Pa). The lowest measured shear stress of 0.003 Pa is three orders of magnitude lower than that has been measured before using micromachined sensors [28]. The maximum observed non-linearity was 1% or better over the four orders of wall shear stress. In addition, the sensors have demonstrated excellent repeatability, long-term stability and minimal drift. We have tested one of the 500 μm floating-element sensors' several times over a period of a year and half. The response of the sensor was found to be identical for each calibration-cycle during that period.

Dynamic Calibrations

The dynamic response of the sensor has also been experimentally verified to 10 kHz. This is the first time that the dynamic response of a micromachined shear-stress sensor has been experimentally verified using a direct method. The dynamic response of the sensor was obtained by providing the sensor system with an oscillating shear-stress input and observing the output. An oscillating shear stress of known magnitude and frequency was generated via acoustic plane wave

excitation, in a custom-designed plane wave tube (PWT). In this technique, the pressure of a plane acoustic wave is directly related to the wall shear stress by the analytical solution to the fluid mechanics problem of pipe-flow driven by an oscillating pressure gradient. The measured fluctuating shear stress showed a $\omega^{1/2}$ dependence, as predicted by the analytical relationship. The sensors demonstrated the square-root of frequency dependence to 10 kHz even though the analytical relationship is valid only to 4 kHz. The limits on the lowest and highest frequency to which the sensor can be dynamically tested are set by the PWT design. The present PWT set-up needs to be modified to allow for calibrations over a wider range of frequencies.

The dynamic test results presented in this thesis show that the sensor can track an oscillating shear stress to 10 kHz. The effect of non-linearities introduced into the system due to the non-linear speaker dynamics (at high operating sound pressure levels) is currently being investigated.

Wind Tunnel Measurements

The sensors have been tested in both laminar and turbulent boundary layers in the low-speed, low-turbulence wind tunnel at MIT. The sensor plug was mounted on a circular port, which was in turn mounted on the wall of the wind tunnel. The laser source was mounted on the opposite wall of the tunnel. The response of the sensor in a laminar boundary layer was found to be linear and the sensor demonstrated the same sensitivity as measured in the laminar-calibration flow cell. The sensor was able to transduce shear stresses of 0.01 Pa and lower, in the laminar boundary layer. The sensors were also calibrated in a turbulent boundary layer over a velocity range of $8\ m/s \le u_\infty \le 12\ m/s$. The sensor response was observed to be linear over the entire velocity range (the shear stress at different velocities was measured using a Preston tube).

One of the issues associated with using the floating-element sensors in a wind tunnel environment, is the measurement errors caused due to the acceleration sensitivity of the devices. This problem can be overcome by making an independent acceleration measurement and adjusting the sensor output voltage to compensate for this (using the data acquisition software).

Design-Improvements in the Second-Generation Sensors

The first-generation devices employed a two-photodiode differential sensing scheme. This scheme was found to be sensitive to non-uniformities in the incident illumination. To overcome this, a new three-photodiode design was developed for the second-generation sensors. The new scheme was designed to null out any linear gradients in the intensity. The new design has been tested and has demonstrated 94% reduction in sensitivity to intensity variations when compared to the earlier design.

Sensor Arrays

The new photodiode design was implemented in the fabrication (using the same process used for the first-generation sensors) of one-dimensional arrays of sensors. The one-dimensional array is comprised of eight floating-element sensors. The array chip was packaged in a custom-made PC-board type package. The package was designed such that the electrical output from the sensor could be directly interfaced with a computer for data acquisition. The sensor arrays were tested in the laminar-calibration flow cell (flow direction perpendicular to the tethers). Under such a flow condition the shear stress imposed on each of the sensors is identical. The sensors exhibited a linear response with identical sensitivities.

The summary of this work is that we have developed a microfabricated shear-stress sensor for turbulent boundary layer research. The sensors have been statically/dynamically tested and have shown to meet the requirements for operation in low-speed turbulent boundary layers. The next stage is to use the individual floating-element sensors to make measurements of fluctuating shear stresses and to measure the spectra of the wall shear in a turbulent boundary layer. In addition, the one-dimensional sensor arrays can be used to obtain cross-correlation measurements in turbulent flows. Such measurements can be used to obtain estimates of the spanwise spacing and streamwise orientation of the coherent structures, thereby providing new insights into the structure of turbulent boundary layers.

The optical shear stress sensor described in this thesis is useful for sensing applications in wall-bounded flows where the laser source can be mounted on a wall opposite to the sensor. In applications involving external flows, this sensor can used to precisely calibrate other devices which can operate in such a flow environment. In future designs it is possible to modify the present scheme to allow for the measurement of shear stresses in two dimensions by the same floating-element structure and to fabricate two-dimensional sensor arrays. Ultimately, one could hope to incorporate such sensor arrays in a system of microfabricated sensors and actuators to perform the task of active control in turbulent boundary layers.

Appendix A
SUPREM Simulations and Spreading Resistance Analysis

The SUPREM input files for the handle and device wafer simulations are given below. The simulation output showing the calculated values (and plots) of the different parameters, follows the input files.

A.1 Handle Wafer Simulation

```
*************************************************************
***                  TMA SUPREM-3 (TM)                    ***
***                    Version 6.1.1                      ***
***              System F (DEC ALPHA: OSF/1)              ***
***              Copyright (C) 1985-1994                  ***
***          Technology Modeling Associates, Inc.         ***
***              All Rights Reserved                      ***
*************************************************************

                    30-Dec-96 21:01:29
Statements input from file /amd/robeson/a/aravind/supreme/handle_old_final.inp

  1... TITLE Handle wafer simulation
  2...  INITIALIZE SILICON <100> THICKNES=7.0  X.LOCAT=0.0  Z.LOCAT=0.0
DX=.001 +
  ...  MIN.DX=0.001 XDX=0.0 SPACES=200 RESISTIV BORON=15
  3... $ grow sro in trenches
  4... DIFFUSION TEMPERAT=950 TIME=10 INERT
  5... DIFFUSION TEMPERAT=950 TIME=128.5 DRYO2
  6... DIFFUSION TEMPERAT=950 TIME=30 INERT
  7... PRINT     LAYERS
  8... $ blanket boron implant
  9... IMPLANT   BORON PEARSON RP.EFF DOSE=0.8e12 ENERGY=70
 10... $ photodiode implant
 11... IMPLANT   PHOSPHOR PEARSON RP.EFF DOSE=5.0e15 ENERGY=90
 12... $ LTO densification
 13... DIFFUSION TEMPERAT=900 TIME=30 INERT
 14... DIFFUSION TEMPERAT=1000 TIME=60 INERT
 15... DIFFUSION TEMPERAT=900 TIME=60 INERT
 16... $ wafer bonding
 17... DIFFUSION TEMPERAT=1100 TIME=70 INERT
 18... $ sro on device wafer before n+ implant
 19... DIFFUSION TEMPERAT=950 TIME=10 INERT
 20... DIFFUSION TEMPERAT=950 TIME=128.5 INERT
 21... DIFFUSION TEMPERAT=950 TIME=30 INERT
 22... $ device wafer n+ drive-in
 23... $ DIFFUSION TEMPERAT=1150 TIME=400 INERT
 24... DIFFUSION TEMPERAT=800 TIME=240 INERT
 25... PLOT      ACTIVE BORON TOP=1e21 COLOR=1 LINE.TYP=1
 26... PLOT      ACTIVE PHOSPHOR TOP=1e22 ADD COLOR=1 LINE.TYP=2
 27... $ get sheet resitivities
 28... ELECTRICAL STEPS=1 EXTENT=5 TEMPERAT=27 DISTRIBU
```

```
 29... END.ELECTRICAL
 30... $ PLOT      ACTIVE ARSENIC ADD COLOR=1 LINE.TYP=2
 31... STOP

Input line #   2
Coefficient data group read
File: /usr/local/tma/supreme3-6.1.1/library/s3cof0
Date: 21-Jun-94 11:39:19
Documentation from data file:

S-3 Rev 6.1 Release Version Default Coefficients
s3init,v 1.1 93/02/25 10:57:04 lynetteq Exp $

Handle wafer simulation
grow sro in trenches

Material layer information
Input line #   7

layer  material     thickness   dx      xdx  top bottom  orientation
 no.                 (um)     (um)    (um) node  node  or grain size
  2    oxide         0.0490  0.0100   0.00  798   808
  1    silicon       6.9784  0.0010   0.00  809  1000      <100>

              Integrated Dopant (#/cm**2)
layer            Net                    Sum
 no.      active      chemical      active      chemical
  2    -8.4936E+09  -8.4936E+09   8.4936E+09   8.4936E+09
  1    -6.2171E+11  -6.2171E+11   6.2171E+11   6.2171E+11
 sum   -6.3020E+11  -6.3020E+11   6.3020E+11   6.3020E+11

              Integrated Dopant (#/cm**2)
layer            boron
 no.      active      chemical
  2     8.4936E+09   8.4936E+09
  1     6.2171E+11   6.2171E+11
 sum    6.3020E+11   6.3020E+11

            Boundary Locations and Integrated Dopant
            Concentrations for Each Diffused Region
layer  region  type      top       bottom        net           sum
 no.     no.           depth       depth     active Qd     chemical Qd
                      (um)        (um)      (#/cm**2)     (#/cm**2)
  2       1      p     0.0000     0.0490    8.4936E+09    8.4936E+09
  1       1      p     0.0000     6.9784    6.2171E+11    6.2171E+11

Handle wafer simulation
get sheet resitivities

Electrical information
Input line #  29

layer region type  Conductor Bias  Electron Bias   Hole Bias
 no.    no.          (volts)        (volts)       (volts)
```

1	2	n	0.0000E+00	0.0000E+00
1	1	p	0.0000E+00	0.0000E+00

Electron Charge, Conductance, and Resistance

layer no.	region no.	type	Electron Charge (#/cm**2)	Sheet Conductance (1/(ohm/sq))	Sheet Resistance (ohm/sq)	Vertical Conductance (mho/cm**2)	Vertical Resistance (ohm-cm**2)
1	2	n	4.578E+15	5.6746E-02	1.7623E+01	4.0765E+02	2.4531E-03
1	1	p	1.137E+07	2.4395E-09	4.0992E+08	0.0000E+00	

Hole Charge, Conductance, and Resistance

layer no.	region no.	type	Hole Charge (#/cm**2)	Sheet Conductance (1/(ohm/sq))	Sheet Resistance (ohm/sq)	Vertical Conductance (mho/cm**2)	Vertical Resistance (ohm-cm**2)
1	2	n	1.099E+02	7.9095E-15	1.2643E+14	0.0000E+00	
1	1	p	8.017E+11	6.0064E-05	1.6649E+04	1.3742E-03	7.2771E+02

*** END SUPREM-3 ***
TOTAL CPU TIME = 0.03 minutes

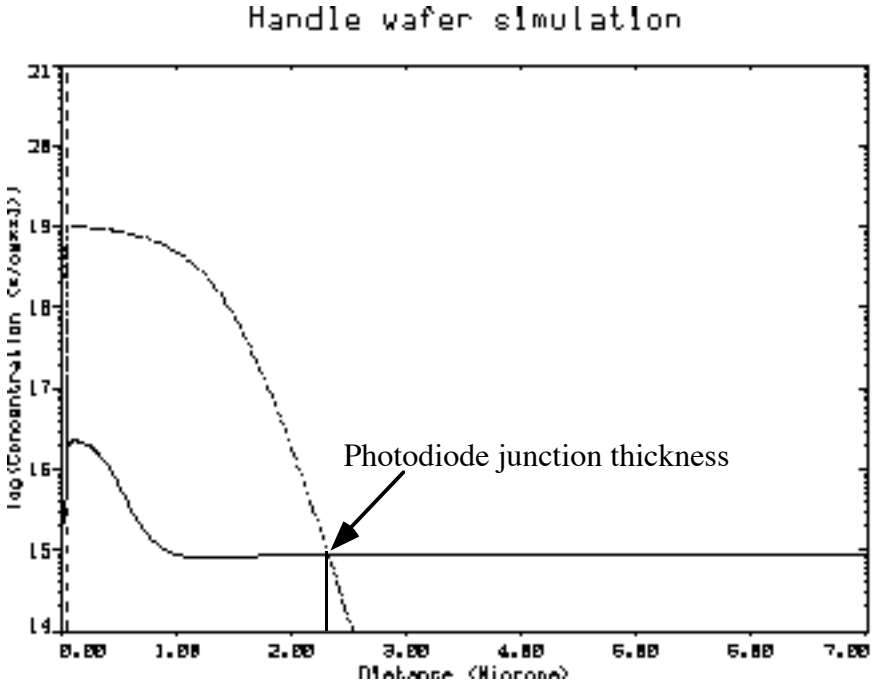

Fig. A1 Carrier concentration versus depth for the handle wafer after all the thermal steps. It can be seen that the estimated junction depth is 2.2 μm and the surface concentration of phosphorus is 1 x 10^{19} cm^{-3}.

A.2 Device Wafer Simulation

```
          ******************************************************
          ***              TMA SUPREM-3 (TM)                 ***
          ***                Version 6.1.1                   ***
          ***           System F (DEC ALPHA: OSF/1)          ***
          ***             Copyright (C) 1985-1994            ***
          ***        Technology Modeling Associates, Inc.    ***
          ***              All Rights Reserved               ***
          ******************************************************
                                14-Jul-96 19:48:54
Statements input from file /amd/robeson/a/aravind/supreme/device_old_final.inp

  1... TITLE photoshear simulation for device wafer
  2...  INITIALIZE SILICON <100> THICKNES=10  X.LOCAT=0.0  Z.LOCAT=0.0
DX=.001 +
  ...  MIN.DX=0.001 XDX=0.0 SPACES=200 CONCENTR BORON=1e15
  3... $ grow sro device wafer
  4... DIFFUSION TEMPERAT=950 TIME=10 INERT
  5... DIFFUSION TEMPERAT=950 TIME=128.5 DRYO2
  6... DIFFUSION TEMPERAT=950 TIME=30 INERT
  7... PRINT     LAYERS
  8... $ ECE junction implant
  9... IMPLANT   PHOSPHOR PEARSON RP.EFF DOSE=1.4e13 ENERGY=180
 10... DIFFUSION TEMPERAT=1150 TIME=1260 INERT
 11... $ wafer bonding
 12...  DIFFUSION TEMPERAT=1100 TIME=70 INERT
 13... $ model ECE
 14...  INVERT
 15...  ETCH      SILICON THICKNES=2.6504
 16... $ sro on device wafer before n+ implant
 17...  DIFFUSION TEMPERAT=950 TIME=10 INERT
 18...  DIFFUSION TEMPERAT=950 TIME=128.5 DRYO2
 19...  DIFFUSION TEMPERAT=950 TIME=30 INERT
 20...  IMPLANT   PHOSPHOR PEARSON RP.EFF DOSE=7e15 ENERGY=90
 21... $ device wafer n+ drive-in
 22... $ DIFFUSION TEMPERAT=1150 TIME=400 INERT
 23...  DIFFUSION TEMPERAT=800 TIME=240 INERT
 24... PLOT      ACTIVE BORON TOP=1e21 COLOR=1 LINE.TYP=1
 25... PLOT      ACTIVE PHOSPHOR ADD COLOR=1 LINE.TYP=2
 26... $  PLOT      CHEMICAL PHOSPHOR ADD COLOR=1 LINE.TYP=3
 27... PRINT     LAYERS
 28... ELECTRICAL STEPS=1 EXTENT=5 TEMPERAT=27
 29... END.ELECTRICAL
 30... STOP

 photoshear simulation for device wafer - RESULTS
 grow sro device wafer

 Material layer information
 Input line #   7
 layer  material     thickness   dx      xdx  top bottom  orientation
  no.                (um)    (um)    (um) node  node  or grain size
   2    oxide         0.0490  0.0100   0.00  798   807
   1    silicon       9.9784  0.0010   0.00  808  1000      <100>
```

Integrated Dopant (#/cm**2)

layer	Net		Sum	
no.	active	chemical	active	chemical
2	-9.3912E+09	-9.3912E+09	9.3912E+09	9.3912E+09
1	-9.8964E+11	-9.8964E+11	9.8964E+11	9.8964E+11
sum	-9.9903E+11	-9.9903E+11	9.9903E+11	9.9903E+11

Integrated Dopant (#/cm**2)

layer	boron	
no.	active	chemical
2	9.3912E+09	9.3912E+09
1	9.8964E+11	9.8964E+11
sum	9.9903E+11	9.9903E+11

Boundary Locations and Integrated Dopant Concentrations for Each Diffused Region

layer no.	region no.	type	top depth (um)	bottom depth (um)	net active Qd (#/cm**2)	sum chemical Qd (#/cm**2)
2	1	p	0.0000	0.0490	9.3912E+09	9.3912E+09
1	1	p	0.0000	9.9784	9.8964E+11	9.8964E+11

photoshear simulation for device wafer

PLOT CHEMICAL PHOSPHOR ADD COLOR=1 LINE.TYP=3

Material layer information

Input line # 27

layer no.	material	thickness (um)	dx (um)	xdx (um)	top node	bottom node	orientation or grain size
3	oxide	0.0490	0.0100	0.00	825	826	
2	silicon	7.3065	0.0010	7.31	827	990	<100>
1	oxide	0.0490	0.0100	0.05	991	1000	

Integrated Dopant (#/cm**2)

layer	Net		Sum	
no.	active	chemical	active	chemical
3	2.1403E+13	2.1403E+13	2.1416E+13	2.1416E+13
2	2.7420E+15	6.9416E+15	2.7435E+15	6.9430E+15
1	-3.5180E+09	-3.5180E+09	4.3786E+09	4.3786E+09
sum	2.7634E+15	6.9630E+15	2.7649E+15	6.9645E+15

Integrated Dopant (#/cm**2)

layer	boron		phosphorus	
no.	active	chemical	active	chemical
3	6.0673E+09	6.0673E+09	2.1409E+13	2.1409E+13
2	7.1261E+11	7.1261E+11	2.7428E+15	6.9423E+15
1	3.9483E+09	3.9483E+09	4.3026E+08	4.3026E+08
sum	7.2263E+11	7.2263E+11	2.7642E+15	6.9637E+15

Boundary Locations and Integrated Dopant Concentrations for Each Diffused Region

layer no.	region no.	type	top depth	bottom depth	net active Qd	sum chemical Qd

```
                    (um)       (um)     (#/cm**2)     (#/cm**2)
  3       1      n    0.0000     0.0490    2.1403E+13    2.1416E+13
  2       1      n    0.0000     7.3065    2.7421E+15    6.9431E+15
  1       1      p    0.0000     0.0490    3.5180E+09    4.3786E+09
1
 photoshear simulation for device wafer
 PLOT      CHEMICAL PHOSPHOR ADD COLOR=1 LINE.TYP=3

 Electrical information
 Input line #  29
Bias step   1
layer region type  Conductor Bias  Electron Bias   Hole Bias
 no.    no.          (volts)       (volts)       (volts)
  2      1     n                 0.0000E+00    0.0000E+00

              Electron Charge, Conductance, and Resistance
           Electron      Sheet       Sheet      Vertical     Vertical
 layer region type   Charge    Conductance  Resistance  Conductance  Resistance
  no.    no.        (#/cm**2)  (1/(ohm/sq))  (ohm/sq)   (mho/cm**2) (ohm-cm**2)
  2      1     n   2.742E+15   3.1306E-02  3.1943E+01   2.3975E+03  4.1710E-04

Hole Charge, Conductance, and Resistance
           Hole        Sheet       Sheet      Vertical     Vertical
 layer region type   Charge    Conductance  Resistance  Conductance  Resistance
  no.    no.        (#/cm**2)  (1/(ohm/sq))  (ohm/sq)   (mho/cm**2) (ohm-cm**2)
  2      1     n   0.000E+00   0.0000E+00              0.0000E+00
 *** END SUPREM-3 ***
 TOTAL CPU TIME =     0.03 minutes
```

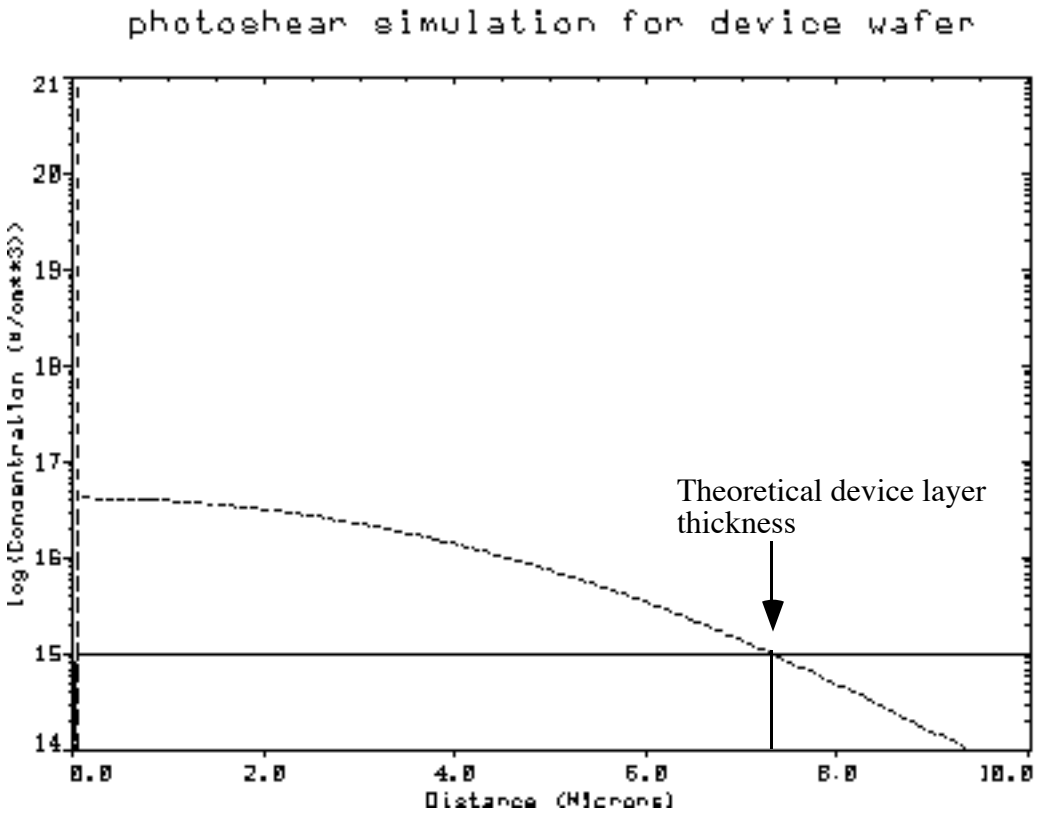

Fig. A2 Carrier concentration versus depth for the device wafer after all the thermal steps. It can be seen that the estimated device layer thickness is 7.2 μm.

A.3 Sheet Resistance Analysis (SRA)

The following figures show the dopant/carrier concentrations as *measured* on monitor wafers, using sheet resistance analysis.

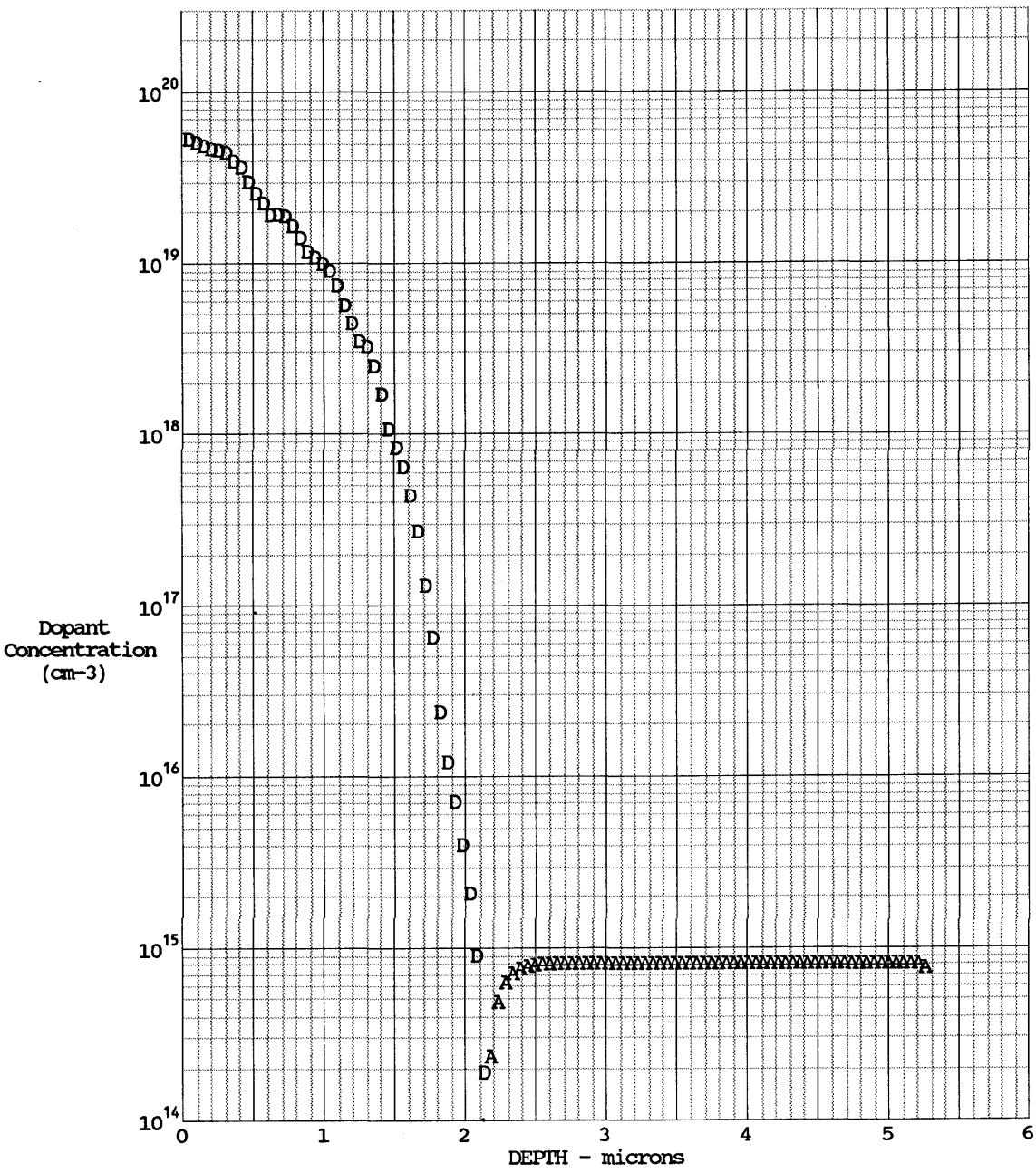

Fig. A3 Dopant concentrations versus depth for the handle wafer (after all thermal steps)

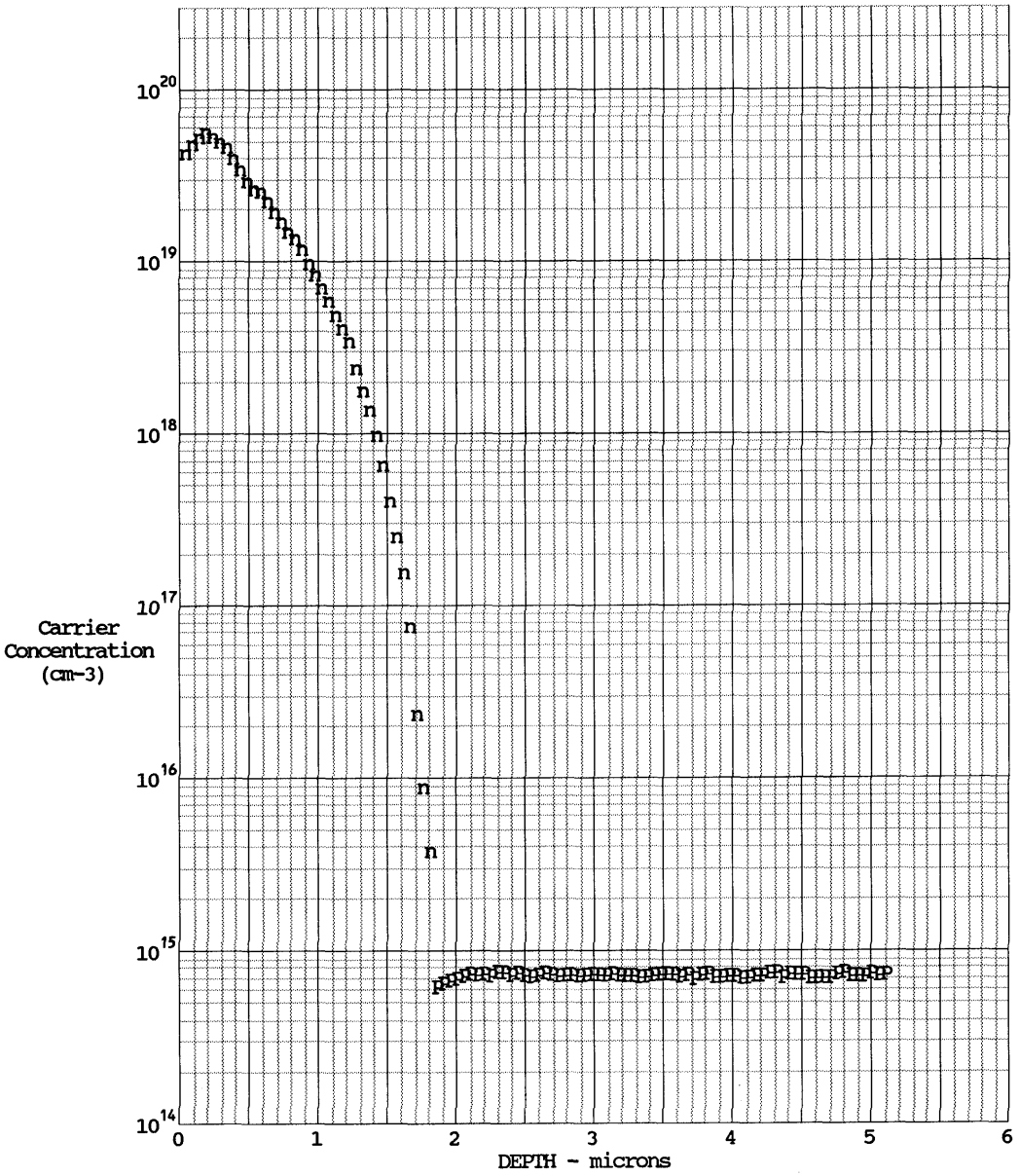

Fig. A4 Carrier concentrations versus depth for the handle wafer (after all thermal steps)

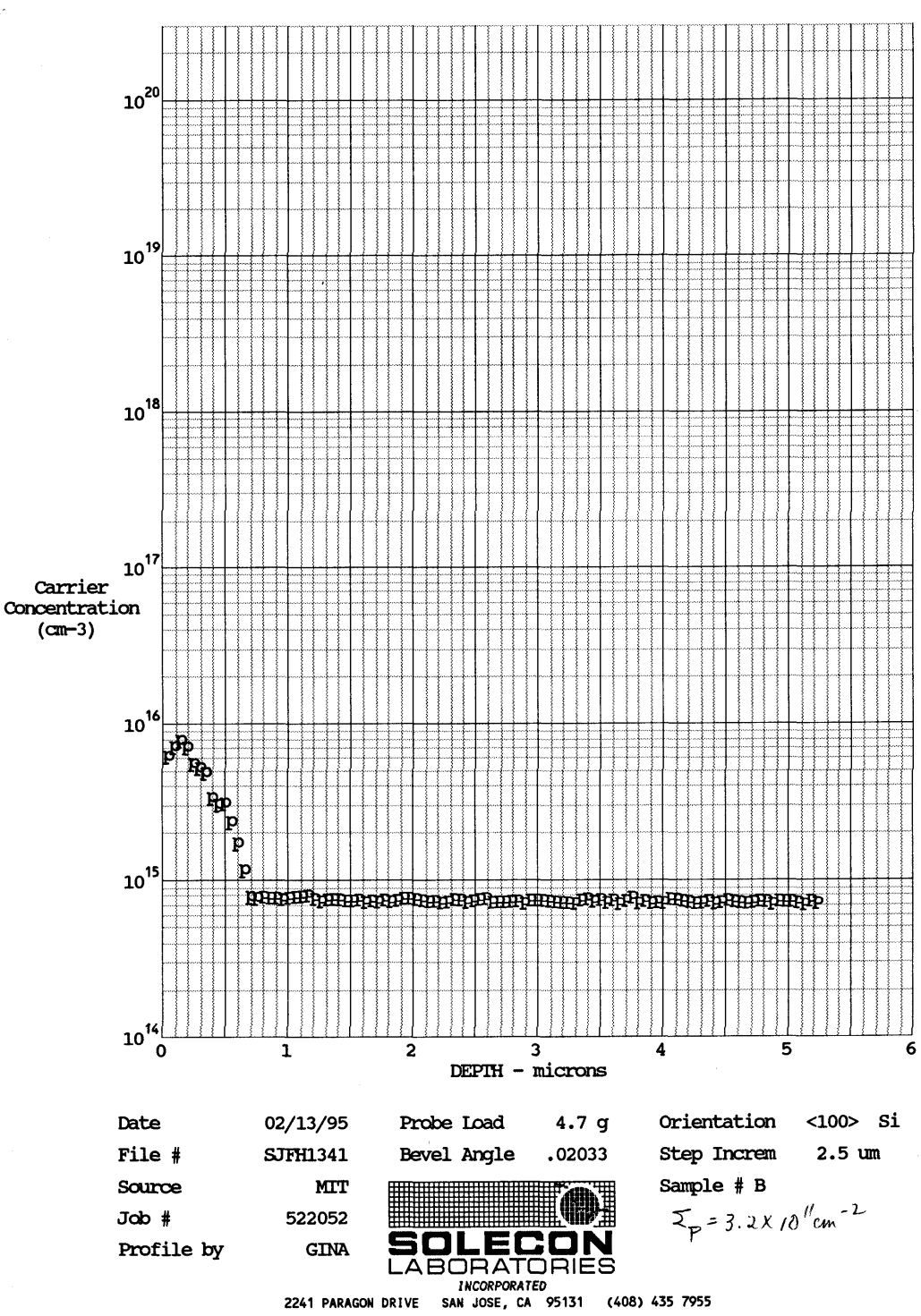

Fig. A5 Carrier concentrations versus depth for a monitor wafer which has not seen the photodiode implant step (step # 6.3 in the process traveler) and has seen all the other thermal steps. This measurement can be used to estimate the surface concentration of boron in the handle wafers, as a result of the blanket boron implant (step # 5.3).

Parameter	SUPREM (Theory)	Sheet Resistance Analysis (Measured)
Photodiode junction depth	2.2 μm	2.1 μm
Peak surface concentration of phsophorus on the handle wafer after all the thermal steps	4 x 10^{19} cm^{-3}	1 x 10^{19} cm^{-3}
Photodiode implant dose	5 x 10^{15} cm^{-2}	3.2 x 10^{15} cm^{-2}
Sheet resistance of the active region on the handle wafer after all thermal steps	17.64 Ω/square	20.5 Ω/square
Surface boron concentration on the handle wafer	9 x 10^{15} cm^{-3}	7 x 10^{15} cm^{-3}

Table A Comparison of the measured values of different parameters and the SUPREM-predicted values

A.4 Notes about SRA and SRA Results

SRA determines a resisitivity-depth profile in silicon. Using published values of carrier mobility, a majority carrier-concentration-depth profile can be calculated. Going one step further, a dopant profile can be calculated by accounting for the space-charge redistribution under the bevel used for the spreading resistance profile. Poisson's equation is solved iteratively, subject to boundary conditions consistent with the carrier concentration profile.

Figure A3 shows a plot of $|N_A \pm N_D|$ versus the depth into the wafer and uses the symbol *A* where the difference is positive and *D* where it is negative. The photodiode junction depth estimated from Fig. A3 is 2.1 μm, which compares well with the value of 2.2 μm predicted by the SUPREM simulations. The peak surface concentration of phosphorus is measured to be 1 x 10^{19} cm^{-3}. This is lower than the SUPREM predicted value of 4 x 10^{19} cm^{-3}, due to the loss of dopant atoms in the oxide layer (due to segregation). The measured dose (due to the photodiode implant) and the sheet resistance in the active region of the handle wafer have been estimated from Fig. A4 as 3.2 x $10^{15}cm^{-2}$ and 20.6 ohms/square respectively. The measured dose is lower than the specified dose of 5 x 10^{15} cm^{-2} because of the loss of dopant atoms due to segregation. Figure A4 shows the carrier concentration profile on a monitor wafer which has seen all the steps (as the real handle wafer) except for the photodiode implant (step # 6.3). The surface boron concentration as a result of step # 5.3 (on the process traveler) was measured from this wafer to be equal to 7 x 10^{15} cm^{-3}. This is about an order of magnitude higher than the surface boron concentration on the unprocessed handles wafers (~ 8 x 10^{14} cm^{-3}). The

higher surface concentration of boron helps to avoid surface-inversion and photodiode cross-talk. A complete comparison of the measured parameters and the SUPREM-predicted values is presented in Table A above.

Appendix B

Derivation of the Expression for the Sensitivity of the Sensor

First-Generation Sensors

The total current generated by a photodiode when it is subjected to incident illumination is given as

$$I_{total} = I_{leakage} + I_{photo} . \tag{B.1}$$

The diodes are designed such that the reverse leakage currents are several orders of magnitude smaller than the photocurrent and hence

$$I_{total} \simeq I_{photo} . \tag{B.2}$$

Substituting for I_{photo} from equation (2.2) we get

$$I_{photo} = \frac{J_{flux}\, q\, (1 \pm r)\, \{1 \pm e^{\pm \alpha_o w}\}}{h\, c\, /\, \lambda}\, A_{diode} . \tag{B.3}$$

This equation can be rewritten as:

$$I_{photo} = C\, A_{diode} = C\, L_{diode}\, x\, W_{diode} \tag{B.4}$$

where $C = (J_{flux}\, q\, (1 \pm r)\, \{1 \pm e^{\pm \alpha_o w}\})/(hc/\lambda)$. The exposed area of the diode can be expressed as the product of the exposed length times the exposed width, i. e., $A_{diode} = L_{diode}$ x W_{diode}. In the absence of any flow the photocurrent generated by each of the photodiodes is given by equation (B.4). This is the undeflected photocurrent. In the presence of a flow the floating-element deflects by δ and hence the exposed areas of the two photodiodes changes. For the leading-edge diode the exposed area is now given as $(W_{diode} + \delta)\, L_{diode}$ and for the trailing edge diode it is $(W_{diode} - \delta)\, L_{diode}$. Substituting these in equation (A.4) we can obtain the expressions for the deflected photocurrents for the two diodes, $I_{diode,\,1}$ and $I_{diode,\,2}$ as

$$I_{diode,\,1} = C\, (W_{diode\,e} + \delta)\, L_{diode} . \tag{B.5}$$

$$I_{diode,\,2} = C\, (W_{diode\,e} - \delta)\, L_{diode} . \tag{B.6}$$

The differential photocurrent (in the deflected position) is given as

$$\Delta I = I_{diode,\,1} - I_{diode,\,2} = 2\, C\, \delta\, L_{diode} . \tag{B.7}$$

Hence the differential deflected photocurrent normalized by the average undeflected photocurrent is obtained by dividing equation (B.7) by equation (B.4) and is given as

$$\frac{\Delta I}{I} = \frac{2\,\delta}{W_{diode}} \,. \tag{B.8}$$

The expression for the sensitivity of the sensor can be obtained by dividing both sides of equation (B.8) by τ_w

$$sensitivity = \frac{\Delta I}{I}/\tau_w = \frac{2\,\delta}{W_{diode}\tau_w} \,. \tag{B.9}$$

By calculating the value of δ for τ_w = 1 Pa, the sensitivity can be expressed as a % change in the photocurrent per Pa change in the shear stress (%/Pa).

Second-Generation Sensors

For the second-generation sensors that employ a three-photodiode scheme, the expression for sensitivity can be similarly calculated. In the three-photodiode scheme the exposed areas of each of the top and bottom diodes is half (A_{diode}) that of the middle diode ($2A_{diode}$). The top and bottom diodes are electrically connected to form photodiode #1 and the middle diode forms photodiode #2. The undeflected photocurrent for each of the diodes is again given as

$$I_{photo} = C\,A_{diode} = C\,L_{diode}\,x\,W_{diode} \,. \tag{B.4}$$

When the floating-element deflects the photocurrents for the three photodiodes are given as

$$I_{diode,\,top} = C\,(L_{diode}W_{diode} + L_{diode}\delta). \tag{B.10}$$

$$I_{diode,\,middle} = C\,(2L_{diode}W_{diode} - L_{diode}\delta). \tag{B.11}$$

$$I_{diode,\,bottom} = C\,(L_{diode}W_{diode} + L_{diode}\delta). \tag{B.12}$$

Since the top and bottom diodes are connected we get

$$I_{diode,\,1} = I_{diode,\,top} + I_{diode,\,bottom} \,. \tag{B.13}$$

$$I_{diode,2} = I_{diode,\,middle} \,. \tag{B.14}$$

The differential photocurrent (in the deflected position) is given as

$$\Delta I = I_{diode,\,1} - I_{diode,\,2} = \quad 3\,C\,L_{diode}\delta \,. \tag{B.15}$$

Hence the differential photocurrent normalized by the average undeflected photocurrent is obtained by dividing equation (B.15) by equation (B.4) and is given as

$$\frac{\Delta I}{I} = \frac{3\,\delta}{W_{diode}} \,. \tag{B.16}$$

Appendix C
Sample Calculation of the Improvement in Sensitivity Obtained using a Three-Photodiode Scheme

The intensity distribution across the spot can be approximated to be a two-dimensional Gaussian (based on the measured intensity distribution). The photocurrent obtained as a result of scanning this spot across the floating-element, can be obtained from a convolution of the Gaussian intensity distribution and the area of the photodiodes (rectangles of constant area). In this Appendix we present a sample calculation which evaluates the typical reduction in sensitivity (to intensity variations) obtained by using three-photodiode scheme instead of the two-photodiode scheme.

The intensity distribution can be approximated as follows:

$$A\, e^{\pm(x^2 + y^2)/2B} \tag{C.1}$$

where A and B are constants obtained from the measured intensity distribution across the spot. The output photocurrent (or voltage) can be obtained from a convolution integral (for each spot position) as follows:

$$Output\ Voltage = \int_{\pm y_{diode}}^{+y_{diode}} \int_{\pm x_{diode}}^{+x_{diode}} A\, e^{\pm(x^2 + y^2)/2B}\, dx\, dy \tag{C.2}$$

where $2x_{diode}$ and $2y_{diode}$ are the length and width of the photodiode, respectively.

By knowing the spot size, spot position relative to the floating-element and the measured values of A and B, the magnitude of $\Delta V/V$ at each spot position for the two schemes can be calculated. We present the results for one position of the spot, x = -0.2 mm (x = 0 mm represents a spot perfectly centered relative to the floating-element) and a spot size of 1 cm. By numerically integrating (C.2) we get $\Delta V/V = 0.09$ for the old sensor and 0.02 for the new sensor. This corresponds to reduction in sensitivity of 78 %. The observed reduction in sensitivity at this spot position was 96 %. We believe that the difference between the two numbers are due to the assumption of a perfect Gaussian function for the intensity distribution (used in this analysis).

Appendix D
Sensor Fabrication

Process Traveler

The following is a process traveler for the optical shear-stress sensor process. Processing was carried out in the Integrated Circuits Laboratory (ICL), Technology Research Laboratory (TRL), Research Group Laboratories (RGL) and MIT Lincoln Laboratories (LL).

OPTICAL SHEAR STRESS SENSOR - Process Traveler

Lot Name : Photoshear
Lot Owner : Aravind Padmanabhan (revised 05/22/96)

Wafer Notation		
H	Handle	4" p-type <100> 10-20 ohm-cm, double polished
D	Device	4" p-type <100> 10-20 ohm-cm, double polished
B	Bonded	handle and device wafers bonded front to front

Wafer	Lab	Step #	Process Description
H	TRL	1	piranha clean
H	ICL	2.1	RCA
H	ICL	2.2	grow SRO - recipe # 210, tube A1 (thickness ~ 460 Å)
H	ICL	2.3	ion implant (backside) - dopant = boron, energy = 100 KeV dose = 5e15 /cm2
H	ICL	2.4	RCA (NO HF DIP)
H	ICL	2.5	drive-in (in N_2) - recipe # 255, time= 2hr, temp= 1150C, tube B1 (total time = 5 hrs 5 mins)
H	ICL	3.1	spin photoresist on backside (1 μm, recipe # 11)

H	ICL	3.2	strip SRO (7:1 BOE) - from frontside
H	ICL	3.3	piranha strip photoresist
H	ICL	4.1	HMDS/coat photoresist on frontside (1 μm, recipe #11)
H	TRL	4.2	pattern trenches on the top surface using CM mask (Mask # 1, Dark Field Mask)
H	ICL	4.3	plasma etch silicon - recipe # 19, etcher-1 (time = 2 mins 20 secs, ~ 1.12 μm trenches)
H	ICL	4.4	piranha strip photoresist
H	ICL	5.1	RCA (only 5 sec HF dip)
H	ICL	5.2	grow SRO - recipe #210, tube A1 (thickness ~ 460 Å)
H	ICL	5.3	ion implant (blanket) - dopant = boron, energy = 70 KeV dose = 8e11 /cm2, 7 deg tilt
H	ICL	6.1	coat photoresist on frontside (2μm, recipe #7)
H	TRL	6.2	pattern diodes using CS mask (Mask #2, CS Dark field mask)
H	ICL	6.3	ion implant - dopant = phosphorus, energy = 90 KeV dose = 5e15, 7 deg tilt (photodiode implant)
H	ICL	6.4	strip photoresist (Ash once + piranha)
H	ICL	7.1	deposit LTO (2000 Å), recipe #462, Tube A7, time = 36 mins
H	ICL	7.2	LTO densification, recipe#322, Tube A3, time = 45mins (total oxide thickness after densification = 2500 Å)
H	ICL	7.3	coat photoresist on frontside (2 μm, recipe #7)
H	TRL	7.4	pattern SRO+LTO using CD mask (Mask #3, Clear field mask)
H	ICL	7.5	strip oxide (7:1 BOE) - Check for dewetting on BOTH SIDES OF THE WAFER
H	ICL	7.6	piranha strip photoresist
D	TRL	8	piranha clean

D	ICL	9.1	RCA
D	ICL	9.2	grow SRO - recipe # 210, tube = A1
D	ICL	9.3	ion implant - dopant = phosphorous, dose = 1.4e13/cm2 energy = 180 keV, 7 deg tilt
D	ICL	9.4	RCA (NO HF DIP)
D	ICL	9.5	drive-in (in N_2) - time = 21hrs, temp = 1150C, recipe # 255, Tube B1
D	ICL	9.6	strip SRO
D, H	TRL	10.1	RCA (Preparation for bonding)
B = D + H	TRL	10.2	wafer bonding (in O_2)
B	ICL	10.3	bonding anneal - temp =1100C, time = 70min, in N_2 atmosphere (Tube A3, recipe # 225)
B	RGL	11.1	strip native oxide (7:1 BOE) for thin-back KOH etch
B	LL	11.2	Grind-back device wafer to a thickness of ~ 100 μm
B	RGL	11.3	electrochemical etch (20% by weight KOH solution) for diffused - junction wafers. And one-sided KOH etch for SOI wafers. (Protect backside of SOI wafers with 2500 Å nitride)
B	RGL	11.4	rinse vigorously in DI water. time = 10min, blow dry in N_2
B	TRL	11.5	acid hood - piranha clean (3:1 H_2SO_4 : H_2O_2) time = 15 min rinse 3 times in dump-to-rinse resistivity tank
B	TRL	11.6	acid hood - dip in 50 : 1 HF for 10 secs rinse three times in dump-to-resistivity tank photo-wet station - spin-dry cycle, monitor resistivity to better than 9 Mohm-cm
B	ICL	11.7	strip nitride in hot phosphoric acid time ~ 1hr (this step is only for SOI wafers)
B	TRL ICL	11.8	RCA station - RCA clean monitor resisvity at the spin-dry cycle with a 160 sec rinse
B	TRL	11.9	HMDS/coat 1 μm of image reversal resist. Pattern with alignment-marks mask. (IR alignment)

	ICL		Plasma etch in etcher -1, time = 10 mins, etch depth ~ 0.4 μm Piranha strip photoresist
B	ICL	12.1	grow SRO - recipe #210, tube = A1
B	ICL	12.2	HMDS/coat photoresist on frontside (2 μm, recipe #7)
B	TRL	12.3	pattern using CP mask (Mask #4, Clear field mask, IR alignment)
B	ICL	12.4	ion implant - dopant = phosphorous, energy = 180 KeV dose = 5e15/cm2, 7 deg tilt (Current-limited implant)
B	ICL	12.5	strip PR (ash 2 times, piranha)
B	ICL	12.6	RCA (for drive-in)
B	TRL	12.7	drive-in (in N2) - time = 4 Hrs, temp = 800 C, tube A3 (Drive-in done with tube in idling condition)
B	ICL	12.8	strip SRO (7:1 BOE) (Check for dewetting)
B	TRL	13.1	pattern for lift-off process using CW mask (Mask #5, Clear field mask) (Image Reversal Resist) 1) HMDS 2) AZ 5214 -E PR 4000 RPM 30 sec, about 1.4 μm 3) 90 C prebake, 30 min 4) 3 sec. exposure, 8.7 mW/cm2 5) 120 C, 90 sec., directly on hot plate 6) 90 sec. flood exposure 7) 80 sec. develop. AZ422-MIF developer
B	TRL	13.2	descum - O2 plasma (~ 40 seconds)
B	ICL	13.3	BOE dip ~ 15 seconds
B	ICL	13.3	e-beam evaporation - on frontside, NO planetary rotation 5000 Å Aluminum
B	TRL	13.4	metal lift-off in acetone - NO ULTRASONIC (after taking wafer out of acetone, immediately squirt some acetone on it, then squirt some methanol, then water. Acetone dries on the surface like glue if immersed in water directly) Spin rinse and dry
B	ICL	14.1	HMDS/coat photoresist on frontside (2 μm, recipe #7)

B	TRL	14.2	pattern for vent holes using CV mask (Mask #6, dark field mask)
B	ICL	14.3	plasma etch silicon, recipe #19, etcher-1, time ~ 13 mins
B	ICL	14.4	ash PR (2 times)
B	TRL	14.5	nanostrip (~ 2 mins to get rid of residual PR)
B	ICL	15.1	HMDS/coat photoresist on frontside (2 μm, recipe #7)
B	TRL	15.2	Pattern structure release using CC mask (Mask #7, dark field mask) Postbake PR for 30 mins. (May need to overexpose and overdevelop to clear the ventholes)
B	TRL	16.1	BOE dip ~ 5 seconds
B	ICL	16.2	e-beam evaporation - on backside 5000 Å Aluminum
B	ICL	17.1	plasma etch silicon, modified recipe #19, etcher-1 (SF_6 = 95 sccm, CCl_4 = 10 sccm)
B	ICL/TRL	17.2	ash PR 2 times, check in TRL fluoroscope to see if PR is cleared
B	ICL	18.1	aluminum sintering - tube B8, recipe #710, approx time = 35 mins

RCA Clean

The RCA clean is a standard wet chemical clean designed to remove organic and ionic contaminants from the wafer surface before entering a high temperature (350°C) diffusion or oxidation step.

The organic clean consists of a 5:1:1 mixture of H_2O:NH_4OH:H_2O_2. The solution is heated to 80°C before the wafers are immersed in it. Following the organic clean (10 mins), the wafers are rinsed in deionized water (DI H_2O) until a resisitivity of 120 Ω-cm is reached. The next step is to dip the wafers in a 50:1 DI H_2O:HF for 15 seconds, to remove any oxide which may have formed during the organic clean. The wafers are rinsed in DI H_2O again. The final step involves the ionic clean of the wafers in a solution of 6:1:1 of H_2O:HCl:H_2O_2. The solution is heated to 80°C before the wafers are immersed in it (for 15 mins). Subsequent to the ionic clean, the wafers are again rinsed in DI H_2O until a resisitivity of 120 Ω-cm is reached and then they are spin-rinsed and dried.

Pirnaha Etch

Piranha is 3:1 solution of H_2SO_4:H_2O_2. This etch is often used to strip photoresist from the wafers (before metallization), to remove any organic contaminants from the wafer or to hydrate (create surface OH^- groups) the wafer surface before the wafer bonding step.

7:1 BOE Etch of Oxide

The buffered oxide etch (BOE) is a 7:1 solution of DI H_2O:HF buffered in NH_4F, which is used for etching oxides. The NH_4F is used to buffer the pH of the solution so that the photoresist layer will not delaminate from the wafer surface during the oxide etch. At room temperature the typical etch rate of thermal oxide in 7:1 BOE is 900 Å/min.

Dry Processes

Plasma Etch

All the plasma etches described in this thesis were carried out in a Lam Research model 480 etcher. The lam etchers are cassette-to-cassette, load-locked, parallel plate electrode single-wafer etchers. The following table describes the parameters and the gas flow rates that were used for the etching of silicon.

Process Parameters	**Step #1**	**Step #2**	**Step #3**	**Step #4**	**Step #5**	**Step #6**	**Step #7**
Chamber Pressure (mTorr)	500	500	200	200	500	500	500
Top electrode RF Power (W)	0	300	0	300	0	0	50
Electrode gap spacing (cm)	1.5	1.5	1.5	1.5	1.5	1.5	1.5
CCL_4 flow rate (sccm)	0	0	130	130	0	3	3
O_2 Flow rate (sccm)	200	200	20	20	0	0	0
He flow rate (sccm)	100	100	70	70	120	120	120
Cl_2 flow rate (sccm)	0	0	0	0	0	0	0
SF_6 flow rate (sccm)	0	0	0	0	0	95	95
Process time	Stabl	6 secs	Stabl	10 secs	90 secs	Stabl	Actual etch time

Photolithography

All the photolithographic steps were performed in TRL using Solitec Inc., Model 5110 manual spinner with Blue M Model DDC - 146C convection ovens for softbake and hardbake steps. A Karlsuss Model MA 4 contact aligner with infrared (IR) alignment capabilities was used for all the patterning steps.

Photoresist

The positive photoresist used in all the photolithographic steps was OCG 825 - 35 CTS (centi Stoke). The photoresist was developed using KTI 934 alkali-ion-free developer. The wafers were coated using a GCA corporation model 1006 Wafertrac. The wafertrac is a cassette-to-cassette process which uses an air-track wafer transport system and hot plate baking modules. Before the coating step, the wafers are primed in a HMDS (hexamethyldisilazane) vapor prime oven (Yield Engineering Systems, Inc., Model 3/10). The standard coating recipe (recipe#11) results in a photoresist layer thickness of 11500 Å. For some of the photolithographic steps we also used a "thick-photoresist" process (recipe#7) which provides a photoresist thickness of 20000 Å. Also, both the recipes could be programmed to incorporate the edge bead removal (EBR) step.

For the metal lift-off step we used an image-reversal photoresist (AZ 5214-E). This photoresist was developed in AZ 422 MIF developer.

Diffusion and Oxidation Steps

All the oxidation and diffusion steps were carried out in ICL using BTU Bruce Engineering Corporation Model BDF-4 furnaces (the atmospheric pressure tubes have an inner diameter of 170 mm and approximate length of 2.11 m). All the furnaces were microprocessor controlled, and wafer lots are introduced into the furnace tubes using suspended, cantilever-loading systems. The oxidation/diffusion recipes used in this thesis were either standard baseline recipes or baseline recipes which were modified for our application.

Appendix E
Detailed Drawings

First-Generation Sensor Plug

- **All dimensions are in <u>inches</u>**
- **Surfaces A and B <u>must</u> be square**
- **Surface S must be flush with the part provided**
- **All Surfaces =** $\sqrt{8}$
- **Material = PMMA**

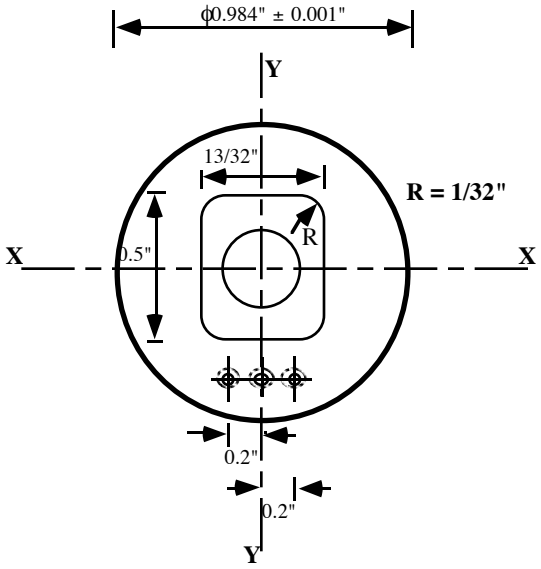

Section YY

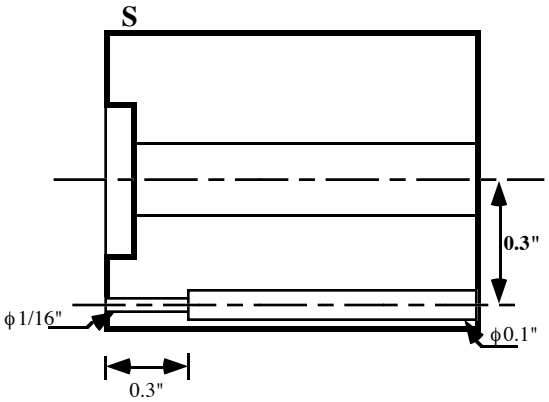

Section XX

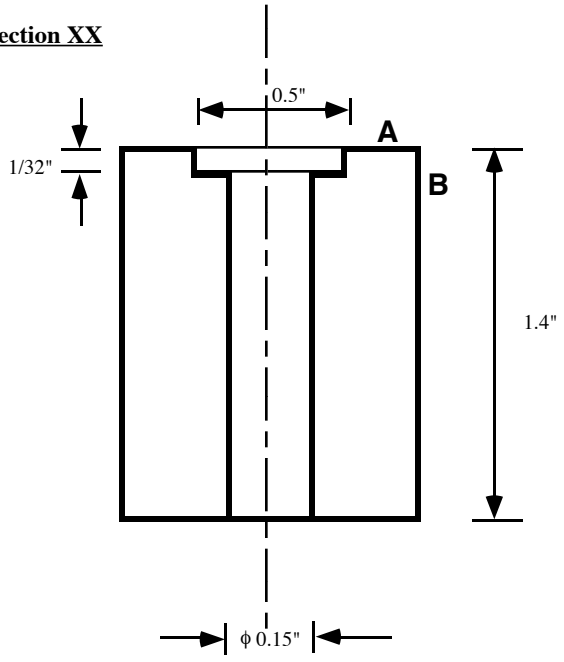

Second-Generation Sensor Plug

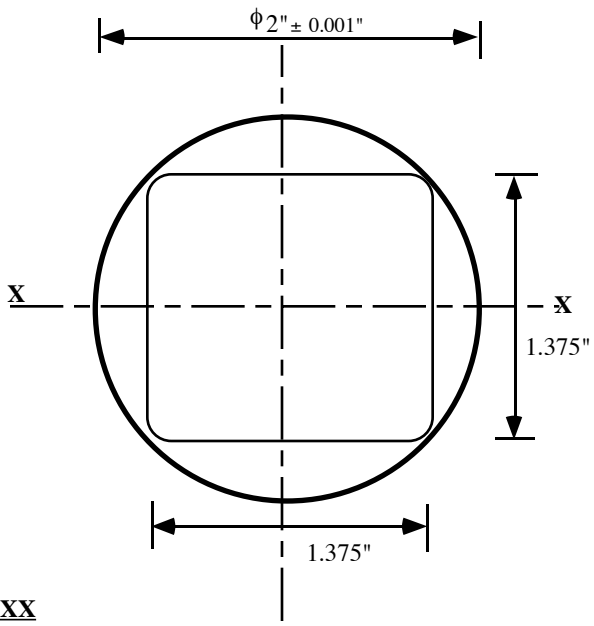

- **All dimensions are in inches**
- **Surfaces A and B must be square**
- **Surface S must be flush with the part provided**
- **All Surfaces =** $\sqrt{8}$
- **Material = PMMA**

Section XX

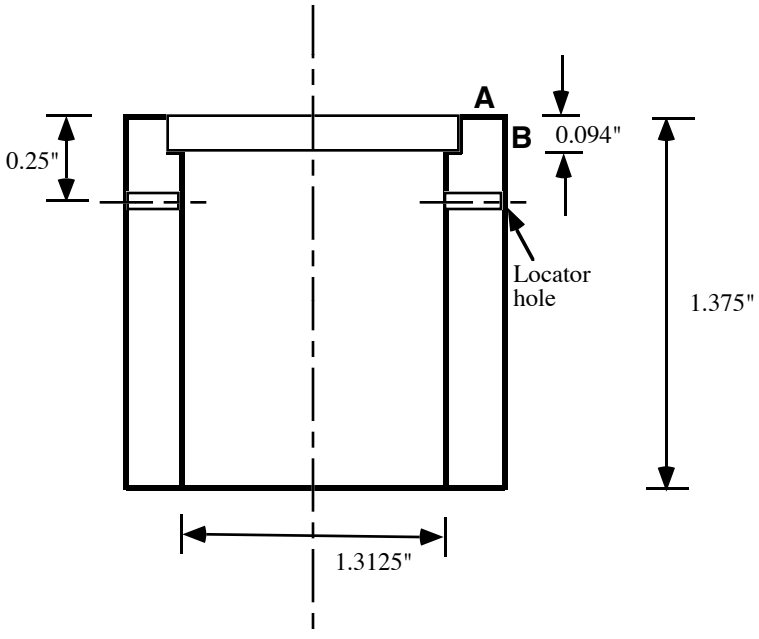

Laminar-Calibration Flow Cell - Bottom Plate

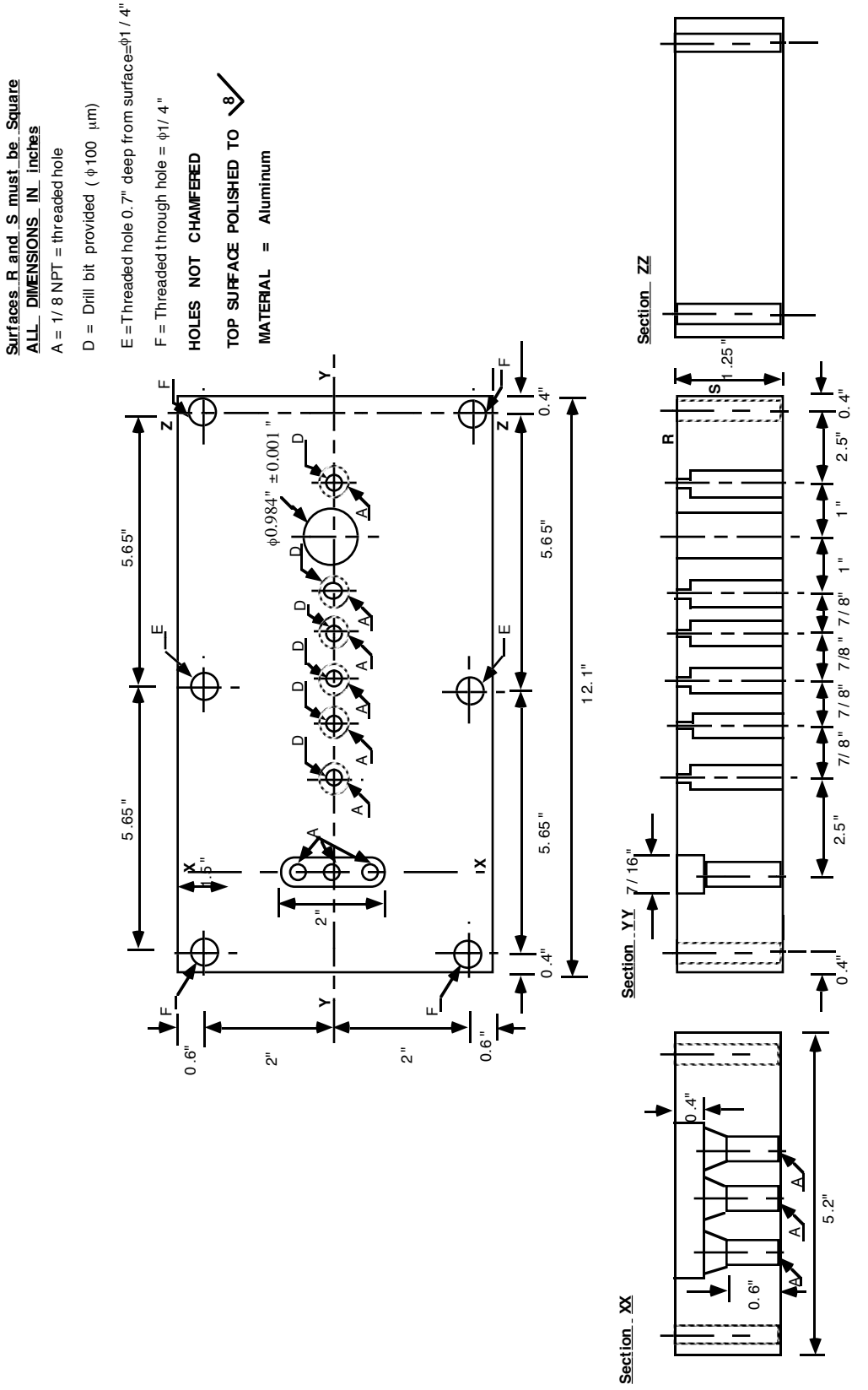

Laminar-Calibration Flow Cell - Top Plate

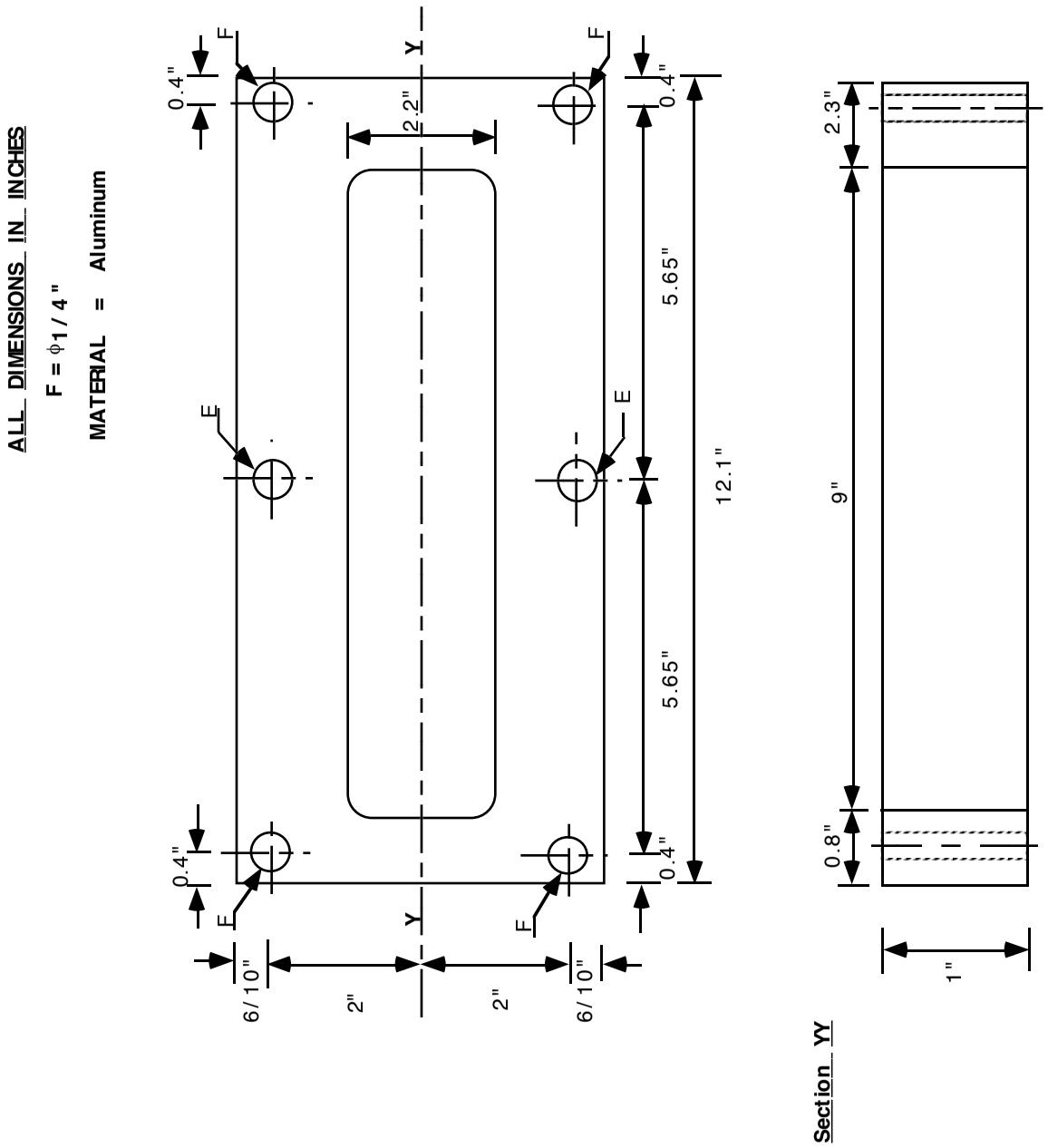

Optical Glass Plate

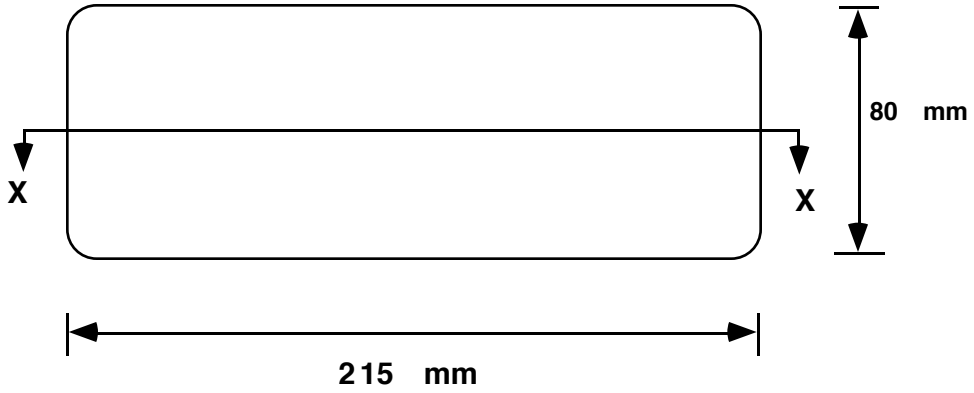

Section XX

length = 215 mm, width = 80 mm, thickness = 15 mm

Specifications

(i) flatness within 1μm or (35/1000000) inches
(ii) surface roughness within 0.1μm or (4/10000000) inches
(iii) rounded corners

Appendix F
Measurement Circuit

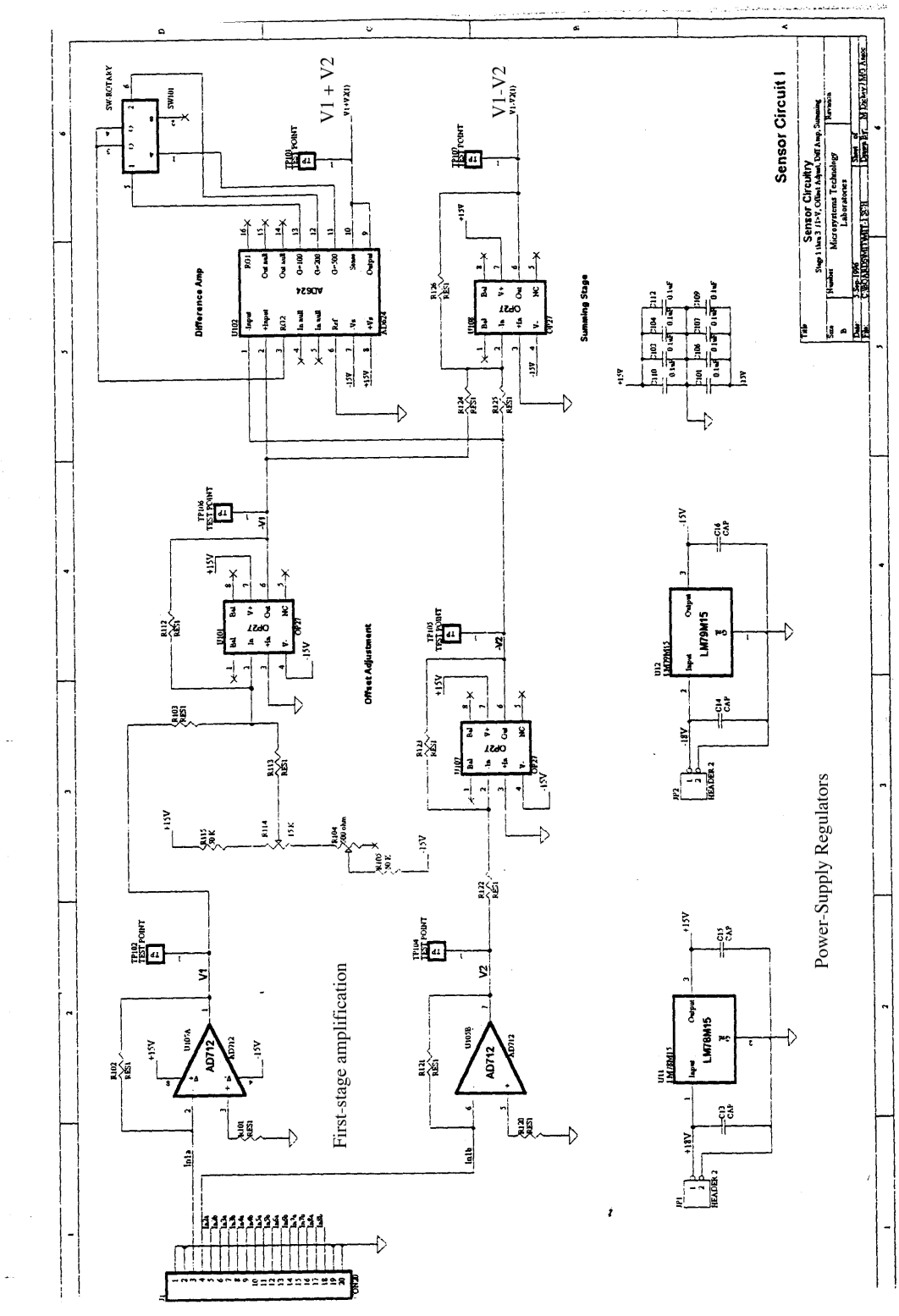

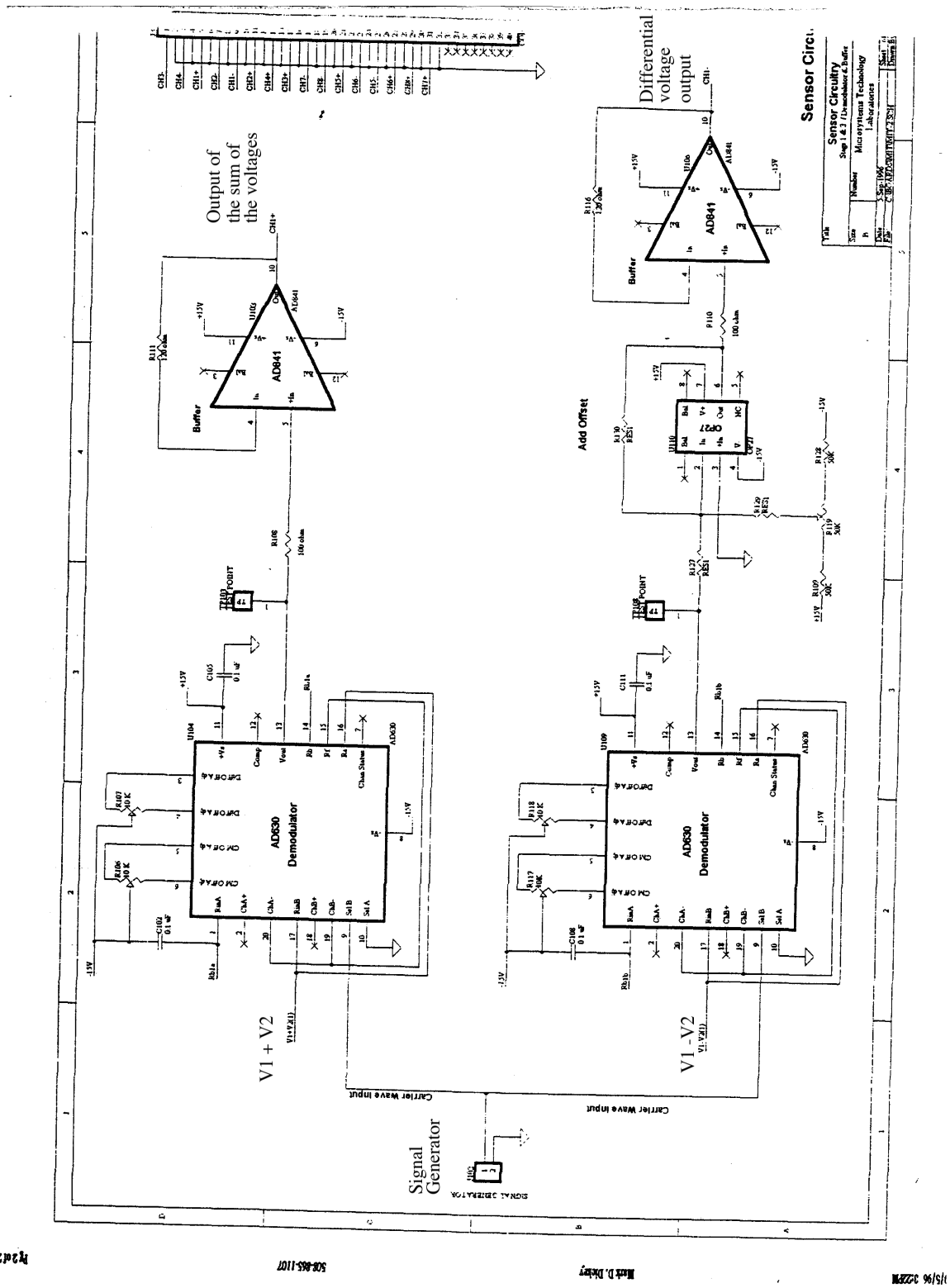
Output of the sum of the voltages
Differential voltage output
Sensor Circuitry
AD841
Buffer
Add Offset
OP27
AD630
Demodulator
V1 + V2
V1 - V2
Signal Generator
Cartier Wave Input
Cartier Wave Input

REFERENCES

[1] K. S. Breuer, "Active control of wall pressure fluctuations in a turbulent boundary layer", *Proceedings of ASME Symposium on Flow Noise Modeling, Measurement and Control*, FED, Vol. 168, pp. 39-48, 1993.

[2] H. Alfredsson, A. V. Johansson, J. H. Haritonidis and H. Eckelman, "The fluctuating wall-shear stress and the velocity field in the viscous sublayer", *Phys. Fluids*, Vol. 31, pp. 1026-1033, 1988.

[3] B. H. Munson, D. F. Young and T. H. Okiishi, *Fundamentals of Fluid Mechanics*, John Wiley & Sons, 1990.

[4] H. Schlichting, *Boundary Layer Theory,* McGraw-Hill, New York, 1972.

[5] K. G. Winter, "An outline of the techniques available for the measurements of skin friction in turbulent boundary layers", *Prog. Aerospace Sci.*, Vol. 18, pp. 1-57, 1977.

[6] T. J. Hanratty, and J. A. Campbell, "Measurements of Wall shear stress", *Fluid Mech. Measurements*, (ed. R. J. Goldstein). Hemisphere Publ. Corp., pp. 559-615, 1983.

[7] J. H. Haritonidis, "The Measurement of Wall Shear Stress", *Advances in Fluid Mechanics Measurements*, Springer-Verlag, pp. 229-261, 1989

[8] R. J. Hakkinen, " Survey of skin friction measurement techniques", *AIAA Minisymposium*, Dayton, Ohio, May 1991.

[9] G. I. Taylor, "Measurements with a Half-Pitot tube", *Proc. Roy. Soc.*, Ser. A, Vol. 166, pp. 476-481, 1938.

[10] L. Trilling, and R. J. Hakkinen, "The calibration of the Stanton tube as skin-friction meter", in "50 Jahre Grenzchichtforschung", F. Vieweg & Sohn, 1955.

[11] T. E. Stanton, D. Marshall, and C. N. Bryant, "On the conditions at the boundary of a fluid in turbulent motion", *Proc. Roy. Soc.*, Series A, Vol. 97, pp. 413-434, 1920.

[12] J. H. Preston, "The determination of turbulent skin-friction by means of pitot tubes", *J. Roy. Aeron. Soc.*, Vol. 58, pp. 109-121, 1954.

[13] H. Ludweig, and W. Tillman, "Untersuchungen uber die wandschubspannung in turbulenten reibungsschichten", *Ing. Arch.*, Vol. 17, pp. 288-299, 1949. Also in English, *NACA TM-1284*, 1950.

[14] H. W. Lipemann, and G. T. Skinner, "Shearing-stress measurements by use of a heated element", *Ph. D Thesis*, California Institute of Technology, 1954. Also *NACA TN-3268.*

[15] B. J. Bellhouse, and D. L. Schultz, "The measurement of skin-friction in supersonic flow by means of heated thin film gauges", *ARC R & M*, **3490**, 1965.

[16] J. S. Murphy, and A. M. O. Smith, "Measurement of wall shearing stress in the boundary layer by means of an evaporating liquid film", *Journal of Applied Physics*, Vol. 27, **9**, pp. 1097-1103, 1956.

[17] A. R. Wazzan, A. M. O. Smith, and R. C. Lind, "Mass-transfer method of measuring wall shear-stresses in supersonic flow, *Phys. Fluids*, Vol. 8, **9**, pp. 1642-1646, 1965.

[18] M. K. Mazumder, S. Wanchoo, P. C. Mcleod, G. S. Ballard, S. Mozumder, and N. Caraballo, "Skin-friction drag measurements by LDV", *Applied Optics*, Vol. 20, pp. 2831-2837, 15th August, 1981.

[19] F. H. Clauser, "Turbulent boundary layers in adverse pressure gradients", *J. Aeron. Sci.*, Vol. 21, **2**, pp. 91-108, 1954.

[20] S. Dhawan, "Direct measurement of skin-friction", *Ph. D.Thesis*, California Institute of Technology, 1951. Also *NACA Report 1121*, 1953.

[21] D. Coles, "Measurements in the boundary layer on a smooth flat plate in a supersonic flow", *Ph. D Thesis*, California Institute of Technology, 1953.

[22] R. J. Hakkinen, "Measurements of skin-friction in transonic flow", *Ph. D Thesis*, California Institute of Technology, 1954. Also, *NACA TN-3486*, 1955.

[23] R. H. Korkegi, "Transition studies and skin-friction measurements on an insulated flat plate at a hypersonic mach number", *Ph. D Thesis*, California Institute of Technology, 1954.

[24] M. Eimer, "Direct measurement of laminar skin-friction at hypersonic speeds", *Ph. D Thesis*, California Institute of Technology, 1955.

[25] R. L. Richmond, "Experimental investigation of thick, axially symmetric boundary layers on cylinders at subsonic and hypersonc speeds", *Ph. D Thesis*, California Institute of Technology, 1957.

[26] J. M. Allen, "Experimental study of error sources in skin-friction balance measurements", *Journal of Fluid Engg.*, Vol. 99, pp. 197-204, 1977.

[27] J. O. Hinze, *Turbulence*, Second Edition, McGraw-Hill, 1975.

[28] M. A. Schmidt, "Microsensors for the measurement of shear forces in turbulent boundary layers", *Ph. D Thesis*, Dept. of Electrical Engineering and Computer Science, M.I.T, 1988.

[29] D. Frei, and H. Thomann, "Direct measurements of skin friction in a turbulent boundary layer with a strong adverse pressure gradient", *Journal of Fluid Mechanics*, Vol. 101, Part 1, pp. 79-95, 1980.

[30] Y. Gur and P. Leehey, "A new wall shear stress gauge", *Experiments in Fluids*, Vol. 8, pp. 145-152, 1989.

[31] P. R. Bandyopadhay and L. M. Weinstein, "A reflection-type oil-film skin-friction meter", *Experiments in Fluids*, Vol. 11, pp. 281-292, 1991.

[32] J. Putz, J. Putz, A. Wicks and T. Diller, "Thin-film shear stress gage", *Microstructures, Sensors, and Actuators*, Vol. 19, pp. 137-147, 1990.
[33] K. E. Petersen, "Silicon as a mechanical material", *Proceedings of the IEEE*, Vol. 70, No. 5, pp. 420-457, 1982.
[34] J. Bryzek, K. Petersen, and W. McCulley, "Micromachines on the march", *IEEE Spectrum*, pp. 20-31, May, 1994.
[35] K. D. Wise, and K. Najafi, "Microfabrication techniques for integrated sensors and microsystems", *Science*, pp. 1335-1342, 29th November, 1991.
[36] L. Ristic, *Sensor Technology and Devices*, Artech House, Boston, 1994.
[37] R. T. Howe, "Surface micromachining for microsensors and microactuators", *Journal of Vacuum Science and Technology*, Vol. B6, pp. 1809-1813, 1988.
[38] M. Mehregany, "Microfabricated silicon electric mechanisms", *Ph. D Thesis*, Dept. of Electrical Engineering and Computer Science, M.I.T, 1990.
[39] L. J. Hornbeck, "Current status of the digital micromirror device (DMD) for projection television applications", *Technical Digest*, IEDM, pp. 15.1.1-15.1.4, 1993.
[40] F. Goodenough, "Airbags boom when IC accelerometer sees 50 G", *Electronic Design*, Cover Feature, 8th August, 1991.
[41] E. W. Becker, W. Ehrfield, P. Hagmann, A. Maner, and D. Munchmeyer, "Fabrication of microstructures with high aspect ratios and great structural heights by synchrotron radiation lithography, galvanoforming, and plastic molding (LIGA process)", *Microelectronic Engineering*, Vol. 4, p. 35, 1986.
[42] H. Guckel, J. Klein, T. Christenson, K. Skrobis, M. Laudon, and E. G. Lovell, "Thermomagnetic metal flexture actuators", *Technical Digest*, Solid-state Sensor and Actuator Workshop, Hilton Head Island, p. 73, 1992.
[43] M. A. Schmidt, R. T. Howe, S. D. Senturia, and J. H. Haritonidis, "Design and Calibration of a microfabricated floating-element shear-stress sensor", *IEEE Transactions on Electron Devices*, Vol. ED-35, pp. 750-757, 1988.
[44] T. Pan, D. Hyman, M. Mehregany, E. Reshotko, and B. Williams, "Characterization of microfabricated shear stress sensors", *Proceedings of 16th International Congress on Instrumentation in Aerospace Simulation Facilities*, WPAFB, OH, July 1995.
[45] Ng, K-Y., 1990, "A Liquid Shear-Stress Sensor Using Wafer-Bonding Technology," *M. S Thesis*, Massachusetts Institute of Technology.
[46] H. D. Goldberg, K. S. Breuer and M. A. Schmidt, "A silicon wafer-bonding technology for microfabricated shear-stress sensors with backside contacts", *Technical Digest*, *Solid-State Sensor and Actuator Workshop*, pp. 111-115, 1994.

[47] B. Oudheusden, and J..Huijsing, " Integrated flow friction sensor, *Sensors and Actuators A*, **15**, pp. 135-144, 1988.

[48] C. Liu, Y. Tai, J. Huang, and C. Ho, "Surface micromachined thermal shear stress sensor", *Proceedings*, The ASME Symposium on Application of microfabrication to Fluid Mechanics, Winter Annual Meeting, Chicago, 1994.

[49] F. Jiang, Y. C. Tai, C. M, Ho and W. J. Li, "A micromachined polysilicon hot-wire anemometer", *Technical Digest*, Solid-state Sensor and Actuator Workshop, Hilton Head Island, pp. 264-267, 1994.

[50] E. Kalvesten, "Pressure and wall shear stress sensors for turbulence measurements", *Ph. D Thesis*, Royal Institute of Technology, Stockholm, Sweden, 1996.

[51] A. Padmanabhan, H. Goldberg, K. Breuer, and M. A. Schmidt, "A wafer-bonded floating-element shear stress microsensor with optical position sensing by photodiodes", *Journal of Microelectromechanical Systems*, Vol. 5, No. 4, pp. 307-315, 1996.

[52] F. Jiang, Y. C. Tai, B. Gupta, R. Goodman, S. Tung, J. B. Huang, and C. M. Ho, "A surface-micromachined shear stress imager", *Proc. IEEE Microelectromechanical Systems (MEMS '96*), San Diego, pp. 110-115, 1996.

[53] V. P. Jaecklin, C. Linder, and N. F. De Rooij, "Optical microshutters and torsional micromirrors for light modulator arrays", *Proc. IEEE Microelectromechanical Systems (MEMS '93*), Ft. Lauderdale, pp. 124 127, 1993.

[54] L. J. Hornbeck, "Deformable-mirror spatial light modulators", Proc. Soc. Photo-Opt. *Instrm. Eng*, **1150**, pp. 86 - 102, 1989.

[55] H. Toshiyoshi, H. Fujita, T. Kawai, and T. Ueda, "A piezoelectrically operated optical chopper by quartz micromachining", *Technical Digest*, *Transducers '93, 7th International Conference on Solid-State Sensors and Actuators*, pp. 128-131, 1993.

[56] E. Abbaspour-Sani, R. S. Huang, and C. Y. Kwok, "A novel optical accelerometer", *IEEE Electron Device Letters*, Vol. 16, No. 5, 1995.

[57] E. W. Jansen, "Electric micromotor with integrated rotor motion sensors", *Ph. D Thesis*, Department of Electrical Engineering and Computer Science, MIT, 1996.

[58] O. Tabata, R. Asahi, N. Fujitsuka, M. Kimura and S. Sugiyama, "Electrostatic driven optical chopper using SOI wafer", *Technical Digest*, *Transducers '93, 7th International Conference on Solid-State Sensors and Actuators*, pp. 124-127, 1993.

[59] G. W. Neudeck, *Volume II*:*The PN Junction Diode*, Second Edition, Addison-Wesley Publishing Company, Massachusetts, 1989. Modular Series on Solid State Devices.

[60] S. M. Sze, *Physics of Semiconductor Devices*, Second Edition, John Wiley and Sons, 1981.

[61] L. K. Anderson, and B. J. McMurtry, “High-speed photodetectors”, *Proceedings of the IEEE*, Vol. 54, No. 10, pp. 1335-1349, 1996.
[62] M. B. Spitzer, S. P. Tobin, and C. J. Keavney, “High-efficiency ion-implanted silicon solar cells”, *IEEE Transactions on Electron Devices*, Vol. ED-31, No. 5, pp. 546-550, 1984.
[63] T. P. Lee and T. Li, Photodetectors. In S. E. Miller and G. Chynoweth, *Optical Fiber Telecommunications*, pages 593-626. Academic Press, NewYork, 1979.
[64] Stanford Electronics Laboratories, Department of Electrical Engineering, Stanford, CA 94305. *SUPREM-III*, version 8520 edition.
[65] J. M. Senior, *Optical Fiber Communications, Principles and Practice*, Pretice-Hall, NewJersey, pp. 327-385, 1984.
[66] P. J. Fish, *Electronic Noise and Low Noise Design*, McGraw-Hill, NewYork, 1994.
[67] T. B. Gabrielson, “Mechanical-thermal noise in micromachined acoustic and vibration sensors”, *IEEE Transactions on Electron Devices*, Vol. 40, No. 5, pp. 903-909, 1993.
[68] S. D. Senturia, and B. D. Wedlock, *Electronic Circuits and Applications*, Krieger Publishing Company, Florida, 1993.
[69] Application Notes, Power Technology Incorporated, Box 191117, Little Rock, Arkansas 72219-1117.
[70] J. M. Gere and S. P. Timoshenko, *Mechanics of Materials*, Second Edition, SPWS Publishers, 1984.
[71] Porges, G., *Applied Acoustics*, Edward Arnold, London, 1977.
[72] S. G. Kelly, *Fundamentals of Mechanical Vibrations*, Mcgraw-Hill, Inc., 1993.
[73] Y-H. Cho, A. P. Pisano, and R. T. Howe, “Viscous damping model for laterally oscillating microstructures”, *J-MEMS*, pp. 81-86, 1994.
[74] E. Arkilic and K. S. Breuer, “Gaseous flow in small channels”, *Proceedings of AIAA Shear Flow Conference*, 1993.
[75] M. M. Denn, *Process Fluid Mechanics*, Prentice-Hall, 1980.
[76] J. B. Starr, “Squeeze-film damping in solid-state accelerometers”, Technical Digest, *Solid-State Sensor and Actuator Workshop*, pp. 44-47, 1990.
[77] F. M. White, *Viscous Fluid Flow*, Mcgraw-Hill, Inc., 1991.
[78] W. C. Tang, "Electrostatic Comb Drive for Resonant Sensor and Actuator Applications," *Ph. D Thesis*, Univ. Of California, Berkeley, 1990.
[79] P. M. Osterberg, R. K. Gupta, J. R. Gilbert, and S. D. Senturia, “Quantitative models for the measurement of residual stress, Poisson’s ratio and Young’s modulus using electrostatic pull-in of beams and diaphragms”, in *Technical Digest*, *IEEE Solid-State Sensor and Actuator Workshop*, (Hilton Head island, South Carolina), pp. 184-188, 1994.

[80] S. J. Kline, W. C. Reynolds, F. A. Schraub, and P. W. Runstadler, P. W., "The Structure of Turbulent Boundary Layers," *The Journal of Fluid Mechanics*, Vol. 30, pp. 741, 1967.

[81] S. A. Jacobson, and W. C. Reynolds, *An Experimental Investigation Towards the Active Control of Turbulent Boundary Layers*, Report No. TF-64, Thermosciences Division, Dept. of Mechanical Engineering, Stanford University, 1995.

[82] K. S. Breuer, J. H. Haritonidis, and M. T. Landahl, "The control of transient disturbances in a flat plate boundary layer through active wall motion", *Phys. Fluids A.* **1**, pp. 574-582, 1989.

[83] H. Choi, P. Moin, and J. Kim, "Active turbulence control for drag reduction in wall-bounded flows", *Journal of Fluid Mechanics*, **262**, pp. 75-110, 1994.

[84] P. R. Bandyopadhay, "Development of a microfabricated surface for turbulence diagnostics and control", *ASME, Application of Microfabrication to Fluid Mechanics*, Chicago, pp. 67-74, 1994.

[85] C. Hsu and M. A. Schmidt, "Micromachined structures fabricated using a wafer-bonded sealed cavity process", *Technical Digest*, *Solid-State Sensor and Actuator Workshop*, pp. 151-155, 1994.

[86] G. C. Billingsley, *Program Reference for KIC*, Electronic Research Lab., Department of Electrical Engineering and Computer Science, UC Berkeley, 1983.

[87] J. B. Lasky, "Wafer-bonding for silicon-on-insulator technologies", *Appl. Phys. Lett.*, Vol. 48, p. 78, 1986.

[88] M. A. Schmidt, "Silicon wafer-bonding for micromechanical devices", *Technical Digest*, *Solid-State Sensor and Actuator Workshop*, pp. 127-131, 1994.

[89] M. Grundner, and H. Jacob, "Investigation on hydrophilic and hydrophobic silicon (100) wafer surfaces by X-ray photoelectron and high-resolution electron energy-loss spectroscopy", *Appl. Phys.*, Vol. A39, p. 73, 1986.

[90] W. P. Maszara, "Silicon-on-insulator by wafer-bonding: A review", *Journal of the Electrochemical Society*, Vol. 138, no. 1, pp. 341-347, 1991.

[91] J. Shajii, "A microfabricated liquid shear-stress sensor utilizing a backside contact process", *MS Thesis*, Department of Electrical Engineering and Computer Science, MIT, 1992.

[92] L. Parameswaran, "Silicon pressure sensor using wafer-bonding technology", *MS Thesis*, Department of Electrical Engineering and Computer Science, MIT, 1993.

[93] C. T. Sah, "The evolution of the MOS transistor", *Proceedings of the IEEE*, p. 1280, 1980.

[94] Motorola Semiconductor Products Sector, Direct Wafer Bonding Group, Phoenix, AZ.

[95] V. M. Mcneil, "A thin-film silicon microaccelerometer fabricated using electrochemical etch-stop and wafer bonding technology", *Ph.D Thesis*, Department of Electrical Engineering and Computer Science, MIT, 1994.
[96] Solecon Laboratories, 2241 Paragon Drive, San Jose, CA 95131.
[97] L. Parameswaran, C. H. Hsu, and M. A. Schmidt, "A merged MEMS-CMOS process using silicon wafer bonding", *Technical Digest*, *International Electron Devices Meeting*, pp. 613-616, 1995.
[98] H. D. Goldberg, and M. A. Schmidt, "Backside contacts for sensor microstructures", United States Patent, April 1996, patent # 5511428.
[99] P. K. Tedrow, and C. G. Sodini, "MIT twin well CMOS process", *Microsystems Technology Laboratories*, *MIT*, July 1993, Version 1.3.
[100] P. M. N. Associates, P. O. Box 354, East Hampstead, New Hampshire, 03826.
[101] R. E. Rayle Jr., "An investigation of the influence of orifice geometry on static pressure measurements", *MS Thesis*, MIT, 1949.
[102] Microswitch, *Pressure Sensors*, Catalog 15, Honeywell Inc., 11 West Spring Street, Freeport IL 61032.
[103] Setra Systems, 45 Nagog Park, Acton, MA 01720.
[104] W. M. Siebert, *Circuits, Signals and Systems*, The MIT Press, Cambridge, MA & McGraw-Hill, NewYork, 1994.
[105] Stanford Research Systems, 1290-D Reamwood Avenue, Sunnyvale, CA 94089.
[106] P. J. Fish, *Electronic Noise and Low Noise Design*, McGraw-Hill, NewYork, 1994.
[107] R. Morrison, *Grounding and Shielding Techniques in Instrumentation*, Third Edition, John Wiley and Sons, NewYork, 1986.
[108] H. N. Norton, *Handbook of Transducers for Electronic Measuring Systems*, Prentice-Hall, Inc., Englewood Cliffs, NewJersey, 1969.
[109] K. Ogata, *Modern Control Engineering*, Prentice-Hall, Inc., Englewood Cliffs, NewJersey, 1970.
[110] P. M. Morris, and K. U. Ingard, *Theoretical Acoustics*, McGraw-Hill, Inc., NewYork, pp. 511, 1968.
[111] "AES Information Document - Plane-wave Tubes: Design and Practice", *AES-1ID-1991*, *Audio Engineering Society*, Inc., NewYork, 1991.
[112] S. Lee, "Stokes' layer calibration of shear-stress sensor thorugh acoustic plane wave excitation", *AUP report*, Department of Electrical Engineering and Computer Science, MIT, 1996 (unpublished).
[113] Prof. K. U. Ingard, Private Communication.

[114] K. S. Breuer, “Stochastic calibration of sensors in turbulent flow fields”, *Experiments in Fluids,* Vol. 19, No. 2, pp. 138-141, 1995.